

**An Experimental Study of Ion Behavior in
the Advanced Toroidal Facility**

**A Dissertation
Presented to
The Academic Faculty
by
Mickey Ray Wade**

**In Partial Fulfillment
of the Requirements for the Degree of
DOCTOR OF PHILOSOPHY**

**Georgia Institute of Technology
September 1991**

An Experimental Study of Ion Behavior in the Advanced Toroidal Facility

APPROVED:

C. E. Thomas, Chairman

Date

W. M. Stacey

J. Mandrekas

A. Zangwill

J. A. Rome

Dedicated
to my parents, Bobby and Ella Wade.

Acknowledgments

First, I would like to thank my thesis advisor, Dr. C. E. (Tommy) Thomas, for his support, guidance, and motivation throughout this project and throughout my stay at Georgia Tech. Special thanks must also be given to Dick Colchin who provided much needed guidance and technical expertise during my research at Oak Ridge National Laboratory (ORNL). I also wish to thank Drs. Bill Stacey, John Mandrekas, Andy Zangwill, and Jim Rome for serving as thesis committee members.

It is impossible to properly thank the many people who have contributed to this work. I am deeply indebted to the ORNL Fusion Energy Division and to the Advanced Toroidal Facility (ATF) staff for the opportunity to perform this research. Special thanks must be extended to John Sheffield and Julian Dunlap for faithfully funding this research in a period when fusion funding was hard to obtain. I would like to thank Masonari Murakami for providing dedicated operational time for these experiments in the midst of an already overextended operating schedule. Special thanks must also be given to the ATF operations crew — namely, Jack Yarber, Chuck Schaich, L. A. Massengill, Tom Rayburn, Jesse Simpkins, and Billy Redmond — for painstakingly keeping ATF operational up to the very end.

The design, installation, operation, and maintenance of the neutral particle analyzer (NPA) required the dedicated efforts of many people. Special thanks is extended to Sid Medley and Lane Roquemore of Princeton Plasma Physics Laboratory (PPPL) for the design and development of the NPA and for Lane's continuing technical assistance and help with the installation and alignment of the NPA on ATF, Keith St. Onge for the design and engineering of the NPA carriage, and Jack Alford and Eugene Purdy for their expert craftsmanship and dedicated work in assembling

the NPA and carriage.

Because the analysis presented in this thesis required measurements from many different diagnostic systems, there are many people to whom I am grateful for providing data from various diagnostics and for timely responses to my various requests. Most notable among these are: Drs. Dave Rasmussen, Al England, and Larry Baylor and the entire RATTS team for providing Thomson scattering data; Drs. Ralph Isler, Lorne Horton, and Charlie Crume for providing spectroscopic data and insight on the simulation of such data; and Drs. Gary Bell and John Wilgen for providing ECE measurements. I would also like to thank Drs. Jim Rome and Jim Lyon for many enlightening discussions on ion behavior in ATF.

Data analysis has benefited from the extensive use of several different computer codes. I especially wish to thank Dr. Ron Fowler for providing his fast-ion Fokker-Planck code and Monte Carlo simulation code and Dr. Herb Howe for use of the PROCTR transport simulation code. Special thanks are also extended to Dave Greenwood, Russ Overbey, and Terrell Patrick for providing excellent (and timely) computer support during my stay at ORNL.

My heartfelt appreciation is extended to my wife, Stephanie, who has faithfully supported me throughout the past five years. Without her love, patience, and undying support, this research would not have been possible. Also, I would like to thank my parents for their encouragement and support over the last five years.

Finally, and most importantly, I would like to thank God for the opportunity and ability to carry out such an endeavor as this.

This work was performed at the Fusion Energy Division of Oak Ridge National Laboratory and was sponsored by the Office of Fusion Energy, U.S. DOE, under contract number DE-AC05-84OR21400 to Martin Marietta Energy Systems, Inc.

Table of Contents

Acknowledgments	iv
Table of Contents	vi
List of Tables	ix
List of Figures	x
Summary	xv
I. Introduction	1
1.1 Plasma Confinement	6
1.2 Plasma Heating	9
1.3 Diagnostics for Fusion Plasmas	13
1.4 Ion Confinement Issues in ATF	15
1.5 Outline of Dissertation	17
References	19
II. Theory of Ion Behavior in Toroidal Devices	20
2.1 Orbit Effects	20
2.2 Effect of Collisions on Ion Behavior	45
2.3 Summary	64
References	66

III. Previous Ion Confinement Studies	69
3.1 Tokamak Thermal Ion Confinement Studies	69
3.2 Tokamak Fast Ion Confinement Studies	74
3.3 Stellarator Ion Confinement Studies	77
3.4 Summary	83
References	85
IV. Ion Orbit Studies in ATF	88
4.1 General Considerations	89
4.2 Effect of Magnetic Configuration	99
4.3 Effect of the Radial Electric Field	107
4.4 Effect of Orbit Topology on Fast-Ion Confinement	110
4.5 Effect of Orbit Topology on NPA Measurements	116
4.6 Summary	120
References	123
V. Thermal Ion Behavior in ATF	124
5.1 Experimental Setup	124
5.2 Diagnostics	126
5.3 Observations	128
5.4 Summary	146
References	148
VI. Fast Ion Confinement Studies in ATF	149
6.1 Operating Regimes during NBI in ATF	149
6.2 NBI Studies in Ultralow-Density Plasmas	152
6.3 NBI Studies in Low-Density Plasmas	176
6.4 NBI Studies in High-Density Plasmas	198

6.5	Conclusions	203
	References	207
VII.	Summary and Conclusions	208
7.1	Review of Results	208
7.2	Proposed Future Work	217
	References	220
A.	Charge-Exchange Neutral Analysis on ATF	221
A.1	Using Charge-Exchange Neutrals as an Ion Diagnostic	221
A.2	Neutral Particle Analyzer on ATF	228
A.3	Data Analysis	241
	References	256
B.	FPACX Simulation Code	259
B.1	Physics Models in FPACX	259
B.2	Restrictions on using FPACX for ATF	272
	References	275
	Vita	

List of Tables

4.1	Dependence of heating efficiency in ATF on electron temperature . .	115
5.1	Dependence of T_i on input parameters to neutral density calculation .	133
6.1	Low-density DESORBS calculation	190
6.2	High-density DESORBS calculation	204
A.1	Detection efficiency of NPA energy channels	240

List of Figures

1.1	Artist's sketch of ATF	5
1.2	Schematic of neutral beam injection process	11
1.3	Orientation of neutral beam injectors and NPA on ATF	12
2.1	Magnetic field strength along a field line in a tokamak and stellarator	25
2.2	Coordinate system for real-space integration	29
2.3	Calculated trajectories for 10-keV protons in ORMAK	34
2.4	Calculated loss regions for 10-keV protons in ORMAK	36
2.5	Minimum B contours in ATF	41
2.6	Example of J^* contours in ATF	44
2.7	Comparison of J^* contours with orbit calculations	44
2.8	Effect of charge-exchange on the fast-ion distribution	59
4.1	Variation of orbit topology with pitch angle in ATF	91
4.2	Calculated loss region for ATF	94
4.3	Orbit classes in ATF	96
4.4	Dependence of orbit topology on particle energy	98
4.5	Variation of magnetic geometry with magnetic configuration in ATF .	100
4.6	Variation of B_{\min} contours with magnetic axis in ATF	102
4.7	Variation of B_{\min} contours with quadrupole moment in ATF	104

4.8	Variation of trapped particle confinement with magnetic configuration in ATF	105
4.9	Dynamic scan of trapped particle fraction in ATF	106
4.10	Effect of the electrostatic potential on the ATF orbit topology	109
4.11	Monte Carlo simulation in ATF	111
4.12	Evolution of constant J^* contours as particle slows down in ATF . . .	113
4.13	Orbit topology viewed by the NPA	117
4.14	Calculated loss region with respect to the NPA viewing orientation on ATF	119
5.1	Typical ECH discharge in ATF	128
5.2	Measured electron density and temperature profiles during ECH . . .	129
5.3	Energy spectrum measured by NPA during ECH	130
5.4	Vertical scanning capability of NPA on ATF	135
5.5	Measured ion temperature profile during ECH	135
5.6	Variation of plasma minor radius along NPA sightlines	136
5.7	Variation of measured ion temperature with magnetic configuration .	141
5.8	High-energy tail measured by NPA during configuration scan	142
5.9	Evolution of extremely low-density ECH discharge	144
6.1	NBI operating regimes in ATF	150
6.2	Evolution of a typical ultralow-density discharge	154
6.3	Evolution of discharges following titanium gettering	156
6.4	Near-tangential charge-exchange energy spectra in a typical ultralow- density NBI discharge	158

6.5	Measured angular dependence of energy spectra in a typical ultralow-density discharge	159
6.6	Co-passing and counter-passing energy spectra in a typical ultralow-density discharge	160
6.7	Perpendicular energy spectra during a typical ultralow-density discharge	161
6.8	FPACX simulation of measured energy spectra in a typical ultralow-density discharge	165
6.9	Origination of charge-exchange flux in a typical ultralow-density discharge	166
6.10	Beam power distribution in a typical ultralow-density discharge . . .	167
6.11	PROCTR simulation of electron line density in a typical ultralow-density discharge	171
6.12	PROCTR simulation of electron temperature in a typical ultralow-density discharge	171
6.13	PROCTR simulation of the plasma stored energy in a typical ultralow-density discharge	172
6.14	Variation of pitch angle as an injected ion slows down in a typical ultralow-density plasma	175
6.15	Evolution of a typical low-density NBI discharge	177
6.16	Tangential energy spectra during a typical low-density discharge . . .	179
6.17	Tangential energy spectra at time of collapse in a typical low-density NBI discharge	180
6.18	Angular dependence of measured energy spectra in a typical low-density discharge	181

6.19 FPACX simulation of tangential energy spectra in a typical low-density discharge	183
6.20 FPACX simulation of tangential energy spectra at various times in a typical low-density discharge	184
6.21 FPACX simulation of energy spectra for various viewing angles in a typical low-density discharge	187
6.22 Beam power distribution in a typical low-density discharge	189
6.23 Comparison of simulated spectral line intensities with measured data in a typical low-density discharge	194
6.24 PROCTR simulation of measured data in a typical low-density discharge	196
6.25 Global power balance in a typical low-density discharge	197
6.26 Evolution of a typical high-density NBI discharge	199
6.27 Measured energy spectrum in a typical high-density NBI discharge	200
6.28 Origination of measured spectra in a typical high-density discharge	201
6.29 Beam power distribution in a typical high-density discharge	203
A.1 Comparison of reaction rates of various ionization processes	223
A.2 Schematic of the $E\parallel B$ analyzer used on ATF	229
A.3 $E\parallel B$ analyzing scheme	230
A.4 Moving carriage for NPA on ATF	232
A.5 Signal and data acquisition system for NPA	234
A.6 Facility used for calibration of NPA	236
A.7 Stripping cell efficiency of NPA	239

A.8	Energy resolution of NPA	239
A.9	Charge-exchange reaction rate at various proton energies	243
A.10	Variation of neutral density profile with edge neutral energy	248
A.11	Computer simulation of origination of measured energy spectra	252
B.1	Variation of normalized minor radius along NPA sightlines	271
B.2	Variation of "viewed" pitch angle along NPA sightlines	271

Summary

Stellarators represent one of the most promising magnetic confinement concepts for a fusion reactor because of their intrinsic ability to operate at steady state, though legitimate concerns about various aspects of the stellarator concept must be addressed. One of these concerns is the seemingly unfavorable single-particle confinement properties inherent to the stellarator design. Although previous experimental studies of ion confinement in stellarators have indicated that the ions behave classically and are generally well confined, these studies were limited in scope. To complement these experiments and to provide additional information about ion behavior in stellarators, an experimental investigation of ion behavior has been performed on the Advanced Toroidal Facility (ATF). Measurements were made of both the thermal- and fast-ion distributions during electron cyclotron heating (ECH) and neutral beam injection (NBI). The purpose of this work was to study thermal- and fast-ion confinement in ATF with particular emphasis placed on constructing a consistent picture of ion confinement based on experimentally measured data. The primary ion diagnostic used in these studies was a two-dimensional scanning neutral particle analyzer (NPA).

Extensive studies of fast-ion behavior in various operating regimes on ATF were conducted. These studies were performed during NBI and encompass a wide range of plasma densities, ranging from extremely low density ($\bar{n}_e \leq 7.5 \times 10^{12} \text{ cm}^{-3}$) to extremely high density ($\bar{n}_e \geq 8.0 \times 10^{13} \text{ cm}^{-3}$). Fokker-Planck simulations of the measured data suggest that the injected ions behave classically and indicate that the injected beam power is not well absorbed at low and intermediate densities because of large charge-exchange and shine-through losses. Further simulations using the

PROCTR transport analysis code indicate that this reduced absorption is probably the cause of the thermal collapse observed in intermediate-density NBI discharges.

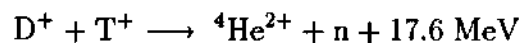
Thermal ion confinement studies were generally confined to ECH-heated discharges with densities below $\bar{n}_e = 8.0 \times 10^{12} \text{ cm}^{-3}$. Typical ion temperatures inferred from NPA measurements were in the range of 100-200 eV. Although these temperatures are consistent with neoclassical heat transport predictions, there are large uncertainties at these temperatures and densities due to the unknown magnitude of the charge-exchange and convective losses.

CHAPTER I

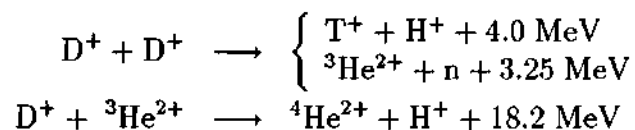
Introduction

Energy — it is the lifeline by which all the industrial nations of the world survive. These nations are not only dependent on the availability of energy but also, and maybe more importantly, addicted to the availability of affordable energy. With the number of industrial societies in the world increasing each year, serious questions are now beginning to surface about the availability of affordable energy in the not-so-distant future. The increasingly rapid pace at which global energy consumption is rising, coupled with the fact that global inventories of fossil fuels such as oil and coal are decreasing just as rapidly, makes the search for new, economically feasible energy sources imperative. With environmental concerns, most notably global warming, receiving higher priority in the world political agenda, these new energy sources must also be inherently environmentally safe.

One of the most promising of the available options is magnetic fusion, which is based on the same physical process that fuels the sun. Under the proper conditions low atomic number elements will react to convert mass to energy via nuclear fusion. For example, the fusion of the hydrogen isotopes deuterium (D) and tritium (T) according to the reaction



produces 17.6 MeV of energy. Similar fusion reactions such as



also produce copious amounts of energy.

In order for a fusion reaction to occur, the two nuclei in each of the above reactions must have sufficient energy to overcome the repulsive Coulomb force and approach each other closely enough that the short-range attractive nuclear force becomes dominant. This means the fusion fuel must be heated to extremely high temperatures. At these elevated temperatures, a large number of the gas molecules will be stripped of their electrons and the fuel will thus be a plasma, consisting almost entirely of free electrons and ions.

The development of magnetic fusion as a commercial source of electricity requires the solutions to a number of challenging physics issues as well as technological problems. The physics issues are traditionally separated into three basic areas: equilibrium and stability, transport, and heating. The basic goal of magnetic fusion research is to study magnetic configurations that are capable of stably confining a sufficiently high-density plasma at a sufficiently high temperature for a sufficient length of time to produce net thermonuclear power. Greatly simplified, the requirements for reaching this goal are expressed in terms of the Lawson criterion, which is derived from elementary power balance considerations.¹ This criterion states that the product of the particle density n and the energy confinement time τ_E in a high-temperature plasma ($T > 10$ keV) should exceed a particular value. For a plasma producing energy by D-T reactions, this product should exceed 10^{14} sec/cm³. The study of the processes that determine the confinement properties of the plasma is therefore essential to understanding how to produce net thermonuclear power in fusion reactors.

At relevant temperatures in a fusion plasma, most of the gas molecules are ionized. In this case, magnetic fields can be used for confinement since charged particles spiral about magnetic field lines with a radius that is inversely proportional to the strength of the magnetic field.² Hence, in regions of strong magnetic field

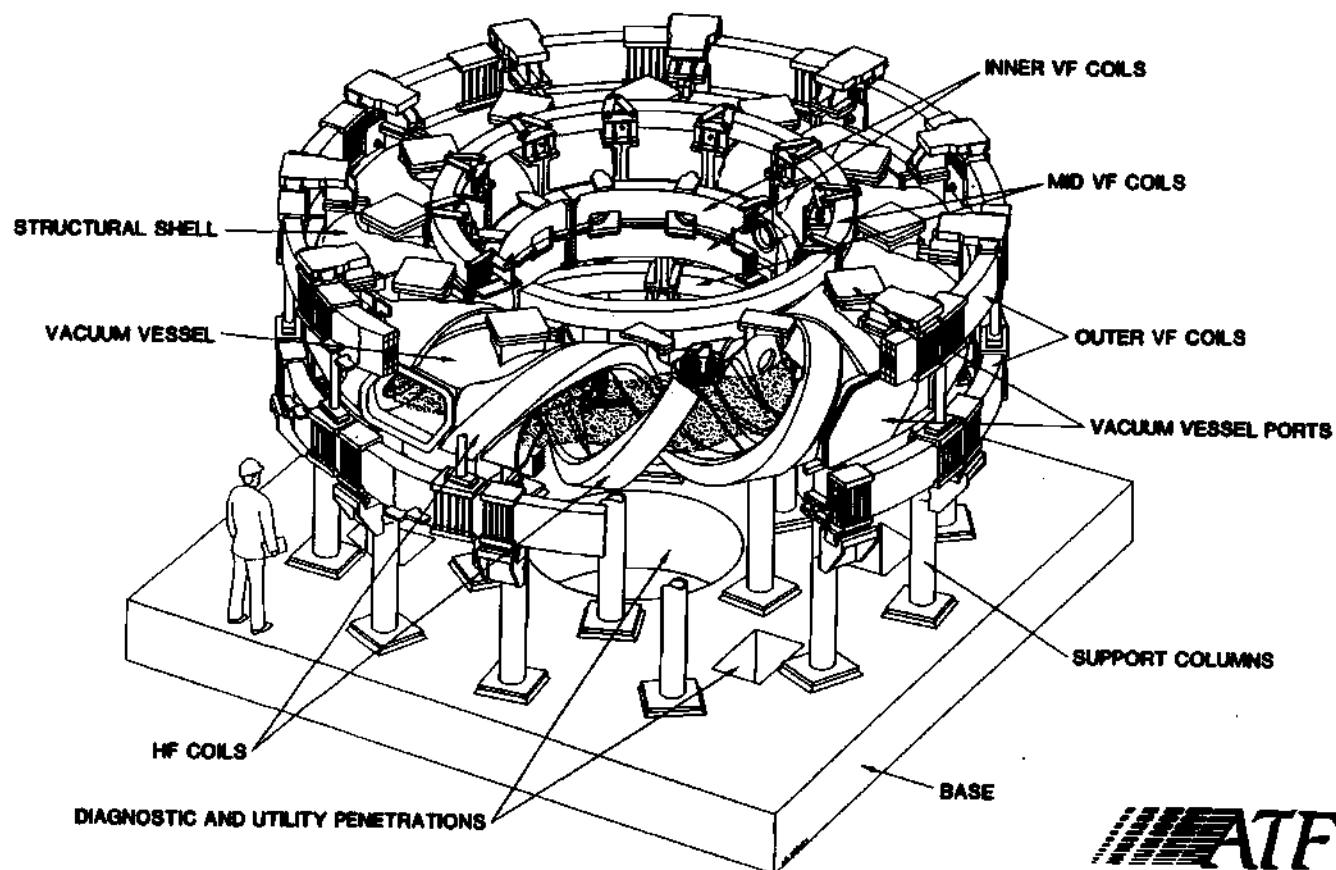
these charged particles are essentially "frozen" to the magnetic field lines.³ Several magnetic confinement schemes have been proposed and investigated over the past 40 years. The most promising options of these schemes are closed toroidal confinement systems where the magnetic field lines are configured such that they close on themselves or ergodically form closed surfaces. The most widely investigated of these concepts are the tokamak and the stellarator. Both of these confinement schemes rely on a closed, helical field to confine the plasma. This helical magnetic field typically consists of a strong toroidal component B_ϕ and a much weaker poloidal component B_θ such that $B_\theta \ll B_\phi$.

The basic difference between tokamaks and stellarators is the manner in which the poloidal field, B_θ , is created. In stellarators, B_θ is produced entirely by means of external magnet coils, as opposed to tokamaks, which use an induced plasma current to produce the necessary poloidal magnetic field. A classical stellarator has ℓ helical conductors with alternately opposing current flow that produces a poloidal field in the plasma.³ This antiparallel configuration effectively cancels the net toroidal field in the plasma; hence, a set of toroidal field coils is still required. A torsatron (a subclass of the stellarator) has ℓ helical windings with current flow in the same direction so that the helical windings produce not only a poloidal field but also a net toroidal field. This eliminates the need for toroidal field coils. The distinct advantages of torsatrons (and of stellarators, in general) are the intrinsic ability to operate steady state and the absence of disruptive terminations of the discharge. In tokamaks, a continuous transformer action is required to induce the plasma current, which in turn produces the poloidal magnetic field. Since this transformer action can only be sustained for a finite amount of time, eventually the discharge must be terminated or some other means of current drive must be used. Since stellarators produce their complete magnetic configuration using external field coils, no transformer action is required and steady-state operation is possible.

One of the biggest concerns of the stellarator concept in terms of its viability as a fusion reactor is ion confinement. This concern is based on the seemingly unfavorable single-particle confinement characteristics inherent in the stellarator design. These confinement characteristics are critically important in an ignited stellarator, in which the alpha particles resulting from the fusion reaction must be confined long enough so that their energy can be recaptured by the plasma. Several stellarator reactor studies have been conducted with the general conclusion reached that ignition is possible in torsatron reactors provided the radial electric field is large enough to reduce the neoclassical stellarator transport coefficients to acceptably small values.⁴ For the present generation of stellarators where ignition is not an issue, ion confinement properties are important in determining heat transport within the plasma and the efficiency of various heating mechanisms.

The research reported here is a study of the ion confinement properties of the Advanced Toroidal Facility (ATF) at Oak Ridge National Laboratory (ORNL). ATF, currently the world's largest stellarator, is an $\ell = 2$, 12-field-period torsatron with a moderate plasma aspect ratio (major radius $R_0 = 2.10$ m, average plasma radius $\bar{a} = 0.27$ m). The ATF magnetic configuration was chosen after a study of a large number of stellarator configurations and was specifically optimized for high-beta operation in the second stability region and for configuration flexibility.⁵ ATF was not optimized in terms of single-particle confinement since it depends critically on the magnitude and sign of the radial electric field, which was unknown.

A sketch of ATF is shown in Fig. 1.1. The main components are two segmented, jointed helical field (HF) coils; three pairs of poloidal field coils labeled inner, outer, and mid-vertical field coils; an exterior shell structure to support the magnetic and thermal loads from the coils; and a thin, helically contoured vacuum vessel, which was designed such that, except for the natural divertor stripe, almost all collisionless orbits that cross the last closed flux surface (which is the customary



ATF
Advanced Toroidal Facility
Oak Ridge National Laboratory

Figure 1.1: An artist's sketch of ATF, showing the main components.

loss region) reenter the plasma before hitting the vacuum vessel wall.⁵ Large (0.9×0.6 m) outer ports and smaller (0.2-m diam) inner ports are located on the vertical midplane at every field period. These ports, coupled with 24 upper and lower square ports (0.35×0.35 m), provide extensive access for diagnostics, neutral beams, ion cyclotron heating antennas, and maintenance.

1.1 Plasma Confinement

From a somewhat oversimplified view of physics, the problem of maximizing the product $n\tau_E$ separates into two relatively independent parts. The maximum energy confinement time τ_E is generally determined by microscopic behavior of the plasma (e.g., collisions), which in turn leads to macroscopic energy transport, which can be either classical or anomalous depending on the processes involved. The maximum density n is generally determined by equilibrium and stability limits set by the magnetic configuration. This is because as the plasma pressure nT (where n is the total density of plasma particles and $T = T_e = T_i$) increases the magnetic pressure must also increase for a stable equilibrium to be maintained. Since the available magnetic pressure is typically fixed for a given configuration, a threshold is reached above which the plasma is unstable. The critical figure of merit in this case is the plasma beta, defined as

$$\beta = 4.03 \times 10^{-16} \frac{n[\text{cm}^{-3}]T[\text{keV}]}{(B[\text{Tesla}])^2}. \quad (1.1)$$

Therefore, the maximum density (for a fixed temperature) is limited by equilibrium and stability requirements.

The confinement properties of a particular magnetic configuration are determined by many different parameters. Although the closed-field-line configurations discussed above constitute the basic ingredient for favorable single-particle confine-

ment, plasma confinement is ultimately determined by collective phenomena, such as stability and transport. In simplest terms, the former limits how much plasma energy can be stored by a given magnetic field strength while the latter determines how much power is necessary to sustain a given plasma energy content. The transport of particles and energy within the plasma is generally governed by the density and temperature gradients in the plasma. However, effects on the motion of the particles due to inhomogeneity of the magnetic field within the plasma along with collective mechanisms can also play important roles in enhancing the transport of energy from the core of the plasma to the edge. There is considerable experimental evidence that suggests that energy and particle transport in tokamaks is anomalous (i.e., not explainable from neoclassical theory, which takes account into the nature of the magnetic field topology when calculating transport- and confinement-related quantities).⁶⁻⁸

Stability requirements place restrictions on various parameters that determine the overall makeup of the magnetic field configuration. These requirements can be determined from a magnetohydrodynamic (MHD) stability analysis of the configuration. The first basic requirement is related to the rotational transform of the magnetic field helix. This quantity is determined by the average amount of poloidal rotation of the helical field line $\Delta\theta$ during one toroidal rotation and is defined as⁹

$$\iota = \frac{\Delta\theta}{2\pi}$$

A more formal expression that is applicable in any magnetic field configuration in a closed toroidal system is¹⁰

$$\iota = \frac{d\psi_{\text{pol}}}{d\psi}, \quad (1.2)$$

where ψ is the toroidal magnetic flux normalized to the total toroidal flux ψ_{tot} and

ψ_{pol} is the poloidal magnetic flux normalized in the same manner.* If the field line pitch becomes too tight (i.e., if τ becomes too large) the plasma becomes unstable to kink-type perturbations. In general, MHD instabilities are either pressure-driven (i.e., driven by gradients in the pressure profile) or current-driven (i.e., driven by the plasma current) since these are the "free" parameters in the MHD equations. Since a torsatron has negligible plasma current, the pressure-driven instabilities are the most dangerous MHD instabilities, with interchange modes being the strongest of these.¹⁰ The stability of these interchange modes is generally determined by the amount of shear in the magnetic field, given by¹¹

$$\hat{s} = \frac{d\tau}{d\psi}, \quad (1.3)$$

and the depth of the magnetic well, given by¹¹

$$V'' = \frac{d}{d\psi} \left(\oint \frac{dl}{B} \right). \quad (1.4)$$

Here, ψ is the normalized flux surface coordinate, dl is an incremental length along a field line, and B is the magnitude of the magnetic field. In general, optimizing the magnetic design in terms of these stability requirements causes a degradation in single-particle confinement, and vice versa. Therefore, the design of the magnetic configuration for a torsatron must represent a compromise between MHD stability requirements and single-particle confinement requirements. Configurations types vary from those with high-transform, high-shear stabilized configurations (such as Heliotron-E) to moderate-transform, low-shear, magnetic-well stabilized configurations (such as Wendelstein VII-AS).

*Since surfaces of constant toroidal magnetic are also surfaces of constant plasma current, pressure, etc., ψ is typically used as the radial coordinate in toroidal geometry.

1.2 Plasma Heating

Since extremely high ion temperatures are also required to reach ignition, any confinement device must also provide for some means of heating the plasma. An intrinsic heating method is built into the tokamak design due to the induced plasma current and the finite resistivity of the plasma. The resistivity of a plasma is determined, as in more conventional conductors, by the amount of freedom that the electrons have to move in the direction of applied voltage. In the case of a plasma, the resistivity is solely dependent on the collision frequency of the electrons. Spitzer² has shown that the resistivity is proportional to $T_e^{-3/2}$, where T_e is the electron temperature. Hence, driving a current through the plasma (known as Ohmic heating) is an excellent means of producing resistive heat within the plasma at low temperatures. In tokamaks, in which a toroidal current is driven in the plasma, this is a substantial means of plasma heating, but it still fails to heat the plasma to fusion temperatures. In a torsatron, in which there is no net toroidal current, this form of heating is not present and plasmas must be generated by some other means of plasma heating. In an ignited device, considerable heating is provided by the thermalization of the energetic alpha particles that result from fusion reactions. Although this heating method should provide enough power to sustain the plasma, some means of heating is necessary in order to reach ignition temperatures in a reactor and for heating purposes in a subignited fusion device.

One of the more established of these heating processes is neutral beam injection (NBI).¹² This involves injecting energetic neutrals into the plasma where they are ionized and subsequently transfer their energy to the background plasma through collisions. A schematic of the basic processes involved is shown in Fig. 1.2. Hydrogen ions (H^+ , H_2^+ , and H_3^+) are first extracted from an ion source. These ions are then accelerated to 30–120 keV (possibly higher for a reactor) by an acceleration

grid. This ion beam is then passed through a hydrogen neutralization cell where a significant fraction of the beam is neutralized by charge-exchange. The fraction of the beam that is not neutralized is then magnetically deflected so that the remaining beam is made up entirely of neutral particles. Within the neutralization cell, each H_2^+ (or H_3^+) ion in the ion beam will charge-exchange and break up into two (or three) H_0 particles each having an energy corresponding to one-half or one-third of the accelerating voltage.¹³ Since most of the H^+ particles are also neutralized by charge-exchange, the neutral beam is composed of three energy components, E_{inj} , $E_{inj}/2$, and $E_{inj}/3$ where E_{inj} is the energy corresponding to the acceleration voltage. The neutral particles can then pass freely across the confining magnetic field lines into the plasma. Within the plasma the energetic neutrals are ionized by collisions with the plasma electrons, ions, and impurities. These energetic ions then slow down collisionally with the target plasma, thus heating the plasma. The confinement of these energetic particles as they slow down is important in determining the overall energy balance of the plasma. If a large fraction of these particles are lost before they have sufficient time to transfer their energy to the background plasma, heating of the plasma will be minimal. Early experiments using NBI were conducted at power levels representing only a perturbation on the Ohmic heating power. Later experiments on larger tokamaks and stellarators have demonstrated the viability of operating with NBI in regimes where the ion, electron, and total plasma power balances are beam-dominated. Fusion-relevant ion temperatures above 10 keV have been attained in the Tokamak Fusion Test Reactor (TFTR) and the Joint European Torus (JET) using high-power NBI.

Another important plasma heating method is radio-frequency (rf) heating, which uses a variety of waves and modes to couple rf power from external sources to the plasma. The frequency ranges of greatest interest for this type of heating correspond to the electron gyrofrequency and ion gyrofrequency (dubbed electron

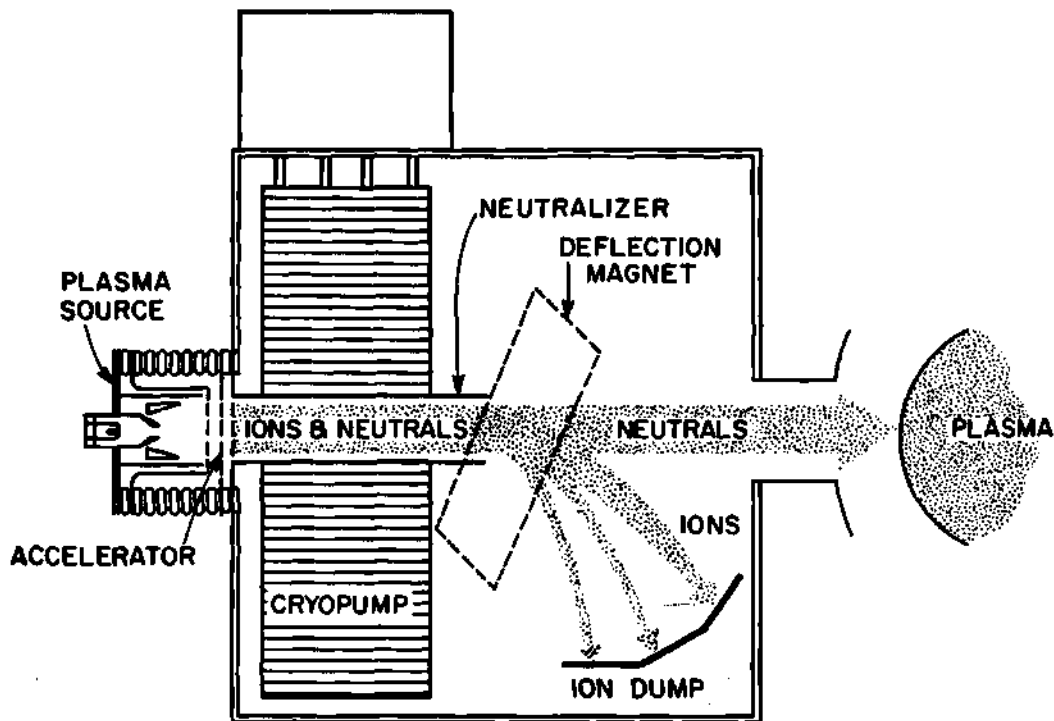


Figure 1.2: Schematic of a typical neutral beam injector [Ref. 12].

cyclotron heating (ECH) and ion cyclotron heating (ICH), respectively). Although still early in their development phase compared with NBI, each of these methods shows promise for extrapolation to reactor-grade plasmas.

ATF is equipped with each of these three forms of auxiliary plasma heating. Target plasmas are produced using 400-kW, 53-GHz ECH with subsequent heating provided by $\simeq 1.7$ MW of NBI and $\simeq 0.2$ MW of ICH. The maximum magnetic field strength available is $B_0 = 1.9$ T, although most of the physics experiments to date have been conducted at a magnetic field of $B_0 = 0.95$ T, which is compatible with second-harmonic, 53.2-GHz ECH.

The orientation of the neutral beam injectors on ATF is shown in Fig. 1.3. These beam lines are aimed tangentially, 13 cm inside the magnetic axis to minimize scrape-off on the vacuum vessel walls. The opposing orientation of the injectors allows balanced injection with only a small amount of momentum input or net

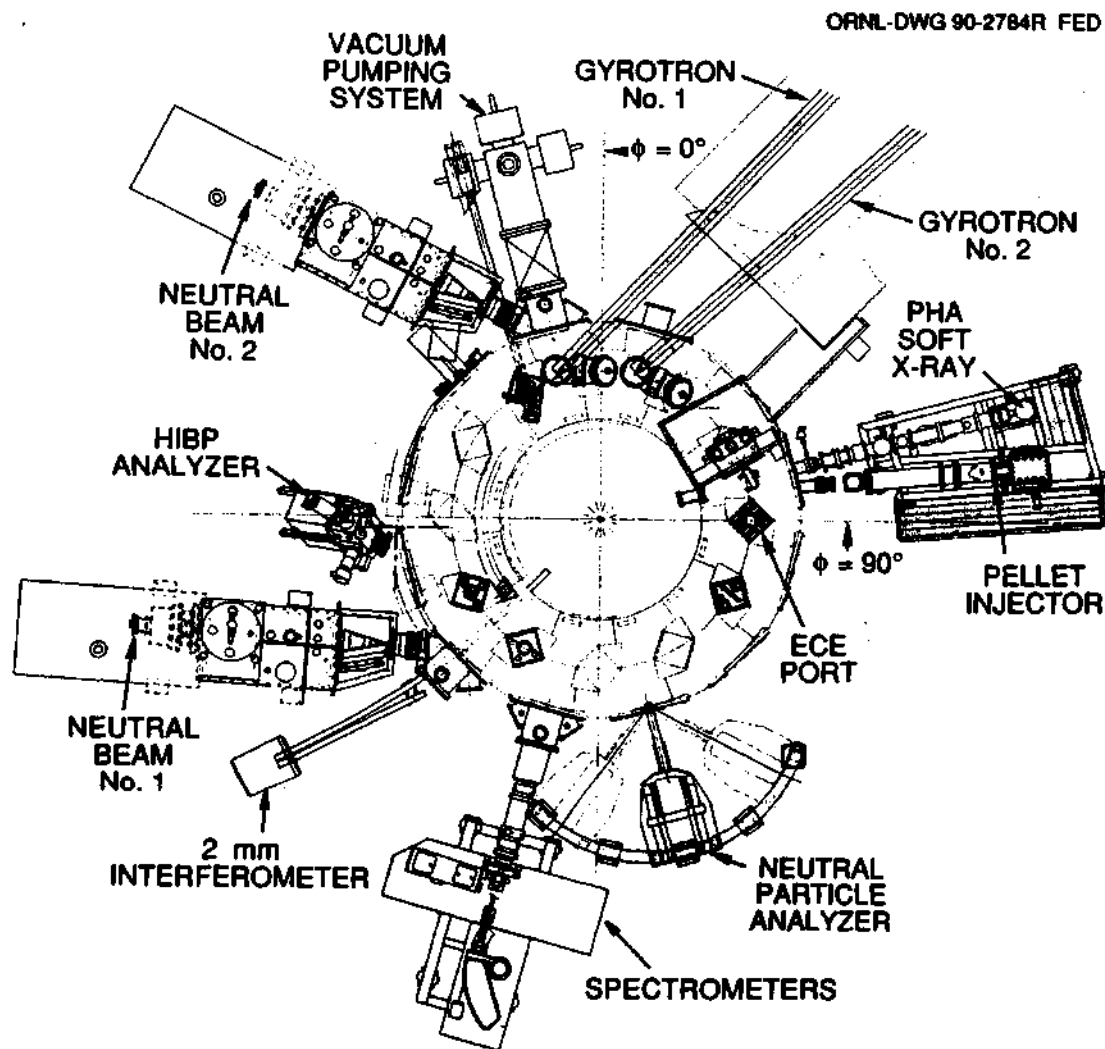


Figure 1.3: Top schematic view of ATF and orientation of the two neutral beam injectors and the neutral particle analyzer (NPA) on ATF. Three of the possible horizontal orientations of the NPA are shown.

beam-driven current. Fast hydrogen neutrals are injected at energies up to 35 keV; the delivered power is distributed among the three energy components (E_{inj} , $E_{inj}/2$, and $E_{inj}/3$) in the ratio 60:20:20. Experiments have been conducted using NBI in a variety of plasma conditions with confinement times of up to 30 msec observed.

Initial ICH experiments have also been carried out using a fast-wave ICH antenna.¹⁴ This antenna is tunable over the 10- to 30-MHz frequency range. Experiments have been conducted with D(H) and D(He³) plasmas with the frequency adjusted to obtain fundamental resonance with the minority species of interest. Although preliminary low-power experiments have not shown any clear indication of plasma heating, numerical studies suggest that more favorable conditions (i.e., higher ICH power and higher plasma density) should produce heating. Initial high-density experiments were very promising, though not conclusive because of the low ICH power (~ 100 kW).¹⁵

1.3 Diagnostics for Fusion Plasmas

To accurately assess the progress toward creating higher temperature, better confined plasmas and to better understand the basic physical processes that govern plasma confinement, measurements of various plasma properties are necessary. There are generally two methods of "diagnosing" the plasma: (1) nonperturbing (passive) techniques that take advantage of inherent loss mechanisms of the plasma (e.g., radiation from impurities, neutron intensities) and (2) active methods that use the interaction of the plasma with probing radiation or particle beams. There are advantages and disadvantages associated with each of these techniques. The passive techniques suffer from only being able to produce chord- or volume-integrated quantities. Although active methods usually produce local measurements, the costs associated with the design and development of these systems are usually quite high.

To produce unambiguous results a large set of diagnostics is typically needed.

In the work reported here, a standard diagnostic for studying ion behavior in fusion plasmas, charge-exchange neutral analysis (CXNA), has been used to study various characteristics of ion confinement in ATF. This technique takes advantage of a direct loss mechanism of the plasma, namely, the loss of ion energy to neutrals resulting from charge-exchange reactions within the discharge. Improvements in plasma confinement as well as increases in the size and density of the device naturally tend to reduce this loss, potentially reducing its usefulness as a diagnostic as well. The main product of CXNA is a direct measurement of the ion energy distribution within the plasma. Knowing the form of this distribution allows the inference of various ion characteristics such as the ion temperature. Also, CXNA can be used to measure the energy distribution of energetic ions produced by NBI or ICH. Comparing the measured distributions against those predicted by classical slowing-down calculations allows one to determine if the thermalization process for these ions is classical or not.

The neutral particle analyzer (NPA) used on ATF is an $E\parallel B$ mass- and energy-analyzing spectrometer designed at Princeton Plasma Physics Laboratory and similar to analyzers used on TFTR.¹⁶ This analyzer has two mass columns (allowing for simultaneous measurements of protons and deuterons) and has an energy range $0.5 \leq A(\text{amu}) \cdot E(\text{keV}) \leq 600$. The NPA is mounted on a carriage that allows it to be horizontally and vertically scanned. When the analyzer is scanned horizontally, its viewing angle can be changed from perpendicular to tangential (in both directions) to the axial magnetic field. The vertical scanning capability allows the analyzer to scan from below to above the plasma column. The location of the NPA and its orientation relative to the neutral beam injectors on ATF are shown in Fig. 1.3. The NPA on ATF is described in more detail in Appendix A.

1.4 Ion Confinement Issues in ATF

As mentioned previously, one of the biggest concerns of the stellarator concept as a viable fusion reactor concept is ion confinement because of its seemingly unfavorable single-particle confinement properties. The purpose of this research is to develop a better understanding of ion confinement in a stellarator through analysis of ion measurements made on an existing device, ATF. This study has been divided into two parts: the study of confinement properties of the thermal ion population and the study of the energetic ions used for heating purposes by NBI and ICH. There are several key issues that must be addressed in each of these areas.

In terms of thermal-ion confinement, the following issues must be addressed to develop a basic understanding thermal ion behavior in ATF:

- Since ATF was not optimized for single-particle confinement, one of the basic questions is whether or not orbit effects play an important role in plasma performance in ATF.
- Does the presence of a radial electric field help in orbit confinement? Although various theoretical studies indicate that single-particle confinement in stellarators is drastically improved in the presence of a radial electric field, this result has not been confirmed experimentally.
- Can orbit effects be measured experimentally? Measurements of expected phenomena would help confirm numerical and analytical studies of the ion orbit topology.
- Since theoretical predictions indicate that the magnitude of ion transport may prohibit a stellarator reactor from reaching ignition, an important issue is whether or not the measured ion heat transport coefficient is consistent with neoclassical theory in ATF.

- Do the orbit confinement properties improve by changing the magnetic configuration in ATF? If so, is this improvement reflected in plasma performance?

In terms of heating via energetic ions in ATF (and stellarators, in general), the following issues must be considered:

- Do the energetic ions behave classically (i.e., is the behavior of the energetic ions determined by classical collisional processes or are the ions subject to anomalous processes)?
- Are the fast ions well confined during NBI and ICH? If not, what are the main loss mechanisms?
- Are the losses large enough to affect plasma performance in various operating regimes?
- Do orbit effects play an important role in the overall heating efficiency of NBI in ATF? Although ATF is equipped with tangential NBI where orbit effects would seemingly be unimportant, the orbit topology should be studied to determine if there are any regimes where heating efficiency might be affected.

Although these issues are by no means a complete list of the issues that are necessary in developing a clear picture of ion behavior in stellarators, the answers to these questions are basic to developing a better understanding of ion behavior in a stellarator and its effect on plasma performance. Therefore, these are the main issues that have been addressed in this work.

1.5 Outline of Dissertation

The NPA has been used to conduct an experimental study of ion behavior in ATF, the results of which are reported here. Special emphasis has been placed on taking available measured data (from the NPA and other diagnostics) and attempting to construct a consistent picture of ion confinement in the plasma and the effect that this confinement has on plasma conditions. Because the processes governing the evolution of the ion distribution and the plasma are quite complicated, a large amount of computational work has been required in developing a consistent picture of the available data.

To establish a basis for the remainder of the thesis, the current theoretical understanding of ion behavior in toroidal devices is summarized in Chapter 2. The theory of collisionless ion trajectories is first presented by starting from first principles and deriving the guiding center equations of motion. Particular emphasis is placed on characterizing the classes of particle orbits expected in toroidal devices and the methods by which loss regions (i.e., regions where a particle's orbit intersects the vacuum vessel wall or limiter) are computed. Second, the effect of collisions on ion behavior is considered. This discussion develops the equations governing the thermal and fast-ion distribution functions in the presence of collisions.

The results of ion confinement studies performed on other devices are summarized in Chapter 3. In general, the results obtained during these studies have indicated that ion behavior can be described by classical collisional and orbit considerations. Because of the vast number of studies conducted in this area, this discussion is limited to a broad discussion of the studies that are directly comparable to the studies carried out on ATF.

Some general considerations about the orbit topology in ATF and its effect on ion behavior are presented in Chapter 4. General features of the orbit topology in

ATF are presented along with the effects associated with the magnetic configuration and the radial electric field. The effects of the orbit topology on the confinement of injected ions during NBI and on NPA measurements are also discussed.

The results of the ion confinement studies on ATF are presented in Chapters 5 and 6. These chapters outline the measurements made by the NPA during various forms of operation of ATF. Chapter 5 is devoted to the measurements of the thermal ion distribution made during low-density ECH discharges. The results of fast-ion confinement studies are presented in Chapter 6, along with further simulations showing how the confinement properties affect the attainable plasma parameters.

A complete description of the NPA installed on ATF is presented in Appendix A along with calibration results and a brief description of how the measured data is analyzed. Appendix B contains a brief description of the Fokker-Planck analysis code used to simulate fast-ion energy spectra measured by the NPA.

REFERENCES

- ¹ J. D. Lawson, Proc. Phys. Soc. London, Sect. B **70**, 6 (1957).
- ² L. Spitzer, Jr., *Physics of Fully Ionized Gases* (Interscience Publishers, New York, 1956).
- ³ W. M. Stacey, *Fusion: An Introduction to the Physics and Technology of Magnetic Confinement Fusion* (John Wiley & Sons, Inc., New York, 1984).
- ⁴ S. L. Painter, *Performance Analysis and Parametric Optimization Study of Toratron Fusion Reactors*, PhD thesis, University of Tennessee, Knoxville, 1990.
- ⁵ J. F. Lyon et al., Nucl. Technol./Fusion **10**, 179 (1986).
- ⁶ L. A. Artsimovich et al., Sov. Phys. JETP **34**, 306 (1972).
- ⁷ J. Hugill, Nucl. Fusion **23**, 331 (1983).
- ⁸ A. J. Wootton, Phys. Fluids B **2**, 2879 (1990).
- ⁹ G. Bateman, *MHD Instabilities* (MIT Press, Cambridge, 1980) 2nd edition.
- ¹⁰ J. P. Freidberg, *Ideal Magnetohydrodynamics* (Plenum Press, New York, 1987).
- ¹¹ B. A. Carreras et al., Phys. Fluids **26**, 3569 (1983).
- ¹² M. M. Menon, Proc. of the IEEE **69**, 1012 (1981).
- ¹³ J. Kim and H. H. Haselton, J. Appl. Phys. **50**, 3802 (1979).
- ¹⁴ F. W. Baity, D. J. Hoffman, and T. L. Owens, AIP Conf. Proc. **129**, 32 (1985).
- ¹⁵ M. Kwon, *Fast Wave Ion Cyclotron Resonance Heating Experiments on the Advanced Toroidal Facility*, PhD thesis, Georgia Institute of Technology, 1990.
- ¹⁶ A. L. Roquemore et al., Rev. Sci. Instrum. **56**, 1120 (1985).

CHAPTER II

Theory of Ion Behavior in Toroidal Devices

2.1 Orbit Effects

In order to understand the dynamics of ion behavior in stellarators/torsatrons, the first essential element is an understanding of collisionless ion trajectories. To first order, particles within any magnetic system follow the magnetic field lines. However, in systems with a high degree of inhomogeneity of the magnetic field (e.g., stellarators and torsatrons), the motion of the particles is more complicated. The main objective in studying ion trajectories is to determine the regions in velocity space (as well as in configuration space) where the ion distribution will be depleted because of lost particles. These loss regions result from orbits that do not close within the device.

Two approaches are generally used to study the features of the loss regions in fusion devices. The first is simply to integrate the equations of motion for a large set of particles — starting each particle at different locations in velocity and configuration space. Although this approach is accurate, the computational time required for such a survey can be enormous, leading one to use another approach. The second approach takes advantage of the fact that the motion in toroidal systems is generally quasi-periodic; hence, there are several constants of the motion that can be used to provide a much quicker survey of the orbit topology and associated loss regions. Each of these approaches has been used in ion orbit studies for both tokamaks¹⁻⁴ and stellarators.⁵⁻⁸ As a brief review, each of these approaches is discussed in this

section. The application of these approaches to the study of ion behavior in ATF is presented in Chapter 4.

2.1.1 General Equation of Motion

The starting point for deriving the equation of motion for a particle in a fusion device is the nonrelativistic Lorentz equation:

$$m\ddot{\vec{\rho}} = e[\vec{E} + \dot{\vec{\rho}} \times \vec{B}] \quad (2.1)$$

where $\vec{\rho}$ is the instantaneous position of the particle, \vec{E} represents the electric field, \vec{B} is the magnetic field, and the dots represent time derivatives.

In general electric and magnetic field configurations, solving this equation is extraordinarily complicated. However, considerable insight can be obtained by examining some relatively simple field configurations. For example, consider the case where a uniform \vec{B} is directed along the z -axis ($\vec{B} = B_z \hat{z}$) in a Cartesian coordinate system with $\vec{E} = 0$. In this case, the equation of motion reduces to

$$m\ddot{\vec{\rho}} = eB_z (\dot{\vec{\rho}} \times \hat{z}). \quad (2.2)$$

The general solution of this equation is well known:

$$\begin{aligned} z &= v_{\parallel} t + z_o, \\ y &= r_L \cos(\Omega t + \alpha) + y_o, \\ x &= r_L \sin(\Omega t + \alpha) + x_o, \end{aligned} \quad (2.3)$$

where $\Omega = qB_z/m$ is the gyrofrequency and r_L is the Larmor radius,

$$r_L = \frac{v_{\perp}}{|\Omega|}. \quad (2.4)$$

Equation (2.3) describes motion along the field line of a guiding center with instantaneous coordinates $(x_o, y_o, z_o + v_{\parallel} t)$ and gyromotion around the field line with

angular frequency Ω and gyroradius r_L . As the magnetic field strength is increased, r_L becomes smaller and the particle is essentially "frozen" to the magnetic field line.

The gyromotion of these charged particles about the magnetic field line produces a circulating electric current. This circulating current produces a magnetic dipole moment whose magnitude is⁹

$$\mu = IA = \left(e \frac{\Omega}{2\pi} \right) (\pi r_L^2) = \frac{mv_{\perp}^2}{2B} \quad (2.5)$$

and whose direction is opposite to the magnetic field. From the general theory of quasi-periodic motions, this quantity is an adiabatic invariant¹⁰ (i.e., it remains constant in fields that vary slowly over distances of the order of the Larmor radius r_L , during the period of time of the order of the gyrofrequency Ω).

In most cases, the rapid change of the phase of the particle's gyromotion about the field line is not of interest. If this is the case, the particle's motion within the system can be approximately described by the motion of a magnetic dipole with magnetic moment μ and charge e . The diamagnetic force acting in an inhomogeneous magnetic field on this dipole is⁹

$$\vec{F}_{\text{dia}} = \nabla(\vec{\mu} \cdot \vec{B}) = -\mu \nabla B, \quad (2.6)$$

where the fact that μ is an adiabatic invariant has been used in the second equality.

The motion of the guiding center of the particle in a general magnetic and electric field configuration is then described by the equation,

$$m \frac{d\vec{v}_{gc}}{dt} = e[\vec{E} + \vec{v}_{gc} \times \vec{B}] - \mu \nabla B, \quad (2.7)$$

where \vec{v}_{gc} is the velocity of the guiding center. This motion can usually be divided into the motion along the field line and the drift across the field line.

Motion of Guiding Center along the Field Line By taking the dot product of Eq. (2.7) with a unit vector, \hat{b} , pointing in the direction of the magnetic field, the motion of the guiding center along the field line is found to be

$$\begin{aligned}\dot{v}_{gc,\parallel} &= \vec{v}_{gc} \cdot \hat{b} \\ &= \frac{e}{m} [\vec{E} \cdot \hat{b} + (\vec{v}_{gc} \times \vec{B}) \cdot \hat{b}] - \frac{\mu}{m} \nabla B \cdot \hat{b} \\ &= -\frac{e}{m} \frac{\partial \Phi}{\partial s} - \frac{\mu}{m} \frac{\partial B}{\partial s},\end{aligned}\tag{2.8}$$

where s is the distance along the field line and Φ is the electrostatic potential. The electric and magnetic fields are assumed to be time independent such that $\vec{E} = -\nabla \Phi$.

Since the motion across the field lines is small compared to the motion along the field lines, the guiding center to first order simply moves along the line of force. The form of Eq. (2.8) suggests that the potential energy of the particle is $\mu B + e\Phi$. Since the total energy of a particle,

$$W = \frac{1}{2}mv_{\parallel}^2 + e\Phi + \mu B = \text{const},\tag{2.9}$$

is conserved, the longitudinal velocity (v_{\parallel}) of a particle moving into a region where the magnetic field is increasing will decrease. Hence, if the magnetic field of interest is inhomogeneous along the field line, the resulting particle orbit types can be subdivided into two classes. The first class consists of those particles with small longitudinal velocities near the minima of the magnetic field. These particles move along the field line in the direction of increasing magnetic field until they reach a location where the conservation of energy requires that the parallel velocity be zero, and the particle is reflected. The other class consists of those particles with sufficient v_{\parallel} to pass over the magnetic hills. The particles of the first type are usually called blocked or trapped particles, while those of the second group are transit (or passing) particles.¹ Since the confinement properties of these two classes of particles

can be extremely different, it is first important to determine the relative number of particles in each class for a given magnetic configuration.

The magnitude of the magnetic field in the case of a circular axisymmetric torus in which the longitudinal magnetic field is much stronger than the poloidal field is given by¹¹

$$B_\phi(r, \theta) = \frac{B_o}{1 + \epsilon_t \cos \theta} \simeq B_o (1 - \epsilon_t \cos \theta). \quad (2.10)$$

Here, $\epsilon_t = r/R_o$ is the inverse aspect ratio, B_o is the on-axis magnitude of the magnetic field, R_o is the major radius of the torus, r is the minor radius coordinate, and θ is the poloidal angle. In this case, the field lines wrap around the torus in the shape of a circular helix whose pitch is dependent on the relative magnitudes of B_ϕ and B_θ .

The conservation of energy [Eq. (2.9)] in this case requires that (assuming that $e\Phi \ll \mu B$)

$$\frac{1}{2}mv_{\parallel}^2(\theta) + \mu B_o (1 - \epsilon_t \cos \theta) = \frac{1}{2}mv_{\parallel}^2(0) + \mu B_o (1 - \epsilon_t) \quad (2.11)$$

or that

$$\begin{aligned} v_{\parallel}^2(\theta) &= v_{\parallel}^2(0) - \frac{4\mu B_o \epsilon_t}{m} \cos \theta \\ &= v_{\parallel}^2(0) - 2v_{\perp}^2(0)\epsilon_t \cos \theta, \end{aligned} \quad (2.12)$$

where Eq. (2.5) has been used in the second equality.

It follows from this equation that a particle is trapped if

$$\frac{v_{\parallel}(0)}{v_{\perp}(0)} < \sqrt{2\epsilon_t}, \quad (2.13)$$

and in a system where the particles have an isotropic velocity distribution the fraction of trapped particles is of the order of $\sqrt{\epsilon_t}$. Although ϵ_t is usually small, its square root is not necessarily a very small quantity and in toroidal magnetic systems

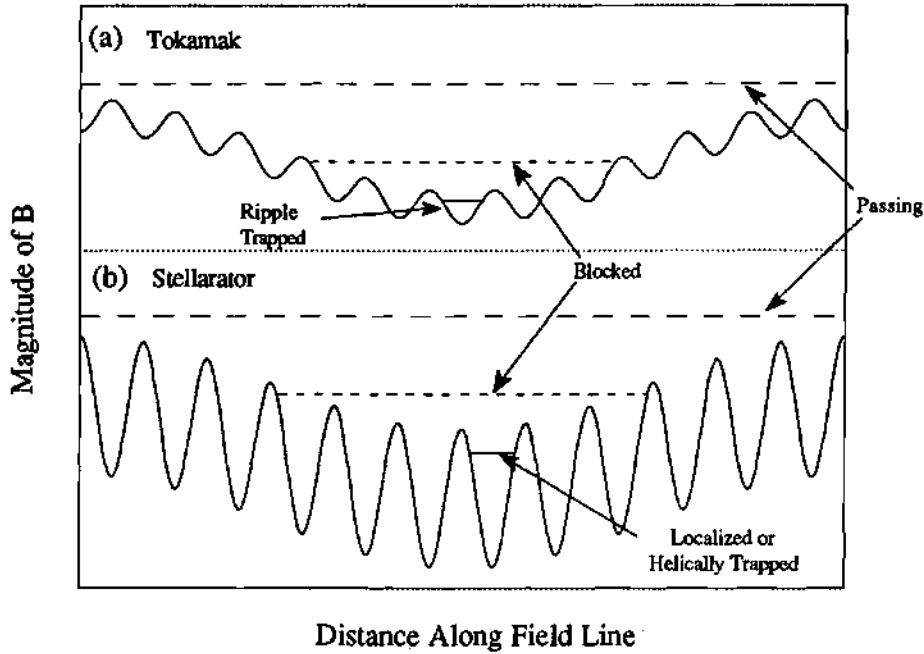


Figure 2.1: Magnitude of the magnetic field along a field line in (a) a tokamak with a small ripple due to the discreteness of the toroidal field coils and (b) a stellarator.

with any substantial modulation of the magnetic field, trapped particles constitute a considerable fraction of all particles.¹

The situation is more complicated in magnetic systems without axial symmetry. The variation of the magnitude of the magnetic field along the field line for two such cases is shown in Fig. 2.1. The first case is for a tokamak with a small toroidal ripple due to the discreteness of the toroidal field coils. The magnitude of the magnetic field along a field line can be represented in the following form:

$$B_{\varphi}(r, \theta) = B_0 [1 - \epsilon_t \cos \theta - \delta \cos(N\varphi)], \quad (2.14)$$

where N is the number of toroidal field coils, δ is the fractional amplitude of the toroidal field ripple, and φ is the toroidal angle. This additional ripple causes a small fraction ($\sim \sqrt{2\delta}$) of the particles to be trapped in a very small region toroidally. Generally, $\delta \ll \epsilon_t$ and the fraction of "ripple-trapped" particles is usually quite small.

The second case shown in Fig. 2.1(b) is that of a stellarator. A simple model for the magnitude of the magnetic field in this case is⁶

$$B = B_0 [1 - \epsilon_t(\rho) \cos \theta - \epsilon_h(\rho) \cos (\ell\theta - N\varphi)], \quad (2.15)$$

where ϵ_t is the toroidal modulation, ϵ_h is the helical modulation due to the helical windings, ℓ is the number of coils, N is the periodicity, θ is the poloidal angle, and φ is the toroidal angle. The deep and more frequent wells in Fig. 2.1 are due to the helical windings while the slow modulation is due to the toroidal curvature of the device. The inhomogeneity caused by the helical windings results in a fraction of particles ($\sim \sqrt{2\epsilon_h}$) being trapped within the length of a period of the helical winding. This class of particles is referred to as localized or helically trapped particles.⁵ Also, as in a tokamak there is a group of particles that are trapped within the toroidal curvature. However, in a stellarator like ATF (where $\epsilon_t \ll \epsilon_h$), there is a much larger fraction of localized particles than trapped particles.

Motion Across the Field Lines If all of the particles in a fusion device moved solely along the magnetic field lines, the computation of the loss region would be trivial. The only particles that would be lost would be those which were "frozen" to magnetic field lines that intersected the vacuum vessel wall or limiter. However, because of the presence of magnetic field gradients and electric fields, particles are not simply "frozen" to the magnetic field lines and can drift substantially from their original field lines. In general, the motion across the field lines, or drift motion, determines the confinement characteristics of a particular particle.

The drift motion of the guiding center can be found by taking the cross product of Eq. (2.7) with \hat{b} ,¹⁰

$$\begin{aligned} \vec{v}_{gc,\perp} &= \vec{v}_{gc} \times \hat{b} \\ &= \frac{e}{m} [\vec{E} \times \hat{b} + (\vec{v}_{gc} \times \vec{B}) \times \hat{b}] - \frac{\mu}{m} \nabla B \times \hat{b} \end{aligned} \quad (2.16)$$

$$= \frac{e}{m} \left[\vec{E} \times \hat{b} - B (\vec{v}_{gc} - \hat{b}(\hat{b} \cdot \vec{v}_{gc})) \right] + \frac{\mu}{m} \hat{b} \times \nabla B.$$

Recognizing $\vec{v}_{gc} - \hat{b}(\hat{b} \cdot \vec{v}_{gc})$ to be $\vec{v}_{gc,\perp}$, this equation can be rearranged to obtain the perpendicular drift velocity,

$$\vec{v}_{gc,\perp} = \frac{\vec{E} \times \hat{b}}{B} + \frac{\mu}{eB} \hat{b} \times \nabla B - \frac{m}{eB} \vec{v}_{gc} \times \hat{b}. \quad (2.17)$$

The three terms on the right-hand side represent the $\vec{E} \times \vec{B}$ drift, the ∇B drift, and the acceleration (centripetal, gravitational, etc.) drift, respectively. For field lines bent around to form a torus, the acceleration drift takes the form¹¹

$$\vec{v}_c = \frac{mv_{\parallel}^2}{eBr} \hat{R} \times \hat{b}. \quad (2.18)$$

This drift is commonly known as the curvature drift and is generally the only type of acceleration drift included in the drift motion equation. Each of these drifts plays an important role in determining the full three-dimensional (3-D) motion of the particles in toroidal devices.

For example, in an axisymmetric tokamak in which the magnitude of the vacuum magnetic field simply falls off as $1/R$, $\vec{v}_{\nabla B}$ and \vec{v}_c are always vertically upward or downward depending on the direction of the magnetic field. For particles that experience the full rotational transform (e.g., passing particles), this drift does not pose a problem since the poloidal rotation of the field lines helps to cancel this vertical drift (on average) by making the ions spend equal time in the upper and lower halves of the torus. However, particles that are trapped within the toroidal curvature of the magnetic field do not experience the full rotational transform and can drift substantially from their original flux surface. The orbits that result have been labeled "banana" orbits because of their characteristic shape when the motion is projected on the r - θ plane. Ripple-trapped particles (either in the toroidal ripple of a tokamak due to the discreteness of the coils or in a ripple due to the helical windings in a stellarator) are confined to a small toroidal region such that the effect

of the rotational transform is negligible. In general, these particles are lost unless another drift mechanism (either from the $\vec{E} \times \vec{B}$ drift or the ∇B drift due to helical windings) effectively causes a poloidal precession of the orbit such that the particle spends equal time in the upper and lower halves of the torus. It should be noted at this point that the curvature drift has very little effect on the drift motion of these ripple-trapped particles. This is because the longitudinal velocity v_{\parallel} of these particles is very small, and the corresponding magnitude of \vec{v}_c is therefore quite small [see Eq. (2.18)].

The most straightforward approach for following the collisionless motion of particles within the plasma is to integrate the guiding center equations of motion numerically. This can be accomplished by integrating the equations of motion either in real-space coordinates or in magnetic coordinates, each approach having its advantages and disadvantages.

The coordinate system usually chosen for the real-space integration is shown in Fig. 2.2. With reference to Eqs. (2.8) and (2.17), the full equations of motion for the guiding center with instantaneous position, \vec{R} , can be written as

$$\frac{d\vec{R}}{dt} = \frac{\hat{b}}{eB} \times \left(\mu \nabla B + mv_{\parallel}^2 \frac{\hat{b}}{B} \cdot \nabla B - e\vec{E} \right) + v_{\parallel} \hat{b}, \quad (2.19)$$

$$\frac{dv_{\parallel}}{dt} = -\frac{e}{m} \hat{b} \cdot \vec{E} - \frac{\mu}{m} \hat{b} \cdot \nabla B, \quad (2.20)$$

where μ is given by Eq. (2.5) and v_{\parallel} is defined as

$$v_{\parallel} = \frac{d\vec{R}}{dt} \cdot \hat{b}(\vec{R})$$

with

$$\frac{d\vec{R}}{dt} = \frac{dR}{dt} \hat{e}_R + R \frac{d\varphi}{dt} \hat{e}_{\varphi} + \frac{dz}{dt} \hat{e}_z.$$

This formulation requires a detailed representation of the magnetic field structure (both in magnitude and direction) within the entire system. This is usually done

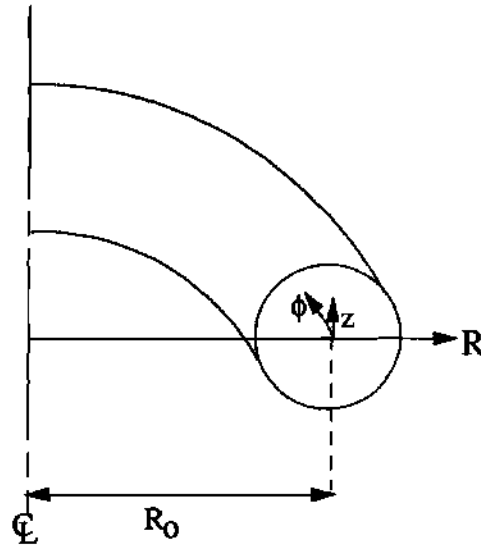


Figure 2.2: Coordinate system to be used for real-space integration.

by modeling the coil set as a set of elementary segments and using the Biot-Savart law to calculate the magnetic field at each point.¹² In general, this approach is very time-consuming, and execution times are generally 10–20 times greater than when magnetic coordinates are used.¹³ Furthermore, the true nature of the orbits is clearer in magnetic coordinates, since the slow motion across the field lines is separated from the fast motion along the field lines.

The most convenient set of magnetic coordinates for this purpose was first introduced by Boozer.¹⁴ In these coordinates the magnetic field lines are assumed to form a set of nested toroidal flux surfaces. The toroidal magnetic flux enclosed by the flux surface labeled ψ is $2\pi\psi\psi_{\text{tot}}$, where ψ_{tot} is the total toroidal flux. The poloidal (θ) and toroidal (φ) angle variables are chosen such that the rotational transform ($\iota = d\psi_{\text{pol}}/d\psi$) is constant on each flux surface so as to make the magnetic field lines straight in this coordinate system. In these coordinates, the magnetic field has the approximate contravariant and covariant representations^{15,16}

$$\vec{B} = \nabla\psi \times \nabla\theta + \nabla\varphi \times \nabla\psi_{\text{pol}} \quad (2.21)$$

$$= \mu_0 [g(\psi)\nabla\varphi + I(\psi)\nabla\theta] , \quad (2.22)$$

where $g(\psi_{\text{pol}})$ is the total poloidal current outside of the flux surface ψ , $I(\psi_{\text{pol}})$ is the toroidal current enclosed by the flux surface ψ , and μ_0 is the permeability of free space.

In the (ψ, θ, φ) coordinates, the guiding-center drift equations are essentially determined by the field strength $B(\psi, \theta, \varphi)$. The Hamiltonian for the drift trajectories is

$$H(p_\theta, \theta, p_\varphi, \varphi) = \frac{1}{2}mv_{\parallel}^2 + \mu B + e\Phi, \quad (2.23)$$

where B is local magnetic field strength and Φ is the electric potential. This formulation of the drift Hamiltonian has only four canonical coordinates. These four coordinates plus the constant magnetic moment μ and the irrelevant gyrophase are the six coordinates necessary to describe the motion of a particle in 3-D space. The canonical momenta P_φ and P_θ are given by¹⁶

$$P_\varphi = m(\mu_0 g/B) v_{\parallel} - e\psi_{\text{pol}} \quad (2.24)$$

$$P_\theta = m(\mu_0 I/B) v_{\parallel} + e\psi \quad (2.25)$$

The guiding centers of motion are then given by Hamilton's equation:

$$\begin{aligned} \dot{p}_\theta &= -\frac{\partial H}{\partial \theta}; & \dot{\theta} &= \frac{\partial H}{\partial P_\theta} \\ \dot{p}_\varphi &= -\frac{\partial H}{\partial \varphi}; & \dot{\varphi} &= \frac{\partial H}{\partial P_\varphi} \end{aligned}$$

The equations of motion in these coordinates can then be derived and are given by¹²

$$\begin{aligned} \frac{d\psi}{dt} &= (g\dot{P}_\theta - I\dot{P}_\varphi)/\gamma, \\ \frac{d\theta}{dt} &= \left(\delta \frac{\partial B}{\partial \psi} + e \frac{\partial \Phi}{\partial \psi} \right) \frac{\partial \psi}{\partial P_\theta} + \frac{e^2 B^2}{m^2} \rho_{\parallel} \frac{\partial \rho_{\parallel}}{\partial P_\theta}, \\ \frac{d\varphi}{dt} &= \left(\delta \frac{\partial B}{\partial \psi} + e \frac{\partial \Phi}{\partial \psi} \right) \frac{\partial \psi}{\partial P_\varphi} + \frac{e^2 B^2}{m^2} \rho_{\parallel} \frac{\partial \rho_{\parallel}}{\partial P_\varphi}, \\ \frac{d\rho_{\parallel}}{dt} &= [-(\rho_{\parallel} g' - \epsilon) \dot{P}_\theta + (\rho_{\parallel} I' + 1) \dot{P}_\varphi] / \gamma, \end{aligned}$$

where the quantities m , e , and $\rho_{\parallel} = mv_{\parallel}/eB$ are the particle's mass, charge, and parallel gyroradius, respectively. The functions γ and δ are defined by

$$\begin{aligned}\gamma &= e [g(\mu_0 \rho_{\parallel} I' + 1) - I(\mu_0 \rho_{\parallel} g' - \epsilon)] \\ \delta &= e^2 \rho_{\parallel}^2 B / m + \mu\end{aligned}$$

where μ is defined by Eq. 2.5. The canonical momenta are given by

$$\begin{aligned}\dot{P}_{\theta} &= -\delta \frac{\partial B}{\partial \theta} \\ \dot{P}_{\varphi} &= -\delta \frac{\partial B}{\partial \varphi}\end{aligned}$$

and the derivatives of ψ and ρ_{\parallel} with respect to the momenta are

$$\begin{aligned}\frac{\partial \psi}{\partial P_{\theta}} &= \frac{g}{\gamma} \\ \frac{\partial \rho_{\parallel}}{\partial P_{\theta}} &= -\frac{(\rho_{\parallel} g' - \epsilon)}{\gamma} \\ \frac{\partial \psi}{\partial P_{\varphi}} &= -\frac{I}{\gamma} \\ \frac{\partial \rho_{\parallel}}{\partial P_{\varphi}} &= -\frac{(I' \rho_{\parallel} + 1)}{\gamma}\end{aligned}$$

The first three equations in Eq. (2.26) are the equations of motion in configuration space while the last equation determines the motion in velocity space. In vacuum fields (i.e., no pressure gradients), $I(\psi) = 0$ and $g(\psi)$ is constant.¹³ Note that only the magnitude of B and its scalar derivatives are required in this approach.

The integration of Eq. (2.26) is straightforward given an accurate representation of the magnetic field. In general, two approaches have been used to model the magnetic field in a stellarator. The simplest expression for the magnitude of the magnetic field is given by Eq. (2.15). The $\epsilon_t \cos \theta$ term represents the finite toroidicity, as in a tokamak, and $\epsilon_h(\rho) = \epsilon_h \rho^{\ell}$ is the normalized amplitude of the dominant helical ripple component of the stellarator field with poloidal symmetry number ℓ , where $\rho = \psi^{1/2}$. This expression simply models the magnetic field strength as being due to the poloidal $\frac{1}{R}$ variation (as in a tokamak) with one helical ripple component.

While the approximation of Eq. (2.15) is useful for analytic studies of particle orbits, a more realistic model is required for detailed studies of orbit topology in a particular device. If accuracy is required, the magnetic field strength can be represented by Fourier decomposition,¹⁷

$$B = B_0 \sum_{n,m} B_{n,m}(\psi) \cos(n\varphi - m\theta). \quad (2.26)$$

Typically, at least 10–15 Fourier harmonics are necessary for accurate results when computing the particle orbits. This approach has been used for the majority of the orbit calculations in this work.

The main disadvantage of using Boozer coordinates is that particles cannot be followed outside the last closed flux surface (LCFS) since these coordinates are not defined outside this surface. This limitation forces the code to treat all particles that pass outside the LCFS as lost. Obviously, this is not realistic since there is a fairly large volume between the LCFS and the vacuum vessel in almost all fusion devices.

2.1.2 Constants of the Motion in Toroidal Devices

Because of the periodic nature of particle motion in toroidal magnetic systems, there are several constants of the motion that can be used to gain insight into the orbit topology without integrating the equations of motion. In general, there are two types of constants of the motion. The first type results from symmetry. When a system has symmetry in a given coordinate direction, that coordinate is considered an “ignorable” coordinate (i.e., the solution does not depend on it). From classical mechanics, it is well established that the component of momentum along an ignorable coordinate is a constant of the motion. For example, in an axisymmetric torus where the system is symmetric in the toroidal angle φ , the canonical momentum in the toroidal direction,

$$P_\varphi = R(mv_\varphi + eA_\varphi), \quad (2.27)$$

is constant. Here, A_ϕ is toroidal component of the magnetic vector potential and is dependent on the current density profile within the plasma. For a known current density profile, the conservation of P_ϕ along with the conservation of the kinetic energy W and the magnetic moment μ makes the motion integrable analytically (i.e., features of the orbit topology can be studied without integrating the equations of motion for each particle). This detailed understanding of particle orbits underlies the rapid and rather complete development of "neoclassical" transport in axisymmetric devices.¹⁸

Using this constants-of-the-motion approach, detailed studies of tokamak orbit topology and the associated loss regions have also been conducted.^{3,4} These studies have shown that for an axisymmetric tokamak, there are two classes of particles: (1) circulating particles that have sufficient parallel velocity to overcome the tendency to reflect in regions of high magnetic field and (2) trapped particles whose orbits trace out "banana-shaped" orbits when projected onto the r - θ plane. Typical tokamak ion orbits in the r - θ plane are shown in Fig. 2.3 (Ref. 3). This calculation is for 10-keV protons that pass through the point $\rho = 0.3$. Particles starting with pitch angles less than 45° are co-passing particles and follow virtually identical orbits. Similarly, particles with pitch angles greater than about 135° are counter-passing particles and also follow virtually identical orbits. For $90^\circ \leq \cos^{-1}(v_\parallel/v) \leq 120^\circ$, the ions are trapped in banana orbits. From this figure, it is apparent that the banana widths for some of these protons are large enough to carry them out of the plasma. For example, particles with pitch angles near 120° follow orbits that carry the particle outside the LCFS. Under these conditions, the particles are considered to be in the loss region of velocity/configuration space.

In determining the loss regions and transport effects associated with the various orbits, the quantity of interest is the maximum distance that the particles deviate from their original flux surfaces while on a particular orbit. Using the

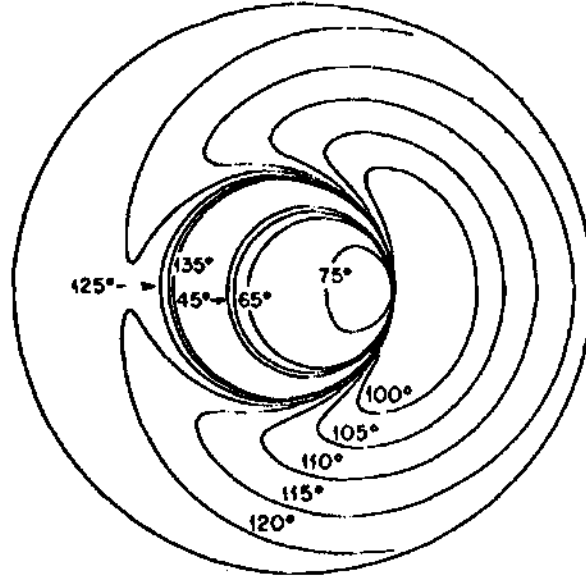


Figure 2.3: Trajectories for 10-keV protons in the Oak Ridge Tokamak (ORMAK) ORMAK that pass through the point $\rho = 0.3$. The various trajectories correspond to orbits with different pitch angles starting at the position $\rho = 0.3$ [Ref. 3].

conservation of canonical momentum [Eq. (2.27)], the deviation of these particles from their original flux surface along any part of the orbit is found to be¹¹

$$\Delta r(\theta) = r(\theta) - r(0) = \frac{2v_{\parallel}(0)}{\Omega_{\theta}} \left[1 + \epsilon_t - \frac{v_{\parallel}(\theta)}{v_{\parallel}(0)} (1 + \epsilon_t \cos \theta) \right], \quad (2.28)$$

where Ω_{θ} is defined as the gyrofrequency associated with the poloidal magnetic field, $\Omega_{\theta} = qB_{\theta}/m$.

For well untrapped (passing) particles the maximum excursion occurs at $\theta = \pi$ (referring to Fig. 2.3) and $v_{\parallel}(\theta) \simeq v_{\parallel}(0)$. The magnitude of this deviation is

$$\Delta r_{\max} = \frac{2v_{\parallel}(0)}{\Omega_{\theta}} [(1 + \epsilon_t) - (1 - \epsilon_t)] \simeq \frac{4v_{\parallel}(0)}{\Omega_{\theta}} \epsilon_t. \quad (2.29)$$

Therefore, passing particles are well confined inside the radius $a - \Delta r_{\max}$, where a is the characteristic cross-sectional dimension of the plasma. Since Δr_{\max} increases with particle energy, higher energy particles are preferentially lost. Also, since Δr_{\max} increases as the poloidal gyroradius ($\propto 1/\Omega_{\theta}$) decreases, losses are mitigated by a larger B_{θ} . For a given machine (where the magnetic configuration is generally fixed)

the only way to increase B_θ is through the current density profile. Therefore, ion confinement improves as the current density is increased.

For banana orbits, the maximum excursion occurs at $\theta = 0$ with $v_{\parallel}(\theta) \simeq v_{\parallel}(0)$. From Eq. (2.28),

$$\Delta r_{\max} = \frac{2v_{\parallel}(0)}{\Omega_\theta} [(1 + \epsilon_t) + (1 + \epsilon_t)] \simeq \frac{4v_{\parallel}(0)}{\Omega_\theta}. \quad (2.30)$$

In this case the quantity Δr_{\max} is known as the banana width of the orbit. Understanding the effect of this equation on the loss region is a little more difficult since a banana orbit has a leg of its orbit in which $v_{\parallel} > 0$ and a leg in which $v_{\parallel} < 0$. The quantity $v_{\parallel}(0)$ as defined in Eq. (2.30) is the value of the parallel velocity at $\theta = 0$, which can be defined on either the inner or outer leg of the orbit. A particle starting at a given radius r and $\theta = 0$ with a negative parallel velocity follows an orbit that carries it inward since Δr_{\max} is negative. In contrast, a particle starting at the same position with positive parallel velocity follows an orbit that carries it outward. Consequently, particles starting at the same location with the same parallel velocity but moving in opposite directions have significantly different confinement properties. Therefore, the loss region in velocity space in a axisymmetric toroidal device such as a tokamak is highly asymmetric.

Using this approach, the loss region for an axisymmetric tokamak can be analytically computed given the magnetic configuration and the current density profile. Figure 2.4 shows the result of such a calculation. Note that this represents only one-half of the velocity space. Almost all particles that have positive v_{\parallel} are contained, and therefore that half of velocity space is not included in this plot. The various curves represent the boundaries of the loss region for particles originating at different normalized minor radii. Any particle originating at a particular minor radius with velocity coordinates above the appropriate curve is lost. From this graph, it is evident that there is a large region of velocity space in which particles

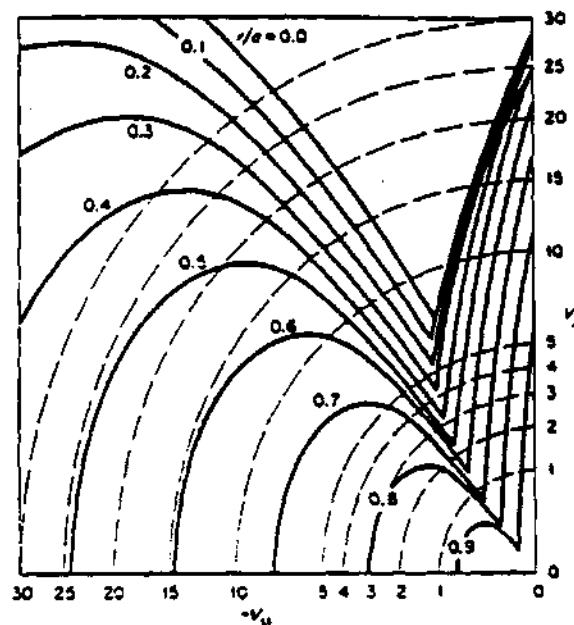


Figure 2.4: Loss region for protons in ORMAK. Any particle originating at a particular minor radius with velocity coordinates above the curve associated with that minor radius is lost. The axis labels are in keV [Ref. 3].

are lost. This is especially true for particles that originate near the edge of the plasma ($\rho = 0.9$) and for higher energy particles.

Unfortunately, since stellarators/torsatrons are asymmetric, another constant of the motion must be introduced to make the problem integrable (or at least analytically tractable). From classical mechanics it is well known that whenever a system has a periodic motion, the action integral $\oint p dq$ integrated over a period is a constant of the motion, where p and q are the generalized momentum and coordinate that repeat themselves in the motion. Even if a slow change is made in the system such that the motion is not quite periodic, the constant of the motion does not change and is called an adiabatic invariant. The magnetic moment μ is an example of an adiabatic invariant where the periodic motion is the gyromotion about the magnetic field line. A second adiabatic invariant exists for particles trapped in a magnetic well. A particle bounces within this well and has a periodic motion with a characteristic bounce time τ_b . Thus, a constant of the motion exists and is

given by $\oint mv_{\parallel} ds$, where ds is a differential path length along a field line. However, since the guiding center of the particle drifts across the field lines, the motion is not exactly periodic and the constant of the motion becomes an adiabatic invariant and is called the longitudinal invariant J .

Various studies of the orbit topology of stellarators indicate that there are three main classes of particles in stellarators. Circulating particles have sufficient v_{\parallel} to overcome the tendency to reflect in regions of high magnetic field strength. These particles simply move around the torus and are generally well confined. Helically trapped particles are trapped in the helical variation of the magnetic field, while blocked particles are trapped by the toroidal variation of B similar to banana orbits in tokamaks. Transitions from one trapping state to another are possible and are quite common for barely trapped particles.

Most analytic studies of orbit topology and confinement have emphasized the confinement of the helically trapped particles. These particles are confined to a small toroidal region, and their motion is periodic if the bounce time τ_b is much smaller than the drift time τ_d . Since the size of the banana orbit is small compared to the dimensions of the plasma, the guiding center of the banana itself can be considered. The drift motion of the banana center may be described by means of the longitudinal adiabatic invariant given by¹⁹

$$J = \oint mv_{\parallel} ds, \quad (2.31)$$

where ds is the incremental distance along a field line. Using the conservation of energy, Eq. (2.9), and the expression for the magnetic field given in Eq. (2.15), the parallel velocity can be written as

$$v_{\parallel} = \left\{ \frac{2}{m} [W - e\Phi - \mu B_0 (1 - \epsilon_t \cos \theta - \epsilon_h \cos \eta)] \right\}^{1/2}, \quad (2.32)$$

where $\eta = \ell\theta - N\varphi$. To first order the integral $\oint ds$ can be written approximately as

$L_c \int d\eta$, where $L_c \simeq R_o/N$ is defined as the "connection length" between successive ripple peaks along the field line.

By inserting Eq. (2.32) into Eq. (2.31), the following equation is obtained:

$$J = (2m)^{1/2} \int_0^{\eta_0} (W - e\Phi - \mu B_1 - \mu B_o \epsilon_h \cos \eta)^{1/2} \frac{R_o}{n} d\eta \quad (2.33)$$

where $B_1 = B_o(1 - \epsilon_t \cos \theta)$. This integral has the general form $\int \sqrt{a + b \cos x} dx$, which when evaluated gives²⁰

$$\int \sqrt{a + b \cos x} = \sqrt{\frac{2}{b}} [(a - b) K(\kappa) + 2bE(\kappa)] ,$$

where

$$\kappa = \sqrt{\frac{a + b}{2b}} ,$$

and $K(\kappa)$ and $E(\kappa)$ are the complete elliptic integrals of the first and second kind, respectively.

Evaluation of Eq. (2.33) then gives

$$J = 16 \frac{R_o}{n} (m\mu B_o \epsilon_h)^{1/2} [(\kappa^2 - 1) K(\kappa) + E(\kappa)] , \quad (2.34)$$

where

$$\kappa^2 = \frac{W - e\Phi - \mu B_o (1 - \epsilon_t \cos \theta - \epsilon_h)}{2\mu B_o \epsilon_h} .$$

The equations of motion in terms of J are¹⁹

$$\frac{dr}{dt} = \frac{1}{eB_o r} \frac{\partial J / \partial \theta}{\partial J / \partial W} , \quad (2.35)$$

$$r \frac{d\theta}{dt} = \frac{1}{eB_o} \frac{\partial J / \partial r}{\partial J / \partial W} , \quad (2.36)$$

which reduce to^{7,8,21}

$$\frac{dr}{dt} = V_{\perp} \sin \theta \quad (2.37)$$

$$\frac{d\theta}{dt} = \frac{V_{\perp}}{r} \cos \theta + \omega_h + \omega_E . \quad (2.38)$$

The toroidal drift velocity V_\perp , the rotational angular velocity due to the helical field ω_h , and the angular velocity due to the $E_r \times B$ drift ω_E are given by:

$$\frac{V_\perp}{r} = \epsilon_t \frac{\mu}{er^2} = -\epsilon_t \omega_o, \quad (2.39)$$

$$\omega_h = -2\ell \left(\frac{E(\kappa)}{K(\kappa)} - \frac{1}{2} \right) \epsilon_h \omega_o = -f(\kappa) \epsilon_h \omega_o, \quad (2.40)$$

$$\omega_E = \frac{E_r}{rB}, \quad (2.41)$$

where $\omega_o = -\mu/er^2$ is approximately the drift frequency. The ratio of the three terms $V_\perp/r : \omega_h : \omega_E$ is approximately $\epsilon_t : \epsilon_h : eE_r r/W_\perp$.

The radial drift [given by Eq. (2.37)] is dominated by the ∇B drift associated with the toroidal curvature — similar to the tokamak case. However, the poloidal drift results from a combination of the toroidal curvature drift, the ∇B drift due to the helical windings, and the $\vec{E} \times \vec{B}$ drift. Some general observations can be made using Eqs. (2.37) and (2.38). First, since a helically trapped particle does not follow the magnetic field line, the particle continually drifts vertically if the drift due to the toroidal curvature $[V_\perp (\sin \theta \hat{r} + \cos \theta \hat{\theta})]$ is not compensated. This compensation must be provided from a combination of the helical ∇B drift and the $\vec{E} \times \vec{B}$ drift that is sufficient to cause the particle to precess poloidally. This poloidal precession will effectively negate the vertical drift since the particle will spend equal amounts of time in the top and bottom halves of the plasma. If the helical ∇B drift and the $\vec{E} \times \vec{B}$ drift approximately cancel each other everywhere, the particle will immediately drift vertically out of the device. For a particular device where the magnetic configuration is fixed (\vec{B} and ∇B are known), the degree to which this compensation can affect confinement is inherently linked to the magnitude of the $\vec{E} \times \vec{B}$ drift. From the ratio of the drift terms given above, the influence of the $\vec{E} \times \vec{B}$ drift is seen to be important when $eE_r r \sim W_\perp \epsilon_h$. For a uniform E_r throughout the plasma, the quantity $E_r r$ in this expression is simply the relative difference between the electrostatic potential at the edge of the plasma and the potential energy at the

center, Φ_{rel} . In general, the magnitude of Φ_{rel} is limited since a fully ionized plasma tends to adjust itself such that quasi-neutrality is maintained. Most theoretical predictions suggest that the maximum attainable Φ_{rel} is on the order of the electron temperature ($e\Phi_{\text{rel}} \sim T_e$). Therefore, the $\vec{E} \times \vec{B}$ drift generally plays an important role only in the confinement of thermal particles.

The confinement of deeply helically trapped particles (i.e., those particles trapped in the bottom of a helical well where $\kappa^2 \sim 0$) can be tracked quite easily using the longitudinal adiabatic invariant J . When Eqs. (2.35) and (2.36) are integrated for these particles using the simple model field of Eq. (2.15), the trajectory on the (ρ, θ) plane is found to be²²

$$\epsilon_h + \epsilon_t \cos \theta - \frac{e\Phi}{\mu B} = \text{const.} \quad (2.42)$$

This equation is equivalent to a trajectory described by $e\Phi + \mu B_{\text{min}} = \text{const}$ where B_{min} is the minimum value of the magnetic field with respect to the toroidal angle,²³

$$B_{\text{min}}(\rho, \theta) = \min_{\varphi} B(\rho, \theta, \varphi). \quad (2.43)$$

Hence, the motion of the “banana” center of the deeply helically trapped particles can be described by simply determining the contours of constant $e\Phi + \mu B_{\text{min}}$ for a given configuration (where B and Φ are prescribed). As an example, the constant B_{min} contours for the standard ATF magnetic configuration are shown in Fig. 2.5. Also shown are representative orbits calculated from an orbit-following code for particles starting at the horizontal midplane ($\theta = 0^\circ$ or $\theta = 180^\circ$). This figure illustrates the accuracy of using the $e\Phi + \mu B_{\text{min}}$ contours to determine the confinement properties of the deeply helically trapped particles. In general, the degree of confinement of the deeply helically trapped particles can be estimated from the parameter

$$f_{\text{TPC}} = \frac{A_{B_{\text{min}}}}{A_{\text{pl}}}, \quad (2.44)$$

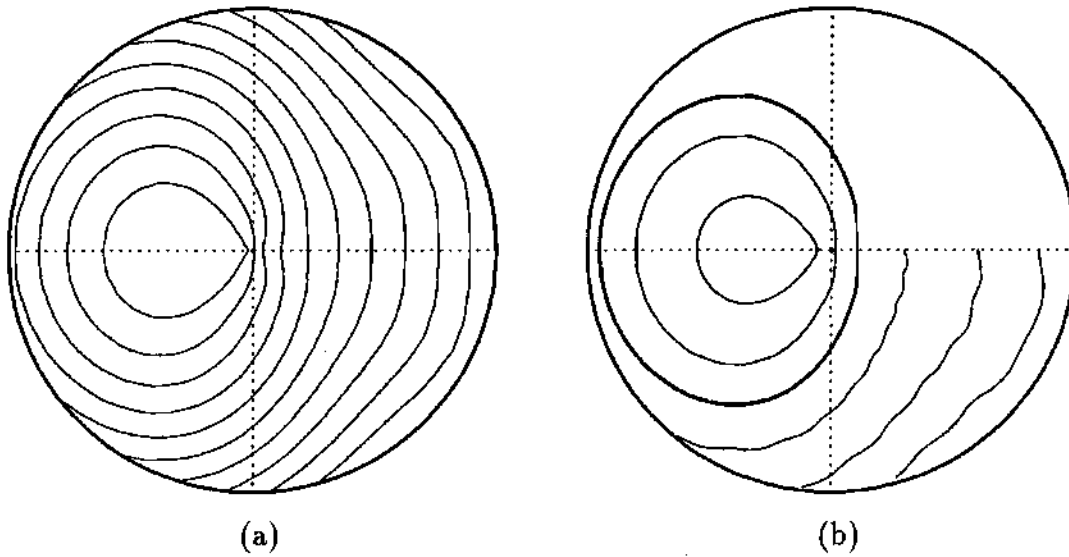


Figure 2.5: (a) Minimum B contours for the standard ATF magnetic configuration shown in the ψ - θ plane, where ψ and θ are the radial and poloidal Boozer coordinates, respectively. (b) Representative orbits of deeply helically trapped orbits started on the horizontal midplane projected on the ψ - θ plane.

where $A_{B_{\min}}$ is the area enclosed by the last closed $e\Phi + \mu B_{\min}$ contour and A_{pl} is the cross-sectional area of the plasma. The application of this approach in studying the ion confinement properties of the various magnetic configurations is discussed in Chapter 4.

More recent studies of particle orbits in stellarators have addressed the issue of orbit confinement for all classes of particles in stellarators. In general, a universal understanding of orbits in an asymmetric torus is impossible because the general problem is not integrable. However, because stellarators/torsatrons fall into a class of machines with a small rotational transform per field period (i.e., $\iota/N \ll 1$) and a small variation of the field strength due to the toroidicity compared with the variation along a field line due to the helical ripple (i.e., $\iota\epsilon_t/N\epsilon_h \ll 1$), an approximate constant of the motion based on the longitudinal adiabatic invariant J can be derived. The criterion $\iota\epsilon_t/N\epsilon_h \ll 1$ essentially divides all particles into two classes: those which are trapped in the local ripple due to the helical windings and those

which are untrapped. The criterion $\epsilon/N \ll 1$ provides a means by which to derive an approximate invariant J^* . In machines that satisfy this criterion, the poloidal rotation of a field line is quite small during one helical field period. In this case, to lowest order the poloidal variables (ψ and θ) are constant and particles move primarily in the toroidal direction.

In this case another adiabatic invariant can be derived from the expression

$$J^* = \int P_\varphi d\varphi,$$

where P_φ is given by Eq. (2.24). Integrating this expression and over a single helical field period and using Eq. (1.2), this invariant takes the form

$$J^*(\psi, \theta) = \mu_0 g(\psi) \int_0^{2\pi/N} d\varphi \frac{mv_{\parallel}}{B} - \sigma_{\parallel} e \frac{2\pi}{N} \int_0^{\psi} d\psi' \epsilon(\psi'), \quad (2.45)$$

where σ_{\parallel} is defined as

$$\sigma_{\parallel} = \begin{cases} \text{sgn}(v_{\parallel}) & \text{for locally passing particles} \\ 0 & \text{for locally trapped particles} \end{cases},$$

$g(\psi)$ is the total poloidal current outside the flux surface ψ , and N is the number of field periods. In contrast to the longitudinal adiabatic invariant $J = \oint m|v_{\parallel}|ds$, the path of integration for J^* is not along magnetic field lines but along quasi-field lines ($\theta = \text{const}$ and $\psi = \text{const}$). This makes the problem more tractable from an analysis point of view and more manageable from a computational point of view. Nonetheless, for deeply trapped particles ($\sigma_{\parallel} = 0$) the two invariants are nearly equal. In the limit of zero ϵ and in the case of the most deeply trapped particles, they are identical.

Equation (2.45) can be integrated quite easily for a given magnetic configuration and a fixed W and W/μ by simply integrating over a single helical field period holding ψ and θ constant. The particle orbits are then most easily determined by plotting constant contours of J^* in the ψ - θ plane. The regions in which each of the

three "sheets" (corresponding to the three values of σ_{\parallel}) of J^* is valid can be determined by calculating the location of the trapping boundary. For a given magnetic configuration and particle energy W , the value of μ uniquely determines the location of the trapping boundary. If $B_{\max}(\psi, \theta)$ is defined as the maximum of $B(\psi, \theta, \varphi)$ with respect to φ (in analogy to the definition of B_{\min}), the trapping boundary is determined by the contour where $e\Phi + \mu B_{\max}$ has the value W . At all points along this contour, a particle of energy W must have no longitudinal velocity ($v_{\parallel} = 0$), which is the condition for trapping. Thus, locations where $e\Phi + \mu B_{\max} > W$ are considered inside the trapping region while locations where $e\Phi + \mu B_{\max} < W$ are considered outside the trapping region (i.e., in the passing region).

An example of this type of calculation is shown in Fig. 2.6, where the three sheets of J^* along with the trapping boundary are shown for two values of W/μ for the standard ATF magnetic configuration (assuming $e\Phi = 0$). The fraction of trapped particles increases as μ increases (or W/μ decreases). Also, it is evident that the degree to which the helically trapped particles (and in general, all particles) are confined is critically dependent on the value of μ , or equivalently the pitch angle v_{\parallel}/v of the particle of interest.

The accuracy of this approach is evident from a comparison of orbits that have been computed from the equations of motion with the corresponding J^* contours. This comparison is shown in Fig. 2.7. Note that the motion predicted by the constant- J^* contours is the motion of the guiding center in the untrapped region and the motion of the banana center in the trapped region. Therefore, details of the exact orbits are not provided by this method. This can be seen in Fig. 2.7 where, although the computed orbits have fairly large excursions from the predicted J^* contour, the guiding centers of the orbits tend to follow the same path. The orbits on the right-hand side of Fig. 2.7(b) are examples of transitional particles that are predicted fairly accurately from the constant- J^* approach. These particles start on

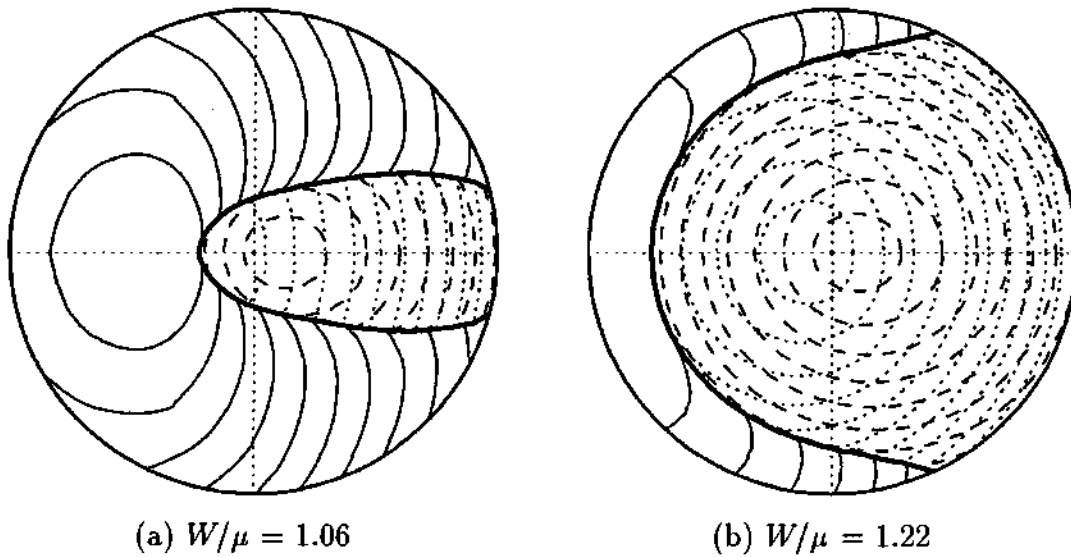


Figure 2.6: Contours of constant J^* for $W = 5$ keV and (a) $W/\mu = 1.06$ and (b) $W/\mu = 1.22$. The J^* contours corresponding to trapped particles are shown as the solid lines while the J^* contours for untrapped particles are shown as the dashed (co-passing) and dotted (counter-passing) lines. The bold solid curve represents the trapping boundary for the particular choice of W/μ .

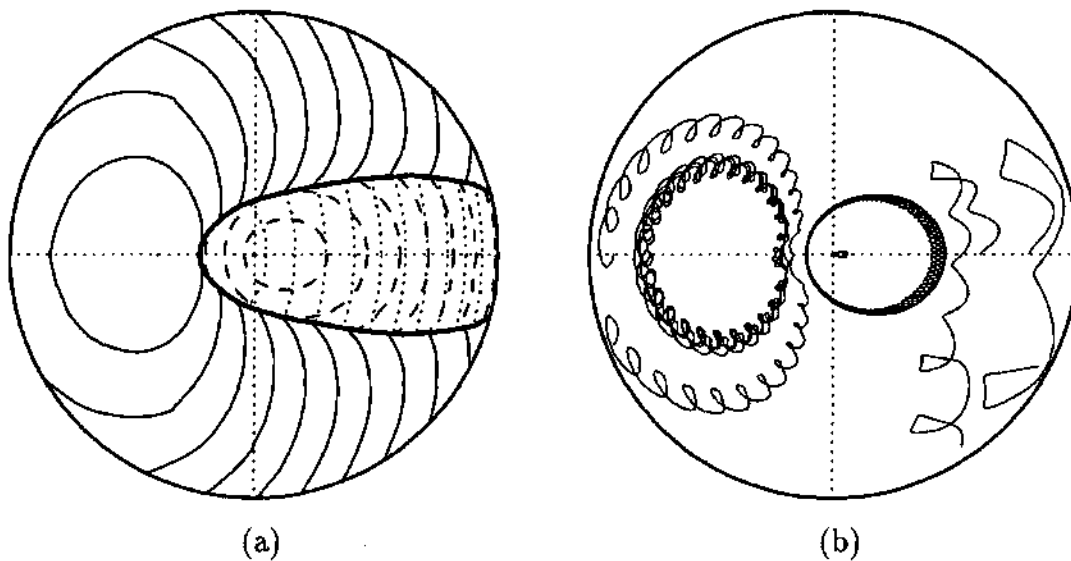


Figure 2.7: Comparison of (a) the J^* contours with (b) orbits computed from an orbit-following code for $W = 5$ keV and $W/\mu = 1.06$.

the horizontal midplane as locally co-passing particles [i.e., they follow a constant J_{co}^* contour ($\sigma_{||} = -1$)]. As these particles reach the trapping boundary [bold, solid line in Fig. 2.7(a)], a transition must occur where the particle continues its orbit on a constant- J_{ctr}^* contour ($\sigma_{||} = 1$) or a constant- J_{trap}^* contour ($\sigma_{||} = 0$). In this case, the particles are reflected at the boundary and follow J_{ctr}^* contours back through the locally passing region. As they encounter the trapping boundary the next time, the particles become helically trapped and subsequently follow the appropriate J_{trap}^* contour out of the confinement region.

A more detailed presentation of this approach in understanding ion behavior in ATF is presented in Chapter 4.

2.2 Effect of Collisions on Ion Behavior

The picture of purely individual motion of particles along their respective orbits is generally incorrect because these particles are, in general, suffering many small-angle "collisions" with other plasma particles along the orbit. The random nature of these collisions disrupts this fixed, calculable motion, and the degree to which the motion is randomized is determined by the degree of collisionality of a particular plasma species. In general, the effects of collisions and orbits are difficult to treat simultaneously. In fact, theoretical studies of ion confinement in a fusion device typically handle the orbit and collision part of the analysis separately. For example, in theoretical studies of particle and heat diffusion in a tokamak, the diffusion coefficient is estimated by using a characteristic collision step length derived from orbit considerations and a characteristic time computed from collisionality considerations.

This section describes the theoretical understanding of the effect of collisions on the ion distribution function. Distribution functions and the collision operator

for plasmas are described in Section 2.2.1. In dealing with ion behavior in a fusion device, there are generally two distinct distributions: a thermalized population characteristic of the background plasma and an energetic population used for heating purposes. Each of these distributions has distinct features that can be used to infer important parameters about ion confinement. In Section 2.2.2 the details of the thermal ion distribution are presented along with a discussion of the particle and heat transport equations for ions. The characteristics of the energetic-ion distribution are presented in Section 2.2.3.

2.2.1 Plasma Distribution Functions

Although, in principle, the characteristics of a plasma can be completely determined by following each particle in the confinement region (including a form of the collision operator along the way), such an approach is impractical except in a limited number of cases because of the large number of particles that must be followed. Instead, a statistical approach must be adopted. The complete statistical description of a system of N particles can be obtained in terms of a distribution function²⁴

$$F(\vec{r}_1, \vec{r}_2, \dots, \vec{r}_N, \vec{v}_1, \vec{v}_2, \dots, \vec{v}_N, t), \quad (2.46)$$

which describes the joint probability of particle 1 being at position \vec{r}_1 with velocity \vec{v}_1 , particle 2 being at position \vec{r}_2 with velocity \vec{v}_2 , and so on for all N particles in the system.

Since the quantity F can neither be calculated nor even estimated, a reduced version of F is necessary. A single-particle distribution function, f_1 , can be defined by integrating F over the spatial and velocity coordinates of all the other $N-1$ particles

$$f_1(\vec{r}_1, \vec{v}_1, t) = \int F(\vec{r}_1, \vec{r}_2, \dots, \vec{r}_N, \vec{v}_1, \vec{v}_2, \dots, \vec{v}_N, t) d\vec{r}_2, \dots, d\vec{r}_N d\vec{v}_2, \dots, d\vec{v}_N. \quad (2.47)$$

This distribution function specifies the probability that particle 1 is at position \vec{r}_1 with velocity \vec{v}_1 without regard to the position and velocity of the other $N-1$ particles and has the normalization

$$\int f_1(\vec{r}_1, \vec{v}_1, t) d\vec{r}_1 d\vec{v}_1 = 1. \quad (2.48)$$

If there are N_α indistinguishable particles of the same type as particle 1 in the system, they must all have the same distribution function. Hence, the distribution function for plasma species α can be defined as

$$f_\alpha(\vec{r}_\alpha, \vec{v}_\alpha, t) = N_\alpha f_1(\vec{r}_1, \vec{v}_1, t) \quad (2.49)$$

The evolution of the distribution function for each plasma species α is governed by the Boltzmann equation:¹¹

$$\frac{df_\alpha}{dt} = \frac{\partial f_\alpha}{\partial t} + \vec{v}_\alpha \cdot \nabla f_\alpha + \frac{e_\alpha}{m_\alpha} (\vec{E} + \vec{v}_\alpha \times \vec{B}) \cdot \nabla_{v_\alpha} f_\alpha = C_\alpha + S_\alpha + L_\alpha, \quad (2.50)$$

where C_α represents the changes in the distribution due to close encounters that can be treated as collisions and take place on a time scale that is short compared to the other phenomena of interest, while S_α represents sources and L_α represents losses. All of the long-range collective interactions and the interactions with the electric and magnetic fields are contained in the LHS (center) of this equation. Exact solutions of this equation are usually difficult to obtain because of its nonlinear character. In general, solutions depend on the form of the collision operator and on the expansion approximations that are often used for linearization purposes.

If the collision time scale is short compared to the time scale of other phenomena that affect the distribution function, the change in the distribution function due to collisions alone can be considered and the result used in Eq. (2.50) under the assumption that collisional effects are instantaneous on the time scale of interest for this equation. In terms of the probability $P(\vec{v}, \Delta\vec{v})$ that a particle changes its

velocity from \vec{v} to $\vec{v} + \Delta\vec{v}$ in time Δt as a result of a collision, the distribution at time t is obtained from the distribution function at time $t - \Delta t$ by²⁴

$$f(\vec{v}, t) = \int f(\vec{v} - \Delta\vec{v}, t - \Delta t) P(\vec{v} - \Delta\vec{v}, \Delta\vec{v}) d(\Delta\vec{v}). \quad (2.51)$$

Since small-angle scattering is the dominant collisional phenomenon in fusion plasmas,²⁵ $\Delta\vec{v}$ may be assumed to be small in a small time interval Δt , and the integrand in Eq. 2.51 can be expanded via a Taylor series, leading to the Fokker-Planck equation²⁴

$$\left(\frac{\partial f_\alpha}{\partial t} \right)_c = - \frac{\partial}{\partial \vec{v}} \cdot \left\langle \frac{\Delta\vec{v}}{\Delta t} \right\rangle f_\alpha(\vec{v}, t) + \frac{1}{2} \sum_{i,k} \frac{\partial^2}{\partial v_i \partial v_k} \left[\left\langle \frac{\Delta v_i \Delta v_k}{\Delta t} \right\rangle f_\alpha(\vec{v}, t) \right]. \quad (2.52)$$

A system in thermodynamic equilibrium satisfies $(\partial f / \partial t)_c = 0$. A system that is not in equilibrium can change in two ways. First, the velocity of a group of particles can change via dynamical friction. This is given by the first term on the RHS of Eq. (2.52). Second, the velocity distribution may spread. This would be termed velocity diffusion and is given by the second term in Eq. (2.52).

To apply Eq. (2.52) to a plasma, the coefficients $\langle \Delta\vec{v} / \Delta t \rangle$ and $\langle \Delta v_i \Delta v_k / \Delta t \rangle$ must be expressed in terms of collision properties representative of the plasma. From a detailed study of the collisional processes in the plasma, the following form of the Fokker-Planck equation is obtained:²⁶

$$C_\alpha \equiv \left(\frac{\partial f_\alpha}{\partial t} \right)_c = \sum_\sigma \frac{4\pi n_\sigma e_\sigma^2 e_\alpha^2}{m_\alpha^2} \ln \Lambda_{\sigma\alpha} \left[- \frac{\partial}{\partial v_i} \left(f_\alpha \frac{\partial h_\sigma}{\partial v_i} \right) + \frac{1}{2} \frac{\partial^2}{\partial v_i \partial v_j} \left(f_\alpha \frac{\partial^2 g_\sigma}{\partial v_i \partial v_j} \right) \right]. \quad (2.53)$$

Here, m_α and e_α are the mass and charge of the test particle, n_σ and e_σ are the density and charge of plasma species σ , $\ln \Lambda_{\sigma\alpha}$ is the Coulomb logarithm given by¹¹

$$\ln \Lambda_{\sigma\alpha} = \ln \left\{ 12\pi \left[\frac{(\epsilon_0 k T)^3}{n_\sigma e_\sigma^2 e_\alpha^2} \right]^{1/2} \right\},$$

and the functions h_σ and g_σ are the Rosenbluth potentials given by

$$g_\sigma(\vec{v}) = \int f_\sigma(\vec{v}') |\vec{v} - \vec{v}'| d\vec{v}', \quad (2.54)$$

$$h_{\sigma}(\vec{v}) = \frac{m_{\sigma}}{\mu_{\sigma}} \int \frac{f_{\sigma}(\vec{v}')}{|\vec{v} - \vec{v}'|} d\vec{v}', \quad (2.55)$$

where $\mu_{\sigma} = (m_{\alpha}m_{\sigma}) / (m_{\alpha} + m_{\sigma})$ is the reduced mass. Equation (2.53) describes the change in the distribution of test particles f_{α} due to collisions with particles of all types σ in the plasma. In practice, f_{α} can be treated as the ion distribution, and Eq. (2.53) describes the effect that collisions with the rest of the plasma have on the ion distribution (including self-collisions).

2.2.2 Characteristics of the Background Plasma

The background plasma is generally assumed to be in thermal equilibrium. In this situation, the solution to Eq. (2.53) takes the form of a Maxwellian energy (speed) distribution characterized by the local ion temperature, $T_i(\vec{r})$,

$$f_i^{\text{Max}}(\vec{r}, v) = \left(\frac{m_i}{2\pi e T_i(\vec{r})} \right)^{3/2} \exp \left(-\frac{m_i v^2}{2e T_i(\vec{r})} \right), \quad (2.56)$$

where m_i is the ion mass and the temperature is expressed in electron volts (eV), and $\int f_i^{\text{Max}}(\vec{r}, v) d\vec{v} = 1$. Unless the plasma consists entirely of nonthermal particles, the ion distribution function will always have a Maxwellian component. Since nonthermal ions are not usually created during Ohmic heating or ECH, the ion distribution function is usually Maxwellian during these heating processes.

The local ion temperature is governed by the particle and heat transport properties of the plasma. These transport properties are usually defined in terms of macroscopic quantities such as the average particle density, $n(\vec{r}, t) = \int f(\vec{r}, \vec{v}, t) d\vec{v}$, and the average particle velocity, $\vec{V}(\vec{r}, t) = \int \vec{v} f(\vec{r}, \vec{v}, t) d\vec{v} / n$. The macroscopic equations that govern the transport of a particular plasma species can be obtained by taking different moments of the Boltzmann equation [i.e., multiplying Eq. (2.50) by \vec{v}^n and integrating over all velocity space].²⁷ For a plasma with a single ion

species, the particle and heat transport equations are (neglecting viscosity):¹¹

$$\begin{aligned} \frac{\partial n_i}{\partial t} + \nabla \cdot \vec{\Gamma}_i &= S_i(r), \\ \frac{3}{2} \frac{\partial (n_i T_i)}{\partial t} + \underbrace{\frac{3}{2} \nabla \cdot (T_i \vec{\Gamma}_i)}_{\text{Convection}} + \underbrace{\frac{3}{2} \nabla \cdot \vec{q}_i}_{\text{Conduction}} &= q_{i,\text{coll}} + q_{i,\text{heat}} - q_{i,\text{loss}}, \end{aligned} \quad (2.57)$$

where $S_i(r)$ is the ion source rate, $\Gamma_i = n_i \vec{V}$, \vec{q}_i is the ion heat flux, $q_{i,\text{coll}}$ is the input power density from collisions with other plasma species, $q_{i,\text{heat}}$ is the input power density from other heating processes, and $q_{i,\text{loss}}$ is the power density lost through charge-exchange and other anomalous processes.

Because particles move freely along field lines and field lines generally ergodically form a flux surface, the density and temperature of the various plasma constituents are generally assumed to constant on a flux surface. Therefore, transport across the magnetic field line is the main channel through which conductive and convective processes transfer particles and heat within the plasma. This reduces the dimensionality of the problem to one, and if a normalized cylindrical geometry is used, these equations reduce to

$$\frac{\partial n}{\partial t} = S_i(r) - \frac{1}{\rho} \frac{\partial}{\partial \rho} (\rho \Gamma_i) \quad (2.58)$$

$$\frac{3}{2} n_i \frac{\partial T_i}{\partial t} = q_{i,e} + q_{i,\text{inj}} + q_{i,\text{ICH}} + q_{i,\text{fus}} - q_{i,\text{cx}} - \frac{1}{\rho} \frac{\partial}{\partial \rho} \left[\rho \left(\frac{3}{2} T_i \Gamma_i - q_i + q_i^{\text{na}} \right) \right] - \frac{3}{2} T_i \frac{\partial n_i}{\partial t}, \quad (2.59)$$

where the conduction term has been divided into two components: q_i , the neoclassical ion heat flux which contains the conduction due to the ion temperature gradient and q_i^{na} , the non-ambipolar ion heat flux due to the helical ripple, derived in Ref. 28. The formulation of the neoclassical heat flux q_i is the same for all toroidal devices; however, the non-ambipolar ion heat flux is only apparent in non-axisymmetric systems (e.g., stellarators). Energy loss due to charge-exchange with the background neutrals is given by $q_{i,\text{cx}}$ while $q_{i,\text{inj}}$, $q_{i,\text{ICH}}$ and $q_{i,\text{fus}}$ represent ion heating due to NBI, ICH, and fusion, respectively. In the cases to be studied for ATF, $q_{i,\text{ICH}} = q_{i,\text{fus}} = 0$.

The neoclassical ion heat flux q_i can be written in terms of the ion temperature gradient by defining an ion thermal conductivity coefficient χ_i such that

$$q_i(\rho) = -\chi_i(\rho)n_i(\rho)\frac{\partial T_i(\rho)}{\partial \rho}. \quad (2.60)$$

The determination of χ_i has been the subject of several efforts, both theoretical and experimental, the history of which is expounded in more detail in Chapter 3. Neoclassical theory for a tokamak, which takes into account the toroidal nature of the field topology when calculating transport- and confinement-related quantities, predicts that the ion thermal transport should be a factor $\sim (m_i/m_e)^{1/2}$ larger than the associated electron thermal transport. However, experiments suggest that the electron thermal diffusion coefficient exceeds the predicted neoclassical value by up to two orders of magnitude, while the ion thermal diffusion coefficient is generally on the order of the neoclassical prediction.^{29,30} The neoclassical predictions for χ_i were first reduced to a single expression by Hinton and Hazeltine.¹⁸ This expression was later modified to include the effect of finite toroidicity by Chang and Hinton.³¹ The form to be used here is a simplified form of the complete expression, given by

$$\begin{aligned} \chi_i^{\text{C-H}} &= K_i q^2 \rho_i^2 \nu_i, \\ K_i &= 0.66 \left(\frac{1.77 \nu_{*i} \epsilon^{3/2}}{1.0 + 0.74 \nu_{*i} \epsilon^{3/2}} + \frac{K_2^* \epsilon^{-3/2}}{1.0 + 1.03 \nu_{*i}^{1/2} + 0.31 \nu_{*i}} \right), \end{aligned} \quad (2.61)$$

where the finite toroidicity correction factor K_2^* is given by

$$K_2^* = 1 + 2.85 \epsilon^{1/2} - 2.33 \epsilon$$

The safety factor q , the toroidal gyroradius ρ_i , the ion collision frequency ν_i , the collisionality ν_{*i} , and the inverse aspect ratio ϵ are defined as

$$\begin{aligned} q &= \frac{1}{\epsilon} = \frac{r B_\phi}{R_o B_\theta}; & \rho_i &= \frac{m_i v_i}{e B_\phi} \\ \nu_i &= \left(\frac{T_e}{T_i} \right)^{3/2} \left(\frac{m_e}{m_i} \right)^{1/2} \left(\frac{n_i}{n_e} \right) \frac{Z_{\text{eff}}}{\sqrt{2} \tau_e} \\ \nu_{*i} &= \frac{\sqrt{2} R_o q \nu_i}{v_i \epsilon^{3/2}}; & \epsilon &= \frac{r}{R_o} \end{aligned}$$

where $v_i = (2T_i/m_i)^{1/2}$ is the thermal ion velocity.

In Eq. 2.59, it has been assumed that the collision term is dominated by contributions from collisions with electrons. This term is given by²⁷

$$q_{i,e} = 3 \frac{m_e}{m_p} \frac{n_e}{\tau_e} [Z] (T_e - T_i), \quad (2.62)$$

where τ_e is the electron-ion energy exchange time,

$$\tau_e = \frac{3m_e^{1/2} T_e^{3/2}}{4 (2\pi)^{1/2} e^4 n_e \ln \Lambda}.$$

The energy loss due to charge-exchange is given by

$$q_{i,cx} = \frac{3}{2} n_i(\rho) n_o(\rho) \langle \sigma v \rangle_{cx} [T_i(\rho) - T_o(\rho)], \quad (2.63)$$

where $n_o(\rho)$ and $T_o(\rho)$ are the local neutral density and temperature, respectively. Although this term is generally quite small, its effect must be included when considering low-density plasmas. The neutral beam heating term $q_{i,inj}$ is derived in Section 2.2.3.

In general, the thermal ion distribution is influenced by orbit effects. As mentioned earlier, neoclassical transport theory takes into account the orbit effects when deriving the ion heat conduction terms. However, there are other orbit effects that are difficult to treat from a theoretical point of view. These effects are usually due to "ripple"-trapped particles in tokamaks or helically trapped particles in stellarators. These classes of particles are not generally treated in the neoclassical description of particle transport because the "bounce" time of these particles is typically much smaller than the collision time. The motion of these particles constitutes a convective loss instead of a conductive loss since the particles flow out of the plasma on a collisionless time scale.

Also, the ion distribution can be distorted by orbit effects. For example, the so-called "helical" resonance (see Section 2.1) has been used to explain a depletion

in the measured charge-exchange spectra on Heliotron-E.³² Similarly, orbit effects may enhance the ion distribution in certain regions. For example, charge-exchange spectra measurements taken on various tokamaks and stellarators indicate an up-down asymmetry of the ion distribution. This asymmetry is theorized to be due to the vertical drift of "ripple-trapped" particles.

2.2.3 Characteristics of the Energetic Ion Distribution

When plasma heating is achieved by means of an energetic population of particles slowing down collisionally on the background plasma, the ion distribution also has a nonthermal component. The structure of this part of the distribution function is again governed by Eq. (2.53) with the test particle distribution f_a taken to be the fast-ion distribution and assuming that the background ion, electron, and impurity distributions are Maxwellian. In general, this is a good approximation, although there may be some distortion of the background distributions due to the dynamic drag caused by this high-energy, directed population.³³⁻³⁵ The most important collision process determining the thermalization of these particles is their loss of energy by dynamic friction and scattering on the background ions and electrons. However, the shape of the energetic ion distribution is not solely determined by these processes, since velocity diffusion through collisions with the faster-moving electrons can result in some ions gaining energy. Other effects must be considered in developing an expression for the evolution of the distribution function. Since there is a significant neutral density, the effect of charge-exchange events taking place before the fast ion completely thermalizes must also be taken into consideration. Furthermore, the existence of a toroidal electric field can affect the energetic ion distribution by accelerating particles injected parallel to the field and decelerating those injected antiparallel.³⁶

Energetic-Ion Fokker-Planck Equation The Fokker-Planck equation for energetic ions was first derived by Cordey and Core³⁶ for an azimuthally symmetric, spherical velocity coordinate system. This equation is given by

$$\begin{aligned} \tau_s \frac{\partial f_b}{\partial t} = & -\frac{\tau_s f_b}{\tau_{cx}} + \frac{1}{v^2} \frac{\partial}{\partial v} \left(v^3 - \frac{2T_e v}{m_b} + v_c^3 + \frac{T_i v_c^3}{m_b v^2} \right) f_b + \frac{1}{v^2} \frac{\partial^2}{\partial v^2} \left[\left(\frac{T_e v^2}{m_b} + \frac{T_i v_c^3}{m_b v} \right) f_b \right] \\ & + \frac{1}{2} \frac{m_i \langle Z \rangle v_c^3}{m_b [Z] v^3} \frac{\partial}{\partial \xi} (1 - \xi^2) \frac{\partial f_b}{\partial \xi} - \frac{e E_{\parallel}^* \tau_s}{m_b} \left(\xi \frac{\partial f_b}{\partial v} + \frac{1 - \xi^2}{v} \frac{\partial f_b}{\partial \xi} \right) + \tau_s S(v, \xi, t) \end{aligned} \quad (2.64)$$

where v_c is the critical velocity corresponding to the energy

$$E_{\text{crit}} = 14.8 T_e \left(\frac{m_b}{m_H} \right)^{1/3} \left(\frac{m_b}{m_i} \right)^{2/3} [Z]^{2/3}, \quad (2.65)$$

$$[Z] \simeq \sum_j n_j Z_j^2 \frac{m_i}{m_j} / \sum_j n_j Z_j, \quad (2.66)$$

$$\langle Z \rangle \simeq Z_{\text{eff}} = \sum_j n_j Z_j^2 / \sum_j n_j Z_j, \quad (2.67)$$

τ_{cx} is the charge-exchange lifetime for the fast ions,

$$\tau_{cx} = \frac{1}{n_o \langle \sigma_{cx} v \rangle}, \quad (2.68)$$

E^* is the neoclassical effective electric field,

$$E^* \simeq E_{\parallel} \left(1 - \frac{Z_b}{\langle Z \rangle} \right), \quad (2.69)$$

τ_s is the Spitzer ion-electron momentum exchange time,

$$\tau_s = \frac{3\pi^{3/2} \epsilon_0^2 m_b m_e v_c^3}{n_e e^4 \ln \Lambda Z_b^2}, \quad (2.70)$$

S represents the ion source, and $\xi = v_{\parallel}/v$ is the pitch angle. The subscript b indicates the beam species while the subscript i represents the plasma ion species.

This equation is valid for particle energies in the range $v_i < v \ll v_e$. The terms on the RHS of Eq. (2.64) represent, respectively, charge-exchange, drag, velocity diffusion, angular scattering, acceleration due to the electric field, and the

source. This equation simply describes the evolution of the fast-ion distribution in velocity space and has no information about configuration space included (i.e., this expression is valid in any magnetic configuration where the above inequality holds). Therefore, configuration effects such as those due to loss regions and radial diffusion of the fast ions are not taken into account by Eq. (2.64). To obtain an understanding of the physical processes wrapped up in the complicated expression given in Eq. (2.64), each term of this equation is examined individually.

The fast ions slow down through drag on electrons, bulk ions, and impurities. The corresponding rate of change of f due to this drag is [see Eq. (2.64)]

$$\left(\frac{\partial f_b}{\partial t}\right)_{\text{drag}} = \frac{1}{\tau_s v^2} \frac{\partial}{\partial v} \left(v^3 - \frac{2T_e v}{m_b} + v_c^3 + \frac{T_i v_c^3}{m_b v^2} \right) f_b, \quad (2.71)$$

where terms containing v_c^3 represent changes due to collisions with ions and the other terms represent changes due to collisions with electrons. The average rate of change of the velocity can be computed from the expression³⁷

$$\left\langle \frac{\partial v}{\partial t} \right\rangle = \frac{\int (\partial f_b / \partial t)_{\text{drag}} v^3 dv d\xi}{\int f_b v^2 dv d\xi}. \quad (2.72)$$

Taking $f = \delta(v - v_o)\delta(\xi - \xi_o)$ and integrating by parts, the following equation is obtained:

$$\left\langle \frac{\partial v}{\partial t} \right\rangle = -\frac{v}{\tau_s} \left[\left(1 - \frac{2T_e}{m_b v^2} \right) + \frac{v_c^3}{v^3} \left(1 + \frac{T_i}{m_b v^2} \right) \right]. \quad (2.73)$$

Note that the terms of order T/E (where $E = m_b v^2/2$ is the particle energy) tend to reduce the slowing-down rate; however, these terms are small with respect to the other terms. Hence, to zero order in T/E , Eq. (2.73) becomes

$$\left\langle \frac{\partial v}{\partial t} \right\rangle = -\frac{v}{\tau_s} \left(1 + \frac{v_c^3}{v^3} \right). \quad (2.74)$$

From this equation it is evident that slowing down due to electron friction is the dominant mechanism for velocities greater than the critical velocity. The critical velocity, v_c [corresponding to E_{crit} , defined in Eq. (2.65)], is the velocity at which the

fast ions slow down at equal rates on the ions and electrons. Since E_{crit} is proportional to the electron temperature T_e , the amount of beam energy delivered directly to the plasma electrons and ions is dependent on this temperature. For example, in the case where T_e is small and $E_{\text{crit}} \ll E_{\text{inj}}$, most of the beam energy is transferred to the electrons. The physical meaning of τ_s is also apparent from Eq. (2.74). If only collisions with electrons are considered, τ_s represents the characteristic slowing-down time of the fast ion.

The amount of time that it takes for a particle to slow down from the injection velocity to a particular velocity can also be computed easily from Eq. (2.74). By defining $w = v^3$, $w_{\text{crit}} = v_c^3$, Eq. (2.74) becomes

$$\frac{\tau_s}{3} \frac{\partial w}{\partial t} = w - w_{\text{crit}}. \quad (2.75)$$

With the initial condition, $w = w_o$, the general solution to this equation is

$$w = (w_o - w_{\text{crit}}) \exp(-3t/\tau_s) + w_{\text{crit}} \quad (2.76)$$

or

$$v = \left[(v_o^3 - v_c^3) \exp(-3t/\tau_s) + v_c^3 \right]^{1/3}, \quad (2.77)$$

and solving for t gives³⁸

$$t = \frac{\tau_s}{3} \ln \left(\frac{v_o^3 - v_c^3}{v^3 - v_c^3} \right). \quad (2.78)$$

As a particle slows down because of drag on the background plasma, it also scatters (i.e., changes its direction in velocity space). This scattering is known as pitch angle scattering since the pitch angle, $\xi = v_{\parallel}/v$, determines the direction in an azimuthally symmetric, spherical velocity coordinate system. The rate of change of f due to pitch angle scattering on the background plasma is given by [see Eq. (2.64)]

$$\left(\frac{\partial f_b}{\partial t} \right)_{\text{scatt}} = \frac{1}{2} \frac{m_i \langle Z \rangle v_c^3}{\tau_s m_b [Z] v^3} \frac{\partial}{\partial \xi} \left[(1 - \xi^2) \frac{\partial f_b}{\partial \xi} \right]. \quad (2.79)$$

This equation can be viewed as a competition between a frictional term ($\partial f / \partial \xi$), which tends to bring f to the average value $\xi = 0$, and a diffusive term ($\partial^2 f / \partial \xi^2$), which tends to make f isotropic in pitch angle.

The average rate of change of ξ due to collisions is³⁷

$$\left\langle \frac{\partial \xi}{\partial t} \right\rangle = \frac{\int \xi (\partial f / \partial t)_{\text{scatt}} v^2 dv d\xi}{\int f v^2 dv d\xi} = -\frac{m_i \langle Z \rangle v_c^3 \xi}{m_b [Z] v^3 \tau_s}. \quad (2.80)$$

Again, for energies well above the critical energy very little pitch angle scattering takes place. This is also a result of the fact that collisions with electrons represent the dominant mechanism at these energies.

The average change in ξ that a fast ion undergoes as it slows down can be estimated from Eq. (2.80). Using Eq. (2.77) for the time-dependent velocity in Eq. (2.80) and then integrating from an initial state i to a final state f leads to³⁹

$$\ln \left(\frac{\xi_f}{\xi_i} \right) = \frac{m_i \langle Z \rangle}{m_b [Z]} \left[\ln \left(\frac{v_f}{v_i} \right) - \frac{1}{3} \ln \left(\frac{v_f^3 + v_c^3}{v_i^3 + v_c^3} \right) \right] \quad (2.81)$$

or

$$\left\langle \frac{\xi_f}{\xi_i} \right\rangle = \left[\frac{v_f^3 (v_i^3 + v_c^3)}{v_i^3 (v_f^3 + v_c^3)} \right]^{m_i \langle Z \rangle / 3 m_b [Z]}. \quad (2.82)$$

For typical injection experiments, $m_i = 2$ and $m_b = 1$. The quantity $\langle Z \rangle$ is almost equivalently Z_{eff} and $[Z] \sim 1$, even for $\langle Z \rangle \sim 10$. Converting from velocity to energy, Eq. (2.82) becomes

$$\left\langle \frac{\xi_f}{\xi_i} \right\rangle = \left[\frac{E_f^{3/2} (E_i^{3/2} + E_{\text{crit}}^{3/2})}{E_i^{3/2} (E_f^{3/2} + E_{\text{crit}}^{3/2})} \right]^{\frac{2}{3} Z_{\text{eff}}}. \quad (2.83)$$

It is evident from Eq. (2.83) that an increased Z_{eff} dramatically enhances the pitch angle scattering of the fast ions. For example, with $E_{\text{crit}} = 10$ keV, $E_i = 30$ keV, $E_f = 20$ keV, and $Z_{\text{eff}} = 1$, Eq. (2.83) gives $\langle \xi_f / \xi_i \rangle = 0.92$. Hence, the pitch angle changes by only 8% while the fast ions slow down from 30 to 20 keV. However, a $Z_{\text{eff}} = 3$ results in a 22% change in ξ for the same values of E_{crit} , E_i , and E_f . As the energies begin to approach the critical energy, collisions with the

bulk ions become increasingly important. Consequently, the average change in pitch angle becomes larger. For instance, as the particles slow down from $E_i = 20$ keV to $E_f = 10$ keV for the case above, the relative pitch angle change is 23% for $Z_{\text{eff}} = 1$ and 54% for $Z_{\text{eff}} = 3$.

As the fast ions are slowing down and pitch angle scattering, there also is a spreading of the distribution. The diffusive spreading in the time interval, δt , is given by³⁷

$$\langle (\Delta v)^2 \rangle = \left(\left\langle \frac{\partial v^2}{\partial t} \right\rangle - 2v \left\langle \frac{\partial v}{\partial t} \right\rangle \right) \delta t. \quad (2.84)$$

and

$$\langle (\Delta \xi)^2 \rangle = \left(\left\langle \frac{\partial \xi^2}{\partial t} \right\rangle - 2\xi \left\langle \frac{\partial \xi}{\partial t} \right\rangle \right) \delta t. \quad (2.85)$$

Here, only the terms of order δt have been retained. Using Eq. (2.74) for $\left\langle \frac{\partial v}{\partial t} \right\rangle$ and Eq. (2.80) for $\left\langle \frac{\partial \xi}{\partial t} \right\rangle$ and deriving similar terms for $\left\langle \frac{\partial v^2}{\partial t} \right\rangle$ and $\left\langle \frac{\partial \xi^2}{\partial t} \right\rangle$, the following equations are obtained:

$$\langle (\Delta v)^2 \rangle = \frac{2\delta t}{\tau_s} \left(\frac{T_e}{m_b} + \frac{v_c^3}{v^3} \frac{T_i}{m_b} \right), \quad (2.86)$$

$$\langle (\Delta \xi)^2 \rangle = \frac{v_c^3}{v^3} \frac{m_i}{\tau_s m_b [Z]} (1 - \xi^2) \delta t. \quad (2.87)$$

In Eq. (2.86), the two terms represent speed diffusion on electrons and ions, respectively. Again, for energies well above the critical energy, $E \gg E_{\text{crit}}$, the velocity diffusion is dominated by collisions of the fast ions with the electrons. The $1 - \xi^2$ dependence of the pitch angle diffusion term [Eq. (2.87)] requires that the pitch angle diffusion vanish at boundaries of the velocity space, defined by $-1 \leq \xi \leq 1$.

As the fast ions are slowing down on the background plasma, they are also encountering a fairly significant neutral population. The effect of these ions suffering a charge-exchange reaction and subsequently being lost from the plasma is included in Eq. 2.64 through the operator

$$\left(\frac{\partial f}{\partial t} \right)_{\text{cx}} = -\frac{f}{\tau_{\text{cx}}}, \quad (2.88)$$

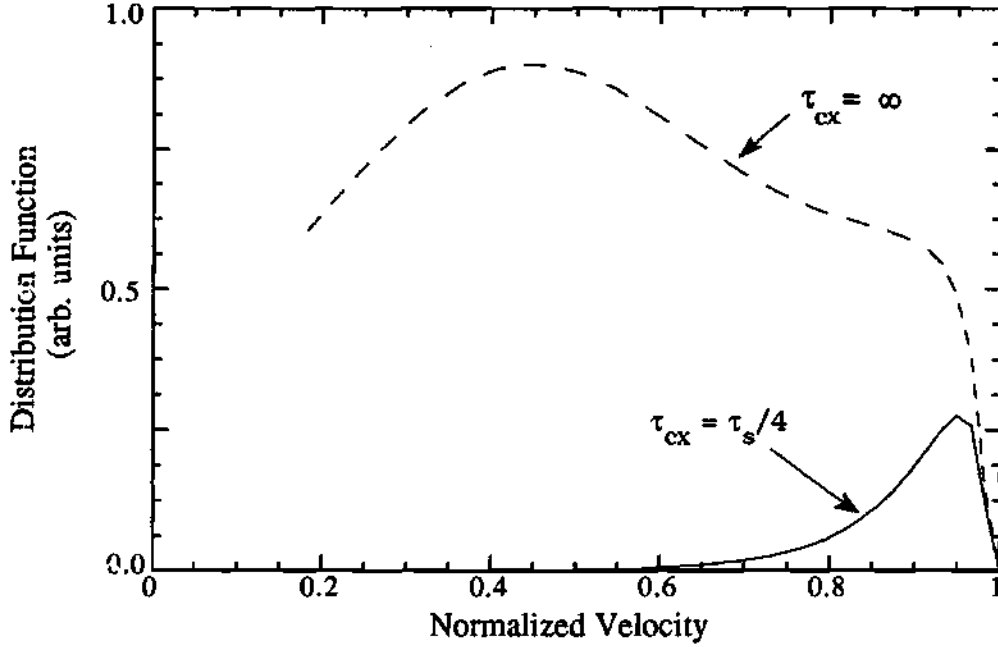


Figure 2.8: Effect of charge-exchange on the energetic ion distribution. Broken curve is $\tau_{cx} = \infty$ (no charge-exchange), and continuous curve is $\tau_{cx} = \tau_s/4$ (charge-exchange dominant). The critical velocity corresponds to $u \simeq 0.4$. The injection pitch angle is $\xi_{inj} = 1.0$ and the observation pitch angle is $\xi = 0.98$ [Ref. 36].

where τ_{cx} is the charge-exchange time given by Eq. (2.68). The conditions for charge-exchange to be important can be found by integrating Eq. (2.88) from an initial state i to a final state f using Eq. (2.78). The result is³⁹

$$\left(\frac{\Delta f}{f}\right)_{cx} = \left(\frac{v_i^3 + v_c^3}{v_f^3 + v_c^3}\right)^{-\tau_s/3\tau_{cx}} - 1. \quad (2.89)$$

The first term on the right-hand side simply represents the probability that a particle will slow down from v_i to v_f without being lost because of charge-exchange. Equation (2.89) shows that charge-exchange only becomes important when $\tau_{cx} \lesssim \tau_s$. The effect of charge-exchange on the distribution function is shown in Fig. 2.8. When $\tau_{cx} = \infty$ (no charge-exchange), the distribution shows no appreciable degradation at lower energies, as opposed to the $\tau_{cx} = \tau_s/4$ case, where the distribution is depleted significantly at lower energies. Since reabsorption of the charge-exchange neutrals by the plasma is not considered in this model, the loss due to charge-exchange may be overestimated.

The overall shape of the distribution function is determined by a combination of all of the above processes. Distinctive features result from the interaction of these processes, and each of these features can be used in investigating fast-ion behavior during NBI. At a particular pitch angle of velocity space, the energetic ion distribution dependence on velocity is determined by a competition between the rate at which particles lose their energy and the rate at which particles are lost (either completely lost from the plasma by charge-exchange or simply scattered out of the region of interest due to pitch angle scattering). The effects of this competition can be seen in Fig. 2.8. Note that the distributions presented here are for a pitch angle close to the pitch angle of the injected particles. The critical velocity is considerably less than the injection velocity; thus, pitch angle scattering is almost negligible for velocities slightly below the injection velocity. Since velocity space is defined by a spherical coordinate system, the region of velocity space defined by a given velocity decreases as the velocity decreases. When there are no losses (i.e., no charge-exchange present and low Z_{eff}), the slowing down of the distribution therefore results in a rise in the distribution function for energies below the injection energy but above the critical energy. However, in a situation where losses (e.g., charge-exchange) are dominant, the distribution is depleted below the injection velocity because of the enhanced losses (see solid curve in Fig. 2.8). The rollover in the distribution function in the case with no charge-exchange occurs at approximately the critical velocity where pitch angle scattering becomes important.

Solutions to the Fokker-Planck Equation If the velocity diffusion and electric field terms are neglected in Eq. 2.64, an exact analytic solution can be obtained^{36,40} by expanding f_b and S in Legendre polynomials and using the WKBJ method. Assuming the source function to be of the form

$$S = S_0 \delta(\xi - \xi_0) \delta(v - v_0) \quad (2.90)$$

where ξ_0 is the injection pitch angle and v_0 is the injection velocity, this solution reduces to³

$$f_b(v, \xi, t) = S_0 U \left[t - \frac{\tau_s}{3} \ln \left(\frac{v_0^3 + v_c^3}{v^3 + v_c^3} \right) \right] \frac{\tau_s}{2\pi(v^3 + v_c^3)} \left(\frac{v_0^3 + v_c^3}{v^3 + v_c^3} \right)^{-\frac{\tau_s}{3\tau_{ex}}} \sum_{n=0}^{\infty} \left(n + \frac{1}{2} \right) P_n(\xi) P_n(\xi_0) \left[\frac{v_0^3 + v_c^3}{v^3 + v_c^3} \right]^{m_i n(n+1)(Z)/6m_b[Z]} U(v_0 - v), \quad (2.91)$$

where U represents the unit step function and the P_n 's represent Legendre polynomials. Although this solution can be used to obtain a physical understanding of the processes that govern the fast-ion distribution, it is not appropriate for exploring the details of the evolution of the ion distribution since this equation assumes steady-state and because the real source term is much more complicated than a simple delta function.

To overcome this problem, several groups have developed numerical codes that solve Eq. (2.64) by transforming the equation into a set of finite difference equations^{41,42} and solving the equation numerically. The principal advantage of solving for f_b through numerical integration of Eq. (2.64) is computational speed. Because the equation is linear, the reliability is usually fairly good given the restrictions outlined below. Generally, Eq. (2.64) is transformed by the transformation $\xi = \cos \theta$ and the boundary conditions are taken to be⁴¹

$$\frac{\partial}{\partial v} \left[\left(\frac{T_e v^2}{m_b} + \frac{T_i v_c^3}{m_b v} \right) f_b \right]_{v=v_{\min}} = 0, \quad (2.92)$$

$$\left(\frac{\partial f_b}{\partial \theta} \right)_{\theta=0} = \left(\frac{\partial f_b}{\partial \theta} \right)_{\theta=\pi} = 0, \quad (2.93)$$

$$f_b(v_{\max}, \theta, t) = 0. \quad (2.94)$$

The first of these boundary conditions specifies that there be no particle flux due to energy diffusion across the velocity boundary at v_{\min} . Typically, v_{\min} is taken to be about twice the ion temperature. The boundary condition given by Eq. (2.93) results from symmetry.

The main problem with using Eq. (2.64) for the distribution function by this method is that the effects associated with the geometry of the system (e.g., radial diffusion, orbit effects) are not taken into account. Since the fast ions will have a velocity only a few times greater than that of the bulk ions, it is reasonable to expect that the fast ions are subject to a certain amount of radial diffusion. To approximate this diffusion, the term⁴³

$$\left(\frac{\partial f}{\partial t}\right)_\rho = -\frac{f_b}{n_b} \frac{1}{\rho} \frac{\partial}{\partial \rho} \left(\rho D_b \frac{\partial n_b}{\partial \rho} \right) \quad (2.95)$$

is incorporated into Eq. (2.64). Here, n_b is the fast-ion density and D_b is the fast-ion diffusion coefficient. Equation (2.64) is then evaluated by alternating between the velocity space integration where $\rho = \text{const}$ and real-space integration where v and ξ are conserved. The fast-ion diffusion coefficient has been estimated by experiments on TFTR to be $D_b < 0.05 \text{ m}^2/\text{s}$ for energetic passing particles.⁴⁴

To properly account for trapped particle effects (such as increased radial diffusion and loss regions), a 3-D version of the Fokker-Planck equation must be solved with the appropriate bounce averages. This is quite complicated, even numerically. There have been a number of attempts by various authors to include these toroidal effects and to take into account the radial excursions of the fast ions as they slow down.^{45,46} The first and most extensively applied of these is reported in Ref. 45. In this work the main interest is to evaluate the importance of loss regions on the slowing-down ion distribution. The approach was to numerically integrate Eq. (2.64) while holding $f_b = 0$ in the loss-region portion of velocity space. This effectively models the physics of a loss region in which particles that scatter into this region are instantly lost from the system. The loss regions for a given flux surface are assigned by approximating the loss regions shown in Fig. 2.4.

Moments of the Fokker-Planck Equation The amount of instantaneous energy delivered to the various plasma constituents as well as the amount

of power lost due to charge-exchange can be calculated using appropriate energy moments of Eq. (2.64).

For example, the amount of energy transferred to the electrons from the energetic ions as they slow down is given by

$$q_{e,inj} = - \int \frac{1}{2} m v^2 \left(\frac{\partial f_b}{\partial t} \right)_{elec} d\vec{v}, \quad (2.96)$$

where $(\partial f_b / \partial t)_{elec}$ is the change in f_b due to collisions with electrons, given by [see Eq. (2.64)]

$$\left(\frac{\partial f_b}{\partial t} \right)_{elec} = \frac{1}{v^2 \tau_s} \frac{\partial}{\partial v} \left(v^3 - \frac{2T_e v}{m_b} \right) f_b + \frac{1}{v^2 \tau_s} \frac{\partial^2}{\partial v^2} \left(\frac{T_e v^2}{m_b} \right) f_b. \quad (2.97)$$

The limits of integration for v are taken to be v_{min} , defined as the velocity at which there is no more energy diffusion, and v_{max} , defined as the velocity above which $f_b = 0$. Substituting Eq. (2.97) into Eq. (2.96) and using a spherical coordinate system, the following equation for $q_{e,inj}$ can be obtained by repeated use of integration by parts:⁴¹

$$q_{e,inj} = \frac{\pi m_b}{\tau_s} \int_0^\pi \sin \theta d\theta \left[v_{min}^2 \left(v_{min}^3 - \frac{2T_e v_{min}}{m_b} \right) f_b(v_{min}, \theta) \right. \\ \left. + 2 \int \left(v^4 - \frac{2T_e v^2}{m_b} \right) f_b dv - \frac{2T_e v_{min}^3}{m_b} f_b(v_{min}, \theta) - \frac{2T_e}{m_b} \int v^2 f_b dv \right], \quad (2.98)$$

where the boundary conditions specified in Eqs. (2.92)–(2.94) have been used to evaluate the boundary terms. The first two terms of the right-hand side of this equation represent the energy flowing into the electrons due to drag while the final two terms represent the energy flowing into the beam distribution from the electrons due to energy diffusion. The term $q_{e,inj}$ is in units of W/cm³; thus, this term represents a power density.

The power density flowing into the ions from the energetic distribution can be computed similarly and is given by⁴¹

$$q_{i,inj} = \frac{\pi m_b}{\tau_s} \int_0^\pi \sin \theta d\theta \left[v_{min}^2 \left(v_c^3 + \frac{T_i v_c^3}{m_b v_{min}^2} \right) f_b(v_{min}, \theta) \right. \quad (2.99)$$

$$+2 \int v \left(v_c^3 + \frac{T_i v_c^3}{m_b v^2} \right) f_b dv - \frac{2T_i v_c^3}{m_b} f_b(v_{\min}, \theta) - \frac{2T_i v_c^3}{m_b} \int \frac{1}{v} f_b dv \Big].$$

As in the electron case, the first two terms of the right-hand side of this equation represent the energy flowing into the ions due to drag, while the final two terms represent the energy flowing into the beam distribution due to energy diffusion.

The power density lost through charge-exchange is given by (in spherical coordinates)⁴¹

$$q_{cx, inj} = \pi m_b \int_0^\pi \sin \theta d\theta \int \frac{v^4}{\tau_{cx}(v)} f_b dv. \quad (2.100)$$

The energy density (i.e., pressure) stored in the beam at a given time can also be calculated from the distribution function from the expression

$$p = \int \frac{1}{2} m_b v^2 f_b d\vec{v}. \quad (2.101)$$

The fast-ion parallel ($p_{b,\parallel}$) and perpendicular ($p_{b,\perp}$) pressures due to the beam are given by⁴⁷

$$p_{b,\parallel} = \pi m_b \int_0^\pi \sin \theta \cos^2 \theta d\theta \int v^4 dv, \quad (2.102)$$

$$p_{b,\perp} = \pi m_b \int_0^\pi \sin^3 \theta d\theta \int v^4 dv. \quad (2.103)$$

2.3 Summary

As should be apparent from this discussion of the theoretical background of plasma ion behavior, the task of fully describing ion behavior in a particular device through experimental observation is monumental. However, several key characteristics of ion behavior can be determined from experimental measurements. For example, the theoretical expressions derived above for the fast-ion distribution can be compared with experimental observations to determine if the injected ions do

thermalize in a manner consistent with the theory. Because ion confinement is crucial to the success of toroidal confinement devices (especially stellarators), several experimental and theoretical studies have been conducted in this area. A brief synopsis of the experiments that have been conducted in regard to ion confinement is presented in Chapter 3. Because of the importance of ion confinement in stellarators, a comprehensive study of ion confinement in ATF has been undertaken using the NPA installed on ATF. The results of this study are presented in Chapters 4-6.

REFERENCES

- ¹ B. B. Kadomtsev and O. P. Pogutse, Nucl. Fusion **11**, 67 (1971).
- ² T. H. Stix, Plasma Phys. **14**, 367 (1972).
- ³ J. A. Rome et al., Nucl. Fusion **16**, 55 (1976).
- ⁴ J. A. Rome and Y. M. Peng, Nucl. Fusion **19**, 1193 (1979).
- ⁵ A. Gibson and J. B. Taylor, Phys. Fluids **10**, 2653 (1967).
- ⁶ A. A. Galeev, R. Z. Sagdeev, H. P. Furth, and M. N. Rosenbluth, Phys. Rev. Lett. **22**, 511 (1969).
- ⁷ K. Miyamoto, Nucl. Fusion **12**, 243 (1978).
- ⁸ H. E. Mynick, Phys. Fluids **26**, 1008 (1983).
- ⁹ J. D. Jackson, *Classical Electrodynamics* (John Wiley & Sons, Inc., New York, 1962).
- ¹⁰ T. G. Northrop, *The Adiabatic Motion of Charged Particles* (John Wiley & Sons, Inc., New York, 1963).
- ¹¹ W. M. Stacey, *Fusion Plasma Analysis* (John Wiley & Sons, Inc., New York, 1981).
- ¹² R. H. Fowler, J. A. Rome, and J. F. Lyon, Phys. Fluids **28**, 339 (1985).
- ¹³ R. H. Fowler, R. N. Morris, J. A. Rome, and K. Hanatani, Nucl. Fusion **30**, 997 (1990).
- ¹⁴ A. H. Boozer, Phys. Fluids **23**, 904 (1980).
- ¹⁵ A. H. Boozer, Phys. Fluids **24**, 1999 (1981).
- ¹⁶ A. H. Boozer, Phys. Fluids **27**, 2441 (1984).
- ¹⁷ G. Kuo-Petravic, A. H. Boozer, J. A. Rome, and R. H. Fowler, J. Comput. Phys. **51**, 261 (1983).
- ¹⁸ F. L. Hinton and R. D. Hazeltine, Rev. Mod. Phys. **48**, 239 (1976).
- ¹⁹ K. Miyamoto, *Plasma Physics for Nuclear Fusion* (MIT Press, Cambridge, 1980).

- ²⁰ I. S. Gradshteyn and I. M. Ryzhik, *Tables of Integrals, Series, and Products* (Academic Press, Orlando, 1980).
- ²¹ K. C. Shaing, J. A. Rome, and R. H. Fowler, *Phys. Fluids* **27**, 1 (1984).
- ²² K. Itoh, S. Itoh, A. Fukuyama, and K. Hanatani, *Nucl. Fusion* **29**, 1851 (1989).
- ²³ C. L. Hedrick, J. R. Cary, and J. S. Tolliver, "Adiabatic and Full Guiding-Center Motion in 3-D Toroidal Systems", to be submitted to *Phys. Fluids*.
- ²⁴ N. A. Krall and A. W. Trivelpiece, *Principles of Plasma Physics* (San Francisco Press, Inc., San Francisco, 1986).
- ²⁵ L. Spitzer, Jr., *Physics of Fully Ionized Gases* (Interscience Publishers, New York, 1956).
- ²⁶ M. N. Rosenbluth, W. M. MacDonald, and D. L. Judd, *Phys. Rev.* **107**, 1 (1957).
- ²⁷ S. I. Braginskii, *Rev. Plasma Phys.* **1**, 205 (1965).
- ²⁸ D. E. Hastings, W. A. Houlberg, and K. C. Shaing, *Nucl. Fusion* **25**, 445 (1985).
- ²⁹ L. A. Artsimovich et al., *Sov. Phys. JETP* **34**, 306 (1972).
- ³⁰ J. Hugill, *Nucl. Fusion* **23**, 331 (1983).
- ³¹ C. S. Chang and F. L. Hinton, *Phys. Fluids* **25**, 1493 (1982).
- ³² K. Hanatani et al., in *Controlled Fusion and Plasma Physics 1987 (Proc. 14th EPS Conf., Madrid, 1987)*, Vol. 11D, Part I, p. 396 (1987).
- ³³ C. E. Thomas and G. Neeley, *Bull. Am. Phys. Soc.* **31**, 9T22 (1986).
- ³⁴ J. G. Cordey, in *Plasma Physics and Controlled Nuclear Fusion Research 1974 (Proc. 5th Int. Conf., Tokyo, 1974)*, Vol. 1, p. 623 (IAEA, Vienna, 1975).
- ³⁵ E. Bittoni, J. G. Cordey, and M. Cox, *Nucl. Fusion* **20**, 931 (1980).
- ³⁶ J. G. Cordey and W. G. Core, *Phys. Fluids* **17**, 1626 (1974).
- ³⁷ R. J. Goldston et al., *J. Comput. Phys.* **43**, 61 (1981).
- ³⁸ J. A. Rome and J. D. Callen, *Bull. Am. Phys. Soc.* **18**, 77 (1973).
- ³⁹ A. Carnevali, *An Experimental Investigation of Fast Ion Confinement on the ISX-B Tokamak*, PhD thesis, University of Tennessee, Knoxville, 1985.

- ⁴⁰ R. J. Goldston, *Fast Ion Diagnostic Experiment on ATC: Radially Resolved Measurements of q , Z_{eff} , $T_{i\parallel}$, and $T_{i\perp}$* , PhD thesis, Princeton University, 1977.
- ⁴¹ R. H. Fowler, J. Smith, and J. A. Rome, *Comput. Phys. Commun.* **13**, 323 (1978).
- ⁴² J. H. Killeen, A. A. Mirin, and M. G. McCoy, Technical Report UCRL-83885, Lawrence Livermore Laboratory (1980).
- ⁴³ G. W. Hammett, *Fast Ion Studies of Ion Cyclotron Heating in the PLT Tokamak*, PhD thesis, Princeton University, 1986.
- ⁴⁴ R. H. Radeztsky, in *Controlled Fusion and Plasma Physics (Proc. 15th EPS Conf., Dubrovnik, 1988)*, Vol. 12B, Part I, p. 79 (1988).
- ⁴⁵ J. A. Rome, J. D. Callen, and J. F. Clarke, *Nucl. Fusion* **14**, 141 (1974).
- ⁴⁶ L. M. Hively, *Fusion-Product Transport in Axisymmetric Tokamaks: Losses and Thermalization*, PhD thesis, University of Illinois at Urbana-Champaign, 1980.
- ⁴⁷ H. C. Howe, Technical Report ORNL/TM-11521, Oak Ridge National Laboratory (1990).

CHAPTER III

Previous Ion Confinement Studies

Numerous experiments have previously been conducted to study the confinement properties of ions in tokamaks. However, because stellarator research has lagged well behind tokamak research since the advent of the tokamak concept in the mid-1960's, the number of ion confinement studies in stellarators to date is quite small. The type of experiments can be divided into two categories: thermal-ion confinement and fast-ion confinement studies. In general, the results produced by these experiments have indicated that ion behavior in most devices is in substantial agreement with the theoretically predicted behavior based on classical collisional processes and orbit effects.

The purpose of this chapter is to briefly review the results of these experiments. Because of the vast number of experiments that have been conducted in this area, a complete discussion of each experiment would be formidable. Thus, this discussion is limited to a broad overview of the conclusions from experiments similar to those presented later in this dissertation. For the interested reader, a fairly exhaustive set of references is included.

3.1 Tokamak Thermal Ion Confinement Studies

As discussed in the Chapter 2, the attainable plasma ion temperature in a fusion device is the result of a balance between the amount of heat supplied to the ions (from collisions and other heating processes) and the loss of energy due to

charge-exchange, particle diffusion (convection), and heat conduction. The first two of these loss processes depend on the background neutral density. Since the central neutral density decreases with increasing plasma size and density, the dominant loss term in the ion energy balance equation is generally heat conduction. Hence, several theoretical and experimental efforts have been made in hopes of quantifying the parameter that determines the magnitude of this conduction, the ion thermal diffusion coefficient χ_i .

In general, if ion temperature profile information is available, χ_i can be calculated fairly accurately by using a neutral transport code to estimate the charge-exchange and convection losses and then solving the ion heat transport equation [Eq. (2.59)] for χ_i . However, because of various experimental problems in measuring the ion temperature profile, full profile information is generally not available. In this case, the standard method of obtaining the central χ_i is to solve coupled one-dimensional transport equations for the electron and ion power flows using measurements of the electron density and temperature profiles and either the central ion temperature or the thermonuclear neutron yield as experimental inputs. The error associated with such a calculation is generally quite large because of the experimental uncertainties associated with various inputs. However, this method should produce results that are at least indicative of the value of χ_i in a particular device. This method is described in more detail in Chapter 5 where the determination of χ_i for various ATF operating conditions is presented.

The earliest work on ion energy transport was performed by Artsimovich on the T-3, T-4, TM-3, and T-6 tokamaks,¹ where the central ion temperature was measured with an NPA during various operating conditions. Artsimovich then compared the measured ion temperature with theoretical predictions by assuming that the ions gained most of their energy by Coulomb collisions with electrons [Eq. (2.62)] and lost most their energy through thermal conduction [Eq. (2.60)].² These assumptions

reduce the ion heat transport equation to the simple form

$$q_{i,e} = q_{i,\text{cond}},$$

where $q_{i,\text{cond}}$ is the heat loss due to the ion heat flux,

$$q_{i,\text{cond}} = \frac{1}{\rho} \frac{\partial}{\partial \rho} \left(\rho \chi_i(\rho) n_i(\rho) \frac{\partial T_i(\rho)}{\partial \rho} \right).$$

The ion thermal diffusion coefficient χ_i used by Artsimovich was a neoclassical form (i.e., taking into account the toroidicity of the device) first derived by Galeev and Sagdeev.³ The functional dependence of this form of the coefficient is given by

$$\chi_{i,\text{neo}}^{\text{Galeev}} \propto \frac{T_{i0}^{3/2}}{\epsilon R B_0^2}, \quad (3.1)$$

where ϵ is the rotational transform, R is the major radius of the plasma (m), and B_0 is the on-axis toroidal magnetic field (T). Integrating the equation $q_{i,e} = q_{i,\text{cond}}$, using Eqs. (2.62), (2.60), and (3.1), and solving for the central ion temperature T_{i0} , the following expression is obtained:

$$T_{i0}^{\text{pred}}(\text{eV}) = 5.1 \times 10^{-4} \left[\bar{a}^2 R B_0^2 \bar{n}_e \epsilon f(T_e/T_i) \right]^{1/3}, \quad (3.2)$$

where \bar{a} is the average minor radius (m), \bar{n}_e is the average electron density (m^{-3}), and

$$f(T_e/T_i) = \left(\frac{T_e}{T_i} - 1 \right) / \left(\frac{T_e}{T_i} \right)^{3/2}. \quad (3.3)$$

This expression is only valid when $T_e > T_i$, which is generally true when the only heat source to the ions is through collisions with the electrons. As Artsimovich pointed out,² the quantity $f(T_e/T_i)$ is nearly constant at 0.34 (within 15%) for $T_e/T_i > 1.6$. In general, the ratio of T_e to T_i is strongly dependent on the heating mechanism being used and the density of the plasma. As the density increases, the ion-electron collisional coupling term gradually increases in magnitude until T_e and T_i are nearly equal. Therefore, the ratio T_e/T_i is typically greater than 1.6 only in

situations where the plasma density is quite low and the primary heating mechanism is through the electron channel.

A similar scaling was also derived by Artsimovich for tokamaks and is given by²

$$T_{i0}^{\text{Artsimovich}}(\text{eV}) = 2.8 \times 10^6 \left(R^2 B_o^2 \bar{n}_e I_p \right)^{1/3}, \quad (3.4)$$

where I_p is the plasma current (A) and the numerical coefficient was obtained by fitting T_{i0} data from the T-3, T-4, TM-3, and T-6 tokamaks. The correct scaling of the measured T_{i0} with the neoclassical prediction in this case provided the first indication that ion heat transport was indeed neoclassical. However, this agreement does not justify the basic assumption that charge-exchange and convection losses are negligible compared to conduction losses or that the ion heat conduction coefficient is correctly given by the formula of Galeev and Sagdeev. Later experimental work showed the importance of convection and charge-exchange losses, especially in low-density plasmas where the neutral density is fairly high.^{4,5} Also, more refined theoretical calculations⁶⁻⁸ have produced expressions for the ion thermal diffusion coefficient that are up to an order of magnitude lower than those predicted by Galeev and Sagdeev. However, the values of the ion thermal diffusion coefficient inferred from measurements on various experiments⁹⁻¹⁵ have generally been in agreement (within a factor of 2) with the best available neoclassical prediction at the time. There were a few exceptions; measurements on the Tokamak Fontenay-aux-Roses (TFR)¹⁶ and Doublet III¹⁷ tokamaks during NBI have indicated anomalous ion behavior (i.e., $\chi_{i,\text{meas}} > \chi_{i,\text{neo}}$).

More recently, in an attempt to understand the processes governing tokamak transport, a community-wide tokamak transport initiative has placed a high priority on theoretical and experimental studies in this area. Several theoretical studies have suggested various mechanisms that may cause an increase in ion conduction, with the most prominent of these theories being the so-called η_i mode. This is an electrostatic

instability driven by the ion pressure gradient that is triggered when the ratio of the gradient scale length of the ion temperature $1/T_i (dT_i/dr)$ and the gradient scale length of the ion density $1/n_i (dn_i/dr)$ exceeds a critical value. Simultaneously, several experimental results using full ion temperature profiles obtained from neutral particle analysis or spectroscopic measurements indicated that χ_i may be 5–20 times higher than neoclassical, suggesting possible turbulent ion energy transport.^{18,19} Upon closer examination of these results, the value of the central χ_i was generally consistent with neoclassical predictions, although the measured χ_i profile differed dramatically from the predicted profiles.

Orbit effects have also been verified through thermal-ion measurements. As mentioned earlier, the so-called “helical” resonance (see Section 2.1) has been used to explain a depletion in the measured charge-exchange spectra on Heliotron-E.²⁰ Another effect that has been observed is due to the drift of ripple-trapped particles in tokamaks. Since these particles are trapped in a very small region toroidally, they drift vertically, up or down, depending on the direction of the toroidal magnetic field. The drift motion is determined by the energy of the particle, the degree of collisionality, and the depth of the magnetic field ripple. Since the magnitude of the drift increases with particle energy, the more energetic ions are more susceptible to being lost. Theoretically, this drift would produce an up-down asymmetry in the thermal ion distribution that becomes more asymmetric with particle energy. The first verification of this effect was seen on the TFR tokamak.²¹ In fact, most profile measurements of the ion distribution using an NPA exhibit this asymmetry when viewing perpendicularly.^{22–24} Further measurements on the Texas Experimental Tokamak (TEXT) have also verified that the observed up-down asymmetry becomes more pronounced as the energy of the particle increases.²⁵

A similar asymmetry has been observed on Heliotron-E, but curiously, the asymmetry becomes more pronounced at lower energies.²⁶ The explanation for this

peculiar dependence was based on an examination of orbit drifts in a stellarator. As discussed in Section 2.1.2, the drift motion of a helically trapped particle in a stellarator is a combination of the vertical drift due to the toroidal curvature and a poloidal precession due to $\vec{E} \times \vec{B}$ drift and the ∇B drift due to the helical windings. In general, the magnitude of the $\vec{E} \times \vec{B}$ drift is small enough that only particles with fairly low energies ($\sim T_e$) are affected by this drift. If the $\vec{E} \times \vec{B}$ drift is sufficient to effectively cancel the drift due to the helical windings (which increases as the energy of the particle increases), the particle can drift vertically due to the toroidal curvature drift, thereby producing the observed asymmetry.

3.2 Tokamak Fast Ion Confinement Studies

To obtain the plasma temperatures necessary for ignition to occur in a fusion reactor, some form of auxiliary heating is required. This auxiliary heating will most likely be supplied by a heating mechanism that uses the thermalization of high-energy particles on the background plasma (e.g., NBI, ICH, etc.). For a favorable power balance, these high-energy particles must be confined for a sufficient length of time such that a large portion of their initial energy is transferred to the background plasma. In terms of present-day devices, the study of fast-ion confinement is necessary to determine the attainable plasma parameters and to understand the physical processes by which heat is transferred from the high-energy population to the thermal population. Furthermore, studying the confinement of the energetic ions produced by NBI and ICH in current experimental devices provides an estimate of how well the energetic ions will be confined in a fusion reactor.

With the advent of NBI in the mid-1970's, several groups began studies of the processes governing the thermalization of the energetic ions and the effect of NBI on the background plasma both experimentally and theoretically. As described

in Section 2.2.3, extensive theoretical studies were conducted, starting with studies of the thermalization process of energetic ions and then extending these results to "real" tokamak geometry. The first measurement of the slowing-down distribution of fast ions in a tokamak was made on the CLEO experiment in 1974.^{27,28} The energy distribution of these ions was measured by a tangentially viewing NPA during co- and counter-injection. The theoretically expected energy spectra were calculated using an analytic solution to the Fokker-Planck equation for the fast-ion distribution (assuming no loss region) and folding in the neutral density profile. The measurements were found to be in substantial agreement with theoretically expected results over the entire energy range and provided the first confirmation that the beam ions in tokamaks slow down according to classical collisional theory.

A somewhat similar sequence of fast-ion measurements was performed on the Adiabatic Toroidal Compressor (ATC), concentrating on the energy range near E_{inj} .²⁹ In these experiments, 1-ms pulses of beam particles were injected tangentially, and the corresponding energy spectra as well as the rise time of the flux at various energies were measured by a tangentially viewing NPA. Theoretical spectra were calculated for the measurements using the actual geometry of the injector and the tokamak itself by first calculating the source of fast ions at each radius and pitch angle. The Fokker-Planck equation was then solved separately on each of 17 separate flux surfaces, to give the slowing-down distribution assuming that no loss regions existed. These distributions were folded together with the neutral density profile and an escape probability calculation to give the expected flux to the analyzer. A comparison of the calculated flux and measured flux for quasi-steady-state parallel injection again showed quite good agreement.

Since the effects of toroidicity (particle trapping and loss regions) are negligible for passing particles, the agreement of these first two experimental results with theory is expected. To study the effects of toroidicity on the slowing-down

distribution, measurements were made of the tangential fast-ion energy spectrum in ATC while using nearly perpendicular co-injection (7° from perpendicular).³⁰ The measurements showed surprisingly good agreement with the theory. The results from nearly perpendicular counter-injection, however, were very different from the theoretical calculations. This result stemmed from the fact that many of the ions were injected onto loss orbits. In addition, the ions that were initially confined would have to scatter through the loss region to be detected by the tangentially viewing analyzer.³¹

Further experiments made on the Oak Ridge Tokamak (ORMAK)⁴ and the T-11 tokamak³² with injected beam powers P_b comparable to or smaller than the Ohmic input power also indicated that the energetic ion distribution behaved classically. In general, the results achieved from these devices during co-injection alone were much better than those achieved during counter-injection, and ion confinement improved as the plasma current was increased. Both of these effects can be explained from orbit considerations, since ion confinement is much better for co-passing particles than for counter-passing particles and the flux surface excursion of a particle's orbit decreases with increasing plasma current [see Eq. (2.29)].

As higher NBI power levels were achieved, scaling results from a number of different tokamaks showed that the global energy confinement time τ_E^* (defined as the ratio of the total stored energy of the plasma to the input power) decreased as P_b was increased.^{33,34} To ensure that this decrease in τ_E^* was not due to an overestimate of the beam power delivered to the plasma, the confinement of fast ions in this power regime was investigated. Energetic ion confinement studies on larger devices like the Impurity Study Experiment (ISX-B),^{35,36} the Princeton Large Torus (PLT),³⁷ TFR,^{16,38} and the Poloidal Divertor Experiment (PDX)³⁹ again indicated that the beam ions behaved classically in this high-power heating regime. Further work on the present generation of machines, including DIII-D,⁴⁰ JET,⁴¹ and TFTR⁴² has also

indicated that the energetic particles deposit their energy into the ion and electron channels classically.

Anomalous fast-ion losses have been reported in the presence of a certain type of MHD oscillations, called "fishbones" because of their characteristic signature on Mirnov coils.⁴³⁻⁴⁵ These low-frequency ($f = 20-40$ kHz) oscillations were originally observed during high-power, near-perpendicular injection into high-beta plasmas on PDX and were generally accompanied by spikes in the measured charge-exchange flux.⁴⁶ Following the bursts, the neutral flux falls to a level $\sim 20\%$ lower than before the burst. This data suggests that there is a resonant interaction between the instabilities and the parallel energy beam ions.⁴⁷

3.3 Stellarator Ion Confinement Studies

As mentioned previously, progress in stellarator research has lagged well behind tokamak research since the advent of the tokamak concept in the mid-1960's. The principal reason for this delay has been the complex engineering required for the magnetic systems of a fusion device based on the stellarator concept. As a result, ion confinement studies in stellarators have been quite limited. Even though ion confinement studies have been conducted in various stellarator devices, many aspects of ion behavior in stellarators are not well established experimentally. Because the research in this area has been scarce, the results of the ion confinement studies in ATF that are presented in Chapters 5 and 6 represent a large fraction of the available database on ion behavior in stellarators. Furthermore, the current generation of stellarators (of which ATF is included) are all unique in their magnetic design, each having their relative advantages and disadvantages. Unlike tokamaks in which the basic magnetic design has only a small impact on ion behavior, changes in the magnetic configuration in stellarators tend to have large effects on ion behavior.

Therefore, it is not obvious that the observed ion behavior on one of these devices would provide an indication of the expected ion behavior on another device. Because it is important to see where the ion confinement studies conducted on ATF and presented in Chapters 5 and 6 fit into research in this area, a brief description of each of these devices is presented here, followed by a discussion of the results of the various ion confinement studies conducted on each device.

Besides ATF, there are three other major stellarator research facilities currently in operation. The first of the current generation of stellarators, Heliotron-E, was built by the Japanese and began plasma operation in 1981. Heliotron-E is an $\ell = 2$, $m = 19$ torsatron with a large aspect ratio, $A_p = 11$ ($R_o = 2.2$ m, $\bar{a} = 0.2$ m). It is equipped with a set of neutral beam injectors, which are capable of providing either purely perpendicular injection or near-perpendicular injection. Several ion confinement studies have been carried out by the Heliotron-E group using a vertically scannable NPA. The results of these studies are discussed later in this chapter.

The Compact Helical System (CHS), which began operation in 1988, is also in Japan. CHS is an $\ell = 2$, $m = 8$ torsatron with a small aspect ratio, $A_p = 5$ ($R_o = 1.0$ m, $\bar{a} = 0.2$ m), and is equipped with two neutral beam injectors, whose injection angle can be scanned from tangential to perpendicular. Although a horizontally scannable NPA has been installed to allow detail studies of the orbit effects on the thermalization of the injected ions, these studies have been limited to date because of the relative infancy of the CHS experimental program.

Wendelstein VII-AS (WVII-AS), built in Germany, also began plasma operation in 1988. The helical magnetic configuration is produced in WVII-AS by a set of modular coils instead of by continuous, helical windings. WVII-AS has an almost shearless magnetic configuration with a moderate aspect ratio, $A_p = 10$ ($R_o = 2.0$ m, $\bar{a} = 0.2$ m). Because of limited access to the vacuum vessel ports due

to the modular coil design, the neutral beam injectors on WVII-AS are oriented perpendicular to the magnetic field. Although this orientation is obviously undesirable from a heating efficiency point of view, the direct, orbit losses associated with perpendicular injection allows control of the magnitude of the radial electric field, allowing studies of the effect of E_r on ion confinement. The predecessor of WVII-AS was similarly a shearless device, Wendelstein VII-A (WVII-A), which had $\ell = 2$, $m = 5$ continuous helical windings at high aspect ratio, $A_p = 15$ ($R_o = 2.0$ m, $\bar{a} = 0.13$ m). WVII-A was also equipped with near-perpendicular neutral beam injectors because of limited access to the vacuum vessel ports. Studies on the WVII series of stellarators have emphasized the effect of the radial electric field on plasma performance and ion confinement properties.

Because ATF, CHS, and WVII-AS have only been in operation a short time, published data dealing with ion confinement studies from these devices have been scarce. Studies on Heliotron-E, however, have been fairly extensive and include detailed studies of both thermal- and fast-ion confinement. Although studies of ion behavior in stellarators have been scarce, the results of the measurements that have been made are encouraging. For example, various thermal ion confinement studies on these devices have generally indicated that thermal ion transport is consistent with neoclassical predictions. In a stellarator, neoclassical theory, which only takes into account the toroidal nature of the field topology when calculating transport- and confinement-related quantities, must be extended to include the effect of non-axisymmetric properties, such as the effect of the helical ripple. Since particles that are trapped in the helical ripple have characteristic orbits that are much different from the orbits of trapped particles in an axisymmetric system, ion heat transport in a stellarator is quite different from that in a tokamak. In a stellarator, the ion heat flux consists of two parts. The first is the neoclassical ion heat flux (similar to the tokamak case), derived from toroidicity arguments and given by Eqs. 2.60 and 2.61.

The second term is the non-ambipolar ion heat flux due to the helical ripple q_i^{na} , given in Ref. 48. Because the radial electric field E_r plays an important role in the confinement of helically trapped particles, it is expected that this non-ambipolar ion heat flux is strongly dependent on the magnitude (and sign) of E_r .

To study ion transport in a particular device, measurements of the ion temperature profile are generally required. Each of the stellarator facilities described above are equipped with diagnostics (either based on NPA or spectroscopic measurements) capable of providing this profile in proper plasma conditions. Complementary studies have been conducted on each of these devices and generally indicate (though not quite as convincingly as the tokamak results) that ion transport in these devices is consistent with neoclassical predictions (i.e., predictions based on χ_i^{C-H} and q_i^{na}). For example, studies on Heliotron-E using a vertical scanning NPA concluded that the measured ion temperature profile was consistent with one to three times neoclassical χ_i^{C-H} values (neglecting the contribution of the non-ambipolar ion heat flux) in ECH-heated plasmas at fairly low densities ($\bar{n}_e \simeq 5.0 \times 10^{12} \text{ cm}^{-3}$).⁴⁹ At higher densities ($\bar{n}_e \simeq 1.0 \times 10^{13} \text{ cm}^{-3}$), the measured ion temperature was much lower than the value expected from neoclassical predictions. Although this would indicate some anomalous effects at higher densities, the authors suggest that the lower temperature may be result from an underestimate of the neutral density in the boundary region where charge-exchange and convection losses dominate the ion power balance.

Because Heliotron-E is a large aspect ratio device and since recent theoretical studies suggest that compact (i.e., small aspect ratio) torsatrons are better suited as a reactor concept, similar studies as those done for Heliotron-E are necessary on a smaller aspect ratio device. Similar experimental results from CHS ($A_p = 5$) also indicate that the experimentally determined ion power balance is consistent with neoclassical predictions, though the authors indicate that more accurate mea-

surements are necessary to confirm this result.⁵⁰ Since ATF is almost twice the size of CHS, the thermal ion confinement studies conducted on ATF and presented in Chapter 5 extend the current experimental database in this area by providing the first experimental information on thermal ion transport in large, small-aspect-ratio stellarators.

To experimentally test the effect of the non-ambipolar ion heat flux on ion transport, ion confinement studies on WVII-A and WVII-AS have concentrated on the effect of the radial electric field, which results from the large, direct losses associated with perpendicular NBI in these devices. Experiments on WVII-A have shown that the ion thermal heat conduction was reduced significantly by the presence of this ambipolar electric field, though the ion power balance at outer radii could not be determined due to uncertainties in the magnitude of the charge-exchange and convection loss terms.⁵¹ Simulations of WVII-AS ion temperature profile data obtained during ECH and NBI discharges have also indicated that the measured ion energy transport lies somewhere between the neoclassical predictions computed with and without the non-ambipolar heat flux.⁵² In the presence of a strong radial electric field ($E_r = -100$ V/cm), the ion heat transport was found to be significantly reduced (up to a factor of three), consistent with neoclassical theory including the effect of the non-ambipolar heat flux.

As in the thermal confinement area, experimental studies of fast-ion confinement in stellarators are scarce. The main exception to this is the work performed on Heliotron-E during NBI in which extensive measurements of fast-ion confinement and thermalization have been conducted.²⁶ The primary ion diagnostic for these studies was a vertically scanning NPA that was used to measure the fast-ion distribution during perpendicular (0°) and off-perpendicular (28°) NBI. Because the injected ions are born (ionized) near the loss region of velocity space, simulations of the fast-ion distribution based on the fast-ion Fokker-Planck equation could not

be used because of the inherent inaccuracies. Therefore, a Monte Carlo simulation code was developed that followed the injected ions by integrating the equations of motion and including a collision operator until they were either thermalized, lost from the plasma due to charge-exchange, or hit the vacuum vessel wall. The NPA was oriented with a fixed perpendicular view of the plasma several helical field periods away from the injector. During perpendicular injection, a high charge-exchange flux was observed, indicating that the deeply trapped injected ions could circulate toroidally around the torus without being lost. This result was consistent with the predictions of the Monte Carlo simulation code, indicating that ion behavior in this case was consistent with drift orbit theory and classical slowing-down of the injected ions. Further studies on Heliotron-E have shown that the fast-ion confinement improves as the magnetic axis is shifted inward.⁵³ These results are also consistent with a classical picture of fast-ion confinement in stellarators. Although much more limited in scope, fast-ion confinement studies on WVII-A during near-perpendicular (6°) NBI also indicate that the injected ions behave classically.⁵¹ This conclusion is again based on the agreement between NPA measurements and Monte Carlo simulations of the injected ions.

Because Heliotron-E and the Wendelstein series of experiments have a much larger aspect ratio than ATF and are equipped with perpendicular neutral beam injection instead of tangential injection, these results are of little value in predicting fast-ion confinement properties in ATF or any small-aspect-ratio device with tangential injection. Although CHS is a small-aspect-ratio device and is equipped with tangential injection and a versatile NPA for measuring the fast-ion distribution, the available data from this device at the present time is extremely limited due to the relative infancy of the CHS experimental program. Preliminary measurements of the fast-ion distribution have been made during both NBI and ICH in CHS; however, detail simulations of the measured data have not been attempted at the present

time.

3.4 Summary

For the most part, experimental studies of the thermal- and fast-ion confinement in tokamaks indicate that the ions behave classically. Studies of thermal ion transport in tokamaks indicate that the measured ion heat transport coefficients are consistent with neoclassical predictions, though there are some experiments that indicate an anomalously high heat transport coefficient. Experimental investigations of fast-ion confinement in tokamaks also indicate that the ions behave classically. However, some anomalous effects have been observed in tokamaks coincident with strong MHD activity.

Although the understanding of ion behavior in tokamaks is fairly well established, the experimental database for ion confinement studies in stellarators is limited. Thermal ion confinement studies in stellarators suggest that the measured ion heat transport properties are consistent with neoclassical predictions. However, these experiments have been limited in scope and are typically subject to large uncertainties because of the unknown magnitude of the charge-exchange and convective ion heat losses. The main source of much of the data in this area has been from Heliotron-E and the Wendelstein series of stellarators, which are all large aspect ratio devices. Since ATF is a fairly small aspect ratio device, the results of the thermal-ion confinement studies conducted in ATF (presented in Chapter 5 of this thesis) represent new and valuable data on thermal ion confinement in a large, small-aspect-ratio stellarator.

Results from fast-ion confinement studies in stellarators suggest that energetic-ion behavior is also explainable from classical processes, though the available database in this area is quite limited. Most of this work has been dedicated to the study of

fast-ion confinement during perpendicular injection, in which a substantial fraction of the injected ions are promptly lost due to unconfined orbits. Confinement studies have yet to be done on devices equipped with tangential injection, such as ATF. Because the work in the area of fast-ion confinement in stellarators has been limited in scope to date, the work presented in Chapter 6, where the fast-ion confinement properties of various operating regimes in ATF are studied, represents the most comprehensive set of experiments performed to date to study fast-ion confinement in stellarators. Furthermore, these studies represent the first published results of fast-ion confinement in a compact (small-aspect ratio) torsatron and in the world's largest stellarator, ATF.

REFERENCES

- ¹ L. A. Artsimovich et al., Sov. Phys. JETP **34**, 306 (1972).
- ² L. A. Artsimovich, Nucl. Fusion **12**, 215 (1972).
- ³ A. A. Galeev and R. Z. Sagdeev, Sov. Phys. JETP **26**, 233 (1968).
- ⁴ L. A. Berry et al., in *Plasma Physics and Controlled Nuclear Fusion Research 1974 (Proc. 5th Int. Conf., Tokyo, 1974)*, Vol. 1, p. 113 (IAEA, Vienna, 1975).
- ⁵ P. Stott, Plasma Phys. **18**, 251 (1976).
- ⁶ F. L. Hinton and M. N. Rosenbluth, Phys. Fluids **16**, 836 (1973).
- ⁷ F. L. Hinton and R. D. Hazeltine, Rev. Mod. Phys. **48**, 239 (1976).
- ⁸ C. S. Chang and F. L. Hinton, Phys. Fluids **25**, 1493 (1982).
- ⁹ M. Gaudreau et al., Phys. Rev. Lett. **39**, 1266 (1977).
- ¹⁰ M. Brusati et al., Nucl. Fusion **18**, 1205 (1978).
- ¹¹ M. Murakami et al., Phys. Rev. Lett. **42**, 655 (1979).
- ¹² M. Kasai et al., Nucl. Fusion **25**, 1437 (1985).
- ¹³ W. W. Heidbrink, J. Lovberg, J. D. Strachan, and R. E. Bell, Nucl. Fusion **27**, 129 (1987).
- ¹⁴ J. Lovberg and J. D. Strachan, Nucl. Fusion **30**, 2533 (1990).
- ¹⁵ A. Ouroua et al., Nucl. Fusion **30**, 2585 (1990).
- ¹⁶ Equipe TFR, Nucl. Fusion **18**, 1271 (1978).
- ¹⁷ R. J. Groebner et al., Nucl. Fusion **26**, 543 (1986).
- ¹⁸ S. Corti et al., in *Controlled Fusion and Plasma Physics (Proc. 15th EPS Conf., Dubrovnik, 1988)*, Vol. 12B, Part I, p. 127 (1988).
- ¹⁹ R. J. Fonck et al., Phys. Rev. Lett. **63**, 520 (1989).
- ²⁰ K. Hanatani et al., in *Controlled Fusion and Plasma Physics 1987 (Proc. 14th EPS Conf., Madrid, 1987)*, Vol. 11D, Part I, p. 396 (1987).
- ²¹ Equipe TFR, in *Controlled Fusion and Plasma Physics (Proc. 7th EPS Conf., Lausanne, 1975)*, Vol. 2, p. 2 (1975).

- ²² V. S. Zaveryaev et al., *Sov. J. Plasma Phys.* **4**, 671 (1978).
- ²³ S. E. Grebenshchikov et al., *Sov. J. Plasma Phys.* **9**, 696 (1983).
- ²⁴ R. D. Bengtson, A. Ouroua, and A. G. Meigs, *Bull. Am. Phys. Soc.* **34**, 8S3 (1989).
- ²⁵ A. Ouroua, *Ion Thermal Diffusion in the Texas Experimental Tokamak*, PhD thesis, University of Texas at Austin, 1989.
- ²⁶ K. Hanatani et al., *Nucl. Fusion* **25**, 259 (1985).
- ²⁷ J. G. Cordey et al., *Nucl. Fusion* **14**, 441 (1974).
- ²⁸ J. G. Cordey et al., *Nucl. Fusion* **15**, 441 (1975).
- ²⁹ R. J. Goldston, *Nucl. Fusion* **15**, 651 (1975).
- ³⁰ K. Bol et al., in *Plasma Physics and Controlled Nuclear Fusion Research 1974 (Proc. 5th Int. Conf., Tokyo, 1974)*, Vol. 1, p. 77 (IAEA, Vienna, 1975).
- ³¹ R. J. Goldston, *Fast Ion Diagnostic Experiment on ATC: Radially Resolved Measurements of q , Z_{eff} , $T_{i||}$, and $T_{i\perp}$* , PhD thesis, Princeton University, 1977.
- ³² V. S. Vlasenkov et al., in *Plasma Physics and Controlled Nuclear Fusion Research 1976 (Proc. 6th Int. Conf., Berchtesgaden, 1976)*, Vol. 1, p. 85 (IAEA, Vienna, 1977).
- ³³ M. Murakami et al., in *Plasma Physics and Controlled Nuclear Fusion Research 1982 (Proc. 9th Int. Conf., Baltimore, 1982)*, Vol. 1, p. 57 (IAEA, Vienna, 1983).
- ³⁴ S. M. Kaye and R. J. Goldston, *Nucl. Fusion* **25**, 65 (1985).
- ³⁵ D. Swain et al., *Nucl. Fusion* **21**, 1409 (1981).
- ³⁶ A. Carnevali et al., *Nucl. Fusion* **28**, 951 (1988).
- ³⁷ H. Eubank et al., in *Plasma Physics and Controlled Nuclear Fusion Research 1978 (Proc. 7th Int. Conf., Innsbruck, 1978)*, Vol. 1, p. 167 (IAEA, Vienna, 1979).
- ³⁸ Equipe TFR, *Nucl. Fusion* **23**, 425 (1983).
- ³⁹ R. Kaita et al., *Nucl. Fusion* **25**, 939 (1985).
- ⁴⁰ W. W. Heidbrink, *Rev. Sci. Instrum.* **59**, 1679 (1988).

- ⁴¹ S. Corti et al., in *Controlled Fusion and Plasma Physics (Proc. 14th EPS Conf., Madrid, 1987)*, Vol. 11D, Part III (1987).
- ⁴² R. H. Radeztsky, in *Controlled Fusion and Plasma Physics (Proc. 15th EPS Conf., Dubrovnik, 1988)*, Vol. 12B, Part I, p. 79 (1988).
- ⁴³ K. McGuire et al., *Phys. Rev. Lett.* **50**, 891 (1983).
- ⁴⁴ J. L. Dunlap et al., *Phys. Rev. Lett.* **48**, 538 (1982).
- ⁴⁵ J. D. Strachan et al., *Nucl. Fusion* **25**, 863 (1985).
- ⁴⁶ P. Beiersdorfer, R. Kaita, and R. J. Goldston, *Nucl. Fusion* **24**, 487 (1984).
- ⁴⁷ W. W. Heidbrink et al., Technical Report PPPL-2405, Princeton Plasma Physics Laboratory (1987).
- ⁴⁸ D. E. Hastings, W. A. Houlberg, and K. C. Shaing, *Nucl. Fusion* **25**, 445 (1985).
- ⁴⁹ H. Zushi et al., *Nucl. Fusion* **24**, 305 (1984).
- ⁵⁰ H. Yamada et al., in *Controlled Fusion and Plasma Physics (Proc. 18th EPS Conf., Berlin, 1991)*, Vol. 15C, Part II, p. 137 (1991).
- ⁵¹ H. Wobig et al., in *Plasma Physics and Controlled Fusion Research 1986 (Proc. 11th Int. Conf., Kyoto, 1986)*, Vol. 2, p. 369 (IAEA, Vienna, 1987).
- ⁵² V. I. Afanasjev et al., in *Controlled Fusion and Plasma Physics (Proc. 18th EPS Conf., Berlin, 1991)*, Vol. 15C, Part II, p. 209 (1991).
- ⁵³ F. Wobig et al., in *Proc. 1st Int. Toki Conf. on Plasma Physics and Controlled Nuclear Fusion (Toki, 1990)*, p. 192 (NIFS, Nagoya, 1990).

CHAPTER IV

Ion Orbit Studies in ATF

In general, the orbit topology in ATF is extraordinarily complicated. Owing to the lack of toroidal symmetry, the loss region is complex and a function of many different parameters. This complexity requires the orbit topology to be computed by numerical codes, either by integrating the equations of motion or using the constant- J^* approach outlined in Chapter 2. A complete description of the orbit topology and associated loss regions in ATF and the many functional dependences would represent a heroic effort. However, to elucidate some of the results discussed in the analysis portion of this thesis, the basic aspects of the orbit topology in ATF are discussed in this chapter.

The analysis of the orbit topology presented here is unique in that it is applied for a particular device currently in operation using accurate representations of the magnetic field structure in ATF. Previous studies of the orbit topology in stellarators have been mostly theoretical in nature, either trying to understand the orbit topology from basic concepts or attempting to optimize ion confinement in various magnetic configurations, and have not been applicable to a particular device. In most of these studies, the model magnetic field of Eq. 2.15 is used to simplify analysis. Although this approach has provided useful information about broad characteristics of the orbit topology in various stellarator magnetic configurations, its use is not appropriate for studying a particular device. The goal of this chapter is elucidate some of the basic aspects of the orbit topology using accurate representations of the ATF magnetic field structure, so as to be as accurate as possible.

First, the general features of the orbit topology and the associated loss regions in ATF are discussed in Section 4.1. As mentioned in the Chapter 1, the basic magnetic design of ATF was determined by finding an optimal magnetic configuration in which neither the MHD stability of the plasma nor the orbit confinement was compromised. The three independent sets of vertical field (VF) coils (labeled the inner-VF, trim-VF, and mid-VF coils) were included in the design to allow for a greater degree of flexibility in choosing the magnetic configuration. In general, the orbit topology is strongly dependent on the magnetic configuration. This dependence is discussed in more detail in Section 4.2.

The radial electric field (or electrostatic potential profile) also plays an important role in the orbit topology. Early numerical work during the design phase of ATF indicated that orbit losses in ATF could be reduced by a factor of 10 in the presence of a strong radial electric field.¹ The effect of this radial electric field on the orbit topology in ATF is discussed in Section 4.3. Orbit effects also have a large impact on fast-ion confinement. Although studying the full slowing-down problem including orbit effects is extraordinarily complicated, some insight into the slowing-down process can be garnered by studying the effects of the orbit topology on the injected ions in ATF. These effects are discussed in some detail in Section 4.4. Finally, the effect of the orbit topology on measurements made by the NPA on ATF is discussed in Section 4.5.

4.1 General Considerations

In general, the confinement properties of a single particle in a particular ATF magnetic configuration are dependent on many different parameters. The velocity-space dependence of the loss region can typically be parameterized in terms of the energy of the particle W and a measure of the pitch angle of the particle. For this

discussion, the quantity $\lambda = \mu B_*/W$ is used as the measure of pitch angle, where μ is the magnetic moment and B_* is defined as the minimum value of the magnetic field in the plasma,

$$B_* = \min_{\phi, \theta, \psi} B(\phi, \theta, \psi).$$

The definition of λ constrains its value to the range $0 \leq \lambda \leq 1$. In configuration space, the location of the loss region is strongly dependent on both plasma radius ψ (or ρ) and the poloidal angle θ and to a lesser extent dependent on the toroidal angle ϕ . The dependence on each of these parameters can be quite complicated. As an example, the orbit topology calculated via the constant- J^* approach introduced in Section 2.1.2 for six different values of λ for a fixed energy $W = 5$ keV in the standard ATF magnetic configuration is shown in Fig. 4.1. The three sets of constant- J^* contours correspond to the three sheets of J^* defined in Section 2.1.2. Particles inside the trapping region follow orbits described by the constant- J_{trap}^* contours, while particles outside the trapping region follow orbits described by either the J_{co}^* ($v_{\parallel}/v < 0$) or the J_{ctr}^* ($v_{\parallel}/v > 0$) contours. As shown in Section 2.1.2, the calculated J^* contours for a particular configuration accurately predict the guiding center motion of the corresponding orbits calculated from an orbit-following code. The bold solid line in this figure represents the trapping boundary. The location of this boundary is defined by the chosen value of λ since at the turning point of an orbit (where $v_{\parallel} = 0$), the conservation of energy [Eq. (2.9)] requires that $\mu B/W = 1$ (assuming $e\Phi = 0$), where B is the magnitude of the local magnetic field. Since μ and W are constants of the motion, the trapping boundary is simply a function of the magnetic configuration. The trapping boundaries shown in Fig. 4.1 were computed by first obtaining the maximum value of the magnetic field with respect to the toroidal angle

$$B_{\text{max}}(\rho, \theta) = \max_{\phi} B(\rho, \theta, \phi).$$

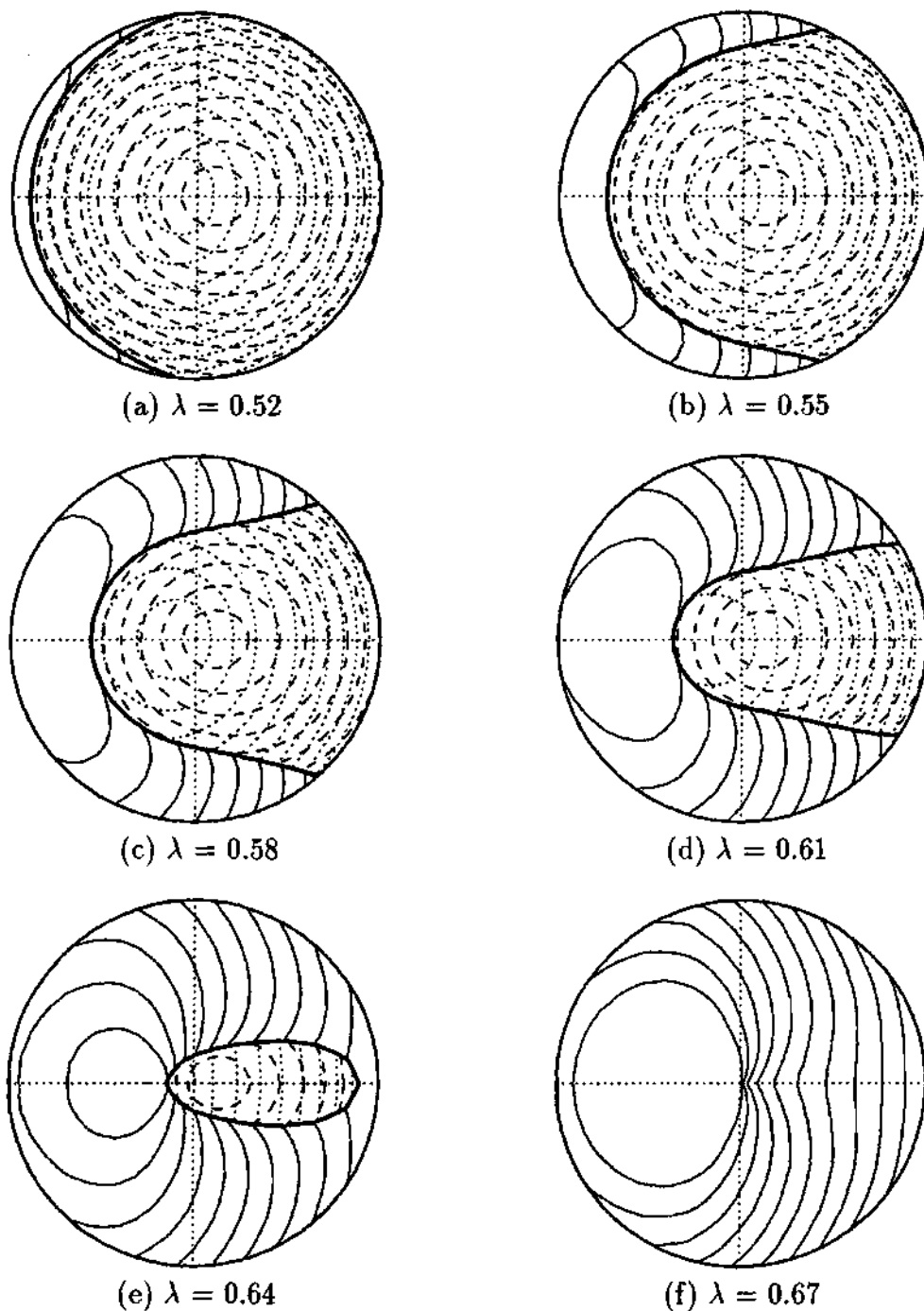


Figure 4.1: Contours of constant J^* for several values of λ in the standard ATF magnetic configuration with $W = 5$ keV. The J^* contours corresponding to trapped particles are shown as solid lines, while the J^* contours for untrapped particles are shown as dashed lines (locally co-passing) and dotted lines (locally counter-passing). The bold solid curve represents the trapping boundary for the particular choice of λ .

The trapping boundary then corresponds to the constant- B_{\max} contour corresponding to the value of W/μ . Note that this is not the trapping boundary for all particles with the specified value of λ but represents the absolute boundary inside of which all particles are locally passing. As expected, the fraction of trapped particles changes dramatically as the parameter λ is increased. For example, in Fig. 4.1(a), where $\lambda = 0.52$, there are very few trapped particles. In contrast, for the case where $\lambda = 0.67$ [Fig. 4.1(f)], there are no passing particles.

At any given point along the trapping boundary, three sheets of J^* are defined, given by J_{trap}^* , J_{co}^* , and J_{ctr}^* . As a particle moving along one of the constant- J^* contours encounters this boundary, it is forced to change state (i.e., it must continue its motion on one of the other sheets of J^*). For example, a locally co-passing particle following a constant- J_{co}^* contour (dashed lines in Fig. 4.1) that intersects the trapping boundary continues its motion either on a constant- J_{ctr}^* contour (dotted lines) that intersects the trapping boundary at the same location or on a constant- J_{trap}^* contour (solid lines). The values of J^* for a given orbit at the intersections of these three sheets are generally not the same; hence, J^* is discontinuous during one of these transitions. Orbits that intersect this boundary are generally in an chaotic location as far as the orbit topology is concerned. The corresponding motion of these orbits is characterized by transitions from one state to another on each encounter of the trapping boundary. Eventually, the orbit will generally sample all of its possible states. Therefore, for the complete orbit to be confined, all of the states of the orbit (corresponding to the three constant- J^* sheets) must be confined. Evident in Fig. 4.1 is the fact that most of the helically trapped J^* contours (solid lines) that intersect the trapping boundary also connect to the LCFS (outer circle of graph). Therefore, a particle that undergoes a transition from locally passing to helically trapped (either collisionlessly or through collisions) finds itself on an orbit that carries it outside the plasma boundary. This figure also shows that the only

helically trapped particles that are confined are those that reside on orbits inside the magnetic axis of ATF ($90^\circ \leq \theta \leq 270^\circ$).

Another feature evident in Fig. 4.1 is the difference between the constant- J_{co}^* contours and the constant- J_{ctr}^* contours. The constant- J_{co}^* contours are essentially concentric circles shifted slightly outside the magnetic axis of ATF. The constant- J_{ctr}^* contours are also concentric circles but are shifted slightly inside the magnetic axis. Although this shift has a small impact on confinement properties when λ is small [see Fig. 4.1(a)], it has a larger impact as the value of λ increases. This is evident by taking a closer look at Fig. 4.1(c). In this figure, the last closed J_{ctr}^* contour encloses a much smaller portion of configuration space than the last closed J_{co}^* contour. Since the orbits that intersect the trapping boundary undergo a transition to helically trapped and are generally lost, the fraction of locally counter-passing particles (particles with $v_{||}/v > 0$) that are confined is much smaller than the fraction of confined, locally co-passing particles (particles with $v_{||}/v < 0$).

The loss region has also been studied by using an orbit-following code that numerically integrates the equation of motion. The result of such a calculation is shown in Fig. 4.2. For this calculation, 5-keV particles were initially distributed uniformly in pitch angle between 35° and 145° along a major radius in the horizontal midplane at the toroidal angle $\phi = \pi/12$. In this figure, the variation in major radius is parameterized by a normalized plasma radius ρ_* such that $\rho_* < 0$ for a major radius outside the magnetic axis of ATF and $\rho_* > 0$ for a major radius inside the magnetic axis. The motion of these particles was then computed by integrating the equation of motion using a full representation of the ATF magnetic field structure. A particle was followed for 1 msec or until the computed orbit passed through the LCFS, in which case the particle was assumed to be lost.

The loss region computed in this way is in substantial agreement with the previous discussions of the orbit topology. The most striking feature in this figure is

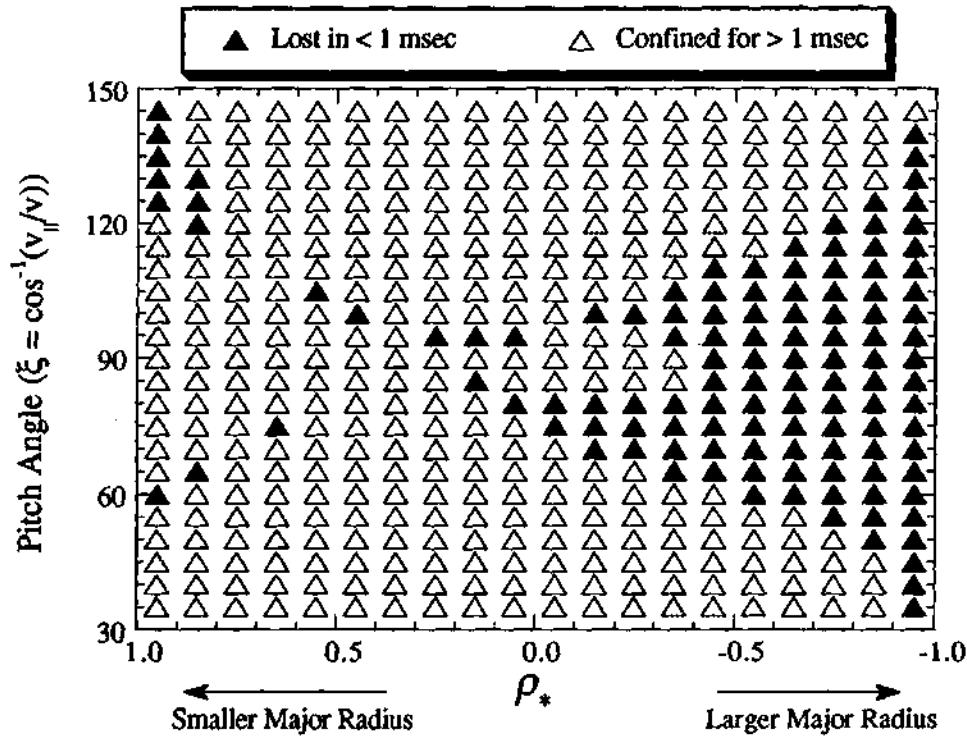


Figure 4.2: Computed loss region in ATF as a function of the initial pitch angle and normalized radius ρ_* . A positive normalized radius in this case corresponds to a major radius inside the magnetic axis of ATF, while a negative normalized radius is outside the magnetic axis. Particles started at the locations denoted by the open triangles are confined, while particles started at the locations denoted by the solid triangles are lost.

that most particles started outside the magnetic axis of ATF ($\rho_* < 0$) are lost while almost all of the particles started inside the magnetic axis ($\rho_* > 0$) are confined. This agrees quite well with observations made earlier concerning the computed constant- J^* contours. Another feature evident in this figure is the slightly better confinement of particles with $v_{\parallel}/v < 0$ (pitch angle $> 90^\circ$) than of those with $v_{\parallel}/v > 0$ (pitch angle $< 90^\circ$).

The small hole (of confined particles) in the computed loss region near perpendicular (pitch angle $= 90^\circ$, $v_{\parallel}/v = 0$) is due to the fact that these particles are deeply helically trapped and are generally well confined. This is apparent upon examination of Fig. 2.5, where the constant- B_{\min} contours are shown for the standard ATF magnetic configuration. The last closed contour in this figure extends slightly outside the magnetic axis of ATF. Since the deeply trapped particles tend to follow the constant- B_{\min} contours (as discussed in Section 2.1.2), the confined region for these particles extends outside the magnetic axis of ATF. In general, the orbit confinement properties of deeply trapped particles in ATF are slightly better than those of particles with slightly larger pitch angles, resulting in the small hole in Fig. 4.2.

The few orbits that are not confined in the upper, right-hand corner of Fig. 4.2 are co-passing particles that start near the inside (in major radius) wall of the device and are lost because of the finite shift of the orbit. This effect can also be seen in Fig. 4.1(a), where it is apparent that the constant- J_{co}^* contour that passes closest to the inside wall is not confined. A similar effect occurs for counter-passing particles that start near the outer wall, as can be seen in Fig. 4.1(a).

The sidebands extending from the main loss region to the right-hand side of Fig. 4.2 are generally coincident with the trapping boundary shown in Fig. 4.3. As discussed earlier, orbits in this region are characterized by many transitions between the helically trapped and passing states and are generally unconfined. Figure 4.3

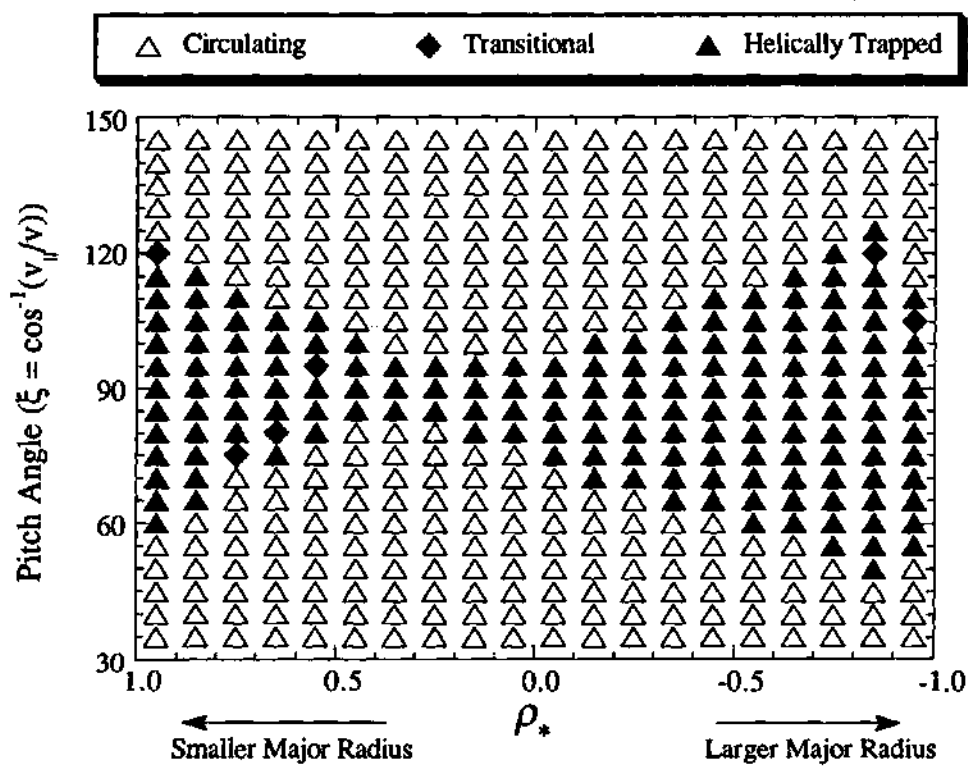


Figure 4.3: Classification of orbits for the calculation presented in Fig. 4.2. The symbols indicate the type of orbits observed: circulating (open triangles), helically trapped (solid triangles), and banana trapped or transitional (solid diamonds).

also illustrates that the trapping boundary does not occur at a fixed pitch angle throughout the plasma. In fact, the pitch angle at which the trapping boundary occurs changes drastically (from $v_{||}/v = \pm 0.5$ for $\rho_* = \pm 1$ to $v_{||}/v = \pm 0.1$ for $\rho_* = 0$).

The orbit topology is also dependent on the particle energy, as illustrated by Fig. 4.4. The orbit topology for the passing particles changes substantially as a function of energy, while the orbit topology for the helically trapped particles remains basically the same. This peculiar result is due to the mechanisms that govern the drift motion of these two classes of particles. In the passing case, the radial drift results from the vertical drift due to the toroidal curvature of the magnetic field and to a lesser extent the ∇B drift due to the helical windings. Since these particles tend to follow the magnetic field lines fairly closely, the poloidal rotation of the field lines helps to cancel this vertical drift by requiring the particle to spend equal amounts of time in the upper and lower halves of the torus. However, because the magnitude of the drift due to the toroidal curvature drift increases as the particle energy increases, the orbit of a higher-energy particle has a much larger radial excursion than a lower-energy particle with the same value of λ . This results in a slightly "larger" orbit when projected on the ψ - θ plane, as is exemplified in Fig. 4.4.

In contrast, helically trapped particles are confined to a small region toroidally and do not experience the full rotational transform of the magnetic field. The motion of the helically trapped orbits in the ψ - θ plane is therefore completely determined by the relative magnitudes of the toroidal curvature drift and the ∇B drift due to helical windings [see Eqs. (2.37) and (2.38)]. Since both of these terms are dependent on the energy of the particle in the same manner, the motion in the ψ - θ plane should be independent of energy. The higher-energy particle does tend to precess poloidally at a quicker rate, but the projection of the orbit on the ψ - θ plane is the same. In the presence of a radial electric field, the dependence of the orbit topology

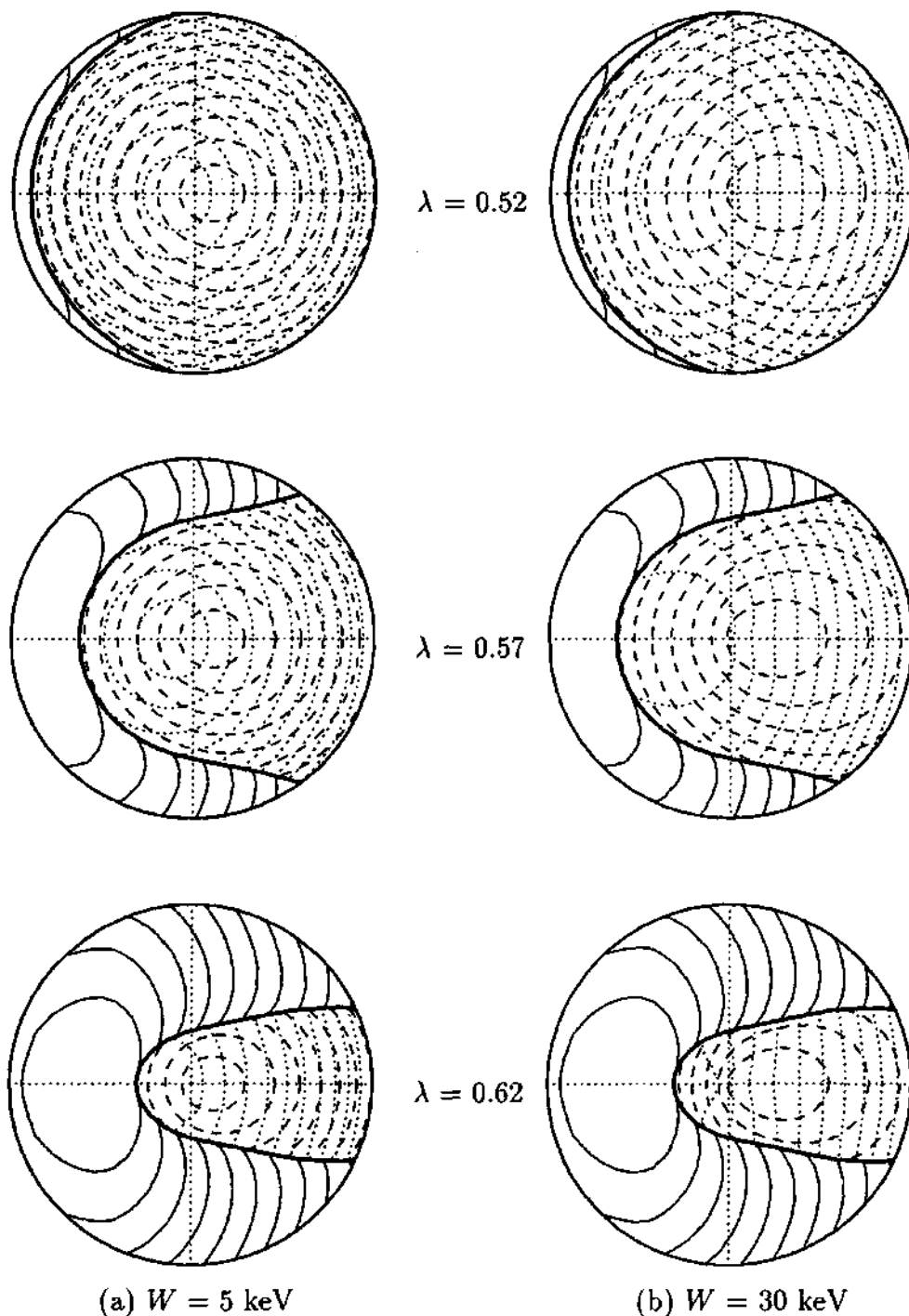


Figure 4.4: Comparison of the orbit topology for particle energies (a) $W = 5 \text{ keV}$ and (b) $W = 30 \text{ keV}$ for three different values of λ in the standard ATF magnetic configuration. The contours are defined similarly to those of Fig. 4.1.

on the particle energy changes radically. This effect is discussed in more detail in Section 4.3.

4.2 Effect of Magnetic Configuration

As discussed in the Chapter 1, the magnetic configuration in ATF can be changed substantially by changing the relative currents flowing in the three sets of VF coils. The plasma can be shifted in major radius by changing the dipole moment of the vertical fields (labeled \hat{Q}_{10}) or can be vertically elongated (or "squeezed") by changing the quadrupole moment of the vertical fields (labeled \hat{Q}_{20}). In this manner, the structure of the magnetic flux surfaces is radically changed, as is illustrated by Fig. 4.5.¹

In general, the degree to which ion orbits are confined in ATF is a strong function of the magnetic configuration. This effect is mainly seen in the confinement properties of the helically trapped particles, since these particles are the most sensitive to changes in the relative magnitudes of the helical and toroidal ripple. For the purposes of this discussion, the orbit confinement properties of a particular configuration are based on the degree to which the deeply helically trapped particles (i.e., particles residing at the very bottom of the magnetic wells with $v_{\parallel} \simeq 0$) are confined. The motivation for this choice is twofold. First, in most configurations the deeply helically trapped particles are much better confined than particles that are not as deeply trapped. Hence, there is generally a much larger population of deeply helically trapped particles, making the computation of their orbit confinement properties more important. The second reason is computational convenience. As discussed in Section 2.1.2, the deeply helically trapped particles follow orbits that can be accurately estimated from computed $e\Phi + \mu B_{\min} = \text{const}$ contours for the given configuration. Since computing the $e\Phi + \mu B_{\min}$ contours is a simple

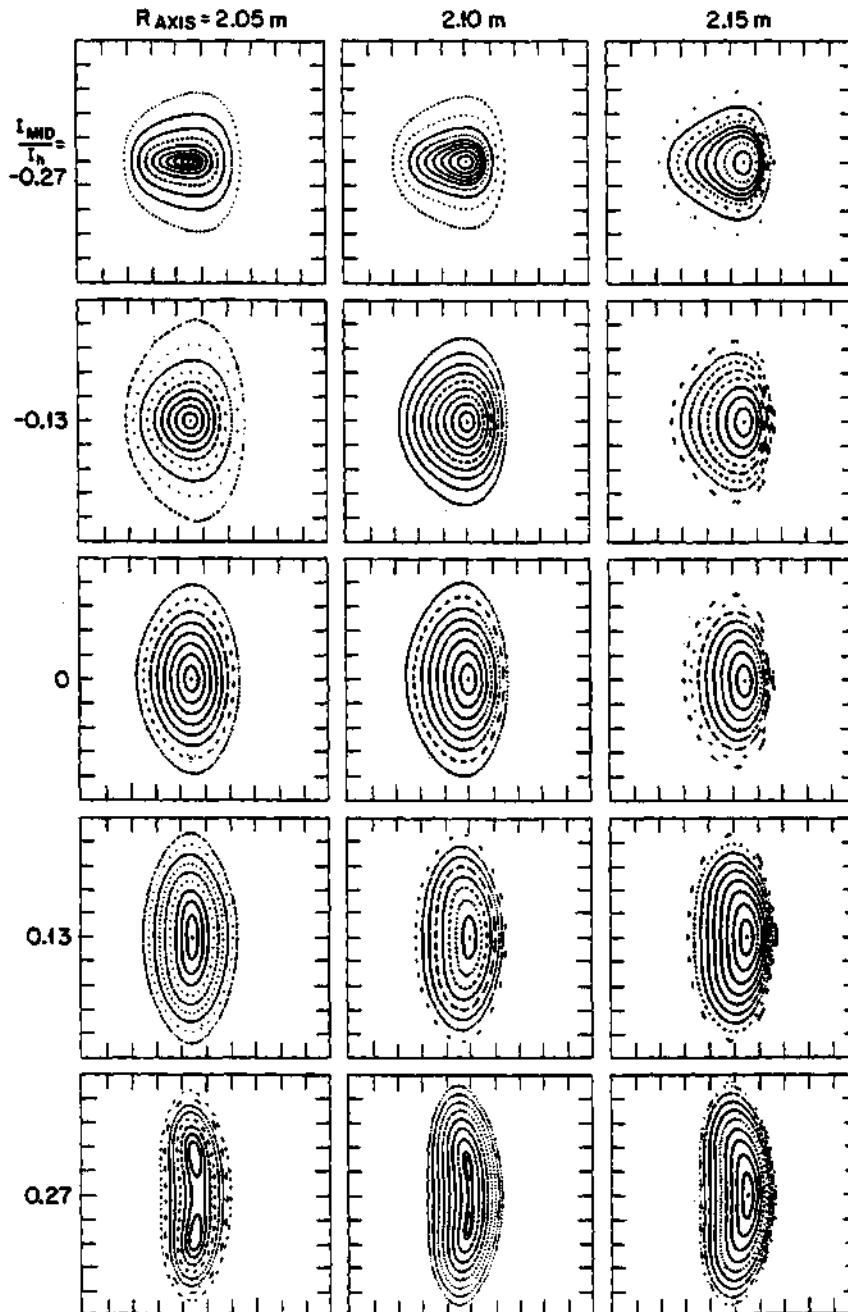
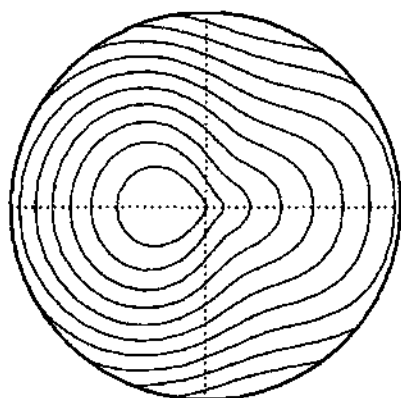


Figure 4.5: Vacuum magnetic flux surfaces for different values of magnetic axis radius and mid-VF coil current (normalized to the HF coil current) [Ref. 1].

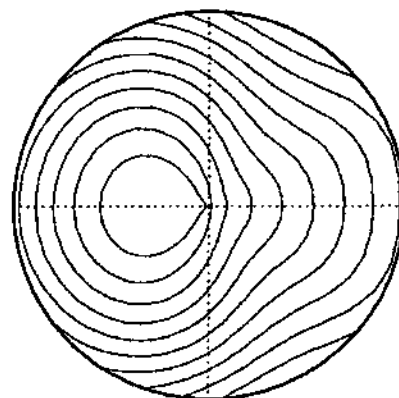
problem compared with computing the orbits of a large number of particles with an orbit-following code, this method requires much less computational time while maintaining a high degree of accuracy. For this discussion the electrostatic potential is assumed to be negligible and the orbit confinement properties are simply based on constant- B_{\min} contours.

In ATF, the constant- B_{\min} contours are radically changed as the magnetic configuration is changed. As an example, the variation of the constant- B_{\min} contours as the plasma is shifted in major radius R_0 is shown in Fig. 4.6. This figure clearly shows that as the plasma is shifted inward (by changing the dipole moment of the vertical field), the computed constant- B_{\min} contours become more omnigenous (coincident) with the plasma flux surfaces, which are circles centered at the origin in these coordinates. In configuration space, the B_{\min} contours remain basically fixed during this variation. Therefore, the variation seen in Fig. 4.6 is mostly due to the shift of the location of the plasma. Taken by itself, the improvement in orbit confinement as the plasma is shifted inward would suggest that the optimal magnetic configuration in ATF is one in which the plasma is shifted inward as much as possible without impinging on the inner vacuum vessel wall. However, as the plasma is shifted inward in ATF, both the depth of the magnetic well [given by Eq. (1.4)] and the magnitude of the shear [given by Eq. (1.3)] are reduced.¹ Since these two quantities play important roles in stabilizing MHD-driven interchange instabilities, plasma performance is affected. In general, as the plasma is shifted inward in ATF, the stability against these instabilities becomes less favorable. Furthermore, configurations that have a large fraction of confined particles may also suffer from instabilities due to this trapped particle population.² Therefore, the optimal configuration for plasma performance cannot be simply determined by finding the optimal configuration in terms of orbit confinement.

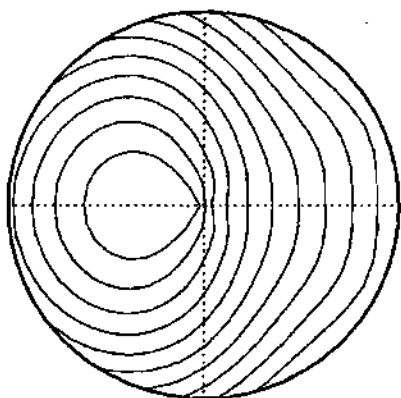
The degree to which the quadrupole moment is changed in ATF is generally



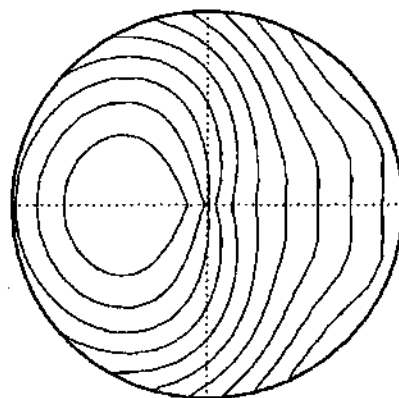
(a) $R_o = 2.02$ m



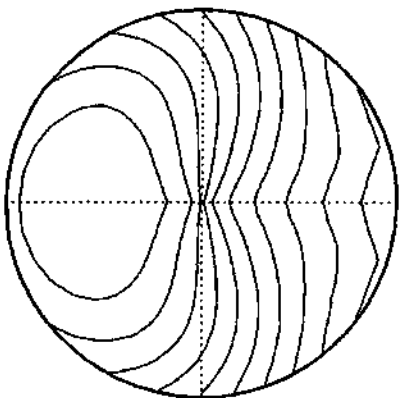
(b) $R_o = 2.05$ m



(c) $R_o = 2.08$ m



(d) $R_o = 2.11$ m



(e) $R_o = 2.15$ m

Figure 4.6: Variation of the constant- B_{\min} contours as a function of nominal major radius in ATF. This shift in the major radius of the plasma is produced by changing the dipole moment of the vertical fields in ATF. The plasma flux surfaces in these coordinates are simply circles centered at the origin.

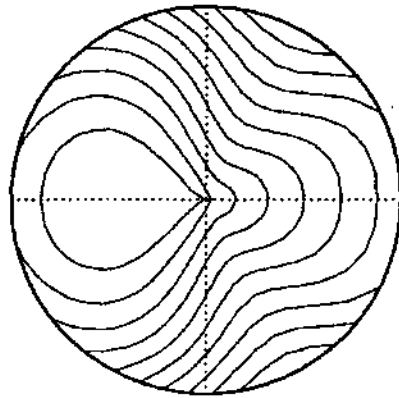
parameterized in terms of the ratio of the current flowing in the mid-VF coils to the current flowing in the helical field coils ($f_{\text{mid}} = I_{\text{mid}}/I_{\text{hf}}$). As illustrated by Fig. 4.7, the structure of the constant- B_{min} contours changes radically as f_{mid} is changed. A positive value of f_{mid} corresponds to a flux surface geometry that is vertically elongated, while $f_{\text{mid}} < 0$ corresponds to a vertically "squeezed" flux surface geometry. This figure shows that the vertically "squeezed" configuration ($f_{\text{mid}} < 0$) has the best orbit confinement properties. However, one must again be careful in assuming that this is the best configuration, since theoretical studies predict that the attainable β [defined by Eq. (1.1)] is strongly coupled to the elongation of the plasma.³

To quantify the degree of orbit confinement of a particular configuration in ATF, the parameter f_{TPC} defined as

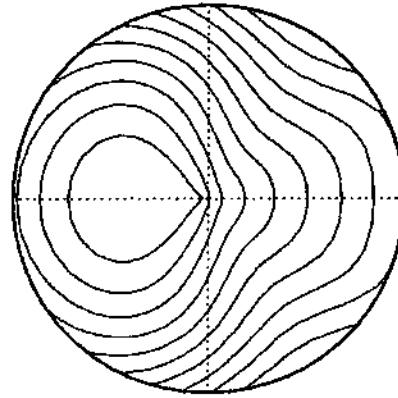
$$f_{\text{TPC}} = \frac{A_{B_{\text{min}}}}{A_{\text{pl}}}, \quad (4.1)$$

is generally used. Here, $A_{B_{\text{min}}}$ is the area enclosed by the last closed B_{min} contour and A_{pl} is the cross-sectional area of the plasma. This parameter should provide a fairly good estimate of the variation of orbit confinement as the configuration is changed since it is an indication of the fraction of deeply helically trapped particles that are confined. The variation of this parameter and the variation of the magnetic well and magnetic shear in the available operating space of ATF (in terms of the relative change $\Delta\hat{Q}_{10}$ and $\Delta\hat{Q}_{20}$ from the standard ATF configuration) are shown in Fig. 4.8. The magnetic well is parameterized in this figure by the normalized radius for which the depth of the magnetic well is zero. This radius therefore corresponds to the location where the magnetic well is no longer useful in stabilizing interchange modes. As previously indicated in Figs. 4.6 and 4.7, f_{TPC} increases as the plasma is shifted inward ($\Delta\hat{Q}_{10} > 0$) and vertically squeezed ($\Delta\hat{Q}_{20} < 0$).

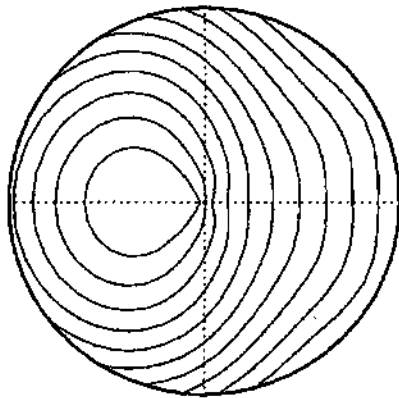
Preliminary experiments have been conducted on ATF to determine the effect of changing f_{TPC} on global plasma performance. Because the plasma perfor-



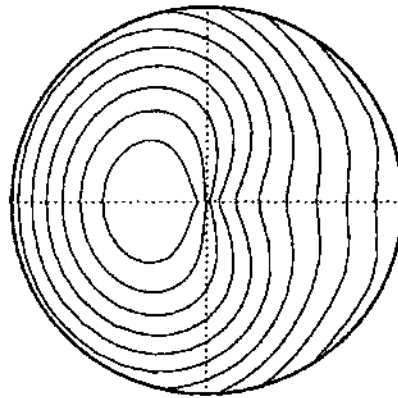
(a) $f_{\text{mid}} = 0.13$



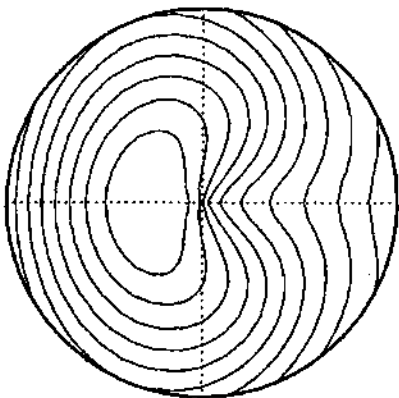
(b) $f_{\text{mid}} = 0.06$



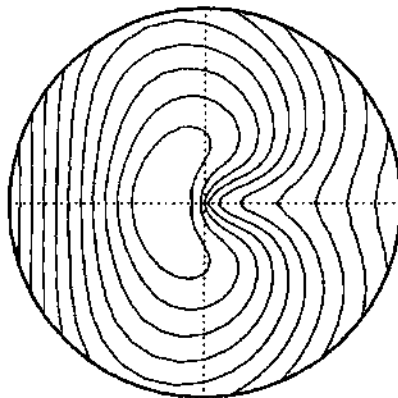
(c) $f_{\text{mid}} = 0.00$



(d) $f_{\text{mid}} = -0.07$



(e) $f_{\text{mid}} = -0.13$



(f) $f_{\text{mid}} = -0.21$

Figure 4.7: Variation of the constant- B_{min} contours with the quadrupole moment of the the vertical field in ATF with R_o fixed at 2.08 m. The quadrupole moment is parameterized in this case by the parameter $f_{\text{mid}} = I_{\text{mid}}/I_{\text{hf}}$, where I_{mid} is the current in the mid-VF coil and I_{hf} is the current in the helical field coils.

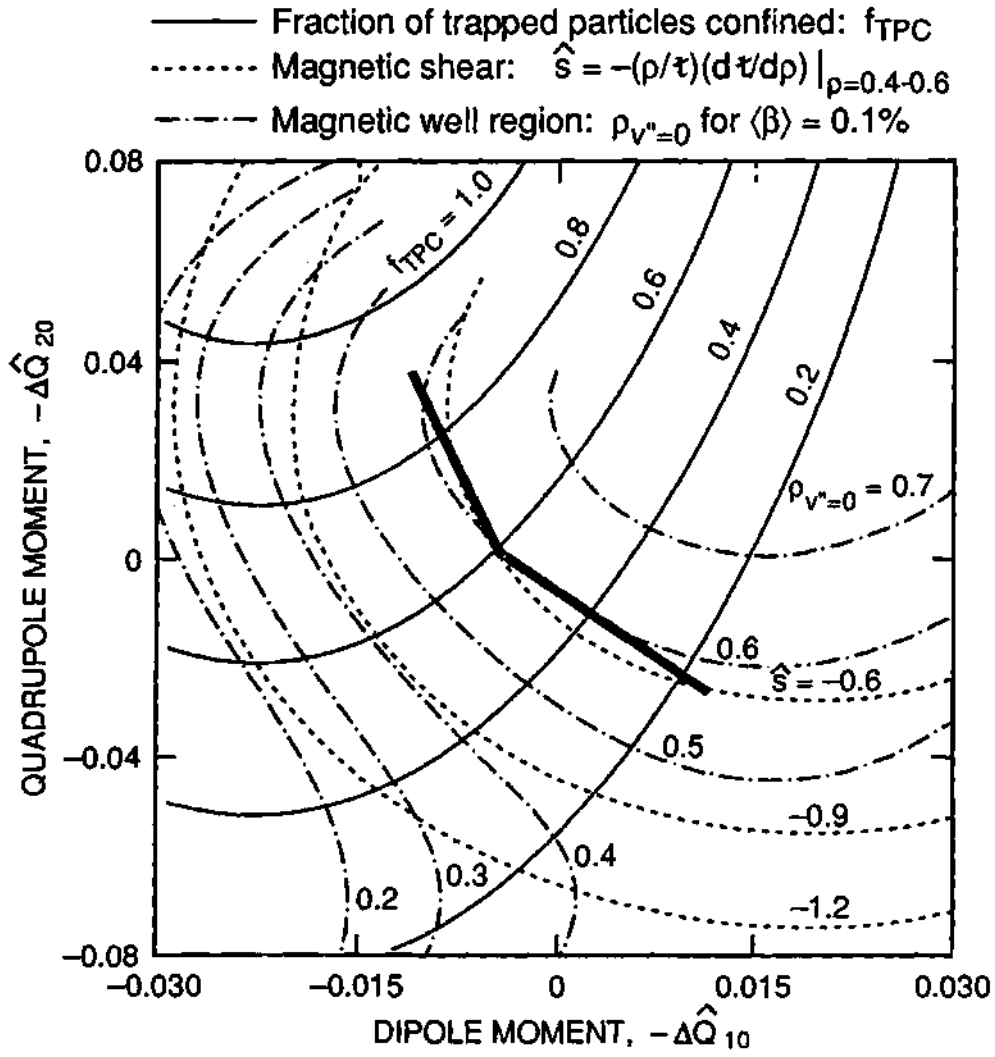


Figure 4.8: Contour plot of the variation of f_{TPC} (solid lines), magnetic shear (dashed lines), and magnetic well (dot-dashed lines) in the available operating space in ATF. The bold solid line represents a path through this configuration in which the magnetic well and magnetic shear remain approximately constant while f_{TPC} changes significantly. (Figure courtesy of Masonari Murakami).

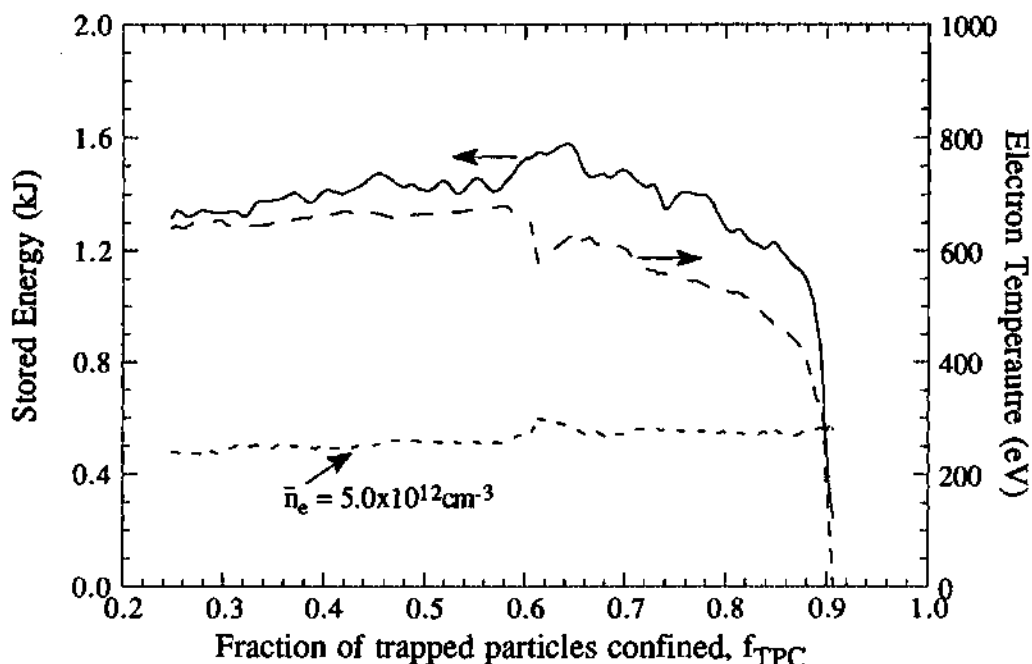


Figure 4.9: Dependence of the electron density, plasma stored energy, and electron temperature on the parameter f_{TPC} during a dynamic configuration scan in ATF. (Data courtesy of Masanori Murakami).

mance of any given magnetic configuration is dependent on several factors, this experiment is not as simple as one might first imagine. However, because the contours of constant magnetic shear and magnetic well are both approximately orthogonal to the contours of constant f_{TPC} over much of the configuration space (see Fig. 4.8), the effects of the trapped particle population may be separated from these other effects. This was accomplished experimentally in ATF by dynamically scanning the magnetic configuration along the bold lines in Fig. 4.8 such that the magnitude of the magnetic well and the magnetic shear are held approximately constant. This dynamic scan was performed during a sequence of two ATF discharges by varying the currents flowing through the three sets of VF coils such that the configuration changed linearly in the fashion shown by the bold lines in Fig. 4.8. These scans were conducted with 400 kW ECH and $B_0 = 0.95$ T. The effect of this scan on plasma performance is shown in Fig. 4.9, where the electron line density, electron temperature, and plasma stored energy are plotted versus f_{TPC} . The discontinuity

in the electron density and temperature near $f_{\text{TPC}} = 0.6$ is simply due to the irreproducibility of the discharges. Remarkably, the global plasma performance is roughly the same over the entire range of f_{TPC} except near $f_{\text{TPC}} = 0.9$. Since the magnetic well and magnetic shear were held constant during this scan, this result suggests that trapped particle effects such as trapped electron instabilities may become important as f_{TPC} is increased above a critical value, though the observed effect may simply result from insufficient coupling of the ECH power in certain configurations. It should be stressed that these data are only preliminary, and conclusions based on these data are therefore subject to change.

4.3 Effect of the Radial Electric Field

As discussed in Section 2.1, the $\vec{E} \times \vec{B}$ drift plays an important role in determining the confinement properties of low-energy particles in toroidal devices. Since, in general, the electrostatic potential is assumed to be constant on a flux surface (i.e., no poloidal dependence), the ambipolar electric field is simply in the radial direction. The $\vec{E} \times \vec{B}$ drift therefore causes a poloidal precession of the particle orbit since the direction of the magnetic field is mostly in the toroidal direction. In a tokamak, this drift has been shown to be unimportant in the confinement of trapped particles since the drift due to the radial electric field is generally much smaller than the poloidal drift due to the toroidal curvature. However, theoretical and experimental studies examining the transition from the L-mode to H-mode regimes in tokamaks suggest that the basic mechanism causing this transition is the presence of a radial electric field.^{4,5}

In ATF, the presence of a radial electric field E_r is also important, but in a slightly different manner. As discussed in Section 2.1.2, the drift motion of the helically trapped particles in a stellarator consists of a vertical drift due to

the toroidal variation of the magnetic field and a poloidal drift consisting of the ∇B drift due to the helical windings $v_{\nabla B_h}$ and the $\vec{E} \times \vec{B}$ drift $v_{E_r \times B}$. For an orbit to be confined, the poloidal precession of the orbit must be large enough to keep the helically trapped particles from simply drifting vertically out of the machine. Therefore, the important quantity of interest is the magnitude of $v_{\nabla B_h} + v_{E_r \times B}$. For a particular energy particle, the magnitude of $v_{\nabla B_h}$ is fixed by the magnetic configuration; therefore, the magnitude of $v_{E_r \times B}$ is extremely important in determining whether an orbit is confined or not. As pointed out in Section 2.1.2, the ratio of these two drifts is given by

$$\frac{v_{\nabla B_h}}{v_{E_r \times B}} = \frac{\epsilon_h W_{\perp}}{e E_r r}, \quad (4.2)$$

where ϵ_h is the magnitude of the helical ripple and W_{\perp} is the perpendicular kinetic energy of the particle. For a uniform E_r throughout the plasma, the quantity $E_r r$ in this expression is simply the relative difference between the electrostatic potential at the edge of the plasma and the potential energy at the center, Φ_{rel} . In general, the magnitude of Φ_{rel} is limited since a fully ionized plasma tends to adjust itself such that quasi-neutrality is maintained. Most theoretical predictions suggest that the maximum attainable Φ_{rel} is on the order of the electron temperature ($e\Phi_{\text{rel}} \sim T_e$). Therefore, the $\vec{E} \times \vec{B}$ drift generally plays an important role in the confinement only for fairly low-energy particles.

This effect is clearly shown in Fig. 4.10, where the $e\Phi + \mu B_{\text{min}} = \text{const}$ contours with three different values of the central electrostatic potential are compared for three different energies. In this case, the electrostatic potential profile is assumed to be of the form $\Phi(\psi) = \Phi_0(1 - \psi)$, where ψ is the normalized magnetic flux coordinate. As discussed earlier, the orbit topology for the deeply trapped particles is independent of the particle energy in the absence of a radial electric field. In contrast, this figure shows that there is a strong dependence on particle energy in the presence of a radial electric field. As expected, the orbit topology for the 5-keV

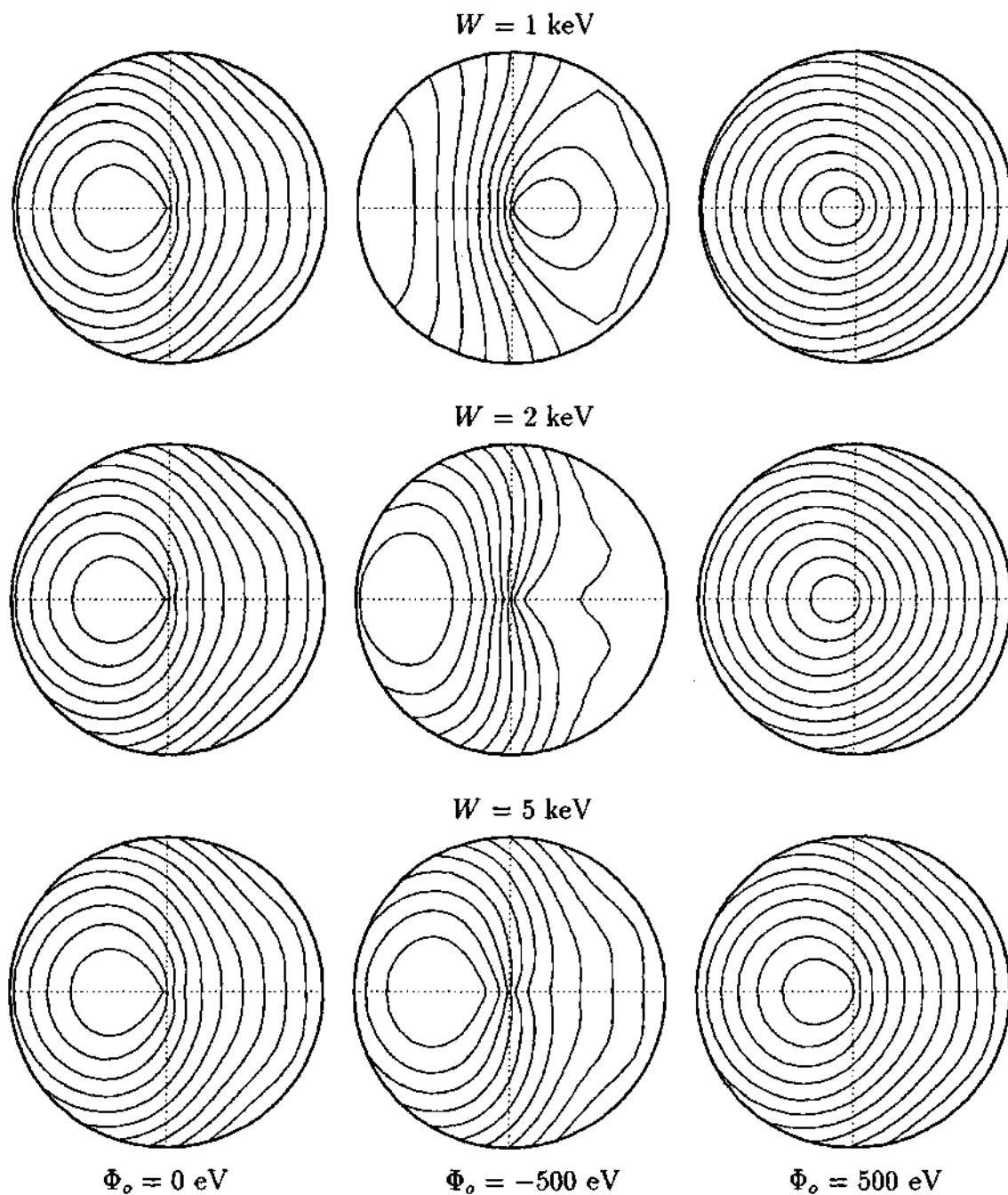


Figure 4.10: Comparison of the $e\Phi + \mu B_{\min}$ contours for three different values of the central electrostatic potential and three different particle energies. The electrostatic potential profile is assumed to be of the form $\Phi(\psi) = \Phi_o (1 - \psi)$.

particles is affected only slightly by the presence of the radial electric field since $W \gg e\Phi_0$. However, at lower energies the effect of the radial electric field becomes more evident. In fact, in the $W = 2$ keV case, only a small fraction of the $e\Phi + \mu B_{\min} = \text{const}$ contours close within the device. This severe deterioration in confinement is due to a resonant effect where the magnitudes of $v_{\nabla B_h}$ and $v_{E_r \times B}$ are nearly equal but opposite in direction. When this happens, the poloidal precession frequency of the particle's orbit is reduced to such a point that the particle is generally lost due to the vertical drift from the toroidal curvature. From Eq. (4.2), this resonance should occur near the energy $W_{\perp} = -\Phi_0/\epsilon_h$. In ATF, the magnitude of the helical ripple at the edge is approximately 0.25. Since in the case of helically trapped particles $W \simeq W_{\perp}$, this resonance should occur at the energy $W \simeq 4.0 |\Phi_0|$. For energies on either side of this resonance, the confinement properties improve drastically as can be seen by examining Fig. 4.10.

4.4 Effect of Orbit Topology on Fast-Ion Confinement

Since the main high-power heating systems on ATF (namely, NBI and ICH) depend on the slowing-down of a high-energy population on the background plasma, the effect of orbit topology on this slowing-down distribution is of the utmost importance in obtaining adequate heating. Orbit effects may be deleterious in the case of ICH since the particles that receive the bulk of the ICH power are given substantial perpendicular energy, pushing them closer to the loss region. This is probably why heating was not observed during low-power, low-density ICH experiments on ATF.⁶ However, these data are preliminary, and thus analysis of ion confinement during ICH has been limited.

In the case of NBI in ATF, naively one would expect the orbit topology to play only a minor role in the confinement of the energetic ions since the beam

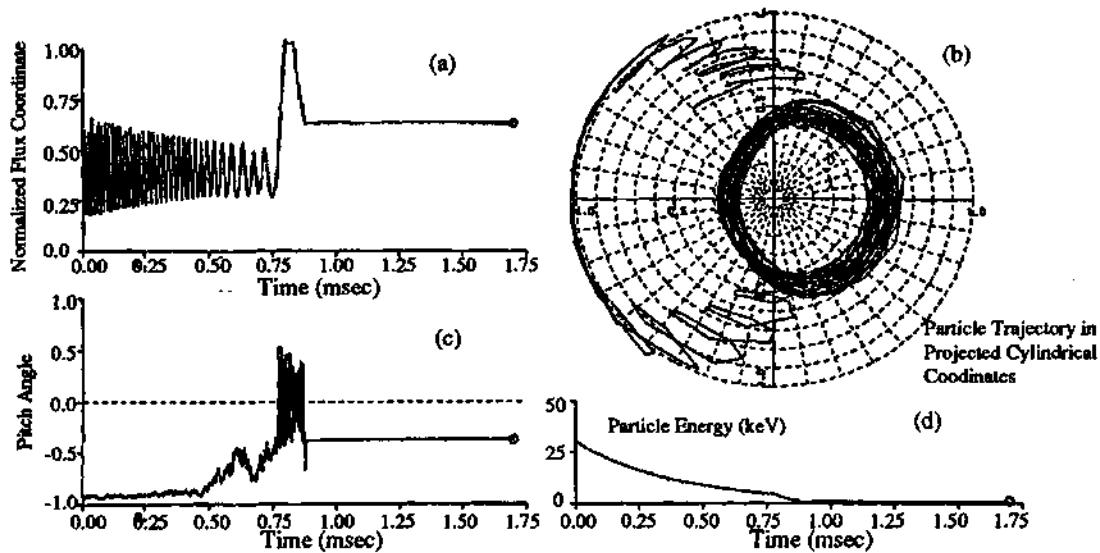


Figure 4.11: Monte Carlo calculation for a tangential injected ion in ATF: (a) the normalized flux coordinate vs time, (b) representation of the particle trajectory projected on ψ - θ plane, (c) the pitch angle of the particle vs time, and (d) the energy of the particle vs time.

ions are injected tangential to the magnetic field, well away from the loss region in velocity space. However, on closer examination of the slowing-down process with respect to the orbit topology, some problems are encountered that may limit the effective heating capabilities of NBI on ATF.

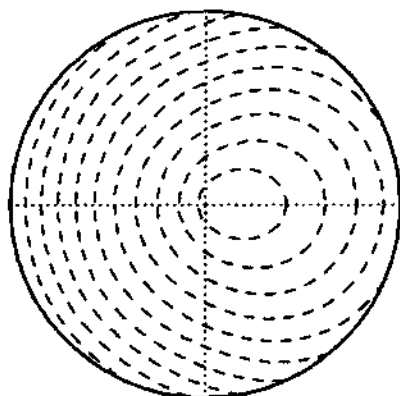
A sample Monte Carlo simulation of the slowing-down of a tangentially injected ion in ATF, obtained using the DESORBS code,⁷ is shown in Fig. 4.11. Charge-exchange has been turned off in this particular calculation so that the particle's motion can be tracked to the thermalization of the particle. This particular particle is born (ionized) near the center of the plasma [see Fig. 4.11(a)] with an initial pitch angle near $\xi = -1$ [see Fig. 4.11(c)], which makes it a co-passing particle. Initially, as the particle slows down, its pitch angle remains fairly constant because the particle's energy is well above the critical energy. The projection of the initial orbit on the ψ - θ plane is simply a circle whose center is slightly shifted outside the magnetic axis [see Fig. 4.11(b)]. However, as the particle slows down further and

its energy approaches the critical energy ($E_{\text{crit}} \simeq 10$ keV in this case), the injected ion starts to suffer substantial pitch-angle scattering (i.e., ξ starts to change) as collisions with ions become more prevalent [see Fig. 4.11(c)]. Eventually, the particle suffers enough pitch-angle scattering that it crosses the trapping boundary and becomes helically trapped. The helically trapped orbit then carries the particle out to the plasma boundary. In this case, with charge-exchange turned off, the particle reenters the plasma since its orbit does not intersect the ATF vacuum vessel. In fact, guiding-center calculations have shown that, although the helically trapped orbits in ATF do go outside the LCFS, these orbits generally return to the plasma without hitting the vacuum vessel wall.⁸ However, since the neutral density is extremely high in regions outside the LCFS, the mean free path against charge-exchange is extremely short in this region, and particles entering this region are generally lost through charge-exchange. Therefore, though the LCFS is not a fixed loss boundary, it is a virtual one because of the large charge-exchange losses. Hence, for the remainder of this discussion, it is assumed that a particle passing outside the LCFS is lost.

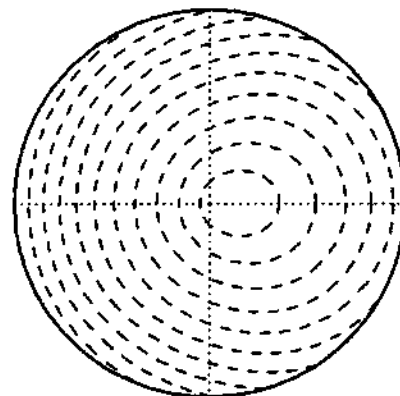
Representative J^* contours are shown in Fig. 4.12 for various stages of the slowing-down process. Neglecting the electrostatic potential, the orbit topology is a function of two parameters: W and λ . When the particle is injected, $W = 30$ keV and $\lambda \simeq 0$ (since $\mu \simeq 0$), and the corresponding orbit topology (for the co-passing case only) is shown in Fig. 4.12(a). The orbit described by the appropriate J^* contour is very similar to the orbit seen in the simulation [Fig. 4.11(b)]. As the particle slows down initially, the value of W varies approximately as

$$W = W_0 e^{-2t/\tau_s},$$

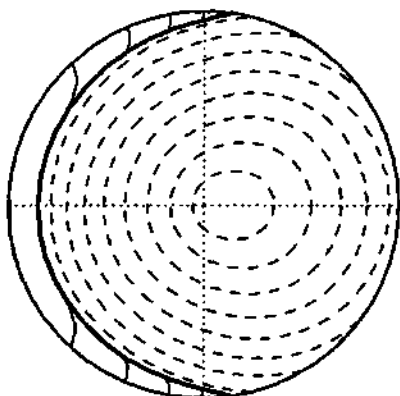
where τ_s is the slowing-down time defined by Eq. (2.70). The value of λ stays approximately constant, though, since the value of μ/W is approximately constant during this part of the slowing-down process.⁹ As discussed earlier, this reduction of



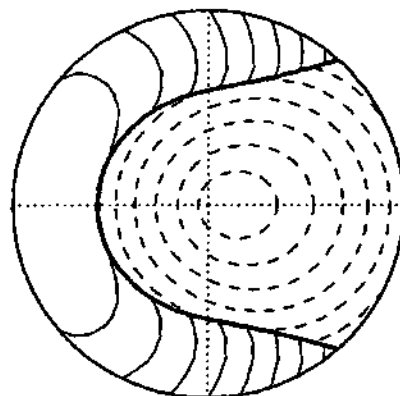
(a) $W = 30 \text{ keV}, \lambda \simeq 0.$



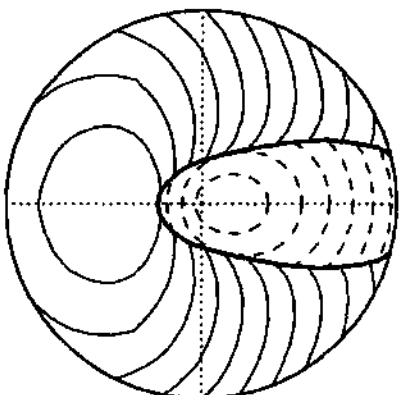
(b) $W = 20 \text{ keV}, \lambda \simeq 0.$



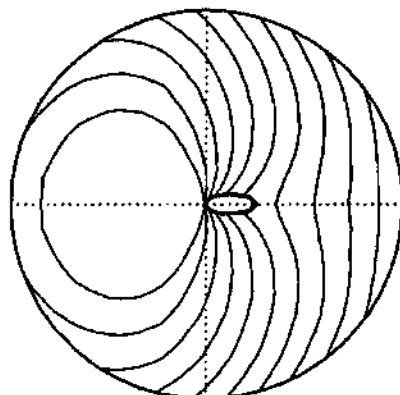
(c) $W = 12 \text{ keV}, \lambda = 0.53$



(d) $W = 10 \text{ keV}, \lambda = 0.58$



(e) $W = 8 \text{ keV}, \lambda = 0.63$



(f) $W = 3 \text{ keV}, \lambda = 0.68$

Figure 4.12: Computed constant- J_{co}^* and J_{trap}^* contours for various times during the slowing-down process of an injected particle in ATF. These times correspond to (a) the time of injection, (b) a time after injection but before the particle has slowed down to critical energy, and (c)–(f) successive times during the slowing-down process after the particle has begun to pitch-angle scatter.

energy simply results in a "shrinking" in the size of the orbit, as seen in Fig. 4.12(b) (similar to the result seen in Fig. 4.4). This can also be seen in the Monte Carlo calculation, where the magnitude of the excursion of the normalized flux coordinate on each transit of the particle decreases as the energy decreases [see Fig. 4.11(a)]. As the particle begins to suffer pitch-angle scattering as it approaches the critical energy, the value of λ also begins to change. As λ decreases, the trapping boundary starts to impinge on the orbit [Figs. 4.12(c) and 4.12(d)] until finally the orbit encounters the trapping boundary. This occurs in the constant- J^* plots at the point where the appropriate J^* contour for this orbit becomes tangent to the trapping boundary [see Fig. 4.12(e)]. In contrast to particles in an axisymmetric tokamak, which undergo this transition at the vertical midplane generally inside the magnetic axis,¹⁰ particles in ATF first encounter the trapping boundary generally outside the magnetic axis at various poloidal angles. Once on this helically trapped orbit, a particle is generally required to make at least one poloidal transit on this helically trapped orbit since it quickly moves away from the trapping boundary and does not encounter this boundary again until it has completed a full transit. As discussed earlier and as is apparent in Figs. 4.12(e) and 4.12(f), the only helically trapped orbits that close within the LCFS are located inside the magnetic axis. Thus, particles that become trapped outside the magnetic axis (as in this case) follow orbits that carry them outside the LCFS.

As far as heating efficiency is concerned, this problem becomes severe only when the average energy at which the injected particles reach the trapping boundary is a substantial fraction of the injection energy. Since the energy at which the tangentially injected ions become trapped is dependent on the critical energy E_{crit} [defined by Eq. (2.65)], the magnitude of this loss should be proportional to $E_{\text{crit}}/E_{\text{inj}}$. Since the magnitude of E_{crit} is determined by the plasma electron temperature, the effect of this loss mechanism becomes more severe as the electron temperature increases.

Table 4.1: Dependence of heating efficiency (computed with DESORBS) on electron temperature in a medium-density plasma wall. The loss boundary is either defined by the LCFS or the vacuum vessel wall.

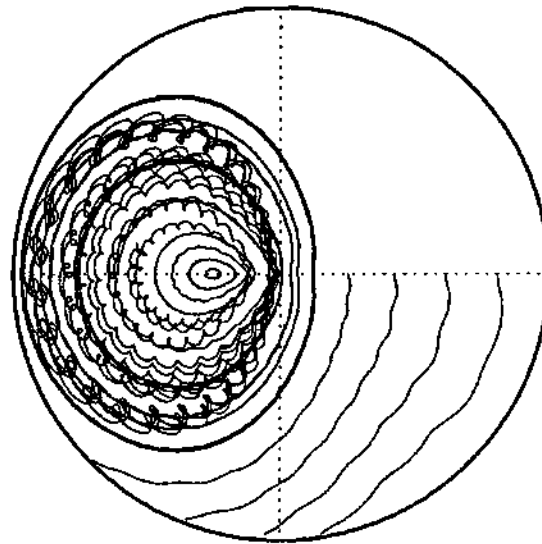
	Power Distribution (%)					
	$T_{eo} = 500 \text{ eV}$		$T_{eo} = 1 \text{ keV}$		$T_{eo} = 2 \text{ keV}$	
	LCFS	Vessel	LCFS	Vessel	LCFS	Vessel
P_{be}	68.5	69.6	54.1	55.1	33.3	38.8
P_{bi}	24.3	24.4	31.2	37.1	41.0	42.0
P_{cx}	0.0	0.5	0.8	2.1	4.7	6.6
P_{orbits}	2.6	0.5	9.8	1.0	18.8	9.1
P_{therm}	4.6	5.0	4.1	4.7	2.2	3.5
Overall Heating Efficiency	97.4	99.0	89.4	96.9	76.5	84.3

To test this hypothesis, the DESORBS Monte Carlo simulation code⁷ was run for several hypothetical cases in ATF to see how the heating efficiency varied as the plasma electron temperature is changed. This simulation was carried out in the standard ATF configuration at medium density ($n_e = 7.0 \times 10^{13} \text{ cm}^{-3}$); the plasma electron temperature was the only variable changed during the simulations. The results are tabulated in Table 4.1. This table clearly shows that as the electron temperature is increased, the overall heating efficiency decreases, principally because of unconfined orbit losses. This is a clear indication that the loss mechanism discussed above could be a major loss mechanism in ATF when the slowing-down time τ_s is fairly small (such that charge-exchange is not the main loss mechanism) and the critical energy E_{crit} is fairly large. These constraints imply that this loss would be most significant in medium-density, high-temperature plasmas. The definition of the loss boundary also has a significant influence on the overall heating efficiency, especially in cases where $E_{crit} \sim E_{inj}$. Because the ATF vacuum vessel was designed so that most particle orbits return to the plasma without hitting the vacuum vessel

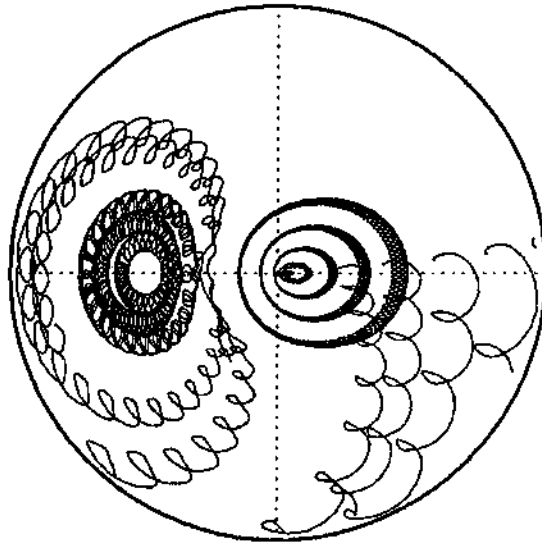
wall, treating the LCFS as the loss boundary results in much larger losses. One inaccuracy built into the DESORBS code that may play a role in the computed heating efficiency is the specification of various plasma parameters outside the LCFS. Because the 3-D representations of these parameters are not well known outside the LCFS, the value of a given parameter outside the LCFS is assumed by DESORBS to be the same as the value at the LCFS. The main consequence of this assumption is the inaccurate calculation of charge-exchange losses outside the LCFS. These losses could be much larger than those computed by DESORBS, depending on the location of various gas sources and to a lesser extent on the electron density profile in this region.

4.5 Effect of Orbit Topology on NPA Measurements

The energy spectra measured by the NPA are also affected by the orbit topology and the associated loss regions, since these loss regions are theorized to deplete the ion distribution function in certain regions of velocity/configuration space. When the analyzer is oriented such that the viewing chord passes through one of these loss regions, the effect of the loss region must be taken into account in the analysis of the measured spectra. The situation is further complicated by the fact that the classes of particles (passing, helically trapped, etc.) viewed by the analyzer change along the analyzer sightline and as the analyzer viewing orientation is changed. This is illustrated in Fig. 4.13 where the orbits of particles started at various locations along the viewing chord is shown for two different viewing orientations of the NPA. For $\phi_{\text{anal}} = 0^\circ$ [see Fig. 4.13(a)], most of the particles that are viewed by the NPA are deeply helically trapped particles, which have orbits characterized by large excursions from the radial location in which the analyzer views the particle. In contrast, for $\phi_{\text{anal}} = 10^\circ$, the NPA is viewing passing particles at chordal locations



(a) $\phi_{\text{anal}} = 0^\circ$, $\theta_{\text{anal}} = 0^\circ$



(b) $\phi_{\text{anal}} = 10^\circ$, $\theta_{\text{anal}} = 0^\circ$

Figure 4.13: Orbit topology viewed by the NPA at two horizontal viewing angles: (a) $\phi_{\text{anal}} = 0^\circ$, and (b) $\phi_{\text{anal}} = 10^\circ$. Orbits on the left-hand side of each plot are those of helically trapped particles, while those on the right of (b) are passing particles. Particle energy is 5 keV.

nearer the NPA [right-hand side of Fig. 4.13(b)] and helically trapped particles at chordal locations farther from the NPA [left-hand side of Fig. 4.13(b)].

In an attempt to understand the orbit topology's effect on the NPA viewing capabilities, an orbit-following code has been used to follow 10-keV protons starting at uniformly spaced locations along various analyzer viewing chords. The particles are followed for 1 msec to determine if their orbits carry them outside the LCFS of ATF. The results of this study are shown in Fig. 4.14. Note that this graph represents only a portion of the viewing capabilities of the NPA. Since most particles that the NPA views at angles $\phi_{\text{anal}} \leq -20^\circ$ and $\phi_{\text{anal}} \geq 20^\circ$ are confined, passing particles, they are omitted from this graph so that the loss region can be seen more clearly. As expected from the earlier discussion, particles started from chordal locations inside the magnetic axis of ATF ($\rho_* > 0$) are generally better confined than those started from locations outside the magnetic axis. The loss region is confined to a fairly small region of the viewing capabilities of the analyzer, since the analyzer can scan from 45° to 135° . Therefore, in most situations the orbit topology does not have a strong influence on the measured spectra. This allows detailed studies of the confinement of the tangentially injected ions in ATF without having to simulate the effects of the loss region.

Another interesting feature of Fig. 4.14 is the loss region directly in front of the analyzer. This feature may explain why the measured energy spectra in ATF do not exhibit the "two-temperature" feature seen in most NPA measurements of the ion temperature. This "two-temperature" feature is theorized to result from the chord-integrated nature of the measurement, with the low-temperature feature arising from contributions near the edge and the high-temperature feature arising from charge-exchange events in the center of the plasma.^{11,12} The presence of these loss regions directly in front of the analyzer in ATF should reduce the contribution from the edge plasma, since it is theorized that the ion distribution function is

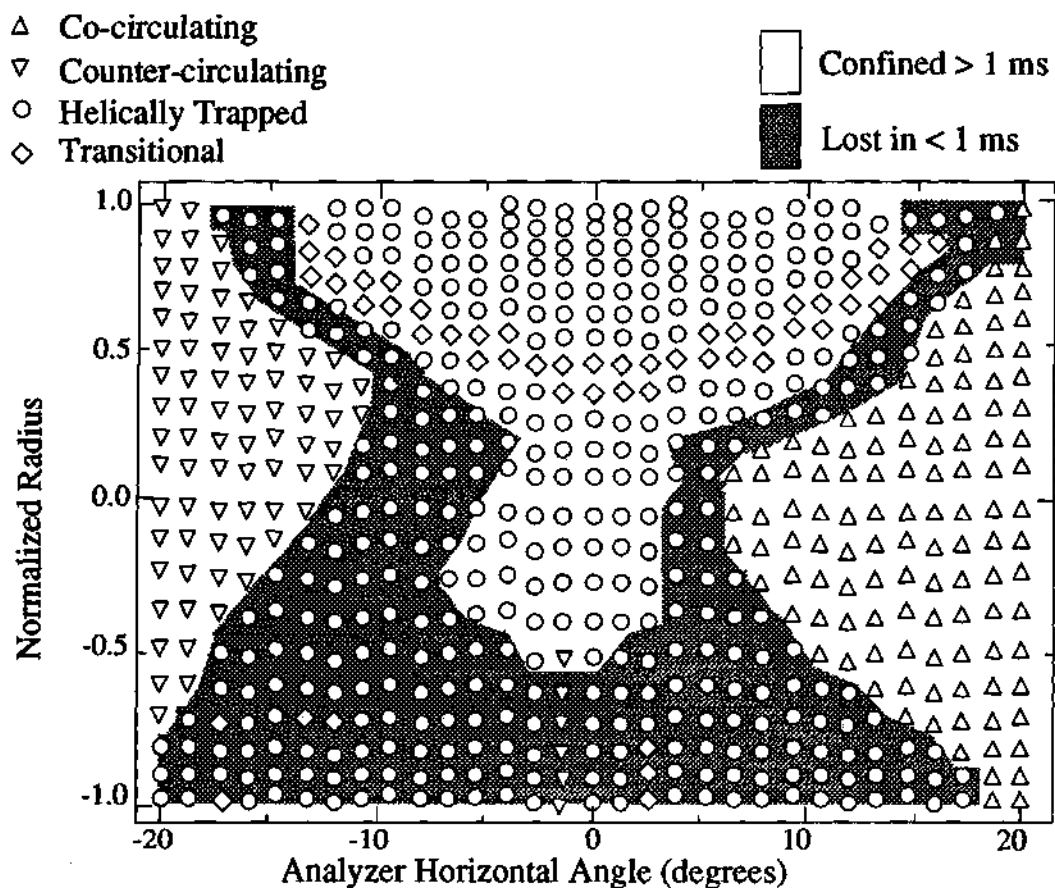


Figure 4.14: Confined region (nonshaded area) for 10-keV protons viewed by the NPA at $B_0 = 1$ T in ATF in the equatorial plane ($\theta = 0^\circ$). The symbols indicate the type of orbit observed: co-circulating (Δ), counter-circulating (∇), helically trapped (\circ), and transitional (\diamond). A positive normalized radius indicates a position inside the magnetic axis, farther from the NPA, while a negative normalized radius indicates a position outside the magnetic axis, nearer to the NPA.

depleted in the vicinity of these loss regions. Consequently, the measured spectra will have features characteristic of the central regions of the plasma.

4.6 Summary

Some of the basic aspects of the orbit topology in ATF have been explored in this chapter. This study has used several numerical techniques in examining these properties, ranging from the calculation of the orbit topology in ATF via the constant- B_{\min} contour and constant- J^* contour approach to numerically integrating the equations of motion for a large set of particles in ATF. In general, the results of these approaches were found to be extraordinarily similar, indicating that the analytic approaches based on the constant- B_{\min} and constant- J^* contour representation of the orbit topology are quite accurate.

In general, the orbit topology in ATF is quite complicated and dependent on many different parameters. For example, the loss region (defined by the region in velocity/configuration space in which particles are lost due to unconfined orbits) was found to be very dependent on major radius. Most particles started from locations inside the nominal magnetic axis of ATF are confined while a significant fraction of particles started outside the magnetic axis are lost (i.e., their orbits carry them outside the LCFS). These calculations also revealed that the most deeply helically trapped particles (pitch angle $\approx 90^\circ$, $v_{\parallel}/v = 0$) are slightly better confined than particles with slightly larger pitch angles, indicating that the loss region in velocity space does not extend all the way to perpendicular in ATF. The orbit topology was also found to be dependent on the particle energy. In general, the orbit topology for passing particles changes substantially as a function of energy, while the orbit topology for the helically trapped particles remains basically the same. This seemingly peculiar result results from the various drift mechanisms that

govern the motion of these two classes of particles.

Studies of the single-particle confinement properties of the possible magnetic configurations in ATF indicate that the single-particle confinement properties of ATF improve as the magnetic axis is shifted inward and as the plasma is vertically squeezed. However, since optimizing plasma performance in a stellarator generally requires compromises between single-particle confinement and MHD stability requirements, this result does not imply that the shifted-in, vertically squeezed configuration is the most favorable configuration for plasma performance in ATF. In fact, preliminary experimental studies, in which the parameters that control the MHD stability in ATF were held constant while the fraction of trapped particles confined f_{TPC} was varied from 0.2 to 0.9, indicate that plasma performance is insensitive to single-particle confinement considerations. Plasma performance was only affected when $f_{\text{TPC}} \geq 0.9$, and instead of improving, plasma performance deteriorated.

Studies of the effect of the radial electric field in ATF indicate that the helical resonance (i.e., the energy at which the $\vec{E} \times \vec{B}$ drift and the helical ∇B drift cancel exactly) occurs approximately at the energy $W = -4.0\Phi_0$, where Φ_0 is the central electrostatic potential. Near this resonance, orbit confinement was shown to be extremely poor, though confinement tends to improve for energies on either side of this resonance and is substantially improved in situations with $\Phi_0 > 0$.

Fast-ion confinement in ATF is also affected by the orbit topology, even in the case of tangential neutral beam injection. It has been shown that as a tangentially injected ion in ATF slows down on the background plasma, the orbit topology of the particle changes. In general, the orbit topology does not begin to change drastically until the particle begins to pitch-angle scatter on the background plasma. Once the particle has suffered sufficient pitch-angle scattering so that it encounters the trapping boundary and becomes helically trapped, it usually follows an orbit that carries it outside the LCFS. The amount of energy lost through this process

is strictly dependent on the amount of energy that a particle has when it becomes trapped. Since the tangentially injected ions, in general, do not begin to pitch-angle scatter until they have slowed down to an energy near the critical energy E_{crit} , the fraction of beam energy lost through this process is dependent on the ratio of E_{crit} and E_{inj} . Because the magnitude of E_{crit} is simply a function of the plasma electron temperature T_e , any increase in T_e increases the loss associated with this mechanism. This hypothesis has been corroborated by DESORBS simulations, which indicate that the amount of injected beam power lost due to unconfined orbits is strongly dependent on the magnitude of T_e . Although this loss is seemingly mitigated in ATF since there is a large volume between the LCFS and the vacuum vessel, increased charge-exchange losses in this region make the LCFS a reasonable choice for the loss boundary.

Finally, the effect of the orbit topology on NPA measurements has been examined. These studies indicate that the orbit topology that the NPA views is extremely complicated and dependent on the viewing orientation of the analyzer. Calculations have shown that there is a large loss region directly in front of the analyzer for horizontal angles near perpendicular ($\phi_{anal} = 0^\circ$). The presence of this loss region may be the reason why the NPA-measured energy spectra in ATF do not exhibit the "two-temperature" feature seen in similar NPA measurements on other devices.

REFERENCES

- ¹ J. F. Lyon et al., Nucl. Technol./Fusion **10**, 179 (1986).
- ² B. B. Kadomtsev and O. P. Pogutse, Nucl. Fusion **11**, 67 (1971).
- ³ J. P. Freidberg, *Ideal Magnetohydrodynamics* (Plenum Press, New York, 1987).
- ⁴ K. C. Shaing et al., in *Plasma Physics and Controlled Nuclear Fusion Research 1988 (Proc. 12th Int. Conf., Nice, 1988)*, Vol. 2, p. 13 (IAEA, Vienna, 1989).
- ⁵ R. J. Groebner et al., in *Controlled Fusion and Plasma Physics (Proc. 16th EPS Conf., Venice, 1989)*, Vol. 13B, Part I, p. 245 (1989).
- ⁶ M. Kwon, *Fast Wave Ion Cyclotron Resonance Heating Experiments on the Advanced Toroidal Facility*, PhD thesis, Georgia Institute of Technology, 1990.
- ⁷ R. H. Fowler, R. N. Morris, J. A. Rome, and K. Hanatani, Nucl. Fusion **30**, 997 (1990).
- ⁸ J. F. Lyon et al., J. Nucl. Mater. **121**, 415 (1984).
- ⁹ L. M. Hively, *Fusion-Product Transport in Axisymmetric Tokamaks: Losses and Thermalization*, PhD thesis, University of Illinois at Urbana-Champaign, 1980.
- ¹⁰ J. A. Rome and Y. M. Peng, Nucl. Fusion **19**, 1193 (1979).
- ¹¹ V. V. Afrosimov and I. P. Gladkovskii, Sov. Phys.-Tech. Phys. **12**, 1135 (1968).
- ¹² R. J. Goldston, in *Diagnostics for Fusion Reactor Conditions, Varenna*, p. 263 (CEC, Brussels, 1982).

CHAPTER V

Thermal Ion Behavior in ATF

As discussed in the Chapter 1, the confinement of the background plasma ions is of utmost importance for a fusion reactor. The average confinement time (both τ_p and τ_E) must be sufficient so that the ions remain in the plasma long enough and remain hot enough that ignition is reached and then maintained. One of the biggest concerns in developing stellarators as a viable reactor concept is the degree to which ions can be confined. This concern is based on the seemingly unfavorable single-particle orbit confinement properties inherent in the stellarator design. As pointed out in Chapter 2, the effect of loss regions in stellarators can be quite severe because of the large fraction of trapped particles. As discussed in Section 4.1, the loss region in ATF is quite large, and it is not obvious *a priori* that a classical helical stellarator can be designed to reduce these losses without compromising MHD stability requirements. The size of these losses may limit the effective energy confinement time to values smaller than those required for a fusion reactor. This chapter presents the results from various thermal ion studies performed on ATF. Because of the low ion temperatures seen to date on ATF, these studies are quite limited, although some conclusions can be drawn from the measured data.

5.1 Experimental Setup

Plasmas in ATF are initiated by up to 400 kW of 53-GHz electron cyclotron heating providing second-harmonic heating for the standard on-axis magnetic field

in ATF, $B_0 = 0.95$ T, and fundamental heating for $B_0 = 1.90$ T. Subsequent heating can be provided by approximately 1.7 MW of NBI and 200 kW of ICH. Conditioning of the vacuum vessel wall has played an important role in the successful operation of ATF. During the early phases of ATF operation, electron-cyclotron-heated discharges displayed uncontrollable rises in electron density and quickly collapsed to low-temperature afterglow plasmas.¹ The most drastic improvement of plasma performance has been seen with the implementation of strong titanium gettering, where a thin layer of titanium is deposited over 70% of the vacuum vessel by evaporation techniques. Following the implementation of titanium gettering, high-density plasmas have been established and maintained throughout the NBI heating phase of the discharge. For all the cases considered here, titanium gettering was used as the standard wall-conditioning technique.

The experiments described in this chapter are generally low-density discharges where the plasma electron density is kept well below the density where the ECH-launched wave reaches cutoff ($\sim 1.2 \times 10^{13} \text{ cm}^{-3}$). The motivation for doing this is twofold. First, operating experience on ATF has shown that it is extremely difficult to couple sufficient NBI power to sustain a plasma density slightly above the ECH cutoff density, as described in detail in Chapter 6. This results in two available operating regimes in ATF: one where the electron density is maintained well below cutoff for which ECH is the primary heating mechanism, and one at very high density where NBI is the primary heating mechanism. Second, since the primary ion diagnostic on ATF, a scanning neutral particle analyzer described in detail in Appendix A, effectively has a density limit above which the measurements are severely affected, the higher-density regime is generally not accessible by NPA measurements.

5.2 Diagnostics

The plasma parameters for these discharges have been measured by a fairly complete set of profile diagnostics. Electron temperature and density profiles are provided at a single time of interest during the discharge by a 15-channel Thomson scattering system.² A 16-channel electron cyclotron emission (ECE) system measuring third-harmonic emission also provided electron temperature profile information, although it was limited near the edge due to nonthermal emission.³ For this work, ECE data have typically been used to follow the evolution of the central electron temperature while Thomson scattering data have been used for profile information. Electron density profile information was also provided by a 15-channel far-infrared interferometer, although only seven channels are currently instrumented.⁴ The plasma electron-line density was monitored by a 2-mm interferometer. Two methods were used to measure the central ion temperature: (1) charge-exchange neutral analysis (described in more detail in Appendix A) and (2) spectroscopy, which relies on the Doppler broadening of central impurity lines (usually O VII at 1623 Å).⁵ All of the ion temperature data presented in this work have been inferred from NPA measurements.

During early operation of the NPA in ECH discharges, the measured count rate was extremely low. Theoretically, the count rate is dependent on the magnitude of the local ion distribution function and the local neutral density at locations along the analyzer chord [see Eq. (A.9)]. If the ion distribution is assumed to be Maxwellian (as should be the case in ECH discharges), the measured flux should take the form of Eq. (A.16). Thus, the flux measured by the NPA is expected to have the approximate energy dependence $\exp(-E/T_{io})E^{1/2}$, where T_{io} is the central ion temperature. For small values of T_{io} , the measured flux is therefore a rapidly decreasing function of energy. As discussed in Appendix A, the inference of the ion

temperature from NPA measurements is based on the measured spectra at energies in the range of 2–10 T_{i0} . If T_{i0} is small enough, this energy range lies in an energy region ($E \leq 1$ keV) where the response function of the NPA detection system is small. In typical ECH discharges in ATF where the ion temperature is approximately 150–200 eV, this is the case. Therefore, the measured count rate is expected to be small. The only truly “controllable” value in Eq. (A.16) that would result in an increase in the measured flux is the local neutral density along the viewing sightline of the analyzer. In general, the neutral density is higher in regions where there is a local gas source such as a gas injector or a limiter (due to recycling). Depending on the size of the gas source, this local enhancement can be as much as 10–100 times the toroidally averaged value of the neutral density. To take advantage of this phenomenon, one of the gas valves used to puff hydrogen gas into ATF during a discharge was moved to the inner port directly opposite the NPA. Since typical ECH discharges require continuous gas fueling throughout the discharge (due to the titanium gettering), it was envisioned that this localized gas source would provide an enhanced neutral density directly in front of the NPA throughout the discharge. In fact, this change increased the count rates measured by the NPA by up to two orders of magnitude, thus making ion temperature measurements possible. The measured count rates are generally sufficient to allow data to be averaged over 20-msec intervals during a 500- to 1000-msec shot, thus providing an effectively continuous measurement. For most ion temperature measurements, the NPA was oriented such that it was viewing perpendicular to the axial magnetic field ($\phi_{\text{anal}} = 0^\circ$).

In general, the ion temperatures inferred from CXNA measurements have been consistent with Doppler broadening measurements. However, at very low ion temperatures (≤ 100 eV), the NPA detection efficiency is extremely low (for the reasons outlined above), and Doppler broadening measurements must be used to

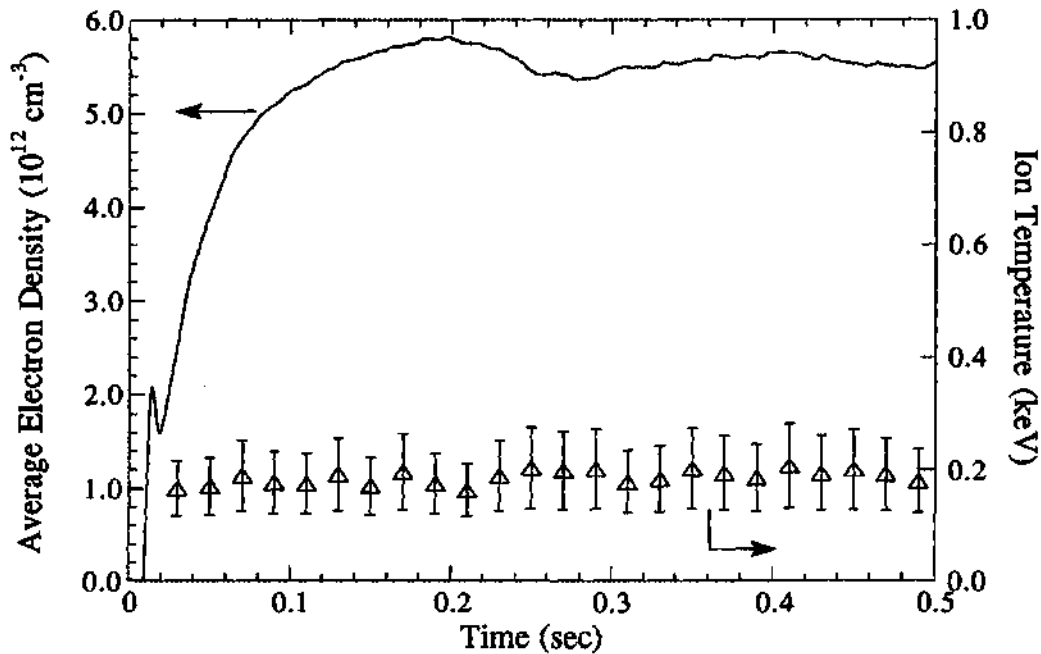


Figure 5.1: Evolution of the average electron density and the central ion temperature measured by the NPA during a typical ECH discharge on ATF.

infer the central ion temperature.

5.3 Observations

5.3.1 Ion Temperature during ECH

Plasmas are initiated in ATF by up to 400 kW of ECH power. The average electron line density and the central ion temperature as measured by the NPA for a typical discharge heated solely by ECH are shown in Fig. 5.1. The plasma reaches equilibrium within approximately 100 ms, and this equilibrium is then sustained throughout the remainder of the discharge. The ECH power is mostly absorbed by the electrons, with the ions subsequently heated by collisions with the electrons. Typical electron temperature and density profiles measured by Thomson scattering for this discharge are shown in Fig. 5.2. This flat density profile is typical of the profiles observed during almost all forms of operation in ATF.

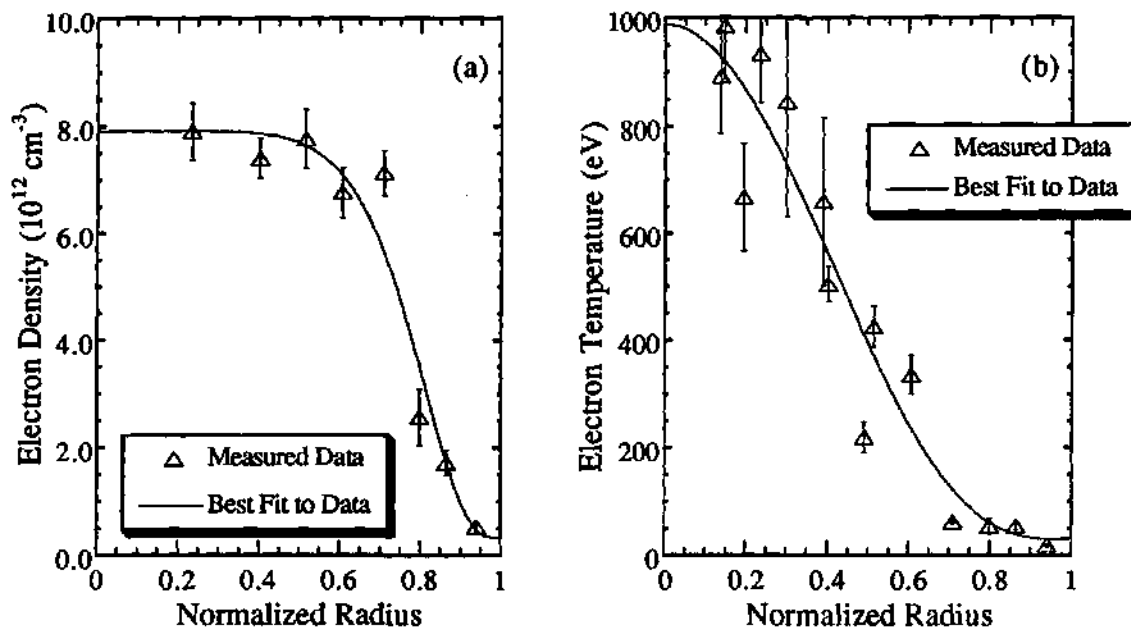


Figure 5.2: Electron density and temperature profiles measured by Thomson scattering for the discharge shown in Fig. 5.1. These profiles were obtained at $t = 0.4$ sec. (Data courtesy of the ATF RATTs group).

A typical energy spectrum measured by the NPA along with the best linear fit to these data is shown in Fig. 5.3. As discussed in Appendix A, the ion temperature is inferred by computing the best linear fit to the measured data. Typically, the ion temperature inferred from NPA data is in the range of 100–200 eV for most ECH discharges in ATF. One of the more interesting aspects of this measured spectrum is the lack of the “two-temperature” feature apparent in most NPA measurements to date.^{6,7} In fact, the measured spectrum tends to fall off at energies below 1 keV. There are two possible explanations for this. First, as discussed in Section 4.5, the orbit topology in ATF is such that the region directly in front of the NPA consists mostly of unconfined orbits. Since the ion distribution is theorized to be depleted in these loss regions, the measured charge-exchange flux originating from this region is expected to be small. Therefore, contributions to the measured spectrum from the edge region is expected to be small. If this is the case, the measured flux should simply be indicative of the ion distribution function in the plasma core, corrected

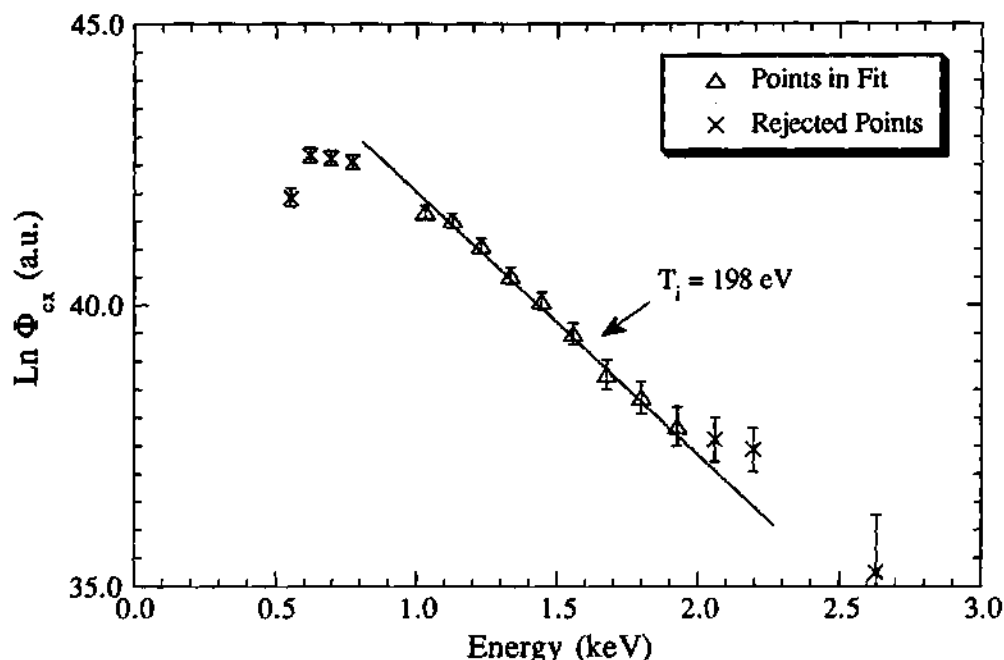


Figure 5.3: Energy spectrum measured by NPA during the discharge shown in Fig. 5.1. This spectrum was obtained from measurements averaged over the time interval from 0.28-0.30 sec. The solid line is the best fit to the spectra after various rejection algorithms have been applied.

by the escape probability of the neutrals exiting the plasma. The corresponding shape of the measured spectra should thus be similar to that seen in Fig. 4.5, since the ion distribution is Maxwellian and the lower-energy particles are less likely to escape from the plasma, resulting in the dropoff at lower energies.

Another possible explanation is related to the energy dependence of the response function of the NPA detection system. The total detection efficiency of the NPA is strongly dependent on the particle energy at lower energies. This is mainly due to the rapid decrease in the stripping efficiency at energies less than 1 keV as a result of increased scattering in the stripping cell. In fact, the detection efficiency at energies below 500 eV is so small that accurate calibration is difficult. Since this uncertainty in the detection efficiency is near the energy range in which the low-temperature feature would appear, the lack of the "two-temperature" feature may simply be the result of inaccurate calibrations in this energy range. The only way to

determine which of these explanations is correct is to increase the ion temperature enough that the low-temperature feature would be in an energy range well above 1 keV. Unfortunately, this requires a central ion temperature on the order of 500 eV, well above the sustainable values on ATF to date.

To see if the measured ion temperatures are consistent with neoclassical transport properties, the PROCTR-MOD analysis code⁸ has been used. For the purposes here, this analysis code simply calculates the expected ion temperature profile using Eqs. (2.58) and (2.59), the experimentally measured electron density and temperature profiles, and a self-consistently calculated neutral density profile. Since the only heat flowing into the ions is through collisions with electrons, the total input power for the ions can be calculated using the experimentally measured profiles. The local heat loss rate is essentially controlled by two quantities: the neutral density profile and the ion heat diffusion coefficient. The neutral density profile determines the magnitude of the charge-exchange and convective losses, while the ion heat diffusion coefficient controls the amount of heat conduction losses.

Several steps are involved in this calculation. First, to estimate the convection and charge-exchange losses, the neutral density profile must be estimated. Using the experimentally determined electron density and temperature as inputs, PROCTR-MOD calculates a self-consistent neutral density from the neutral source rate at the edge and the average edge neutral energy. The neutral source rate is estimated from the particle balance equation

$$\frac{dN}{dt} = -\frac{N}{\tau_p} + R\frac{N}{\tau_p} + S_{\text{ext}}, \quad (5.1)$$

where N is the total number of electrons in the plasma, τ_p is the global particle confinement time, R is the wall recycling coefficient, and S_{ext} is the neutral source rate from external sources. Since the wall recycling coefficient is generally not known, the two source terms on the right-hand side of this equation are combined to give a

total source rate S_{tot} . In steady state, Eq. (5.1) then reduces to

$$S_{\text{tot}} = \frac{N}{\tau_p}. \quad (5.2)$$

If this neutral influx is assumed to be uniformly distributed over the entire surface area of the plasma A_{pl} , the neutral flux at the edge is given by

$$\Gamma_o = \frac{N}{\tau_p A_{\text{pl}}}. \quad (5.3)$$

In general, the exact value of the particle confinement time τ_p is not known. Typically, the value of τ_p is adjusted in the calculation until the calculated neutral density profile is consistent with an estimate of the central neutral density from NPA measurements. Care must be taken in making this adjustment since the central neutral density inferred from NPA measurements may be enhanced by the gas source directly across from the analyzer. Although 3-D Monte Carlo neutral transport calculations have not been done for ATF, other work in this area suggests that the neutral density near a gas source is 10-100 times the toroidally averaged value of the neutral density.^{9,10} Hence, the toroidally averaged neutral density computed by PROCTR-MOD should be much lower than the value inferred from NPA measurements. For most of the cases considered in this analysis, assuming that $\tau_p = 20$ msec produced calculated neutral density profiles that were consistent with the central neutral density inferred from NPA measurements.

For the analysis discussed here, the average edge neutral energy is assumed to be ~ 5 eV. The charge-exchange and convective loss terms in Eq. (2.59) can then be computed. In general, the agreement between the predicted and measured ion temperature is quite dependent on the assumptions made in computing the neutral density profile. The charge-exchange and convective losses are very dependent on the assumed τ_p and E_{edge} and can become dominant in the transport equation if the resulting neutral density is large.

Table 5.1: Variation of the central ion temperature T_{io} and the apparent ion temperature T_i^{app} with neutral density inputs for a typical ECH discharge.

	$\tau_p = 10$ msec		$\tau_p = 20$ msec		$\tau_p = 30$ msec	
	$T_{io}(\text{eV})$	$T_i^{app}(\text{eV})$	$T_{io}(\text{eV})$	$T_i^{app}(\text{eV})$	$T_{io}(\text{eV})$	$T_i^{app}(\text{eV})$
$E_{edge} = 5$ eV	135	131	172	164	186	177
$E_{edge} = 10$ eV	118	115	162	157	180	173
$E_{edge} = 50$ eV	109	108	151	148	171	168

Assuming that the ion thermal diffusion coefficient is given by the expression derived by Chang and Hinton¹¹ χ_i^{C-H} [Eq. (2.61)], PROCTR-MOD calculates the ion temperature profile using the steady-state version of Eq. (2.59), including the heat conduction due to the non-ambipolar flux. To compare the results of the analysis to the ion temperature measured by the NPA, PROCTR-MOD then integrates the expected charge-exchange flux using Eq. (A.16) and the calculated (or measured) values for the local neutral density, ion temperature, ion density, and electron density. As in the analysis of NPA data, an apparent ion temperature T_i^{app} can then be calculated from the best fit to the slope of the resulting spectra. This T_i^{app} can then be compared with the ion temperature inferred from NPA measurements.

Typically, the predicted T_i^{app} is consistent with the measured ion temperature, indicating that the thermal transport properties are consistent with neoclassical theory (i.e., using χ_i^{C-H} and q_i^{na}). However, as just pointed out, these results are quite sensitive to the assumptions made in computing the neutral density profile. This is evident in Table 5.1, which gives the results of a set of PROCTR-MOD calculations in which the parameters that control the neutral density profile were varied. As the global particle confinement time τ_p is decreased or the average edge neutral energy E_{edge} is increased, the predicted T_{io} and T_i^{app} decrease. Because there is little experimental information concerning the neutral density profile, de-

termining the relative magnitude of the charge-exchange and convective losses and the conduction losses is difficult, especially in low-density discharges where all of these terms are of nearly equal magnitude. This makes it difficult to determine if the measured ion temperatures are consistent with neoclassical predictions. To make this determination, ion temperature measurements should be made in slightly higher-density plasmas where the charge-exchange and convective losses are negligible. Unfortunately, access to this density regime is limited because of the lack of ECH absorption above the cutoff density and the lack of NBI coupling at these intermediate densities.

Using the vertical scanning capability of the NPA on ATF, the ion temperature profile has been measured during ECH. The data presented here are for the standard ATF magnetic configuration with the horizontal position of the analyzer fixed such that it is viewing perpendicularly ($\phi_{\text{anal}} = 0^\circ$). As illustrated by Fig. 5.4, the analyzer can view from above to below the plasma column when scanned vertically at this horizontal angle. Ion temperature measurements are made at several vertical angles during a sequence of reproducible discharges with the analyzer moved between successive discharges. The variation of the inferred ion temperature with analyzer vertical angle is shown in Fig. 5.5. This variation is typical of most data taken during ECH operation. Measurements for angles larger than $\pm 15^\circ$ have generally suffered from insufficient count rates. This is most likely because the maximum temperature along these chords is ≤ 100 eV, such that the majority of the charge-exchange flux is in an energy range where the detection efficiency is small ($E \leq 1$ keV).

The ion temperature profile can be obtained from the measurements by two methods. The first is to use standard Abel inversion techniques. However, because the measured flux is a function of the neutral density profile, which is experimentally unknown and difficult to quantify analytically, this technique is extraordinarily

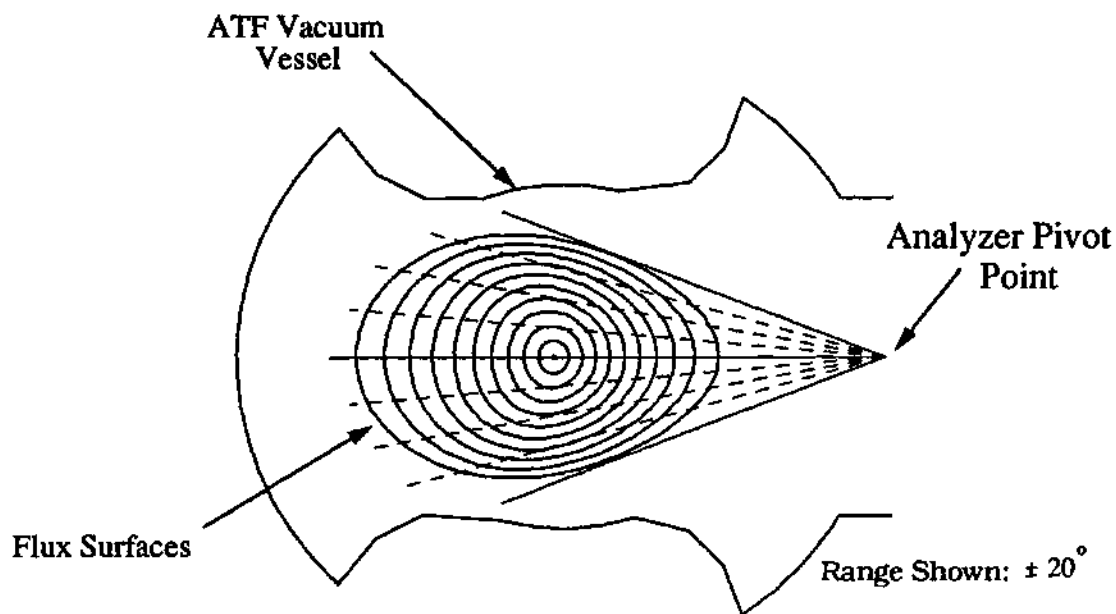


Figure 5.4: Schematic showing the vertical scanning capability of the NPA for the standard ATF magnetic configuration. When viewing perpendicularly, $\phi_{\text{anal}} = 0^\circ$, the analyzer can view from above to below the plasma column.

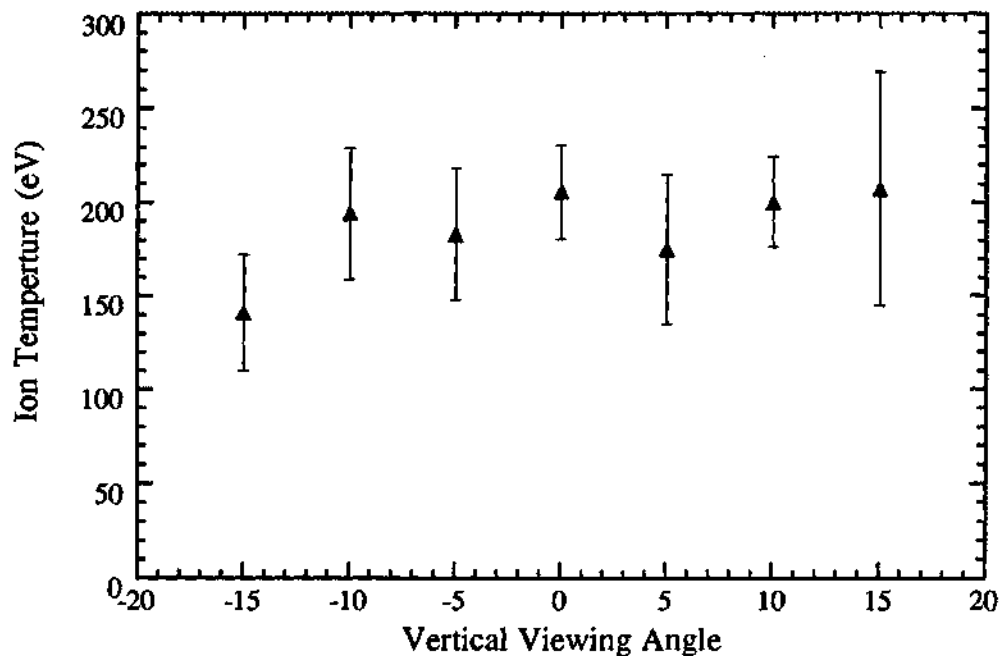


Figure 5.5: Variation of the measured ion temperature as a function of the NPA's vertical viewing angle with the horizontal viewing angle fixed at $\phi_{\text{anal}} = 0^\circ$.

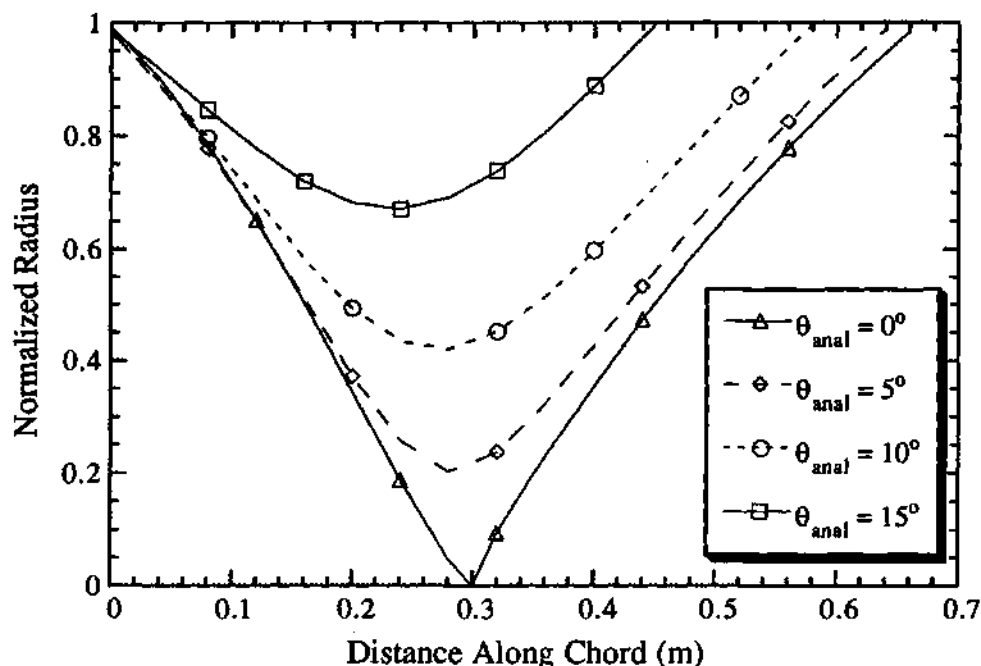


Figure 5.6: Variation of the normalized plasma radius as the NPA is scanned vertically, $\phi_{\text{anal}} = 0^\circ$. The minimum of each curve represents the location at which the maximum ion temperature is expected to occur, assuming $dT_i/d\rho > 0$.

difficult to use. The second method employs the asymptotic slope method used for inferring the central ion temperature from the measured energy spectrum (as discussed in Appendix A). This method assumes that the high-energy portion of the chord-integrated energy spectrum measured by the NPA is dominated by the contribution from the “hottest” location along the chord. This is generally interpreted to be the point at which the viewing chord passes closest to the center of the plasma. Figure 5.6 shows the variation of the plasma normalized radius with the distance along the NPA’s sightline for several vertical angles. As the analyzer is scanned from $\theta_{\text{anal}} = 0^\circ$ to $\theta_{\text{anal}} = \pm 15^\circ$, the normalized radius corresponding to the “hottest” location along the chord changes from $\rho = 0$ to $\rho = 0.70$. By making the appropriate transformation, an ion temperature profile over the normalized radius can then be constructed.

Use of this method in the above case (Fig. 5.5) would seemingly imply that the measured ion temperature profile is flat inside $\rho \simeq 0.50$. However, some justifi-

cation of this result is necessary. The asymptotic slope method used here assumes that the high-energy portion of the measured energy spectrum is dominated by the contribution from the "hottest" location along the chord. A basic assumption built into this method is that the "hottest" location along the chord is in fact the point at which the viewing chord passes closest to the center of the plasma. This generally implies that the ion temperature profile is a monotonically decreasing function of radius (i.e., $dT_i/d\rho < 0$ at all radii). If the ion temperature profile is in fact flat (or hollow), this method may be invalid. Furthermore, the contribution to the charge-exchange flux of a particular location along the analyzer chord is proportional to $n_i(s)n_o(s) \exp[-E/T_i(s)]$. Since the neutral density is a rapidly increasing function of radius, the largest contribution to the observed charge-exchange flux could easily come from a location well away from the calculated "hottest" point when the ion temperature profile is flat and the ion density profile is flat or hollow. In fact, if the ion temperature profile were also hollow, this method would produce results that indicated that the ion temperature profile was flat. This could conceivably be the case in ATF, where the electron density profiles as measured by laser Thomson scattering are typically flat or hollow (see Fig. 5.2). This implies that the ion density profile is also flat or hollow through the principle of quasi-neutrality.

Fortunately, it is generally quite difficult for the ion temperature profile to be hollow since heat transport in the core of the plasma is dominated by heat diffusion. Because there is a heat source in the core of the plasma (e.g., collisions with electrons), the basic heat transport equation (neglecting charge-exchange and convective losses) requires a nonhollow profile. This can be seen by solving the steady-state version of the heat transport equation [Eq. (2.59)] neglecting the charge-exchange and convective loss terms. In this case, this equation takes the form

$$-\frac{1}{\rho} \frac{\partial}{\partial \rho} \left[\rho \chi_i(\rho) n_i(\rho) \frac{\partial T_i}{\partial \rho} \right] = q_{i,e}.$$

Integrating this equation gives the result

$$\frac{\partial T_i}{\partial \rho} = -\frac{1}{\rho \chi_i(\rho) n_i(\rho)} \int \rho q_{i,e} d\rho,$$

which implies that $\partial T_i / \partial \rho \leq 0$ since all of the quantities on the right-hand side of this equation are positive definite. Note that this is for the central regions of the plasma where heat transport is assumed to be dominated by heat diffusion.

Another assumption built into the asymptotic method is that the flux measured by the NPA originates from ions that are localized near a particular radial location (i.e., confined to a particular flux surface). This is not the case in ATF as is illustrated by Fig. 4.13. It is evident from this figure that the ion population sampled by the NPA at $\phi_{anal} = 0^\circ$ is not localized (i.e., the ions do not remain close to a particular radial coordinate) due to the large radial excursions of the characteristic orbits of these particles. Because of this non-localization of the sampled population, it is not obvious that the inferred ion temperature from NPA measurements is truly representative of the ion temperature of the radial coordinate corresponding to the "hottest" location along the analyzer chord. This effect is mitigated in plasma conditions where the ions suffer many collisions during a poloidal transit; however, in ECH plasmas where the collisionality is quite low, this phenomenon must be considered when interpreting the measured data. Another ramification of this effect is an increase in the convective transport of heat from the center to the edge of the plasma. This mechanism may cause the inferred flat ion temperature profile, since the NPA may be sampling the same ion population, just on different portions of the characteristic helically trapped orbit. This problem is quite intriguing, yet very difficult to handle from an analytic or computational point of view. Because ion temperature profile measurements have been limited to low-temperature ECH discharges, no effort has been made to resolve this issue either theoretically or experimentally.

Neglecting the possible effect associated with the discussion in the previous paragraph, the the inferred ion temperature profile from NPA measurements is fairly flat inside $\rho = 0.5$. This result is consistent with ion temperature profiles inferred from spectroscopic measurements made during the same type of discharges⁵ and is also consistent with PROCTR-MOD calculations, the worries about

5.3.2 Effect of Magnetic Configuration

As discussed in Chapter 4, the degree to which trapped particles are confined in ATF is critically dependent on the magnetic configuration. To determine how the magnetic configuration affects the confinement of thermal particles in ATF, several configuration scans have been performed. This is easily done in ATF by changing the relative currents flowing in the three sets of VF coils. As discussed more extensively in Section 4.2, the plasma can be shifted in major radius by changing the dipole moment of the vertical field or vertically elongated (or "squeezed") by changing the quadrupole moment of the vertical field. As illustrated by Fig. 4.8, the degree of confinement changes drastically as the magnetic configuration changes, with the shifted-in, vertically "squeezed" configuration having the best single-particle confinement properties.

Bootstrap current studies conducted in ATF while varying the magnetic configuration have shown that the measured plasma current is consistent with neoclassical predictions of the bootstrap current,¹² suggesting that transport in ATF is indeed consistent with neoclassical theory. The effect of changing the magnetic configuration on the central ion temperature has been tested by performing various scans of the magnetic configuration. The primary scans that have been made are independent variations of the dipole and quadrupole moments of the vertical fields; these discharges were heated solely by 400 kW of ECH power. To control the conditions of the discharge during the scans, the amount of gas injected into each

discharge was adjusted such that the line-averaged electron density ($\int n_e(\ell) d\ell / \int d\ell$) for each discharge was maintained at a predetermined level. The central ion temperatures measured by the NPA during these scans are shown as the open symbols in Fig. 5.7. It is apparent from Fig. 5.7 that the magnetic configuration has only a small effect on the attainable ion temperature, though there is evidence that the maximum ion temperature is attained in the slightly shifted-in ($R_0 = 2.08$ m), standard elongation ($f_{\text{mid}} = 0$) configuration. Similar variations are seen in the plasma stored energy and central electron temperature as the magnetic configuration is changed,¹² indicating that this configuration is the optimal configuration for plasma performance in ATF.

The predicted T_i^{app} for the discharges in these scans are shown as the solid symbols in Fig. 5.7. These predictions were computed, assuming the thermal ion diffusion coefficient is given by $\chi_i^{\text{C-H}}$ and q_i^{na} , $\tau_p = 20$ msec and using measured n_e and T_e profiles. Although the predicted and measured values of T_i agree quite well, it should be realized that this does not justify the choice of χ_i and τ_p . In fact, large variations of the amount of gas fueling required during these scans suggest that τ_p is far from constant. The purpose of fixing the value of τ_p during the analysis is for convenience, since deducing its value for each configuration is generally quite difficult. As shown in Table 5.1, the predicted ion temperature is very sensitive to the assumed value of τ_p in these low-density plasmas. Therefore, conclusions based on the agreement between the measured and predicted values would be tenuous at best.

One of the most intriguing features of the thermal ion measurements made by the NPA on ATF is the existence of a high-energy tail in certain magnetic configurations. This feature (shown in Fig. 5.8) is most vividly seen during ECH-only quadrupole scans where the external gas source rate is fixed during the scan (instead of maintaining a constant line-averaged electron density as before). As the magnetic

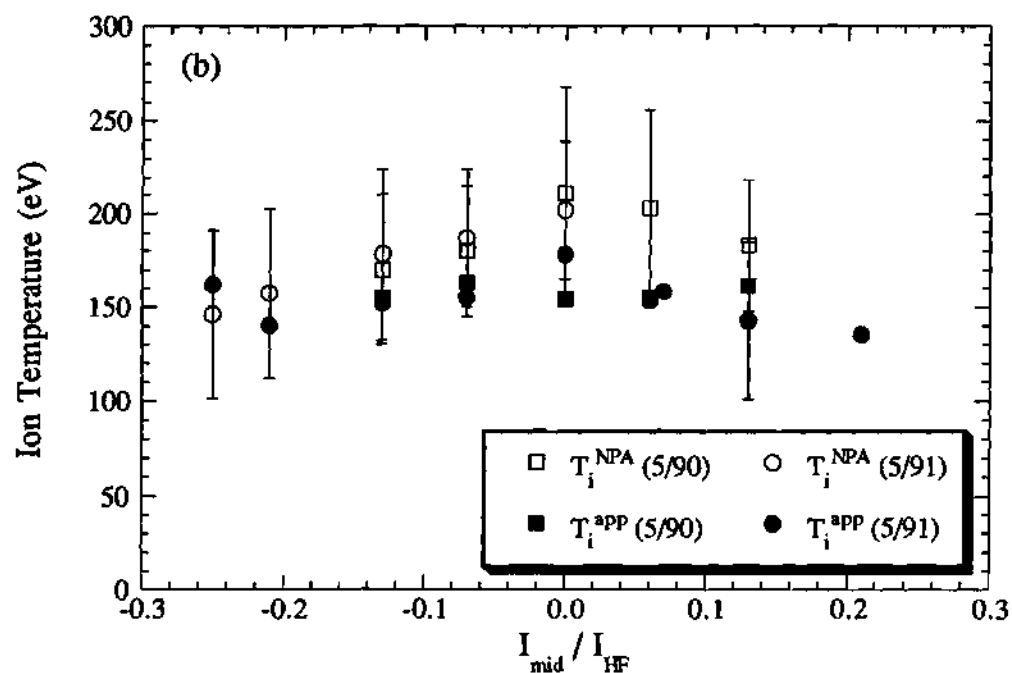
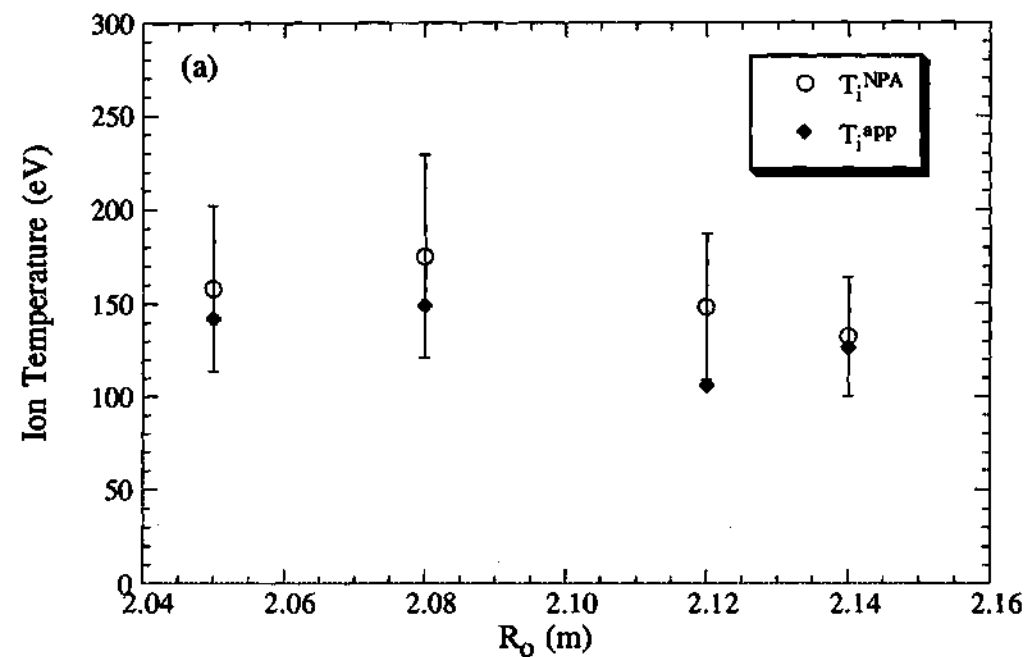


Figure 5.7: Variation of the measured (open symbols) and predicted (solid symbols) ion temperatures during (a) dipole and (b) quadrupole scans in ATF.

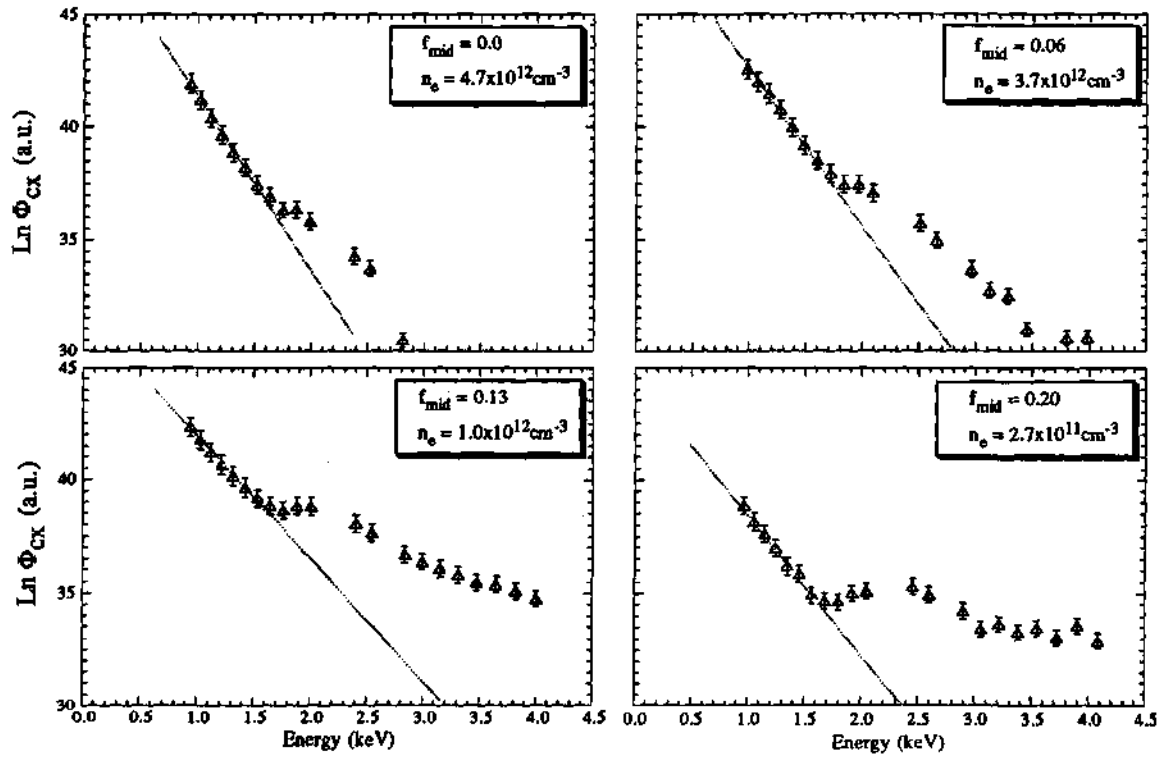


Figure 5.8: NPA spectra measured at $\phi_{\text{anal}} = 0^\circ$ during a quadrupole scan of the magnetic configuration in ATF. The high-energy tail (above $E = 2$ keV) became more distinct as the configuration became more elongated (f_{mid} increasing).

configuration was changed from "squeezed" to elongated, the high-energy tail became more distinct in the measured spectra. It is not obvious whether this feature is related to the magnetic configuration or to the plasma density. In general, the vertically elongated configurations ($f_{\text{mid}} > 0$) require quite a bit more fueling than the vertically "squeezed" configuration to maintain the same average electron density, thereby indicating a smaller global confinement time. Therefore, in this case where the external gas source rate is maintained constant during the scan, the vertically elongated configurations have a much smaller plasma density. This reduction in the plasma density as f_{mid} is decreased may be the reason for the observed enhancement of the tail in the measured energy spectra. This explanation is strengthened by the fact that no such tails are observed in configuration scans where the line-averaged electron density is held fixed.

Further data taken during very low density, vertically elongated, ECH discharges suggest that these tails may be the result of some sort of collisionless ion heating. Ion temperatures up to 500 eV have been measured in these types of discharges when the average electron line density is only $9.0 \times 10^{11} \text{ cm}^{-3}$ and the central electron temperature is approximately 1500 eV. The energy spectra measured by the NPA are typically Maxwellian in shape, indicating that the measurement is representative of the bulk thermal distribution. Theoretically, one would expect the ion temperature in such a low-density plasma to be very small, since the electron-ion collisional coupling term is proportional to n_e^2 . Because this term is so small when the density is small, it is difficult to imagine such a high ion temperature from classical collisional arguments, since there is a lower limit on the magnitude of the charge-exchange, convective, and conductive losses. In fact, PROCTR-MOD analysis predicts an ion temperature of only 40 eV. Therefore, it seems that this high ion temperature must be the result of some form of collisionless ion heating. Similar measurements of high ion temperatures in low-density plasmas have been

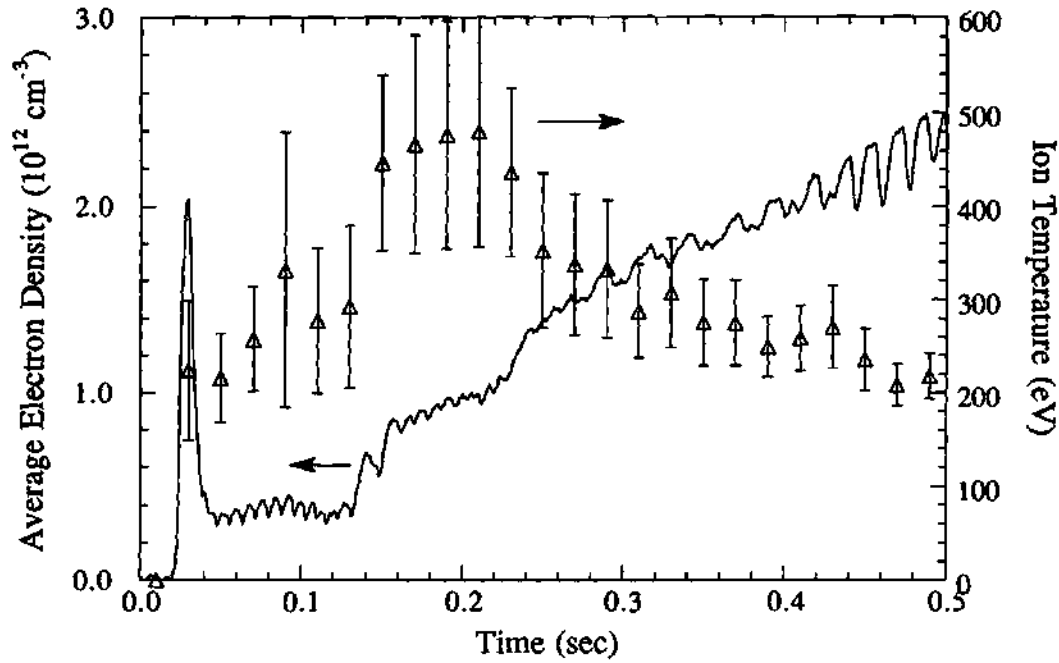


Figure 5.9: Evolution of the electron density and ion temperature (for $\phi_{\text{anal}} = 0^\circ$) during a very low density, vertically elongated plasma ($f_{\text{mid}} = 0.13$) in ATF. Parallel and antiparallel ion temperature measurements produce similar results.

made on the L-2 stellarator¹³ and were attributed to turbulence associated with plasma instabilities.

To test the density dependence of this phenomenon, the plasma density was ramped in a linear fashion during a 500-msec discharge. The evolution of the plasma density and ion temperature of such a discharge is shown in Fig. 5.9. The ion temperature attains a maximum value of approximately 500 eV when the average electron density is still quite low ($\bar{n}_e \simeq 8.0 \times 10^{11} \text{ cm}^{-3}$). As the electron density increases, the ion temperature decreases in an almost linear fashion. This is quite peculiar, since the functional dependence of the electron-ion coupling term is of the form [see Eq. (2.62)]

$$q_{i,e} \propto \frac{\gamma - 1}{\gamma} \frac{n_e^2}{T_e^{1/2}},$$

where γ is the ratio T_e/T_i . ECE measurements indicate that the electron temperature is also decreasing throughout the discharge. Therefore, the magnitude of $q_{i,e}$ should increase since $(\gamma - 1)/\gamma$ is a slowly varying function of T_e/T_i for $T_e \gg T_i$.

Furthermore, both the heat conduction loss and the convective loss terms are decreasing functions of the electron density, such that an increase in the plasma density should reduce the losses associated with these mechanisms. Therefore, according to classical transport arguments, the ion temperature should increase as the density rises, contrary to the observed trend. These data further suggest that some form of collisionless ion heating is taking place during the low-density phase of the discharge with classical ion-electron coupling providing the ion heating in the latter phases of the discharge.

The relatively high temperatures seen during these discharges should provide an excellent opportunity to study orbit effects in ATF using the NPA. These studies have been severely hampered by the presence of the gas injector directly in front of the NPA since this local gas source greatly complicates the interpretation of the measured data. As mentioned previously, the main reason for having this gas injector in front of the NPA is to increase the measured flux seen by the NPA to a usable level. If the ion temperature could be maintained at approximately 500 eV, the count rates should be sufficiently large that the gas injector would not be necessary. Furthermore, the high temperature and low density of these plasmas would make them ideal for orbit studies, since the collisionality of the ions is quite small in these conditions. The velocity space dependence of the distribution function could then be measured quite easily by scanning the NPA over its available orientations. The interpretation of this measured data should then be fairly simple since the neutral density would not vary as a function of viewing angle and the effect of collisions would be small. Unfortunately, these experiments have not been carried out to date, but they have been suggested for future work.

5.4 Summary

The existence of the high-energy tails on the ion distribution and collisionless ion heating in certain magnetic configurations are quite fascinating. Although these features may be used to help study orbit effects in ATF, their usefulness beyond this is quite limited because both phenomena seem to appear only in extremely low-density plasmas. Since fusion reactors must operate at significantly higher plasma densities, the characteristics of these features are only interesting from a basic science point of view.

The primary caveat that applies to most of the data presented in this chapter is that thermal ion studies in ATF to date have been severely hampered by two limitations. First, the lack of significant ion temperatures in ATF has severely limited the usefulness of the NPA in inferring thermal ion characteristics in ATF. At the low temperatures observed, the charge-exchange neutrals exiting the plasma have energies in the range where the detection efficiency of the analyzer is quite small, such that the count rates were quite small. The insufficient count rates necessitated the placement of a gas valve directly in front of the analyzer to enhance the background neutral density, thereby increasing the flux measured by the NPA to a usable level. Unfortunately, analysis of these measurements is then extraordinarily difficult, if not impossible, because of the local enhancement and the 3-D nature of the neutral density profile in front of the analyzer.

The second limitation results from the available operating regimes in ATF. Because steady-state plasmas that are accessible to NPA measurements cannot be attained for densities above $\bar{n}_e \simeq 8.0 \times 10^{12} \text{ cm}^{-3}$, most of the NPA measurements have been made in plasmas where the background neutral density is still significant. Therefore, it is very difficult to determine independently the relative magnitude of the charge-exchange, convective, and conductive loss terms in the ion heat equation.

With these limitations in mind, the basic results (if found to hold true in higher-density, higher-temperature regimes) indicate that ion behavior in ATF is consistent with neoclassical transport theory for stellarators (i.e., given by χ_i^{C-H} and q_i^{na}). In general, the measured ion temperature is in agreement with predictions of neoclassical theory, though these comparisons are quite sensitive to the assumptions used in computing the neutral density profile. The ion temperature profile inferred from NPA measurements is fairly flat inside $\rho \approx 0.5$, which is also consistent with neoclassical calculations.

Changes in the magnetic configuration of ATF seem to have a very small influence on the attainable ion temperature in ECH-only discharges. The optimal configuration in terms of the attained ion temperature is the slightly shifted-in ($R_o = 2.08$ m), standard elongation ($f_{mid} = 0$) configuration, which is consistent with optimization studies of the plasma electron temperature and stored energy. Furthermore, spectroscopic measurements of the central ion temperature during NBI indicate the attainable ion temperature is very dependent on R_o .¹⁴ For example, moving the plasma inward from $R_o = 2.10$ m to $R_o = 2.075$ m makes a dramatic difference in the maximum ion temperature (increases from 400 eV to 800 eV). These observations are consistent with the theoretical results presented in Section 4.2 where the degree of confinement of deeply trapped particles was seen to improve as the plasma was shifted inward.

REFERENCES

- ¹ R. C. Isler et al., Nucl. Fusion **29**, 1384 (1989).
- ² R. R. Kindsfather et al., Rev. Sci. Instrum. **57**, 1816 (1986).
- ³ G. L. Bell, *Third-Harmonic Electron Cyclotron Emission Studies on the Advanced Toroidal Facility*, PhD thesis, Auburn University, 1990.
- ⁴ C. H. Ma, D. P. Hutchinson, and K. L. Vander Sluis, Rev. Sci. Instrum. **61**, 2891 (1990).
- ⁵ R. C. Isler et al., Nucl. Fusion **29**, 1391 (1989).
- ⁶ V. V. Afrosimov and I. P. Gladkovskii, Sov. Phys.-Tech. Phys. **12**, 1135 (1968).
- ⁷ R. J. Goldston, in *Diagnostics for Fusion Reactor Conditions*, Varenna, p. 263 (CEC, Brussels, 1982).
- ⁸ H. C. Howe, Technical Report ORNL/TM-11521, Oak Ridge National Laboratory (1990).
- ⁹ G. H. Neilson, Technical Report ORNL/TM-7333, Oak Ridge National Laboratory (1980).
- ¹⁰ W. A. Davis and R. J. Colchin, Phys. Fluids **29**, 2249 (1986).
- ¹¹ C. S. Chang and F. L. Hinton, Phys. Fluids **25**, 1493 (1982).
- ¹² M. Murakami et al., Phys. Rev. Lett. **66**, 707 (1991).
- ¹³ E. D. Andryukhina et al., in *Plasma Physics and Controlled Fusion Research 1984 (Proc. 10th Int. Conf., London, 1984)*, Vol. 2, p. 409 (IAEA, Vienna, 1985).
- ¹⁴ R. C. Isler et al., in *Controlled Fusion and Plasma Physics (Proc. 18th EPS Conf., Berlin, 1991)*, Vol. 15C, Part II, p. 157 (1991).

CHAPTER VI

Fast Ion Confinement Studies in ATF

Because the primary heating mechanisms on ATF (NBI and ICH) rely on the thermalization of an energetic ion population, the study of the confinement of these energetic ions is essential in understanding the global power balance in ATF. Fast-ion confinement studies on ATF have been conducted during both NBI and ICH. However, because of limited operating experience with ICH, very little information is available. In contrast, an abundance of data is available for NBI in several different operating regimes. This chapter discusses the analysis of these data in terms of determining the fast-ion confinement characteristics in ATF and their effect on plasma performance.

6.1 Operating Regimes during NBI in ATF

Operating experience on ATF has shown that the available operating space (in terms of plasma electron density) during NBI is limited. Quasi-steady-state plasmas have only been attained in two situations: low density (below the ECH cutoff density, $\bar{n}_e \leq 7.5 \times 10^{12} \text{ cm}^{-3}$) and extremely high density ($\bar{n}_e \geq 8.0 \times 10^{13} \text{ cm}^{-3}$). For intermediate densities, the plasma either undergoes a thermal collapse (loss of all thermal energy) or has peculiar transient behavior. The temporal evolution of the average electron line density and the plasma stored energy for four different density regimes is shown in Fig. 6.1. For the purposes of this work, these regimes are deemed the ultralow-, low-, medium-, and high-density regimes.

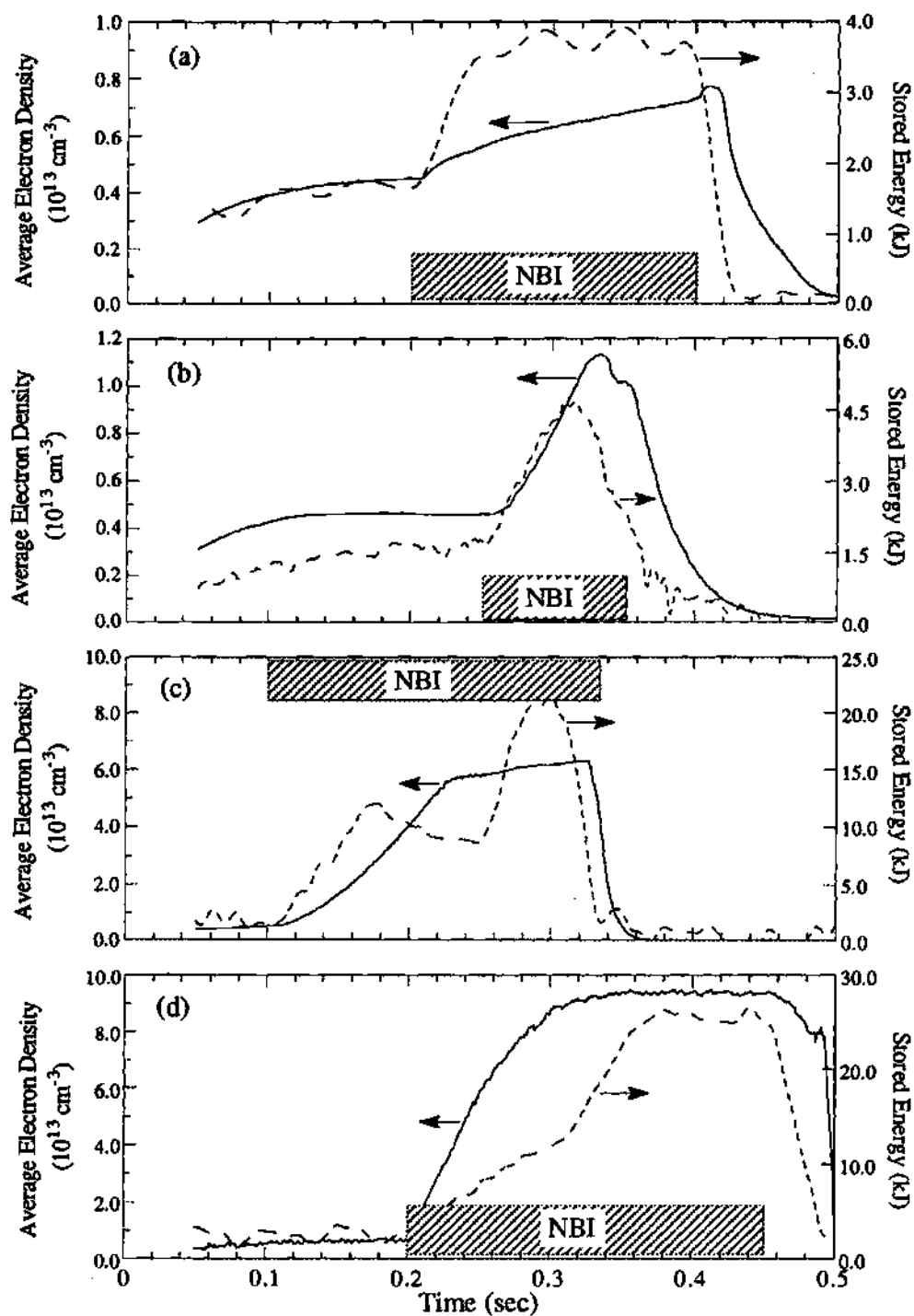


Figure 6.1: Time evolution of the average electron line density and plasma stored energy in ATF for typical (a) ultralow-density, (b) low-density, (c) medium-density, and (d) high-density discharges.

Historically, the low-density regime [Fig. 6.1(b)] is the operating regime with which there is the most experience on ATF. This regime is characterized by a thermal collapse that occurs approximately 50–75 msec after the initiation of NBI. Considerable effort has been put forth in trying to understand the mechanisms by which the plasma collapses in this regime. These discharges are obtained when a small amount of gas is injected (via gas valves) at the onset of NBI. As the amount of injected gas was increased, the attainable density also increased. With innovative gas programming, the medium-density [Fig. 6.1(c)] and high-density [Fig. 6.1(d)] discharges, which exhibit substantially higher energy confinement times than the low-density discharges, have been obtained. The ultralow-density discharge [Fig. 6.1(a)] is the result of careful control of the plasma density through wall conditioning and gas programming. As explained in the Section 6.2, this particular type of discharge was difficult to maintain. However, enough reproducible discharges have been made that reliable NPA measurements are available.

In the following sections, the fast-ion confinement properties of three of these operating regimes are explored. For purposes of clarity, the ultralow-density case is discussed first in Section 6.2, followed by the low-density case (Section 6.3) and then the high-density case (Section 6.4). Because of the lack of available data, the medium-density case has not been analyzed. The emphasis of this analysis is to determine if reduced confinement of the injected ions is the main reason for this limited operating space. This reduction in confinement is theorized to be due to two primary mechanisms. First, the amount of neutral beam power absorbed by the plasma is a strong function of the plasma density, since both the shine-through losses (beam neutrals not ionized by the plasma before striking the opposite wall) and charge-exchange losses are reduced substantially as the density is raised. The target plasmas in ATF are produced by 53-GHz ECH so that the ECH-launched wave is cut off at a fairly low density ($n_e = 1.2 \times 10^{13} \text{ cm}^{-3}$). Therefore, the initial

phase of injection is into a low-density plasma where the shine-through and charge-exchange losses are quite large. Since there is typically a large influx of particles from the beam duct and the walls during NBI, the density level quickly rises, making the NBI coupling somewhat better. Since the ECH launched wave is not absorbed above the cutoff density and because the beam shine-through and charge-exchange losses are so large at the onset of injection, the density must rise quickly and attain a fairly high value before these losses are reduced to the point where a favorable global power balance is achieved.

The second loss mechanism is theorized to be due to orbit effects. As discussed in Section 4.4, the orbit topology in ATF is such that when a passing particle (e.g, a tangentially injected ion) becomes helically trapped, the resulting helically trapped orbit takes the particle out near the edge of the plasma. Two possible types of losses can then result. First, the helically trapped orbit may not be confined (i.e., it hits the ATF vacuum vessel or limiter). Second, the probability of the helically trapped particle being lost because of charge-exchange is significantly increased in the edge region due to the large neutral density. As discussed in Section 4.4, this loss mechanism has the largest impact in medium-density, fairly high temperature plasmas where $E_{crit} \sim E_{inj}$. This is because the energy at which the injected particles enter the trapping region is correlated with the critical energy. Hence, a higher value of the critical energy results in more energy being lost through this loss mechanism.

6.2 NBI Studies in Ultralow-Density Plasmas

The first type of discharge to be discussed is the ultralow-density NBI discharge. The available data for this operating regime are limited. However, there were enough reproducible discharges so that a rather complete set of NPA measurements could be made. The data presented here represent measurements taken

during a set of reproducible discharges in July 1990. The ATF sequences included in this set of data are 90071704, 90071705, and 90071901. For these sequences, hydrogen neutrals were injected by the beams into a deuterium plasma. This allowed simultaneous measurements of the fast- and thermal-ion distribution functions by the NPA.

6.2.1 Experimental Setup

The evolution of the electron line density, the plasma stored energy inferred from a diamagnetic loop measurement of the perpendicular plasma pressure, the central electron temperature from ECE measurements, and the ion temperature from the NPA for a typical discharge of this type are shown in Fig. 6.2. The target plasma is created by 400-kW, 53-GHz ECH power and is subsequently heated starting at 200 ms by approximately 650 kW of balanced NBI. The plasma quickly reaches a new equilibrium after the beginning of NBI, and this equilibrium is sustained throughout the length of the discharge. The length of time that this equilibrium could be maintained was limited only by the available pulse length of the neutral beam injectors used on ATF (~ 350 msec). The electron temperature decreases at the onset of injection to a steady-state NBI level of 900 eV. In contrast, the ion temperature increases from an ECH-only level of 150 eV to a steady-state NBI level of 400 eV.

Note that the average line density remains well below the density at which the ECH-launched wave is cut off, enabling the full ECH power to be absorbed by the plasma. The reasons for doing this are discussed more thoroughly in Section 6.3. Maintaining the plasma density below the cutoff density proved to be extremely difficult because of the added influx of neutrals from the beam duct during NBI. Generally, a thin layer of titanium was deposited over 70% of the vacuum vessel by evaporation techniques just prior to operation to take advantage of titanium's

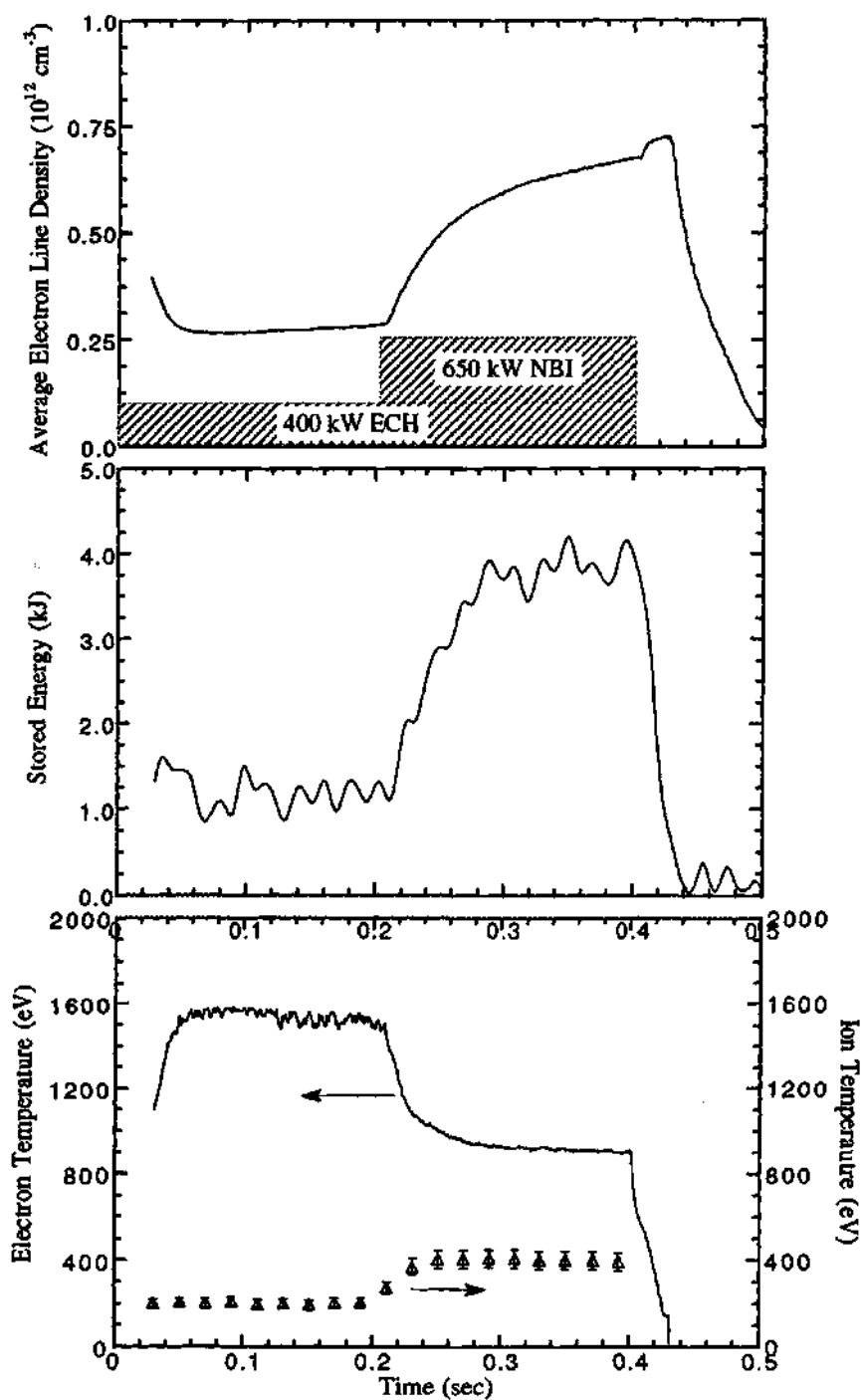


Figure 6.2: Time evolution of (a) average electron line density, (b) plasma stored energy, and (c) central electron and ion temperatures for a typical ultralow-density discharge in ATF.

intrinsic capacity to adsorb hydrogen gas. This increased pumping capacity, coupled with a programmed gas puff that was dropped to zero during the NBI phase of the discharge, allowed excellent control of the growth rate of the density during the NBI portion of these discharges. Unfortunately, the ability to maintain this density control only lasted for a few discharges because of "saturation" of the freshly deposited titanium. The effect of this "saturation" is shown in Fig. 6.3, where the evolution of a succession of ultralow-density discharges shortly after titanium evaporation is shown. The microwave leakage power shown in this figure is an indication of how much ECH power is not absorbed by the plasma. A small value of this signal corresponds to good absorption, with increasing values indicating a deterioration in absorption. These three successive discharges exhibit higher and higher electron line densities during the NBI phase until the density reaches a critical value where the ECH leakage power begins to rise, correlated with a decrease in the central electron temperature. This correlation indicates that the ECH-launched wave is not fully absorbed. Eventually, this reduction in absorption causes the plasma to collapse [i.e., $T_e(0) \rightarrow 0$]. The density at which the microwave leakage power begins to rise is approximately $\bar{n}_e = 7.5 \times 10^{12} \text{ cm}^{-3}$. Since the measured electron density profiles in ATF are typically flat, this average density roughly corresponds to the central electron density. The density at which absorption starts to decrease is substantially below the ECH cutoff density of $n_e = 1.2 \times 10^{13} \text{ cm}^{-3}$, indicating that deterioration of ECH absorption begins at a density limit well below the ECH cutoff density. This observation is used in modeling the low-density discharges discussed in Section 6.3.

6.2.2 Experimental Results

To assess the confinement characteristics of the ions injected by the neutral beam in this density regime, the scanning NPA was used to measure the fast-ion slowing-down distribution during these discharges. The evolution of the tangential

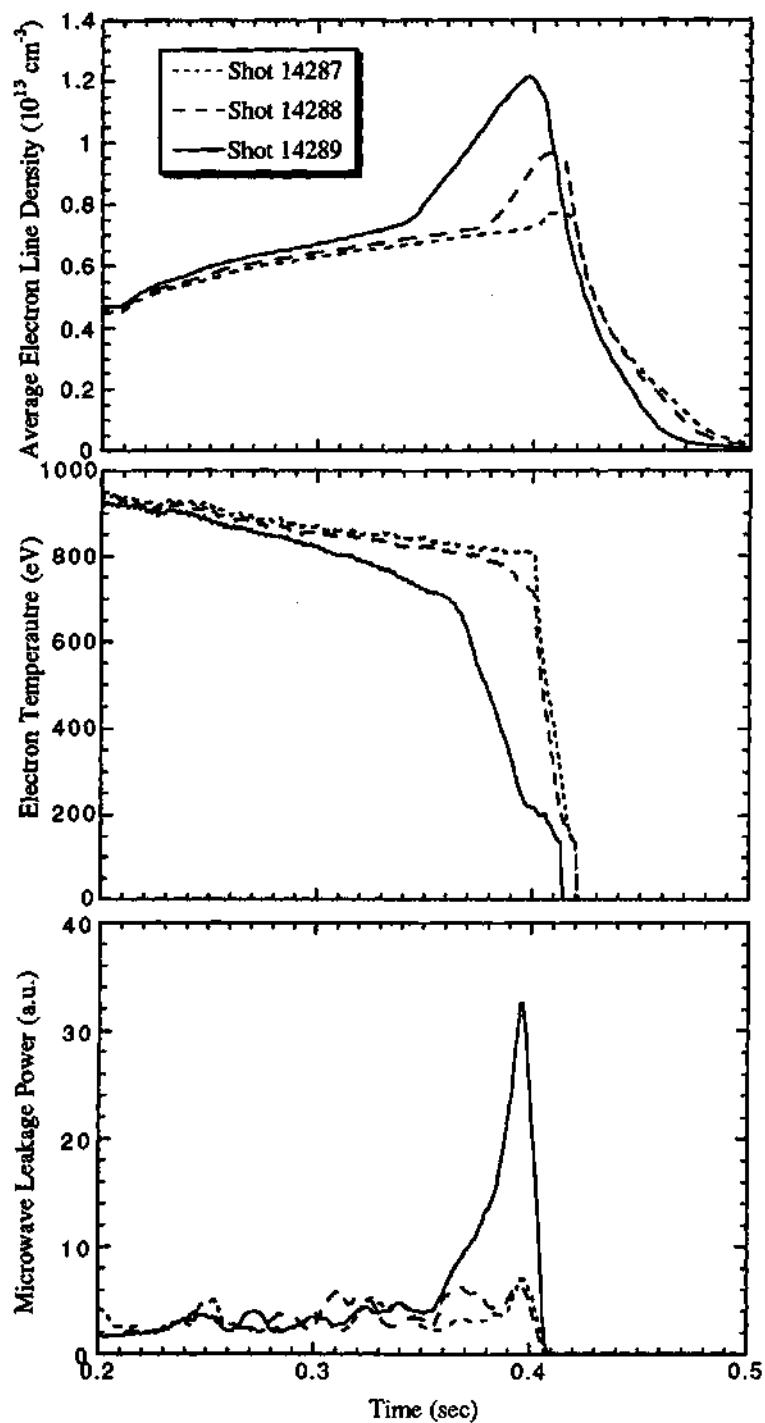


Figure 6.3: Evolution of a succession of ultralow-density discharges immediately following titanium gettering. The signals shown are (a) the average electron line density, (b) the central electron temperature, and (c) the measured microwave leakage power.

slowing-down distribution as measured by the NPA is shown in Fig. 6.4. The tangency radius for this viewing angle of the analyzer ($\phi_{\text{anal}} = 35^\circ$) is slightly smaller than the tangency radius of the beam. The three peaks in the energy spectra correspond to the full, one-half, and one-third energy components of the injected beam. The sharp decrease in the measured flux below each energy peak is evidence that the beam ions are not well confined in this case. The reasons for this degradation in confinement are discussed in Section 6.2.3. From Fig. 6.4, it is evident that after approximately 50 msec ($t = 250$ msec), a steady-state slowing-down distribution is attained and then maintained throughout the remainder of the discharge.

Using the scanning capability of the NPA, measurements of the slowing-down distribution for several NPA viewing angles near tangential were also made. The variation of the measured energy spectra near the injection energy as a function of the NPA viewing angle is shown in Fig. 6.5. These spectra were taken during the steady-state phase of this discharge ($t = 350$ msec) on separate, nearly identical discharges with the analyzer moved to the desired angle between discharges. The tangency radius of the viewing angle $\phi_{\text{anal}} = 45^\circ$ roughly corresponds to the tangency radius of the beam with smaller values of ϕ_{anal} indicating the movement of the analyzer away from this tangency radius. The detected flux diminished as the analyzer was moved away from the beam tangency radius. This is expected since the movement of the NPA away from the beam tangency radius moves the average pitch angle that the NPA is "viewing" away from the nominal initial pitch angle of the injected beam ions.

The unique viewing capabilities of the NPA also allowed measurements of the slowing-down distribution for both co-passing and counter-passing particles without changing the direction of the magnetic field. This measurement was made during the steady-state phase of this discharge ($t = 350$ msec) on separate, nearly identical discharges with the analyzer located at $\phi_{\text{anal}} = \pm 35^\circ$. The viewing geometry of the

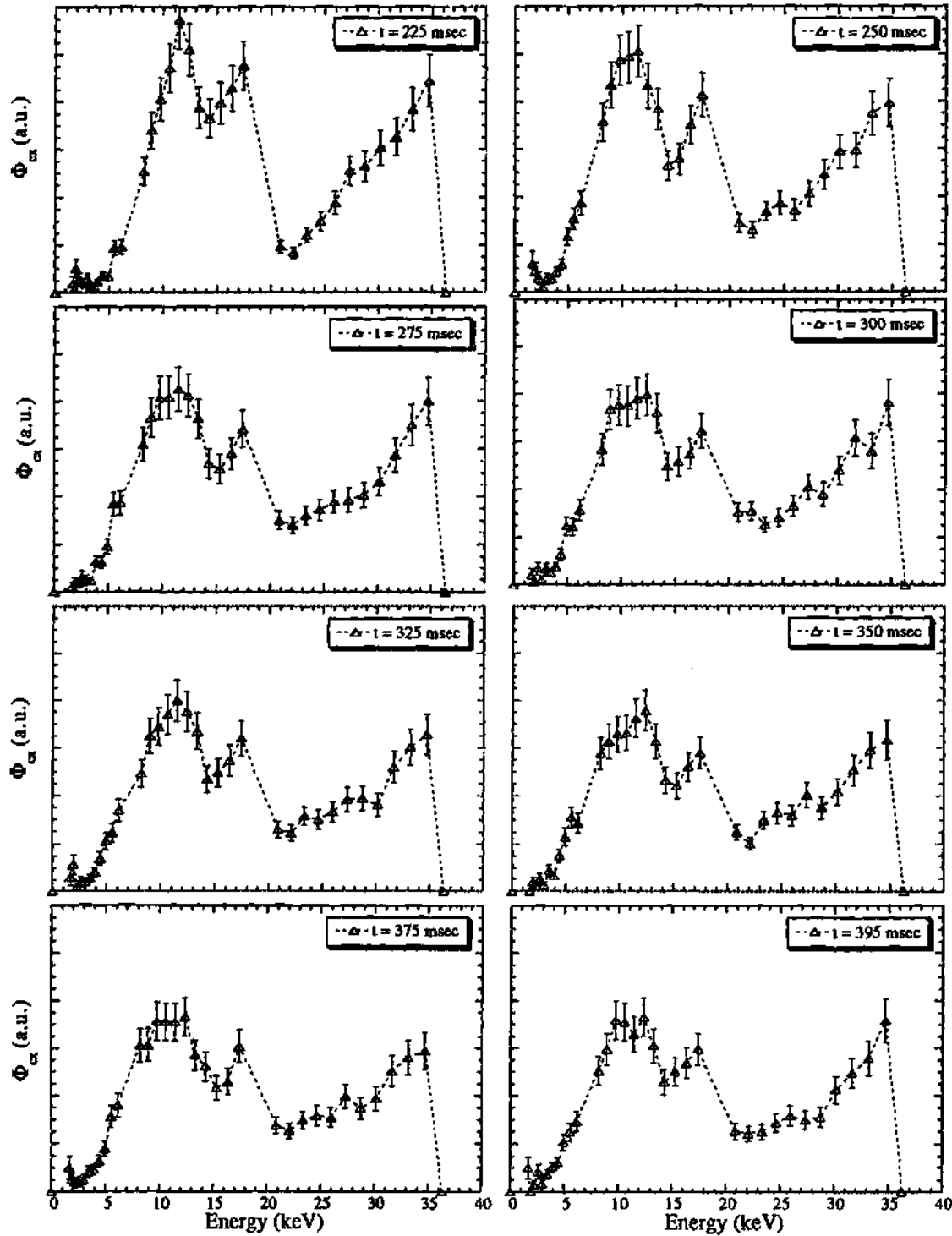


Figure 6.4: Near tangential ($\phi_{\text{anal}} = 35^\circ$) energy spectra measured by the NPA at various times during ultralow-density NBI discharges.

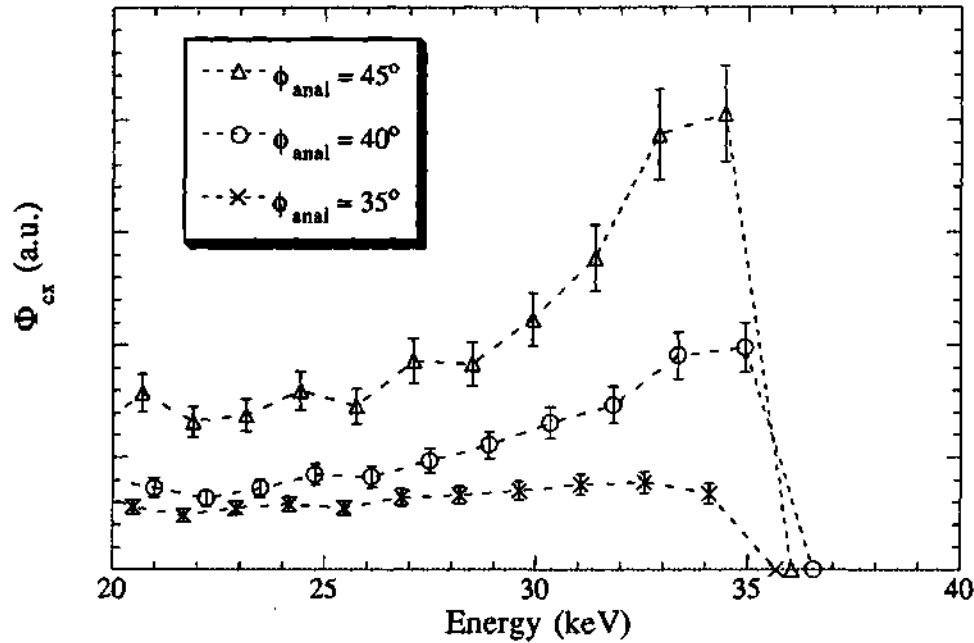


Figure 6.5: Measured energy spectra for three different NPA viewing angles near tangential for energies near the injection energy ($E_{inj} = 35$ keV).

NPA is such that the particles measured at $\phi_{anal} = -35^\circ$ are co-passing particles injected by neutral beam injector 1 and the particles measured at $\phi_{anal} = 35^\circ$ are counter-passing particles injected by neutral beam injector 2. The measured spectra in these two cases are almost identical, as illustrated by Fig. 6.6. This agreement is expected since the orbit topology has very little influence on particles (either co- or counter-passing) that are well away from the trapping boundary. The slight difference in the measured spectra as the particle energy increases is probably due to orbit effects. As discussed in Chapter 4, the co-passing and counter-passing orbits in ATF are typically concentric circles that are shifted slightly outside or inside the magnetic axis of ATF, respectively. Since the NPA is located on the outboard side of ATF, the NPA theoretically should measure more flux originating from co-passing particles than from counter-passing particles, resulting in a slightly higher flux. Since the magnitude of the shift of the passing orbits is proportional to the energy of the particle, the difference in the measured spectra increases as the particle energy increases.

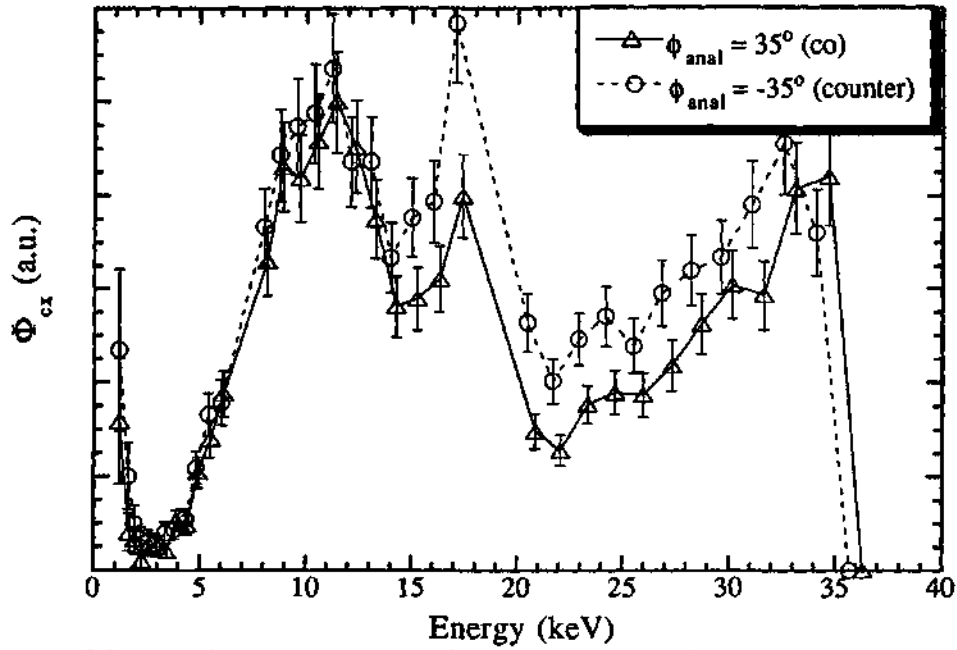


Figure 6.6: Measured energy spectra for co-passing and counter-passing particles during an ultralow-density discharge.

Measurements of the perpendicular ($\phi_{\text{anal}} = 0^\circ$) slowing-down distribution were also taken by the NPA during this set of discharges. The evolution of the measured energy distribution is shown in Fig. 6.7. As in the tangential case, the measured spectra reach equilibrium in approximately 50 msec and then remain constant for the remainder of the discharge. The “hole” in the spectra below 4 keV (or “bump” at 6 keV) is intriguing, since such a distribution is not expected from collisional slowing-down arguments. The possible causes of this feature are discussed in Section 6.2.3.

6.2.3 Analysis and Discussion

As mentioned in Section 6.2.2, several intriguing features are apparent in these data. To develop a better understanding of the physical mechanisms causing these features, theoretical spectra based on the fast-ion Fokker-Planck equation [Eq. (2.64)] have been calculated using the FPACX simulation code (described in

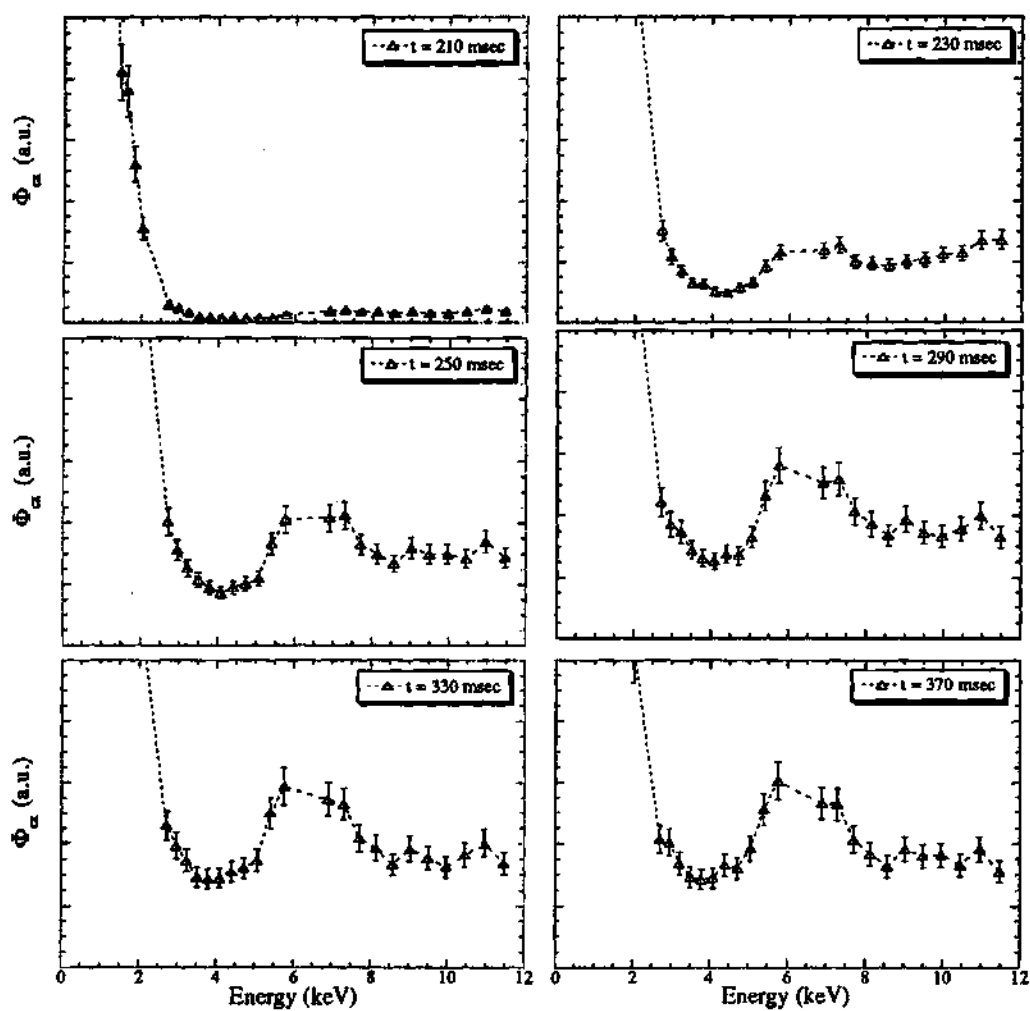


Figure 6.7: Energy spectra measured by the NPA at various times when viewing perpendicularly ($\phi_{\text{anal}} = 0^\circ$) during ultralow-density discharge.

detail in Appendix B). This code computes the theoretical spectra in four steps. From the available experimental data, the code first calculates the fast-ion source distribution [S in Eq. (2.64)], which is determined by where in real and velocity space the injected neutrals are ionized. Second, a self-consistent neutral density profile is computed using a neutrals transport code. Third, the energetic ion distribution is computed on each of 50 different radial mesh locations. Finally, the charge-exchange flux is integrated along the analyzer sightline using the calculated energetic-ion distribution function and neutral density profile as well as other experimental inputs.

To simulate the experiment as much as possible, input parameters to the code are based on experimentally measured values. The electron temperature and density profiles were measured at several different times during the discharge by Thomson scattering. The temporal evolution of the central electron temperature was monitored by the central channel of a 16-channel ECE diagnostic. The central ion temperature is provided from either NPA measurements or Doppler broadening of central impurity lines.

The most critical unknown in this simulation is the neutral density profile. Since all of the other information necessary for this simulation is available from experimental measurements, the parameters that determine the magnitude and shape of the neutral density profile (namely, the global particle confinement time τ_p and the average neutral edge energy E_{edge}) can be left as variable inputs to the code. These parameters are then adjusted on subsequent runs of the code so as to obtain the best match to the measured spectra.

Care must be taken in assuming that the neutral density profile computed in this way is actually representative of the actual profile. This can be understood by exploring the physical processes being modeled. In general, the energy dependence of the ion distribution function results from a competition between the rate at which the injected ions slow down and the rate at which these ions are lost (ei-

ther completely lost from the system by charge-exchange or unconfined orbits or simply scattered out of the region of interest due to pitch angle scattering). Since the parameters governing the slowing-down process (the electron temperature and density and Z_{eff}) are fairly well known from experimental data, the rate at which the injected ions slow down and pitch-angle scatter can be computed quite accurately. However, the fast-ion loss rate is a combination of effects (charge-exchange loss, unconfined particle orbits, anomalous effects) that are difficult to quantify from experimental data. Of these losses, the charge-exchange loss is generally considered to be predominant and is the only effect included in the fast-ion Fokker-Planck equation [Eq. (2.64)]. A more rigorous form of this equation results if the term $-f/\tau_{\text{cx}}$ is replaced by $-f/\tau_{\text{loss}}$, where τ_{loss} is the characteristic loss time given by

$$\frac{1}{\tau_{\text{loss}}} = \frac{1}{\tau_{\text{cx}}} + \frac{1}{\tau_{\text{anom}}}. \quad (6.1)$$

Here, τ_{anom} represents the characteristic loss time due to orbit effects and anomalous effects.

Physically, the shape of the measured spectra is determined by this combination of losses. Hence, the theoretical spectra that provide the best match should theoretically be represented by τ_{loss} instead of τ_{cx} . There are two ways to handle this from a computational point of view. The first approach is to develop separate expressions for τ_{cx} and τ_{anom} and separately adjust these in trying to obtain the best match to the measured spectra. Since τ_{cx} and τ_{anom} are difficult to quantify from experimental data, independently adjusting these quantities to obtain the best match would be extraordinarily difficult. The second approach is simply to estimate the form of τ_{loss} and adjust the magnitude to obtain the best match to the measured spectra. This is the method used here. Because, in general, the dominant loss mechanism is due to charge-exchange, the form of τ_{loss} is chosen to be similar to that of τ_{cx} . In cases where charge-exchange is in fact dominant and other effects are negligible, this method provides a good estimate of the neutral density profile. However,

if the anomalous effects are not negligible, the neutral density profile computed by this method may not be representative of the actual profile.

The agreement between the theoretical spectra calculated by FPACX and the measured data in this case is quite good, as is evidenced by Fig. 6.8. The theoretical spectra shown here were obtained using input parameters of $\tau_p = 20$ msec and $E_{\text{edge}} = 5$ eV for the neutral density calculation, which are consistent with those used in Chapter 5. An important consideration in using the NPA-measured spectra to infer information about general fast-ion confinement properties is whether the measured flux is coming mainly from the central regions of the plasma or from the edge. Because of the chord-integrated nature of the measurement, the measured flux could be dominated by contributions from near the edge of the plasma. As a by-product of the FPACX simulation, the contribution of each differential segment along the NPA viewing chord to the total measured flux for a particular energy can be computed. The variation of the contribution along the NPA sightline for $E = 20$ keV is shown in Fig. 6.9. Therefore, the measured flux results predominantly from charge-exchange events occurring in the central regions of the plasma. Hence, the energy spectrum measured by the NPA is indeed indicative of the fast-ion distribution function in the center of the plasma.

The characteristic fast-ion slowing-down time τ_s [defined by Eq. (2.70)] in this case is approximately 80 msec, while the charge-exchange loss time τ_{cx} [defined by Eq. (2.68)] is on the order of 10 msec. Hence, the probability of an ion completely thermalizing is very small. In fact, only a very small fraction of the full-energy particles thermalize before being lost from the plasma because of charge-exchange. Since the injected ions tend to charge-exchange long before they thermalize, the amount of injected beam power actually absorbed by the plasma is quite small. To quantify this assertion, Eqs. (2.98)-(2.100) were used to compute the amount of beam power delivered to the electron and ions and the amount of beam power

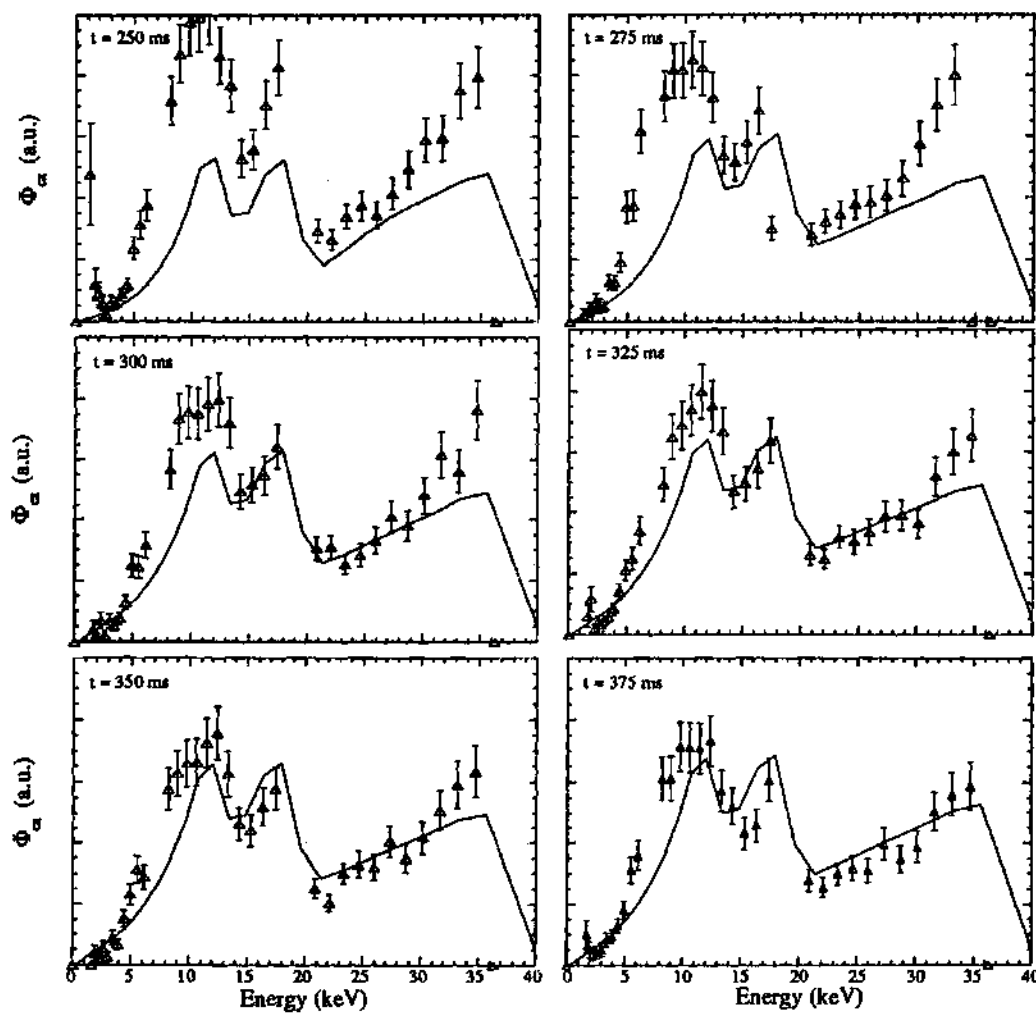


Figure 6.8: Comparison of the theoretical spectra computed by FPACX (solid line) and the measured data (Δ) at several different times in an ultralow-density discharge.

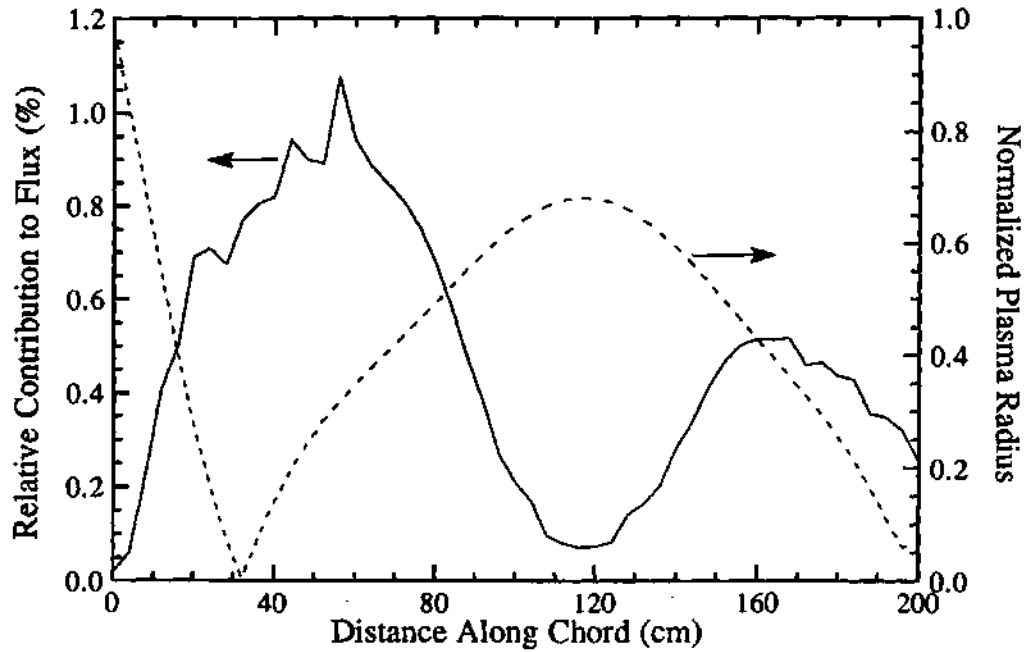


Figure 6.9: Relative contribution to measured flux for $E = 20$ keV of each differential segment along the NPA viewing chord in an ultralow-density discharge along with the normalized radius corresponding to the location in the plasma of each differential segment. The plasma center is at $\rho = 0$.

lost through charge-exchange. This is done by numerically computing the integrals in Eqs. (2.98)–(2.100) at each radial mesh location using the fast-ion distribution function computed for each mesh location by FPACX. The total power associated with each process can then be computed by simply performing a volume integral.

The result of this calculation for this case is shown in Fig. 6.10. The shine-through loss in this figure is defined as the amount of power that is lost because of incomplete ionization of the beam as it passes through the plasma. In low-density discharges, this effect can be large since the mean free path against ionization of the incoming beam is inversely proportional to the plasma density. This term is generally calculated from the formula

$$P_{\text{shine}} = P_{\text{input}} \left(1 - \int H(\rho) d\rho \right), \quad (6.2)$$

where $H(\rho)$ is the normalized beam deposition profile derived in Appendix B and P_{input} is the injected neutral beam power. Evident from this figure is the fact that

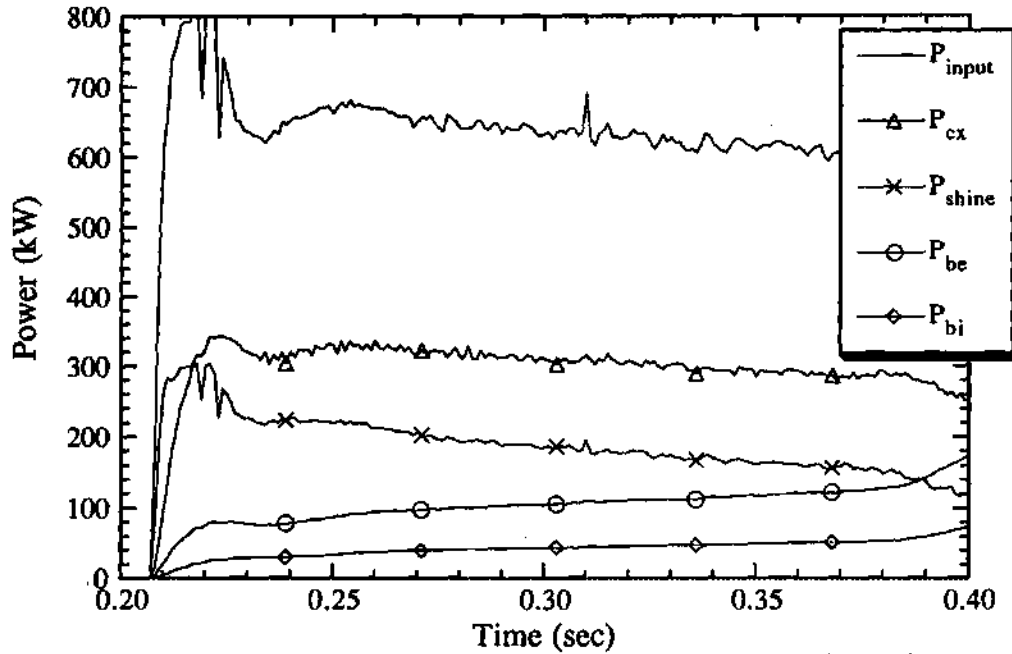


Figure 6.10: Time dependence of the amount of injected power (P_{input}), power loss through charge-exchange (P_{cx}), power loss through shine-through (P_{shine}), power absorbed by the electrons (P_{be}), and power absorbed by the ions (P_{bi}) in a typical ultralow-density discharge.

only about 20% of the injected beam power is actually absorbed by the plasma (i.e., $P_{\text{be}} + P_{\text{bi}} \simeq 0.2P_{\text{input}}$). Hence, ECH (which provides approximately 400 kW) is the primary heating mechanism in this case.

To study the effects that this reduced coupling has on global plasma properties, the PROCTR transport analysis code has been used to model the plasma evolution during these discharges. The physics models used in PROCTR are described in detail in Ref. 1. For the purposes here, PROCTR was used to predict the evolution of various plasma parameters by solving the ion, electron, and neutral transport equations self-consistently in the full 3-D ATF geometry using experimental data as benchmarks.

The first step in this modeling effort was to choose the models to use for the electron and ion heat thermal diffusion coefficients and particle source rates. To simulate the discharge as much as possible, various experimental inputs were used to

force the simulation to follow the evolution of certain parameters of the discharge. The main experimental "feedback" used in this calculation was the electron line density measured by a 2-mm interferometer. PROCTR has several options by which the simulated electron line density can be adjusted to evolve in the same manner as the measured electron line density. The magnitude of the electron line density (assuming a fixed profile) is generally dependent on three factors: (1) the amount of gas injected for fueling purposes, (2) the degree to which particles exiting the plasma are reflected back into the plasma (known as recycling), and (3) the magnitude of the particle diffusivity coefficient D_e . The only factor whose effect can be quantified from experimental data is the amount of gas injected for fueling purposes. For the simulation to be discussed here, the method chosen for "feedback" control was to allow the recycling rate to vary during the discharge such that the simulated electron line density was maintained at the same level as the measured data. The motivation for this choice was touched upon earlier in this section. Because of the extensive titanium gettering required to obtain this type of discharge, it was envisioned that the recycling coefficient was lower than during normal operation of ATF. Also, the recycling coefficient probably changed substantially as NBI was applied because of the high amount of shine-through beam power incident on the wall during injection. Allowing the recycling coefficient to vary in the simulation allowed an assessment of these hypotheses.

The form of the electron thermal diffusion coefficient χ_e was chosen to be anomalous for this simulation with the magnitude and profile adjusted such that the predicted electron temperature profile was similar to the electron temperature profile measured by Thomson scattering. This approach is necessary because the electron thermal conductivity is in general anomalously high compared to neoclassical theory and therefore difficult to quantify computationally. The χ_e profile is held constant throughout the discharge. The electron particle diffusivity D_e was taken to be $0.2\chi_e$,

which is consistent with measurements made during ECH on ATF. To produce the flat and sometimes hollow electron density profiles measured by Thomson scattering, an anomalous outward convective term was also required in the density equation. The magnitude of this term was adjusted such that the measured density profiles were reproduced in the simulation. Neoclassical heat transport, including transport due to the helical ripple,² was assumed for the ions. The effect of impurities on the plasma evolution was neglected in this model.

The neutral density profile was self-consistently calculated using a cylindrical neutrals transport model.³ The neutral source rate at the edge is determined in PROCTR at each time step from the amount of recycling and external gas fueling. Volumetric neutral sources, such as those due to neutral beam ionization via charge-exchange or electron-ion recombination, are not taken into account in this model. Although the source rate due to electron-ion recombination is expected to be small in this low-density plasma, some explanation is required for neglecting the neutral source due to beam ionization via charge-exchange, since this effect could conceivably be quite large. Estimates of the total fueling rate by the beams in ATF are on the order of 0.6 torr-L/sec per 100 kW of deposited power ($P_{\text{input}} - P_{\text{shine}}$).⁴ Since in this case the amount of deposited power is only 450 kW, the fueling rate is fairly small (~ 2.7 torr-L/sec) compared to the fueling rate from recycling and external gas fueling (~ 50 torr-L/sec). As in Chapter 5, the average edge neutral energy is assumed to be 5 eV.

The heating profile resulting from ECH was approximated by a linear-absorption, multi-reflection model for second-harmonic heating.⁵ In this model the shape of the absorption profile is assumed to be proportional to the product of the local electron density and temperature. The waves are assumed to pass multiple times through the plasma (being reflected from the vacuum vessel wall after each pass) before being completely absorbed. On each pass, a fraction of the power is

assumed to be absorbed by the plasma and by the wall. The fraction of incident power absorbed by the plasma f_{abs} can be obtained from the formula

$$f_{\text{abs}} = F_1 + \frac{F_p(1 - F_w)(1 - F_1)}{1 - (1 - F_w)(1 - F_p)}, \quad (6.3)$$

where F_1 is the fraction of the wave power absorbed on the first pass through the plasma, F_p is the fraction absorbed on subsequent passes after reflection from the wall, and F_w is the fraction absorbed by the wall on each reflection. The quantities F_1 and F_p have been estimated using a ray-tracing code.⁵ The loss to the wall at each bounce of the wave is due to the finite resistivity of the stainless steel walls in ATF and to power lost to wall sections not covered with steel (i.e., ports). An estimate has been made⁶ that 2% of the microwave power is lost per bounce ($F_w = 0.02$). This estimate is based on approximately 1% of the ATF vacuum chamber wall being hole area and 1% loss per bounce in the stainless steel.

The heating resulting from NBI has been handled in a manner similar to the calculation used in FPACX. The fast-ion distribution is solved at 10 radial mesh points using FIFPC.⁷ The amount of power absorbed by the plasma is again calculated using Eqs. (2.98)–(2.100).

The results of this simulation are shown in Figs. 6.11–6.13, where the simulated electron line density, plasma stored energy, and central electron temperature are compared to the corresponding measured values. The agreement in the electron line density is expected since the code uses the measured data for feedback control of the density in the simulation. The apparent discrepancy in the simulated electron temperature from the measured data during the ECH portion of the discharge is probably due to the effect of nonthermal electrons. The presence of these nonthermal electrons (whose population increases as the plasma density decreases) distorts the temperature inferred from measurements of the ECE emission since when third-harmonic emission is measured, the ECE signal varies as $n_e T_e^3$.

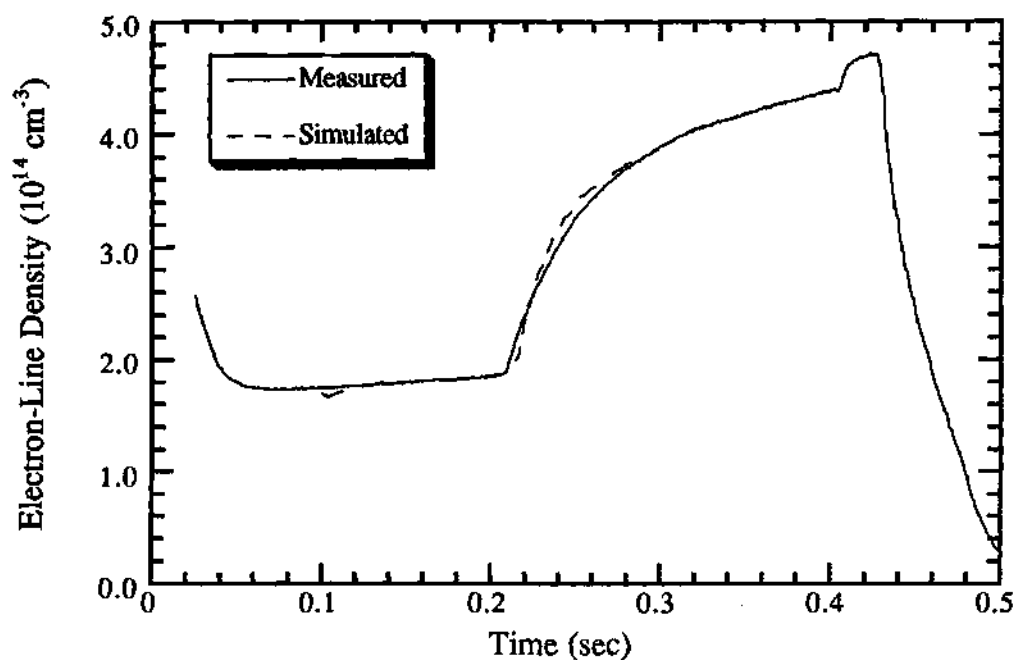


Figure 6.11: PROCTR simulation of the electron line density in a typical ultralow-density discharge.

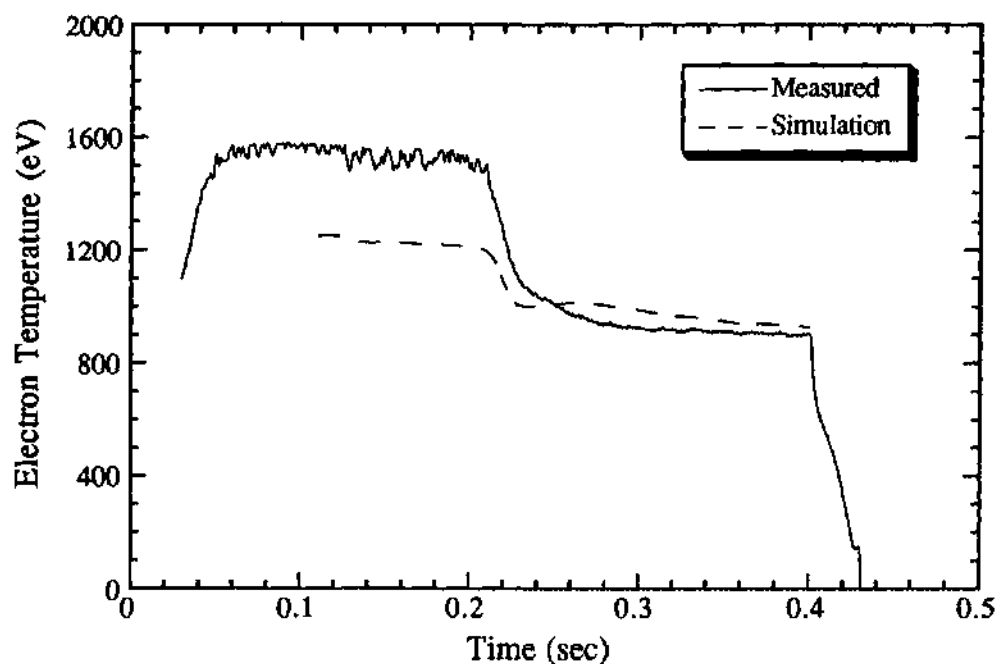


Figure 6.12: The simulated central electron temperature (dashed line) and the central electron temperature measured by ECE (solid line) in a typical ultralow-density discharge.

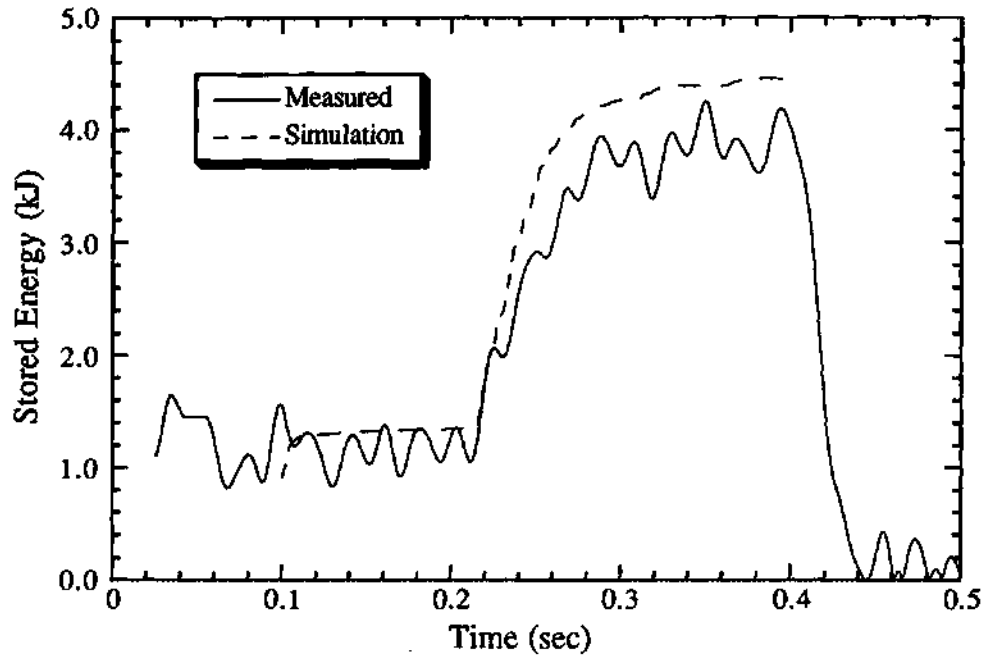


Figure 6.13: The simulated plasma stored energy (dashed line) and the stored energy measured by a diamagnetic loop (solid line) for a typical ultralow-density discharge.

Hence, any nonthermal tail present in the electron distribution (characterized by $T_{\text{tail}} \gg T_e$) tends to enhance the emission seen by the ECE system, and thus the inferred temperature will be artificially high.

The plasma stored energy is measured experimentally by a diamagnetic loop, which responds to perpendicular pressure within the plasma. In the case of NBI, this perpendicular pressure is made up of two parts: the thermal plasma pressure $[\frac{3}{2}(n_e T_e + n_i T_i)]$ and the perpendicular pressure exerted by the beam [given by Eq. (2.103)]. The amount of pressure due to the beam can be significant in some cases, especially with perpendicular injection. In this case, calculations indicate that the beam contributes only about 10% of the total stored energy. This result is expected since the beam ions are injected tangentially in ATF, and because of the large charge-exchange losses, are lost well before many of them have substantial perpendicular energy.

One aspect that has not been yet been addressed in this modeling is the

effect of the loss region on the thermalization of the injected ions. As discussed in Chapter 4, the loss region in ATF is confined to a region in velocity space near perpendicular. Since the injected ions in this case are lost well before they have pitch-angle scattered enough to reach this region in velocity space, the effect of the loss region should be negligible. However, various measurements suggest that the loss region may contribute a small amount to the total beam power loss. For example, the slight discrepancy between the simulated and measured stored energy in Fig. 6.13 may be due to the neglect of the loss region in the simulation.

The measured spectra shown in Fig. 6.7 provide further proof that the slowing-down distribution is affected by the loss regions. From classical slowing-down arguments, one would expect the thermal distribution (energies less than 3 keV) to merge smoothly with the energetic-ion distribution. This is clearly not the case in Fig. 6.7, where the measured spectra exhibit either a "hole" near 4 keV or a "bump" near 6 keV. Similar spectra have been obtained during operation at $B_0 = 1.9$ T, indicating that the measured effect is not dependent on the magnetic field. Since possible mechanisms that could cause an enhancement in confinement at 6 keV are not known, it will be assumed that the measured spectra are due to a deterioration in confinement of 4-keV particles.

This "hole" is likely due to an effect associated with the radial electric field. As discussed in Section 4.3, the radial electric field plays an important role in the confinement of low-energy helically trapped ions. If the electric field is of the right magnitude to cancel the ∇B drift due to the helical windings, the helically trapped ion will drift vertically out of the device due to the uncompensated toroidal curvature drift. This effect has a resonant feature in energy since the ∇B drift is a function of particle energy and the $\vec{E} \times \vec{B}$ drift is not. As discussed in Section 4.3, the energy at which this resonance occurs in ATF is approximately $4.0e|\Phi_0|$ where Φ_0 is the magnitude of the central electrostatic potential. For this so-called helical resonance

to occur, Φ_0 must be negative. Typical electrostatic potential profiles measured by a heavy-ion beam probe⁸ in ATF during ECH indicate that the potential decreases in a linear fashion in the region between $\rho = 0.2$ and $\rho = 0.8$ with $\Phi(\rho = 0.2) = +300 (\pm 100)$ V and is relatively flat for $\rho > 0.8$. Since the measured potential is positive, the helical resonance should not occur in ECH plasmas in ATF. There is experimental evidence from both Wendelstein WVII-A and Heliotron-E that the potential does become negative during NBI.^{9,10} However, since both of these devices use perpendicular injection where large, direct ion losses are expected, it is not obvious that these results are applicable to ATF where tangential injection is used. More recent results from CHS using tangential neutral beam injection also have shown that the radial electric field is directed inward (indicating a negative central potential).¹¹ These measurements suggest that the helical resonance is the likely source of the measured spectra. Unfortunately, potential measurements are currently not available during NBI on ATF. Therefore, a definite conclusion as to whether the helical resonance is the cause of the measured spectra cannot be made at this time.

Another possible explanation of the observed spectra can be obtained by exploring the motion of the particle as it changes state from a passing particle to a trapped particle. As discussed in Section 4.4, when a particle undergoes this transition, the orbit topology is such that the particle is on a helically trapped orbit that carries it out near the edge of the plasma. Since the edge neutral density is extremely high, there exists a high probability that the particle is lost due to charge-exchange. If this scenario is correct, the energy at which the particle enters the trapping region should correspond to the energy at which the "holes" are seen in Fig. 6.7.

Naively, one would think that this energy would be the critical energy [defined by Eq. (2.65)] since the pitch-angle scattering term is dominant below this

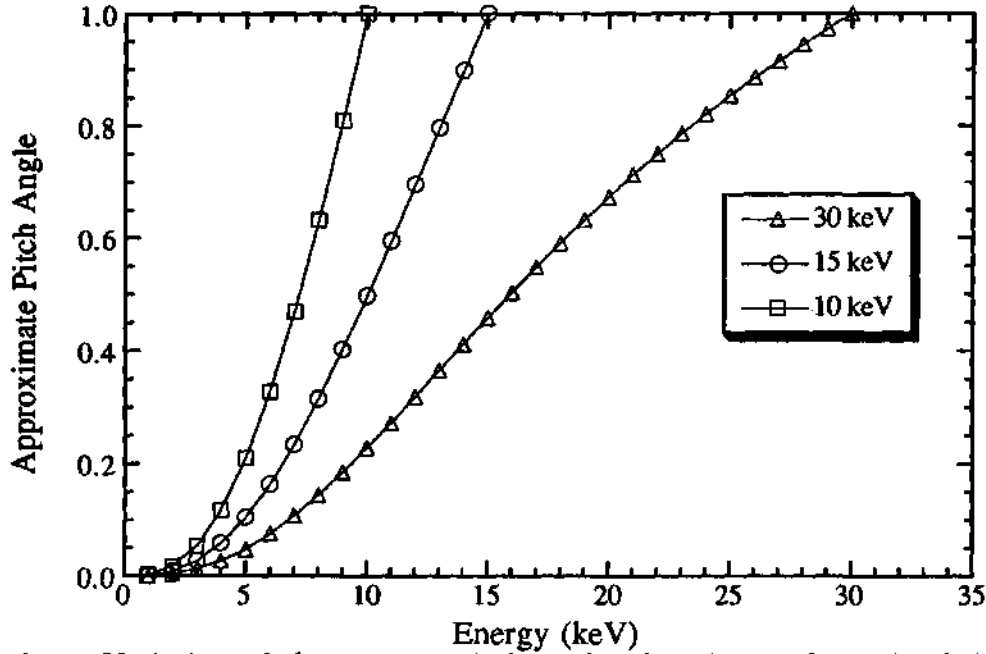


Figure 6.14: Variation of the average pitch angle of an injected ion (with initial energy given by E_{inj} , $E_{inj}/2$, and $E_{inj}/3$ as it slows down in an ultralow-density plasma. For this calculation, the parameters $Z_{eff} = 3.0$, $\xi_i = 1.0$, and $E_{crit} = 15$ keV are used.

energy. However, this is not necessarily the case. The average change in pitch angle as the particle slows down can be calculated from Eq. (2.83). The results of this calculation for the three energy components assuming that $Z_{eff} = 3.0$, $\xi_i = 1.0$, and $E_{crit} = 15$ keV are shown in Fig. 6.14. Since orbit calculations indicate that the approximate location of the trapping boundary in the center of the plasma is at $\xi = 0.1$ (see Fig. 4.2), the one-half and one-third energy particles, on average, reach the trapping boundary at an energy near 5 keV — consistent with the “holes” seen in the measured spectra. The full-energy particles reach the trapping boundary at a much higher energy, but in this case the number of these particles has already been significantly reduced by charge-exchange. This suggests that the observed “holes” could be due to the lack of confinement of the injected ions as they become helically trapped.

From the above results, it is apparent that this type of discharge is mainly supported by ECH with small additional heating provided by NBI. Maintaining the

electron density below the ECH cutoff density is therefore imperative for successful operation in this regime. The relatively high ion temperature attained in this regime ($T_{i0} \simeq 400$ eV) is mainly due to beam heating of the ions, although some of the increase results from the increased ion-electron coupling caused by the slightly higher electron density. Similar experiments have been performed with $B_0 = 1.9$ T, but the operating mode has not yet been refined enough to avoid thermal collapses. However, transient ion temperatures on the order of 1 keV have been measured in these discharges.

6.3 NBI Studies in Low-Density Plasmas

The NBI operating regime with which there is the most experience on ATF is at low density ($\bar{n}_e \leq 5 \times 10^{13} \text{ cm}^{-3}$). Consequently, the amount of data available for data analysis purposes is considerable. Various studies of these discharges have been conducted at 0.95 T and 1.90 T as well as using co-, counter-, and balanced injection. The data to be presented here represent measurements taken during a set of extremely reproducible discharges in January 1990 and are part of ATF sequence 90011701. For this set of discharges, only a single neutral beam is used (NB 2 injecting in the co- direction) and the on-axis magnetic field is 0.95 T.

6.3.1 Experimental Setup

The evolution of the average line density, the plasma stored energy from a saddle loop, the central electron temperature from ECE measurements, and the ion temperature from spectroscopic measurements for a typical discharge of this type are shown in Fig. 6.15. The target plasma is created by 400 kW of 53-GHz ECH power and is subsequently heated starting at 250 msec by approximately 520 kW of co-injected neutral beam power. The plasma density increases nearly linearly

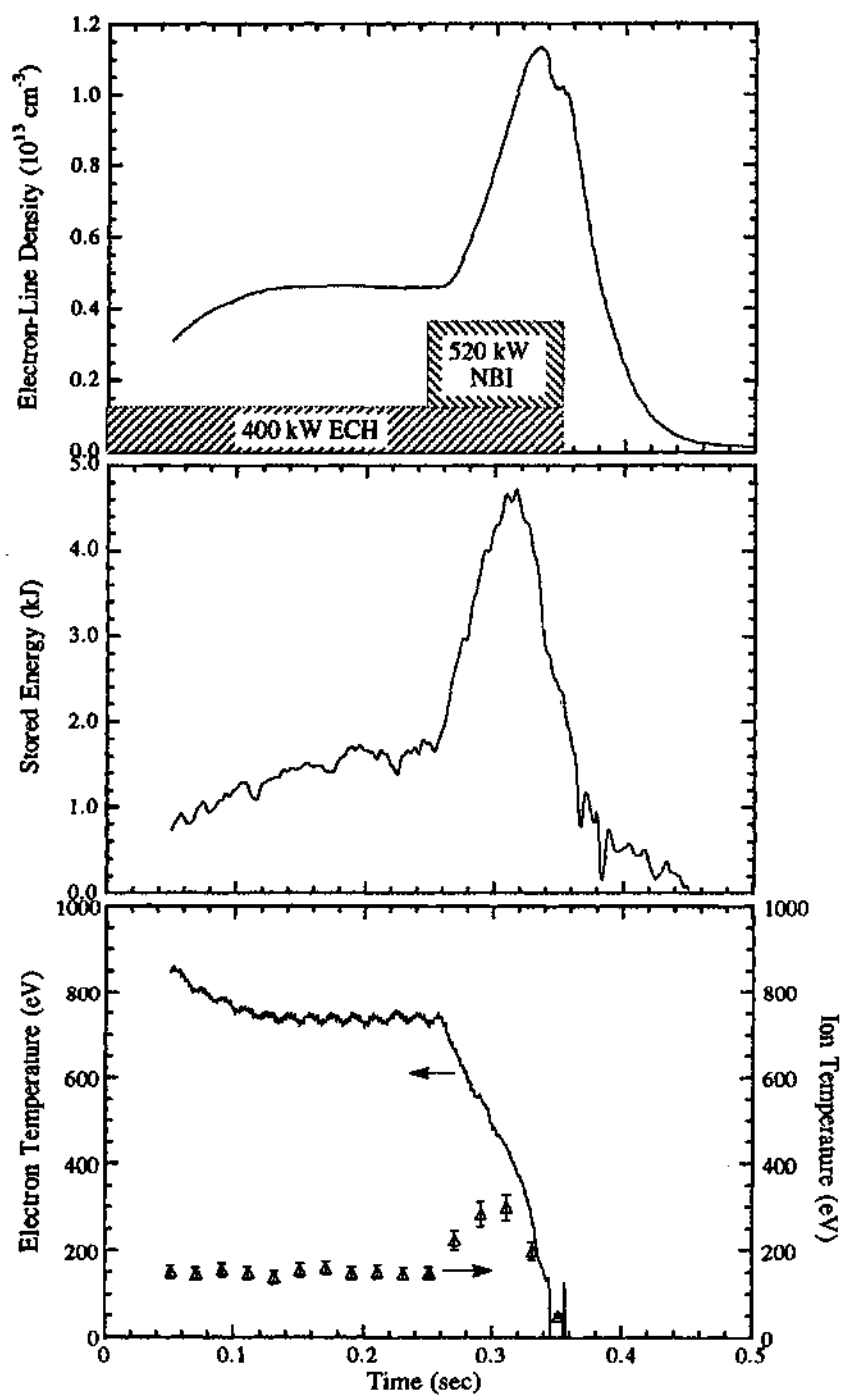


Figure 6.15: Time evolution of various parameters for a typical low-density discharge in ATF.

from the value obtained in the ECH phase of the discharge. This increase results from a combination of beam fueling and external gas fueling. At the same time, the stored energy increases while electron temperature monotonically decreases from its ECH value (after a small initial rise in some discharges). The stored energy attains a maximum at 315 msec and thereafter rapidly decreases. About 20 msec later, when the plasma has cooled enough that it is not fueled efficiently by the recycling hydrogen, the electron density begins to decline also. The measured ion temperature increases at the onset of NBI until about 320 msec when it begins to decrease in a fashion similar to the electron temperature. The plasma Z_{eff} during the discharge was approximately 4.0 during the ECH phase and decreased to 2.5 near the time of collapse, principally due to the large influx of hydrogen gas associated with NBI.

As mentioned previously, these discharges were extremely reproducible. A sequence of 40 discharges was taken during the particular sequence studied here with the last discharge having approximately the same measured properties as the first discharge. This reproducibility allowed detailed studies of the fast-ion distribution function using the scannable NPA. A complete angular scan of the NPA was made by moving the analyzer between successive discharges.

6.3.2 Experimental Results

The evolution of the typical tangential slowing-down distribution as measured by the NPA during these discharges is shown in Fig. 6.16. These data were taken at an analyzer angle ($\phi_{anal} = 47.5^\circ$) that roughly corresponds to the beam tangency radius. The sharp peaks in the spectra measured at 260 msec are characteristic signatures of the ion distribution at the onset of NBI in ATF. These peaks are expected since the fast-ion slowing-down time at the beginning of injection is on the order of 120 msec and this measurement was taken only 3–5 msec after injection began. Since the injected particles have not had enough time to slow appreciably,

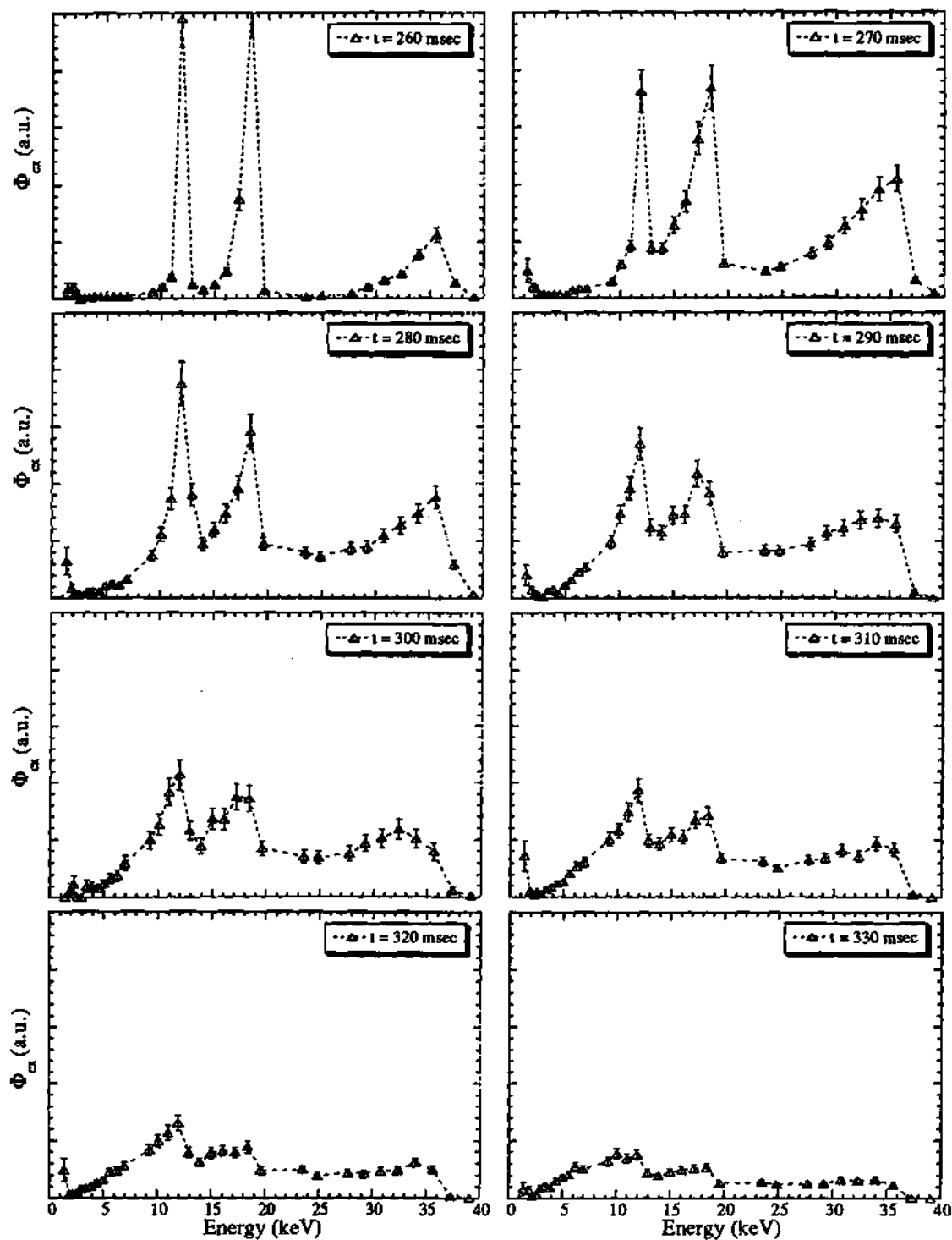


Figure 6.16: Tangential energy spectra measured by the NPA at various times during a typical low-density NBI discharge. The vertical scale is the same for each graph.

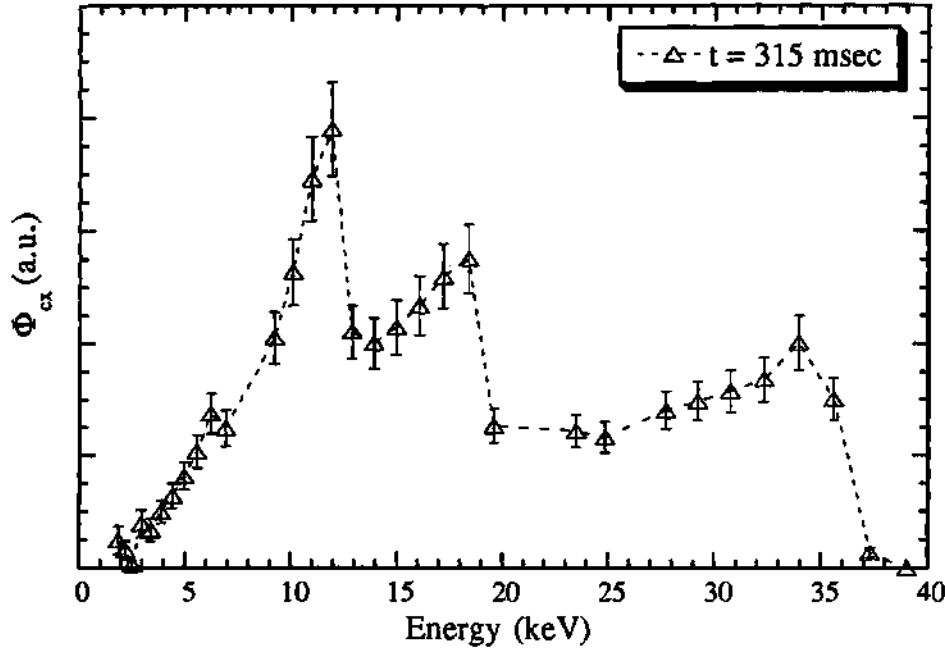


Figure 6.17: Tangential energy spectra measured by the NPA near the time of collapse during a typical low-density NBI discharge.

the distribution function is peaked around the three energy components of the beam. The gradual spreading of these peaks results from the changing plasma conditions that tend to reduce the ratio τ_s/τ_{ex} . The magnitude of the measured flux also gradually decreases as the plasma conditions change, indicating that the magnitude of the charge-exchange loss is decreasing during the discharge. However, as illustrated by Fig. 6.17, the spectrum measured at the time of the collapse ($t = 315$ msec) still exhibits substantial declines for energies below the energy components of the beam. This data suggests that the confinement of the energetic ions is not very good even at the time of the collapse.

Extensive measurements have also been made of the dependence of the measured spectra on the viewing orientation of the NPA. The spectra measured near the time of the collapse ($t = 315$ msec) at several different angles ranging from near perpendicular ($\phi_{anal} = 20^\circ$) to tangential ($\phi_{anal} = 45^\circ$) are shown in Fig. 6.18. As in the ultralow-density case, the magnitude of the measured flux decreased as the

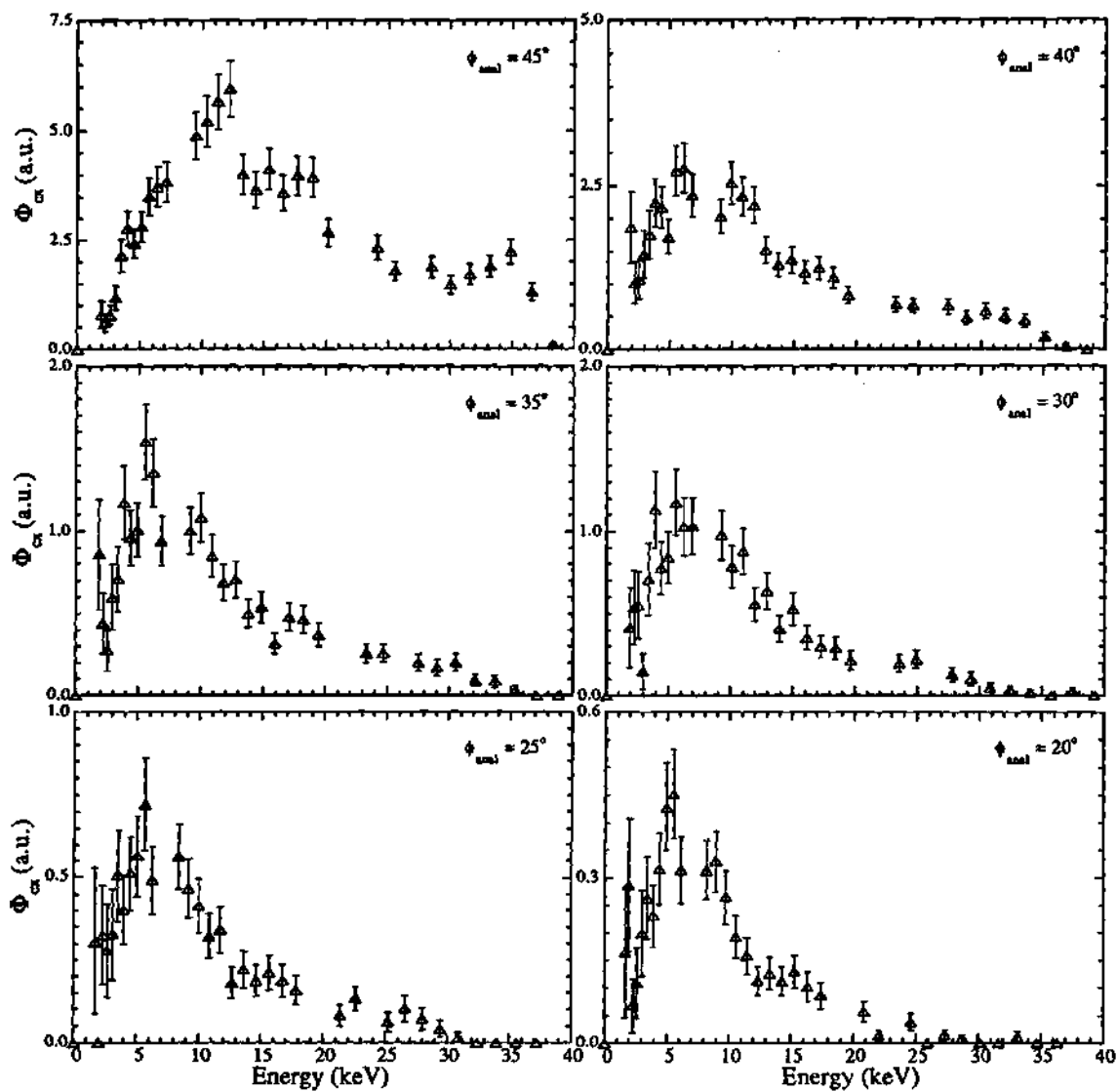


Figure 6.18: Energy spectra measured near the time of the collapse at various NPA viewing angles during a typical low-density NBI discharge.

analyzer angle was moved away from tangential. The absence of the peaks in the off-tangential spectra is expected since the ions are injected tangentially and must undergo substantial pitch-angle scattering to be seen by the NPA at these angles.

6.3.3 Analysis and Discussion

The FPACX code was again used to simulate the measured spectra in a manner similar to the analysis of the ultralow-density case. However, because of the extensive data set available for this type of discharge, a more extensive modeling effort was put forth. The main thrust of this effort involved attempting to simulate simultaneously the measured spectra from several different NPA viewing angles. The comparisons to be presented here represent the case that produced the best overall match between the simulated spectra and the measured spectra for several different analyzer viewing angles.

Because of the transient behavior of this type of discharge, measurements of the temporal evolution of the electron temperature and density profiles are crucial to the modeling. Unfortunately, the Thomson scattering diagnostic installed on ATF can only obtain these profiles at a single time during a discharge. However, since this experiment involved a long sequence of reproducible discharges, the Thomson scattering laser firing time was adjusted between successive discharges such that electron temperature and density profiles could be obtained for as many times as possible. For times intermediate to the Thomson scattering laser firing times, FPACX assumes that the profile is fixed, with the time dependence of the central electron temperature obtained from ECE measurements. Although this method is not precise, the associated error in calculating the measured spectra is negligible compared to other sources of error such as the neutral density profile calculation.

As in the ultralow-density case, the agreement between the simulation and measured data for the tangential viewing case ($\phi_{\text{anal}} = 45^\circ$) is quite good for times

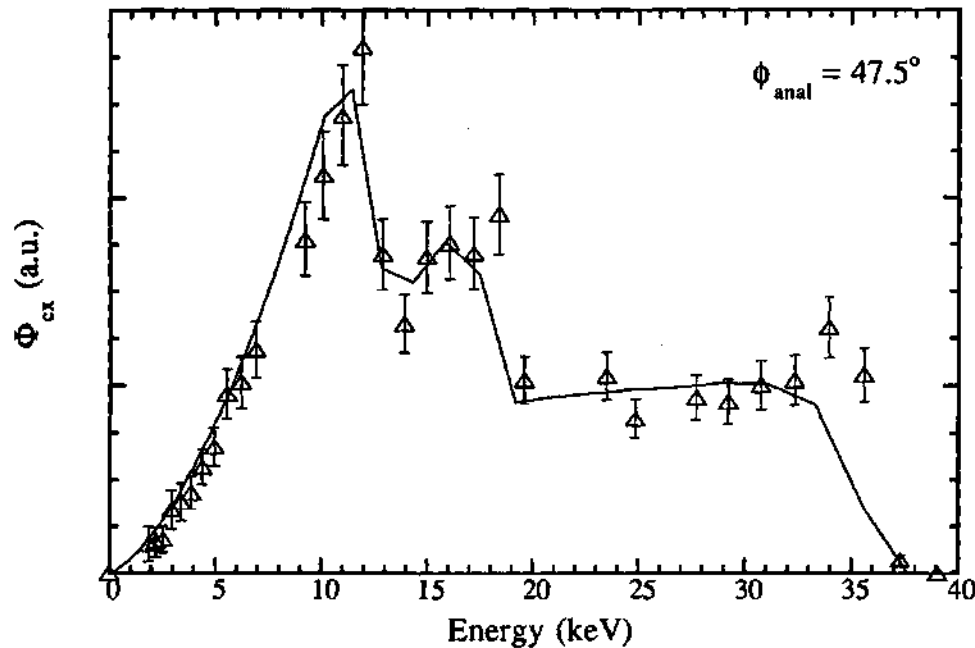


Figure 6.19: Comparison of the theoretical spectra computed by FPACX (solid line) and the measured data (Δ) near the time of collapse in a low-density discharge.

well after the onset of NBI as illustrated by Fig. 6.19. The measured spectrum shown here was taken near the time of the collapse in the stored energy — almost 70 msec after the beginning of NBI.

The agreement is not quite as good for times shortly after injection begins, as illustrated in Fig 6.20, where the simulated and measured spectra are compared for several different times. This discrepancy is probably due to inaccurate modeling of the fast-ion source function. The first source of error results from improper modeling of the form of the source function due to computational requirements. In reality, the energy distribution of the injected neutrals is basically three delta functions at energies E_{inj} , $E_{inj}/2$, and $E_{inj}/3$. As discussed in Appendix B, the form used to model the energy dependence of the source distribution in FPACX is a Gaussian distribution whose characteristic energy width is defined by the user. To properly simulate the delta functions, this width should be as small as possible. However, several runs of the code indicated that there is a limitation on the smallness of

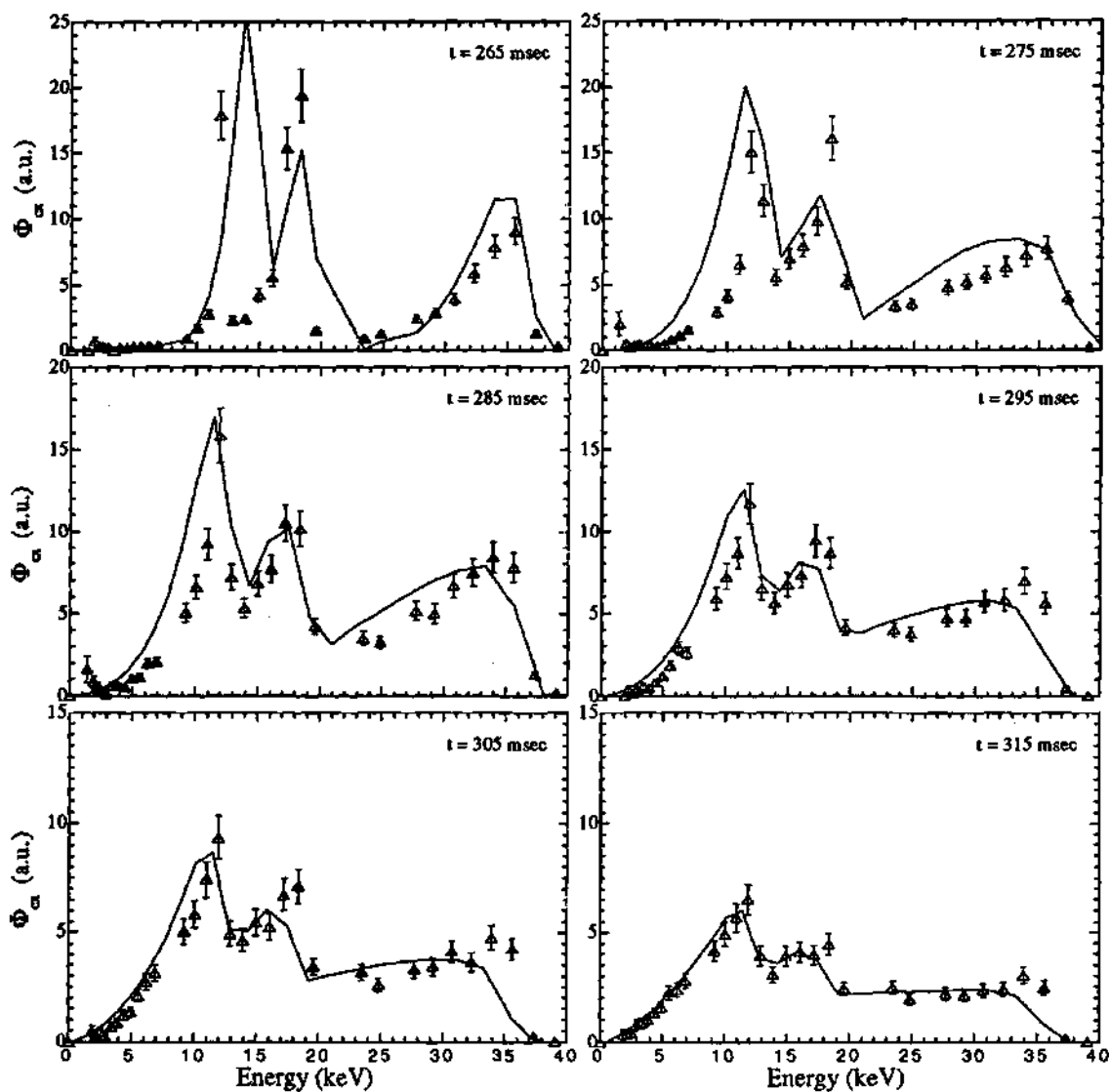


Figure 6.20: Comparison of the theoretical spectra computed by FPACX (solid lines) and the measured data (Δ) for a tangential NPA viewing angle ($\phi_{\text{anal}} \approx 45^\circ$) at several different times in a low-density discharge.

this parameter due to numerical problems. If the specified width is too small, the distribution function around the three peaks is computed inaccurately. For the simulations presented here, the Gaussian width is 3% of the injection velocity. For an injection energy of 35 keV, this results in a FWHM of the modeled distribution of approximately 1.5 keV — clearly not representative of the injected neutrals. The wide peaks in the spectra calculated by FPACX in the early stages of NBI are due to this inaccuracy in the modeling. At later times in the discharge, the distribution is dispersed in energy by interactions with the plasma, and the error associated with the choice of the energy width of the source distribution becomes negligible. The agreement of the simulation with the measured spectra at later times in the discharge supports this claim.

The second problem in computing this source function immediately after the onset of injection is related to the transient nature of the injection process itself. When the injector is turned on, there is a large transient in both the applied voltage V_{beam} and the beam current I_{beam} . The perveance, which governs the maximum beam current that can pass through the beam duct, is dependent on both of these quantities and has the functional dependence $I_{\text{beam}}/V_{\text{beam}}^{3/2}$. To obtain an optimal perveance value, the applied voltage and beam current are generally adjusted independently. During the early phases of injection, the large transients in the beam voltage and current result in improper perveance values, which in turn reduce the output power of the beam. Furthermore, there is experimental evidence that there is a considerable amount of "beam blocking" (reionization of the beam in the beam duct due to a high neutral pressure) during the early phases of NBI in ATF. Beam neutrals that are reionized in this way are deflected out of the beam because of stray magnetic fields from ATF. These energetic ions then collide with walls of the beam duct, generally desorbing neutral gas from the wall in the process. This increases the neutral pressure in the beam duct, resulting in a cascading effect. The magnitude

of this effect is reduced later in the discharge by a reduction of the neutral density in the beam duct.

In ATF, the time dependence of the amount of power actually injected into the plasma cannot be measured experimentally since power calibrations of the beam are carried out by calorimetry techniques. The neutral beam power waveforms stored in the ATF database and used by FPACX are computed using a calibration constant that is averaged over the entire injection pulse length. Because the two problems discussed earlier tend to reduce the beam power in first 50 msec of the beam pulse, the injected power used in FPACX is probably an overestimate in the early phases of the discharge.

Another discrepancy evident in Fig. 6.20 is the different shapes of the simulated and measured spectra at high energies ($E_{inj}/2 \leq E \leq E_{inj}$). This difference is most likely due to inaccuracies in the modeling as a result of the assumption that the injected ions remain on the flux surface on which they were born. In reality, the injected ions have fairly large excursions ($\sim a/3$ at high energy) from their original flux surface. Thus, the ions experience, on average, slightly different plasma conditions from those on their original flux surface. Since the parameter that determines the shape of the spectrum, the ratio of the local charge-exchange time and the local slowing-down time, varies with plasma radius, the calculated shape in the simulation is probably slightly inaccurate, especially at higher energies where the flux surface excursion is the largest.

The simulated spectra also exhibit remarkable agreement with the measured data for a wide range of analyzer viewing positions, as illustrated by Fig. 6.21. This agreement is quite remarkable considering the complicated physical processes that are being modeled. However, this agreement is better understood since the range of velocity space that is being viewed by the NPA (from $v_{||}/v \simeq 1.0$ for $\phi_{anal} = 45^\circ$ to $v_{||}/v \simeq 0.4$ for $\phi_{anal} = 20^\circ$) is well away from the trapping boundary. Because

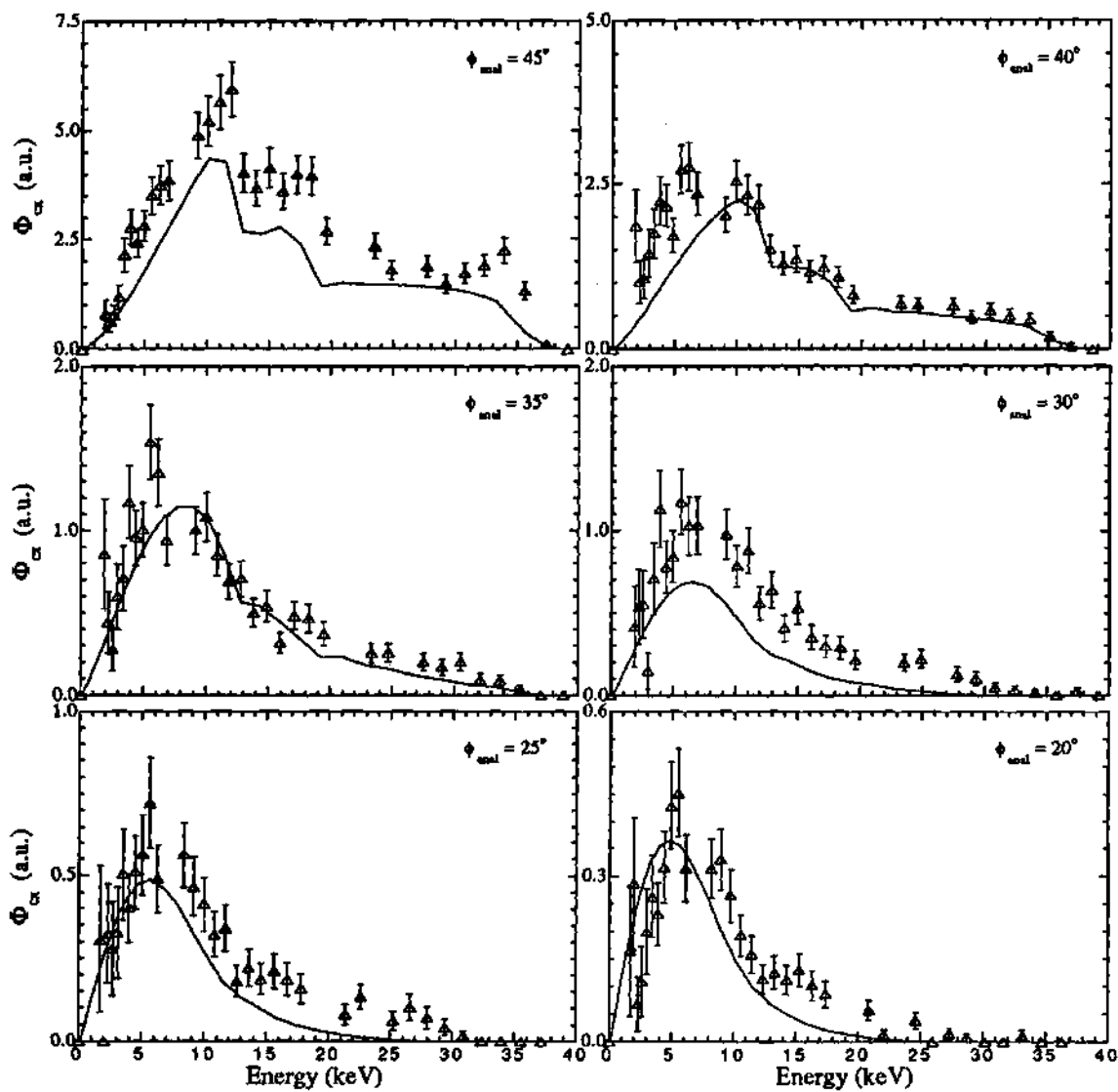


Figure 6.21: The simulated spectra (solid lines) and the measured data (Δ) for several different analyzer viewing angles in a low-density discharge.

the measured ions have not passed through a loss region, the distribution function measured by the NPA at off-tangential angles should simply be governed by CX losses and collisions of the beam ions with the plasma.

The results of this simulation can be used to examine various aspects of the global effects of NBI in this low-density discharge. At the onset of injection, the characteristic slowing-down time and the charge-exchange loss time are similar to their values in the ultralow-density case ($\tau_s \simeq 120$ msec, $\tau_{ex} \simeq 10$ msec). However, by the end of the discharge, the slowing-down time has been reduced to approximately 15 msec, while the charge-exchange time has increased to approximately 35 msec. This trend is due to the substantial increase in the electron density and the substantial decrease in the electron temperature during the discharge. Using Eqs. (2.98)–(2.100) and Eq. (6.2), the beam power lost through the various channels (including absorption) was computed using the fast-ion distribution function that provided the best match to the measured spectra. The result of this calculation is shown in Fig. 6.22. As expected, the power lost via shine-through and charge-exchange decreases continuously during the discharge because of the increasing plasma density. At 270 msec, 80% of the beam power is lost through shine-through and charge-exchange, with only approximately 10% coupled to the electrons. This amount of power is insufficient to maintain the electron temperature at the preinjection value since the electron density has risen over 20%. When the stored energy begins to decrease ($t = 315$ msec), the power lost through charge-exchange and shine-through is still on the order of 60% of the injected power. The remaining 40% of the power is coupled to the plasma but is insufficient to keep the plasma from collapsing.

Similar results were found when using the DESORBS simulation code.¹² The power balance for the three energy components of the beam as well as the total power distribution for a time near the collapse is shown in Table 6.1. These calculations were based on following 32 particles of each energy component. The

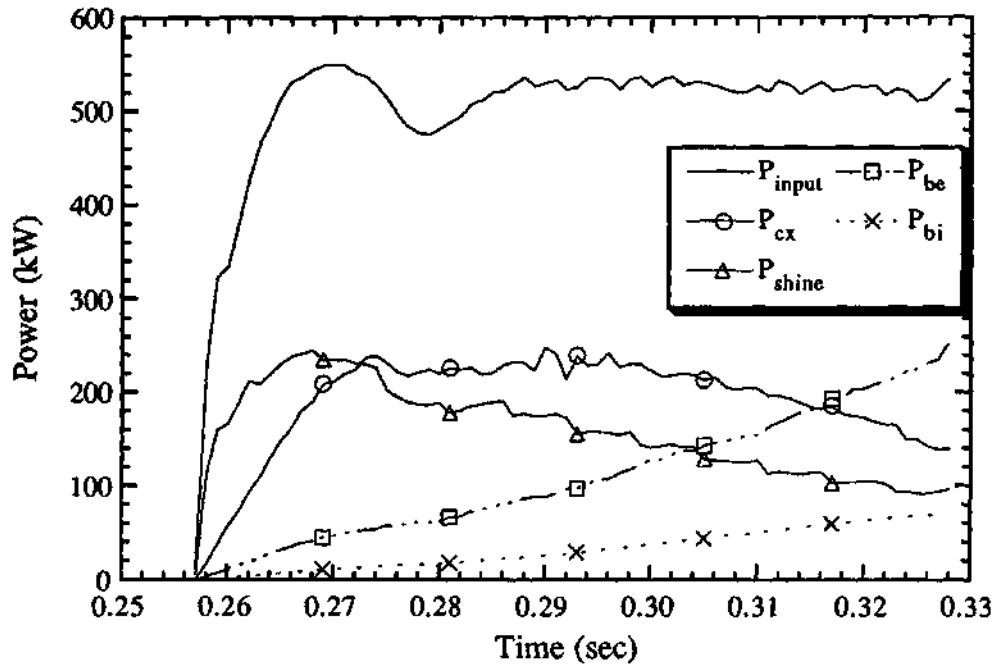


Figure 6.22: Time dependence of the amount of injected power lost through charge-exchange (P_{cx}), lost via shine-through (P_{shine}), absorbed by the electrons (P_{be}), and absorbed by the ions (P_{bi}) in a typical low-density discharge.

particles are followed from their birth (ionization) until they are either lost (i.e., hit the vacuum vessel wall) or reach the energy $3T_i/2$, in which case they are considered thermalized. The total power distribution was then computed by taking into consideration the relative fraction of each energy component in the beam. The ratio of power contained in the E_{inj} , $E_{inj}/2$, and $E_{inj}/3$ components of the beam is assumed to be 60:20:20. As expected, the charge-exchange loss is the dominant loss mechanism for all three components of the beam. Charge-exchange and shine-through losses constitute approximately 50% of the injected beam power at the time of the collapse.

To determine if the reduced absorption of the beam power may be the cause of the thermal collapse, the PROCTR transport analysis code was again used to model the plasma evolution during these discharges. Because of the transient nature of the collapse, the modeling of this discharge proved to be quite difficult, and the physics models chosen to simulate this discharge were generally quite different from

Table 6.1: DESORBS calculation of beam power distribution in a low-density discharge. $Z_{\text{eff}} = 2.0$ is assumed for these calculations.

	Power Distribution (%)			
	E_{inj}	$E_{\text{inj}}/2$	$E_{\text{inj}}/3$	Total
P_{be}	20.9	7.0	5.0	32.9
P_{bi}	5.2	3.7	5.9	14.8
P_{cx}	22.7	7.7	7.0	37.4
P_{shine}	10.0	1.3	0.9	12.2
P_{orbits}	0.6	0.1	0.4	1.1
P_{therm}	0.6	0.2	0.8	1.6

those chosen in the ultralow-density case.

Again, feedback control is used to force the simulated electron line density to match the measured electron line density. However, feedback was accomplished in this case by allowing the external gas source rate to vary such that the simulated electron line density was maintained at the same level as the measured data. The wall recycling coefficient was chosen to be 0.95. As before, neoclassical heat transport including transport due to the helical ripple² is assumed for the ions.

As in the ultralow-density case, the electron thermal diffusion coefficient profile $\chi_e(\rho)$ was chosen to be anomalous. The magnitude and profile were adjusted such that the predicted electron temperature profile was similar to the electron temperature profile measured by Thomson scattering. This adjustment was made for a profile measured during the ECH portion of the discharge. The calculated profile was then held fixed throughout the remainder of the discharge. However, the magnitude of χ_e was scaled according to the global LHD scaling law using the equation

$$\chi_e = \gamma \frac{\bar{a}^2}{4\tau_E^{\text{LHD}}},$$

where γ is a fractional multiplier determined by the magnitude of χ_e during ECH, \bar{a} is the average minor radius, and τ_E^{LHD} is an empirically determined global energy confinement time for stellarators,¹³

$$\tau_E^{\text{LHD}} = 0.17 P^{-0.58} n^{0.69} B^{0.84} \bar{a}^{2.0} R_o^{0.75}.$$

The definitions of the symbols and their units are as follows: energy confinement time τ_E^{LHD} (sec), absorbed power P (MW), average electron density n (10^{20} m^{-3}), magnetic field strength B (T), average minor radius \bar{a} (m), and major radius R_o (m). The motivation for using this type of scaling is that studies have shown that typically χ_e decreases as the plasma density increases and the electron temperature decreases. Therefore, in the discharge being simulated the amount of heat lost through electron conduction should decrease dramatically during NBI. If a constant χ_e were used in the simulation as was done in the ultralow-density case, the calculated heat conduction loss would be overestimated and might artificially cause a thermal collapse in the simulation.

ECH absorption was approximated by the model discussed in Section 6.2.3 with a feature added to handle absorption near the cutoff density. The standard absorption model used by PROCTR assumes that no power is absorbed inside the outermost flux surface where the wave frequency equals the cutoff frequency of the wave. Since the wave launched by ECH is extraordinary mode (X-mode) at second harmonic, the cutoff density is

$$n_e = n_c/2, \quad (6.4)$$

$$n_c = \frac{m_e}{4\pi e^2} (2\pi\nu_{\text{ECH}})^2, \quad (6.5)$$

where ν_{ECH} is the wave frequency and n_c is the plasma density where the wave frequency equals the plasma frequency. The factor of 1/2 results from assuming that the wave frequency is twice the electron cyclotron frequency. For normal ATF

operation, this cutoff density occurs at a value of $n_e = 1.2 \times 10^{13} \text{ cm}^{-3}$. However, as discussed in Section 6.2.1, there is considerable experimental evidence to support the assertion that ECH absorption in ATF begins to deteriorate well before this density limit is reached. This reduction in absorption is probably due to refractive effects that are not taken into account by this model. In this low-density case, the reduction in absorption is critical to the energy balance of the plasma since the absorbed neutral beam power is quite small. Therefore, a better model of the ECH absorption near the cutoff density had to be developed. Because the physics describing the propagation and absorption of the ECH-launched wave in the plasma is quite complicated, developing a complete expression for the ECH absorption near cutoff is beyond the scope of the present work. For the purposes here, the following empirical expression, based on data similar to that shown in Fig. 6.3, was used for the variation of the absorbed power as the density approached the cutoff density:

$$f_{\text{abs}} = \begin{cases} 1, & n_{el} < n_1 \\ 1 - \left(\frac{n_{el} - n_1}{n_2 - n_1} \right)^4, & n_1 \leq n_{el} \leq n_2 \\ 0, & n_{el} > n_2 \end{cases}$$

Here, n_{el} is the plasma electron line density, $n_1 = 5.0 \times 10^{14} \text{ cm}^{-2}$, and $n_2 = 7.5 \times 10^{14} \text{ cm}^{-2}$.

A further complication encountered in simulating this discharge was the effect of impurities. Because the electron temperature drops quickly during the discharge, the amount of radiation from impurities tends to rise quickly. To properly account for this energy loss, the impurities must be taken into account in the simulation. To do this, a multi-charge-state impurity transport model, which includes radial transport and ionization and recombination between the various charge states, was used.¹⁴ The impurity diffusion coefficients and anomalous pinch terms were chosen to be the same as those chosen for the electrons. The impurity source rates were then adjusted on subsequent runs of the code such that the predicted spectral line-integrated intensities agreed with the measured intensities for the spectral lines

emitted from the plasma interior. The simulated time-dependent spectral intensities reproduce the measured emission levels quite well, as illustrated by Fig. 6.23. To obtain this match, the impurity source rates were increased linearly from their ECH value starting at 250 msec to a new value at 300 msec and then held constant. The origin of this increased source rate is believed to be a higher edge temperature during the early phases of NBI, which increases the sputtering rate of the metallic impurities. A small amount of this increase is also attributable to the interaction of the beam particles with the walls (via shine-through or unconfined orbits).

The amount of power radiated from each impurity species can then be computed using the calculated impurity density n_{Ij} . The radiation from impurity species j is given by the formula¹

$$q_{\text{rad}}^{Ij} = n_e \sum_{\ell} n_{Ij}^{q\ell} \langle \sigma v \rangle_{\text{cx}}^{\ell} + \sum_{q=0}^{Z-1} X_R^q n_{Ij}^{q+1} \langle \sigma v \rangle_r^q + 1.6 \times 10^{-32} n_e T_e^{1/2} \sum_{q=1}^Z q^2 n_{Ij}^q, \quad (6.6)$$

where the superscript q refers to the charge state of the impurity and the superscript ℓ refers to a particular spectral line. The first term in this equation represents line radiation summed over the strongest lines, while the second is recombination with the average radiated energy per recombination event given by X_R^q . The third term represents impurity bremsstrahlung. The computed radiated power was then used in the electron energy balance equation. For this simulation, radiation from the metallic impurities represents about 75% of the total radiation, which is consistent with spectroscopic analysis of radiated power in similar discharges.¹⁵ The effect of the impurity radiation was found to be important in the electron energy balance equation only when the plasma electron temperature falls below a certain threshold. Once the electron temperature reaches this threshold, the impurity line radiation quickly becomes the dominant loss mechanism. These results are consistent with detailed spectroscopic studies of plasma cleanliness in these discharges, which have shown that radiation is an unlikely candidate for initiating the collapse, although it

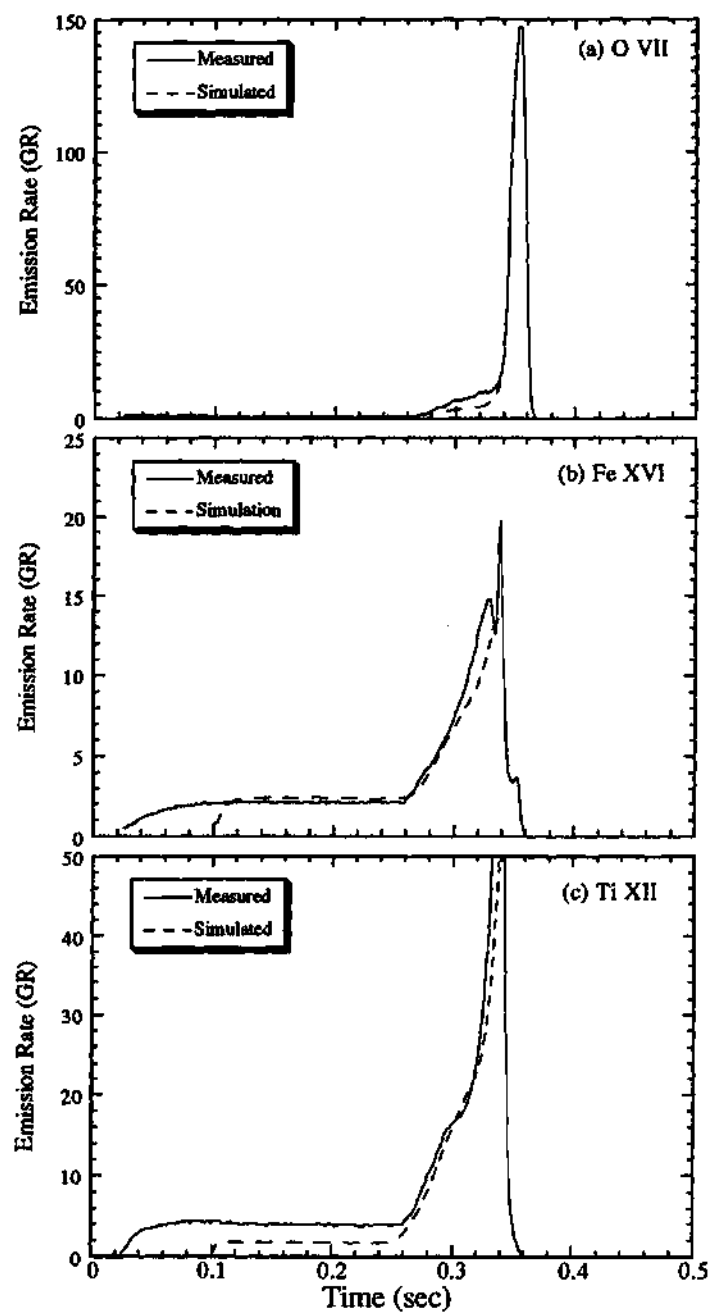


Figure 6.23: Comparison of simulated spectral line intensities with the measured values for (a) O VI (1032 \AA), (b) Fe XVI (361 \AA), and (c) Ti XII (461 \AA). (Data courtesy of the ATF spectroscopy group).

may become an important loss mechanism once the electron temperature falls below a certain threshold.¹⁵

The results of the PROCTR simulation of this low-density discharge are shown in Fig. 6.24, where the simulated electron line density, plasma stored energy, central electron temperature, and plasma current are compared to their corresponding measured values. The evolution of the electron line density, the central electron temperature, and the plasma stored energy is approximately reproduced in the simulation. The constant offset evident in the simulated plasma current is probably due to the neglect of the bootstrap current in the model. Studies in ATF have shown that the magnitude of this current (approximately 1.5 kA in this case) is consistent with neoclassical predictions of the bootstrap current.¹⁶ If this constant offset were applied to the simulated current, the time dependence of the current due to the beam-driven current and the induced current would be approximately reproduced during the neutral beam phase.

The simulated time-dependent global power balance for this case (Fig. 6.25) illustrates the transient nature of this discharge. Because of the reduction in ECH absorption as the plasma density approaches cutoff, the amount of ECH power coupled to the electrons continuously decreases during NBI. As discussed earlier, the amount of coupled beam power increases continuously during NBI as the shine-through and fast-ion charge-exchange losses decrease because of the rising density. The radiation also increases during injection (as a result of the decreasing temperature and increased impurity influx in the model) and eventually surpasses the heating power (but well after the initiation of the thermal collapse). At the peak of the stored energy, the simulation indicates that approximately 40–50% of the heating power is being radiated but this ratio is a strongly increasing function of time. The unstable nature of the collapse is due to the unstable dependence of the impurity line radiation on the plasma electron temperature. For temperatures be-

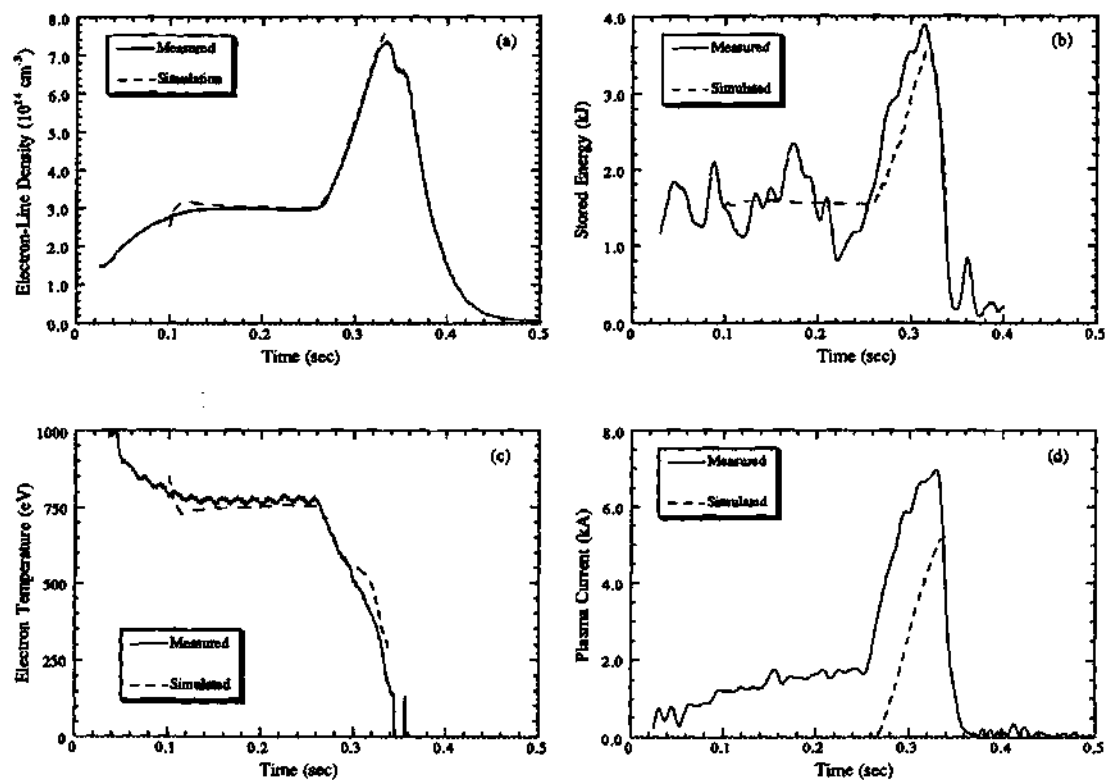


Figure 6.24: Simulated (dashed lines) and measured (solid lines) values of the (a) electron line density, (b) plasma stored energy, (c) central electron temperature, and (d) plasma current in a typical low-density discharge.

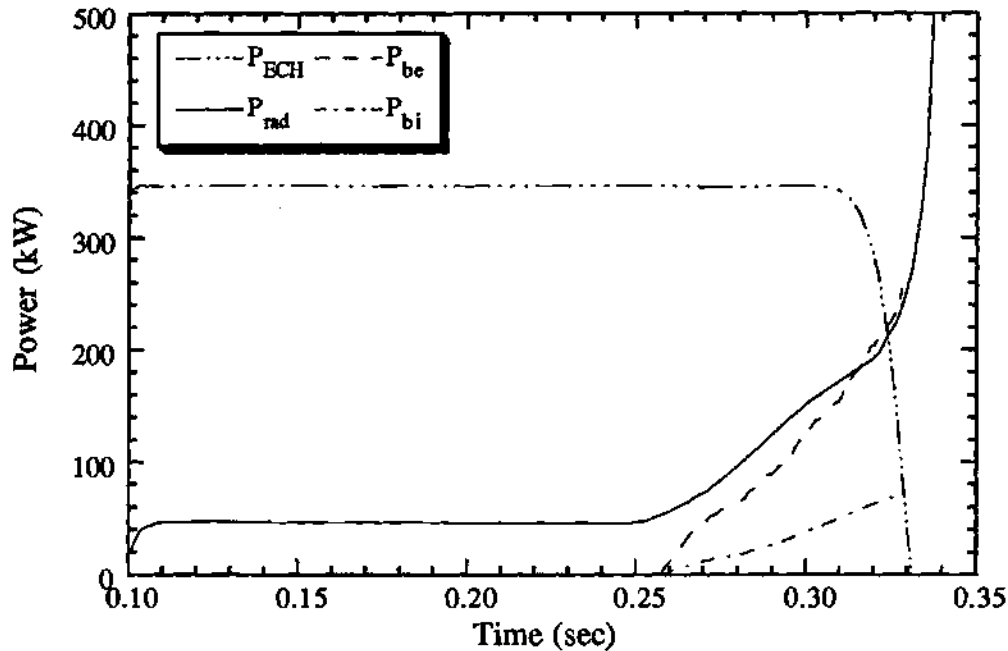


Figure 6.25: Simulated time-dependent global power balance in a low-density discharge.

low 100 eV, any decrease in temperature results in an increase in the line radiation, which further cools the plasma. The electron temperature profile typically collapses inward from the edge as large radiation from the outer region of the plasma progressively cools adjacent plasma until all the stored energy is radiated in a brief (5- to 10- msec) burst of radiation.

The model used for ECH absorption was found to be crucial in simulating this discharge. When the standard ECH absorption model, in which the power is assumed to be fully absorbed until the cutoff density is reached, was used in PROCTR, the simulation did not predict a thermal collapse. Since the power provided by ECH is only 400 kW, this indicates that the global power balance in this case is marginal and that the loss of a large amount of the beam power due to shine-through and charge-exchange is crucial to the thermal collapse.

6.4 NBI Studies in High-Density Plasmas

The other ATF operating regime in which a quasi-steady-state plasma has been attained during NBI is in high-density ($\bar{n}_e \geq 8.0 \times 10^{13} \text{ cm}^{-3}$) plasmas. The plasmas attained in this case exhibit the largest global energy confinement times of any discharges yet attained on ATF. Unfortunately, the number of discharges of this type to date has been quite small. Therefore, the data available for analysis is quite limited. The data presented here are from a sequence of discharges taken in March 1990 and are part of ATF sequence 90031601.

6.4.1 Experimental Setup

The evolution of several plasma parameters for this type of discharge is shown in Fig. 6.26.¹⁷ In this case the target plasma is created by 400 kW of 53-GHz ECH power and is subsequently heated starting at 200 ms by approximately 1.3 MW of balanced NBI. The ECH power is turned off at 200 msec since the plasma density quickly rises quickly above the ECH cutoff density. The plasma density rises quickly from its ECH-phase value due to a large gas puff that is injected coincident with the onset of NBI. Due to this large increase in density, the electron temperature drops very quickly from its ECH-phase value of 1 keV to approximately 150 eV. After approximately 100 msec the plasma density attains a steady-state value, while the electron temperature begins to recover and eventually "reheats" to a value of approximately 250 eV. The attained stored energy for this particular discharge is 28 kJ, which gives a global energy confinement time (defined as the ratio of the plasma stored energy to the absorbed power) on the order of 30 msec — the highest attained thus far on ATF.

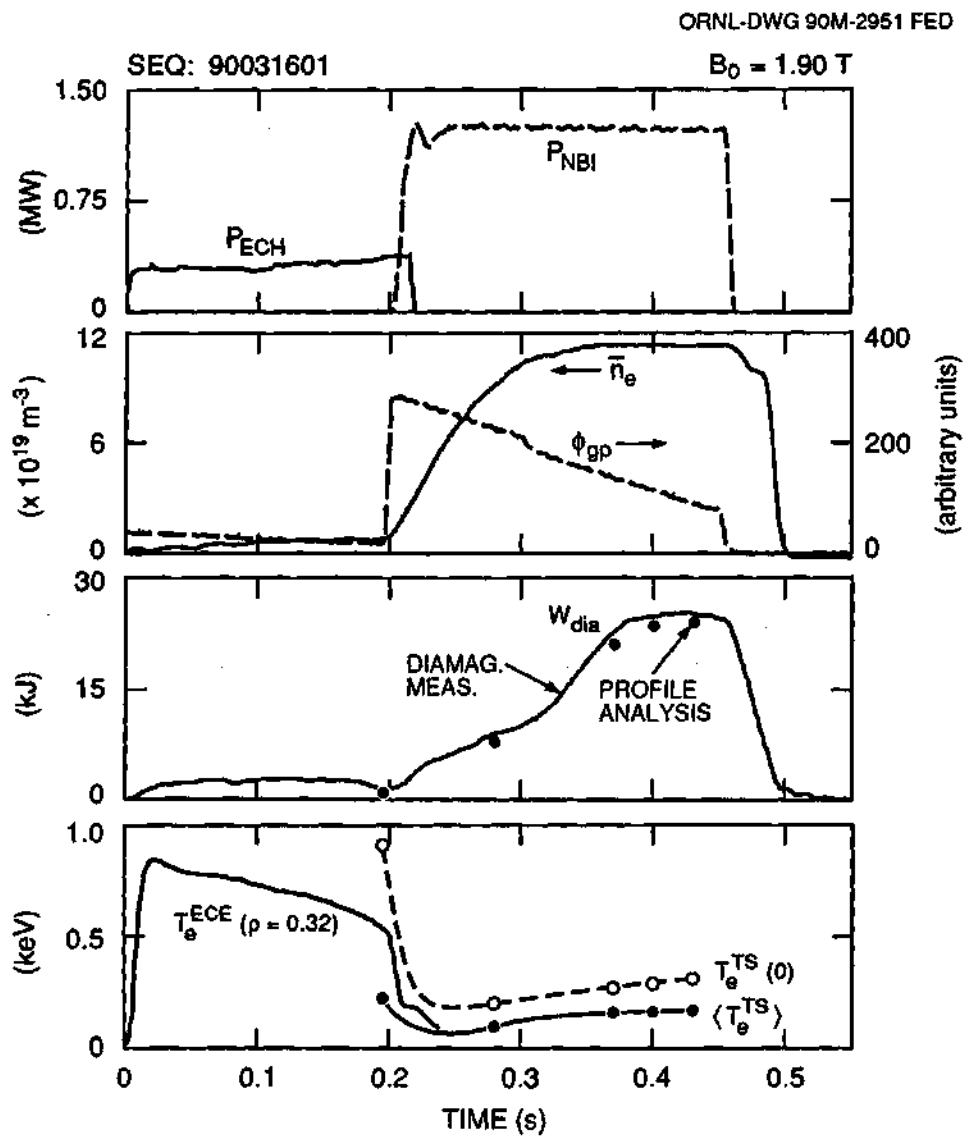


Figure 6.26: Evolution of a high-density discharge in ATF [Ref. 17].

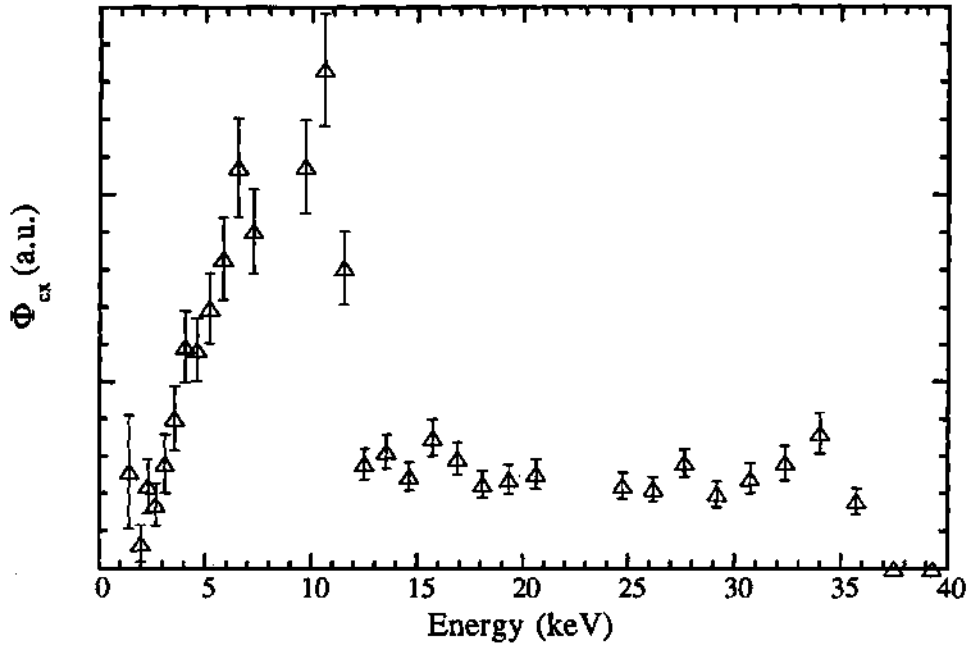


Figure 6.27: Energy spectra measured by the NPA during the steady-state portion of a typical high-density NBI discharge.

6.4.2 Experimental Results and Analysis

A typical measurement of the tangential slowing-down distribution made by the NPA during the steady-state portion ($t = 350$ msec) of this discharge is shown in Fig. 6.27. Although this measured spectrum has several of the same features as the spectra measured in the low-density case, the origin of the spectrum in this case is mostly from the edge of the plasma. This is clearly shown in Fig. 6.28, where the relative contribution to the measured flux as a function of distance along the NPA viewing chord is plotted. The reasons behind this result are twofold. First, the high plasma density reduces the neutral density in the core of the plasma to a very small level, so that the charge-exchange reaction rate $n_o \langle \sigma v \rangle_{cx}$ in the core of the plasma is very small. Therefore, very few neutrals are created by charge-exchange events in this region. The second problem is that the probability of a neutral escaping from the core of the plasma once it has been created is dependent on the line-integrated plasma density that the neutral encounters on its path out of

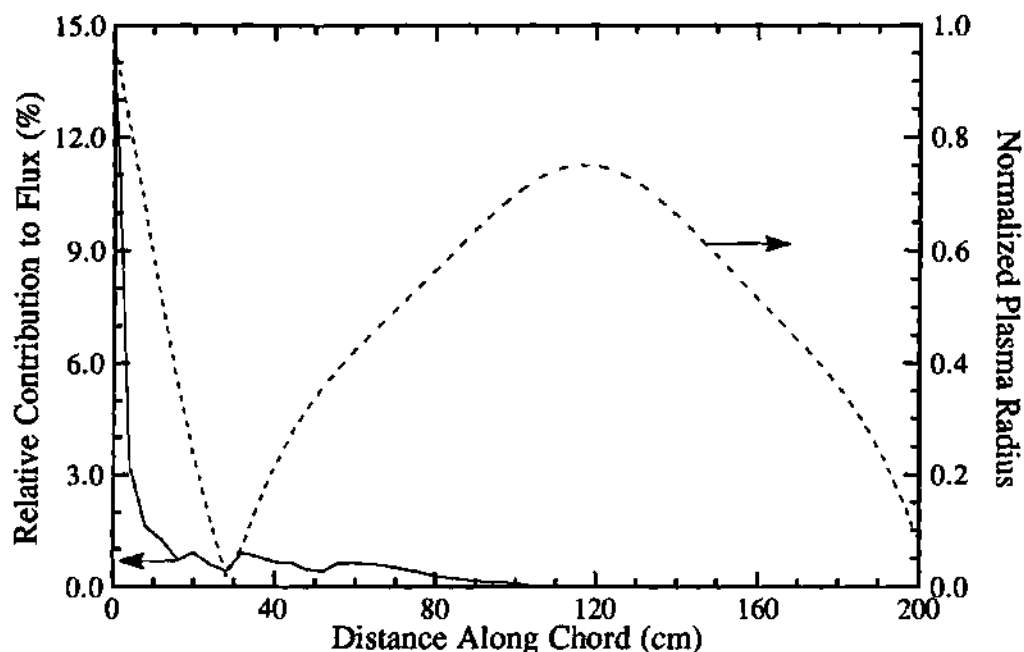


Figure 6.28: Relative contribution to measured flux for $E = 20$ keV of each differential segment along the NPA viewing chord in a high-density discharge along with the normalized radius corresponding to the location in the plasma of each differential segment.

the plasma [see Eq. (A.8)]. As the plasma density increases, the ratio of the number of neutrals that reach the edge of the plasma to the number produced decreases exponentially. These two effects combine to reduce the amount of neutrals actually born (neutralized by a charge-exchange reaction) and able to exit the plasma from the central region to a very small number. Thus, the spectrum measured by the NPA is dominated by contributions from the periphery region of the plasma.

Typically, most of the injected ions are deposited (ionized) in the central regions of the plasma. These ions remain approximately on the flux surface on which they were deposited. Since the NPA measurement is weighted toward the periphery of the plasma in this case, very little information is contained in the NPA measurement. Therefore, it is difficult to justify using NPA measurements to garner information about global fast-ion confinement properties in these discharges and the corresponding effect on the global power balance of the plasma.

However, the success in accurately simulating the measured data with the FPACX code in the previous two cases suggest that some useful information can be obtained by the same type of modeling in this case. Hence, the fast-ion distribution function was computed in the same way as earlier, except that no attempt was made to match the measured spectrum with the simulated one. Although a reasonable match could probably be found between the simulated and the measured spectrum, the reasons for not doing this are twofold. First, since the measured flux is postulated to emanate from the edge regions of the plasma, the magnitude and shape of the energy spectrum are dependent on edge quantities, which are typically not very well known from experimental data in ATF. Second, the amount of information gained for the amount of effort put forth in simulating this energy spectrum would be small since the energy spectrum only contains information about the fast-ion distribution in the edge of the plasma.

As mentioned previously, the central electron temperature inferred from Thomson scattering measurements is $\simeq 250$ eV during the steady-state phase of this discharge, while the central electron density is $\simeq 8.0 \times 10^{13} \text{ cm}^{-3}$. Thus, the slowing-down time of the injected ions is $\simeq 2$ msec. Although the central neutral density is difficult to quantify in these high-density discharges, the charge-exchange time is expected to be on the order of hundreds of milliseconds, such that $\tau_s \ll \tau_{cx}$ and charge-exchange losses are minimal. Furthermore, shine-through losses are also minimal in this case because of the high plasma density. Therefore, a large majority of the beam power is absorbed by the plasma in this case, as is evidenced by Fig. 6.29. Approximately 95% of the injected beam power is absorbed by the plasma. Simulations using the DESORBS code produced similar results (see Table 6.2). To test the effect of the definition of the loss boundary on the calculated power distribution, similar runs of the DESORBS code were made with the loss boundary defined as either the ATF vacuum vessel wall or the LCFS. The comparison of

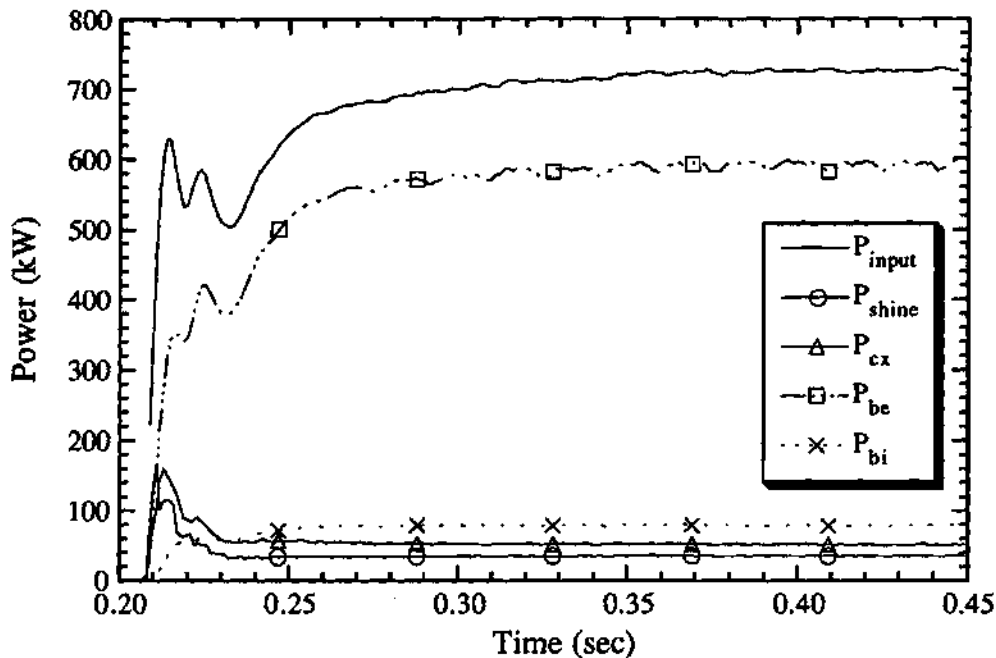


Figure 6.29: Time dependence of the amount of injected power (P_{input}), power loss through charge-exchange (P_{cx}), power loss through shine-through (P_{shine}), power absorbed by the electrons (P_{be}), and power absorbed by the ions (P_{bi}) in a typical high-density discharge.

these results is also shown in Table 6.2. Surprisingly, the definition of the loss boundary makes little difference in the results. This is postulated to be due to the low electron temperature, such that $E_{crit}/E_{inj} \ll 1$. As discussed in Section 4.4, in these conditions, the injected ions give up most of their energy before becoming helically trapped. Since the helically trapped orbits generally pass outside the LCFS but inside the vacuum vessel wall, the results from these two assumptions for the loss boundary could be quite different if $E_{crit}/E_{inj} \sim 1$.

6.5 Conclusions

The most significant result of these fast-ion confinement experiments is the realization that the limited operating space (in terms of plasma electron density) in ATF during NBI is quite likely due to insufficient heating power at intermediate

Table 6.2: DESORBS calculation of power distribution for a high-density discharge.

	Power distribution (%)	
	Loss Boundary Location	
	LCFS	Vessel
P_{be}	77.7	79.5
P_{bi}	14.6	15.2
P_{cx}	0.0	0.0
P_{shine}	0.0	0.0
P_{orbits}	3.1	0.0
P_{therm}	4.6	5.3

densities. This lack of heating power is mainly due to the fairly low value of the ECH cutoff density in ATF ($n_e \simeq 1.2 \times 10^{12} \text{ cm}^{-3}$). Since the ECH power is generally not absorbed by the plasma above the cutoff density, the density of the target plasmas created by ECH in ATF is constrained to be below this density. Furthermore, ECH power is effectively useless in plasmas with densities above this limit. At densities characteristic of target plasmas created by ECH, NBI heating is extremely inefficient ($\sim 20\%$) due to large shine-through and charge-exchange losses. Therefore, the effective heating power for plasmas with densities near the ECH cutoff density is quite limited, which in turn limits the possible scenarios for quasi-steady-state NBI operation in ATF.

Only two experimental methods have been shown to be successful. The first of these is the ultralow-density case, where the plasma density is maintained below the ECH cutoff density throughout the NBI portion of the discharge. Although approximately 650 kW of NBI power was injected during this discharge, the plasma is mainly sustained by the 400 kW of ECH power, since the NBI heating efficiency is $\simeq 20\%$ due to large charge-exchange and shine-through losses. The other operating

scenario that is successful in attaining quasi-steady-state plasmas during NBI is the high-density case, in which a large amount of gas is puffed in simultaneously with injection such that the plasma density rises very quickly above the ECH cutoff density. This rapid increase in the density is necessary to raise the NBI heating efficiency to a level where the plasma can be sustained solely by NBI heating.

Operation at density levels intermediate to these two cases has generally been unsuccessful. The operating regime with which there is the most experience in ATF is the low-density regime where a thermal collapse occurs shortly after the onset of NBI. Three mechanisms have been proposed to explain this collapse: (1) impurity radiation, (2) excitation of an electron instability driven by the highly anisotropic nature of the NBI process, and (3) poor coupling of the beam ions to the background plasma. Detailed spectroscopic studies of plasma cleanliness have shown that radiation is an unlikely candidate for initiating these collapses, though it may become an important loss mechanism once the electron temperature has fallen to a low level.¹⁵ Also, a specific electron instability has not yet been identified during injection. However, the work presented here suggests that this collapse is due to an unfavorable power balance at the time of the collapse due to poor confinement of the injected ions. The poor confinement in this case is principally due to charge-exchange losses.

The excellent agreement between the measured and predicted NPA energy spectra indicates that the fast-ion thermalization process in ATF is governed by the classical slowing-down processes embodied in the fast-ion Fokker-Planck equation. Furthermore, the agreement of the calculated beam power distributions in FPACX and DESORBS suggests that losses due to orbit effects are negligible for the types of discharges discussed in this chapter. However, there is some evidence that orbit losses do play a role in the peculiar transient behavior of the medium-density discharges [see Fig. 6.1(c)]. Unfortunately, the fast-ion confinement properties of these discharges could not be determined because of insufficient NPA data.

REFERENCES

- ¹ H. C. Howe, Technical Report ORNL/TM-11521, Oak Ridge National Laboratory (1990).
- ² D. E. Hastings, W. A. Houlberg, and K. C. Shaing, *Nucl. Fusion* **25**, 445 (1985).
- ³ K. H. Burrell, *J. Comput. Phys.* **27**, 88 (1978).
- ⁴ Private communications with M. M. Menon, ORNL (1990).
- ⁵ R. C. Goldfinger and D. B. Batchelor, in *Applications of Radio-Frequency Power to Plasmas*, AIP Conf. Proc. No. 159, p. 65 (American Institute of Physics, 1987).
- ⁶ Private communications with T. S. Bigelow, ORNL (1991).
- ⁷ R. H. Fowler, J. Smith, and J. A. Rome, *Comput. Phys. Commun.* **13**, 323 (1978).
- ⁸ S. C. Aceto et al., in *Controlled Fusion and Plasma Physics (Proc. 18th EPS Conf., Berlin, 1991)*, Vol. 15C, Part II, p. 161 (1991).
- ⁹ H. Wobig et al., in *Plasma Physics and Controlled Fusion Research 1986 (Proc. 11th Int. Conf., Kyoto, 1986)*, Vol. 2, p. 369 (IAEA, Vienna, 1987).
- ¹⁰ K. Kondo et al., *Rev. Sci. Instrum.* **59**, 1533 (1988).
- ¹¹ K. Ida et al., *Phys. Fluids B* **3**, 515 (1991).
- ¹² R. H. Fowler, R. N. Morris, J. A. Rome, and K. Hanatani, *Nucl. Fusion* **30**, 997 (1990).
- ¹³ S. Sudo et al., *Nucl. Fusion* **30**, 11 (1990).
- ¹⁴ K. Behringer, Technical Report JET-R(87)08, JET Joint Undertaking (1987).
- ¹⁵ R. C. Isler et al., *Nucl. Fusion* **31**, 245 (1991).
- ¹⁶ M. Murakami et al., *Phys. Rev. Lett.* **66**, 707 (1991).
- ¹⁷ M. Murakami et al., "Energy Confinement and Bootstrap Current Studies in the Advanced Toroidal Facility", presented at the 13th International Conference on Plasma Physics and Controlled Fusion, Washington, D.C., October 1-6, 1990.

CHAPTER VII

Summary and Conclusions

7.1 Review of Results

An experimental investigation of ion behavior in the Advanced Toroidal Facility (ATF) has been presented in this thesis. Since one of the biggest concerns of the stellarator concept as a viable fusion reactor is the degree to which the ions (both thermal and energetic) are confined, the study of ion behavior in the present generation of stellarators (e.g., ATF) is crucial in developing the stellarator concept beyond its current status. This work represents the first major attempt to develop an experimental understanding of ion behavior in small-aspect-ratio, medium-size stellarators. Because studies of ion confinement in stellarators have been limited to date, the studies presented here have greatly enhanced the understanding of ion confinement in stellarators and provided the first information on ion confinement in a small-aspect-ratio, medium-size stellarator. Note that even though ATF is only "medium size" in comparison to present-day tokamak devices, at the time of this writing it remains the world's largest stellarator. This chapter reviews the results of the ion confinement investigations conducted on ATF and presents some conclusions based on these studies.

The primary ion diagnostic used in these studies is a two-dimensional scanning neutral particle analyzer (NPA). Charge-exchange neutral analysis (CXNA) is a well-established diagnostic technique to infer the ion distribution function, from which basic information on ion confinement and behavior can be drawn. In thermal-

ion confinement studies, the quantity of interest, the central ion temperature T_{i0} , can be directly inferred from NPA measurements. The inferred T_{i0} can then be compared with a predicted ion temperature derived from neoclassical heat transport considerations. The degree to which the measured and predicted temperatures agree provides a basis for determining if the thermal ions are well confined. The situation is much more complicated when inferring the fast-ion confinement properties from NPA-measured data. The primary reason for this added complexity is the complicated functional dependence of the fast-ion distribution on many different parameters, such that it generally cannot be represented by a simple analytical expression. Therefore, NPA measurements of the fast-ion distribution are typically compared to predictions of finite-difference solutions to the fast-ion Fokker-Planck equation to assess whether the energetic ions behave classically or are subject to anomalous processes.

The thermal-ion confinement studies presented in Chapter 5 were generally confined to ECH-heated discharges with densities below $\bar{n}_e = 8.0 \times 10^{12} \text{ cm}^{-3}$ because of difficulties in attaining steady-state discharges that had densities above this level and that were accessible by NPA measurements. This limitation severely hampered efforts to determine the local heat diffusion coefficient χ_i since in these low-density plasmas, the magnitudes of the charge-exchange and convection losses are roughly the same as that of the heat diffusion losses. Typical ion temperatures inferred from NPA measurements were in the range of 100–200 eV. These low ion temperatures limited the usefulness of the NPA in inferring thermal ion characteristics in ATF and required the placement of a gas valve directly in front of the analyzer to enhance the background neutral density, thereby increasing the flux measured by the NPA to a usable level. The measured ion temperatures are consistent with neoclassical predictions of the ion heat transport, including the effect of the non-ambipolar heat flux. This agreement is, however, subject to large uncertainties

because the relative magnitude of both the charge-exchange and convection losses are comparable to the conductive losses in the cases studies. Furthermore, since the charge-exchange and convection losses are dependent on the neutral density, which is experimentally unknown, the magnitude of these losses cannot be accurately determined. Hence, similar to other ion confinement studies in stellarators, the data obtained in ATF suggest that thermal ion confinement in ATF can be explained by neoclassical predictions but is insufficient to make a definite conclusion at this time. Further experiments in slightly higher density (above the ECH cutoff density) plasmas are required to resolve this question. Possible methods are discussed in Section 7.2.

Attempts to measure the ion temperature profile have been limited by the low ion temperature; these measurements indicate that the profile is flat inside $\rho \simeq 0.5$, which is consistent with spectroscopic measurements. Typical thermal energy spectra measured by the NPA do not exhibit the "two-temperature" feature apparent in most NPA measurements on other devices, possibly confirming the existence of computed loss regions directly in front of the NPA. Although (as pointed out in Chapter 4) changing the magnetic configuration of ATF should produce large changes in single-particle confinement properties, measurements made during various magnetic configuration scans showed that these changes had only a very small effect on the attainable ion temperature in ATF. One of the most intriguing features of the thermal-ion measurements made during these studies is the existence of a high-energy ion tail in certain magnetic configurations at very low plasma densities. Substantial evidence indicates that some form of collisionless ion heating is the primary mechanism causing this phenomena.

Extensive studies of the fast-ion confinement properties in various operating regimes on ATF have also been conducted. Data were collected encompassing a large range of plasma conditions, including plasmas heated by neutral beam injection

(NBI) and ion cyclotron heating (ICH). Although operating experience with ICH on ATF has been limited, an abundance of data has been collected during NBI in several different operating regimes. Cases considered explicitly for these studies include several different density regimes, ranging from extremely low density ($\bar{n}_e \leq 7.5 \times 10^{12} \text{ cm}^{-3}$) to extremely high density ($\bar{n}_e \geq 8.0 \times 10^{13} \text{ cm}^{-3}$).

Comparisons of the NPA-measured data with Fokker-Planck predictions demonstrated that fast-ion behavior in ATF is well described by classical processes. From these comparisons, fast-ion confinement was found to be poor in both the ultralow-density ($\bar{n}_e \leq 7.5 \times 10^{12} \text{ cm}^{-3}$) and low-density ($\bar{n}_e \leq 5 \times 10^{13} \text{ cm}^{-3}$) cases, mostly because of large charge-exchange losses. Beam power losses due to shine-through also were found to be significant in these regimes. As a result, the amount of beam power actually coupled to the plasma in these cases is quite limited. In fact, simulations predict that only 20% of the injected power is coupled to the plasma in the ultralow-density case, and only 40% is coupled in the low-density case. These results indicate that NBI heating is extremely inefficient at densities characteristic of target plasmas created by ECH in ATF. In contrast, simulations of the high-density regime indicate that fast-ion confinement in this regime should be very good, although this result could not be confirmed by NPA measurements. These simulations predict that almost all of the injected power is absorbed by the plasma in this case.

Similar heating efficiency results were found using a code that simulates the injection and thermalization of the beam ions via Monte Carlo techniques. Because the Fokker-Planck prediction of heating efficiency does not take into account the effect of loss regions, the agreement between the Monte Carlo and Fokker-Planck predictions indicates that losses due to orbit effects are negligible for the types of discharges studied. However, this result does not necessarily imply that orbit losses are insignificant in all operating regimes of ATF. In fact, studies of hypothetical

operating regimes indicate that orbit losses become increasingly important as the plasma electron temperature increases (at a fixed electron density).

Further numerical studies using the PROCTR transport analysis code were conducted to determine the effect of the reduced beam absorption on plasma performance in the ultralow- and low-density cases. These studies were quite successful in producing simulations that were consistent with the measured data from a large number of plasma diagnostics. In the ultralow-density case, the primary conclusion was that the plasma is mainly sustained by ECH, though some additional heating is provided by NBI. Maintaining the electron density well below the ECH cutoff density was crucial in attaining these quasi-steady-state discharges. Discharges with slightly higher plasma densities inevitably suffered from thermal collapses approximately 50-70 msec after the initiation of NBI. The PROCTR simulations of the low-density case indicate that these collapses are the result of insufficient absorption of the beam power by the plasma, coupled with a deterioration in ECH absorption at densities near the ECH cutoff density.

The results of these studies suggest that the available operating regime (in terms of plasma density) in ATF is limited because of insufficient heating power at intermediate densities. There are several reasons for this lack of heating power at these densities. First, since the ECH power is generally not absorbed above the cutoff density ($n_e \simeq 1.2 \times 10^{13} \text{ cm}^{-3}$), the density of the target plasmas created by ECH in ATF is constrained to be below this density limit. At these densities, NBI heating is extremely inefficient ($\sim 20\%$) because of large shine-through and charge-exchange losses. Therefore, the effective heating power for plasmas with densities near the ECH cutoff density is quite limited, which in turn limits the possible scenarios for quasi-steady-state NBI operation in ATF.

Naively, one might think that increasing the injected beam power would be a possible remedy for this situation, since the total absorbed beam power should

simply scale proportional to the injected beam power. The beam power can be increased by either increasing the injection energy (V_{beam}) or increasing the number of injected particles (or beam current I_{beam}). An increase in the injection voltage would not help in these low-density discharges since the shine-through losses increase with the injection voltage because of a large decrease in the cross sections of the various ionization processes above 30 keV. Unfortunately, NBI is also generally more efficient in plasma fueling than in plasma heating at these low densities, since particles lost from the plasma (via charge-exchange, unconfined orbit, etc.) usually are recycled from the wall at very reduced energies. Therefore, the NBI fueling efficiency is very high even when its heating efficiency may be very low. Hence, increasing I_{beam} simply causes the electron density to rise more quickly without necessarily providing a large increase in beam power. Therefore, this scenario would most likely result in the same type of thermal collapse when the density increased above the ECH cutoff density.

Reducing V_{beam} and increasing I_{beam} is another possibility since the reduced voltage should reduce the shine-through losses. However, since the amount of beam current that can be extracted from the accelerator grid is determined by the perveance ($I_{\text{beam}}/V_{\text{beam}}^{3/2}$), the amount of current that can be obtained at a reduced voltage is limited. If the maximum beam current is extracted when the perveance is optimal (i.e., $I_{\text{beam}}^{\text{max}} \propto V_{\text{beam}}^{3/2}$), the amount of power contained in the beam as it passes through the vacuum vessel port is approximately proportional to $V_{\text{beam}}^{5/2}$, though there is a slight improvement in the neutralization of the beam in the neutralization cell. The amount of the injected power that is absorbed by the plasma is then solely dependent on the mean free path of the fast neutrals as they pass through the plasma. This mean free path is dependent on the plasma density and the energy of the fast neutrals. Assuming the same plasma conditions (i.e., the same plasma density profile), the fraction of the absorbed power is then strictly dependent

on the energy dependence of the cross sections of the various ionization processes. Although the cross sections do increase as the energy of the neutral decreases, the change in the cross sections is not nearly enough to make up for the loss of power due to the reduced injection energy. For example, reducing V_{beam} for 30 keV to 20 keV reduces the shine-through losses by approximately 20%; however, the available input power is reduced by approximately 65%. Therefore, reducing the injection voltage V_{beam} is not a viable option.

The use of high-power ICH is another alternative, although the current antenna structure on ATF limits its use at densities characteristic of the ECH cut off density because of reduced coupling. The lack of success of the low-density ICH experiments are principally due to this limitation.¹ At slightly higher densities, the coupling of the ICH-launched wave with the plasma increases drastically. However, scenarios which use minority heating, in which a high-energy tail in the minority ion species is created and then allowed to slow down collisionally on the background plasma, suffer from the same problems (i.e., high charge-exchange losses) at these densities as NBI. Orbit effects also play a more important role, since the ions heated by ICH are given substantial perpendicular energy, pushing them closer to the loss region. Given these problems, it still seems plausible that ICH can provide sufficient heating to sustain an intermediate density plasma.

The best possible scenario for improving this situation is to raise the effective ECH cutoff density by increasing the frequency of the ECH-launched wave. For example, if the frequency of the launched wave were 106 GHz, the ECH cutoff density would be increased by a factor of four, since the cutoff density is proportional to the square of the frequency of the launched wave. Since the power absorbed by the plasma is a strong function of density, the degree to which the beam power would be absorbed would be much greater at these densities, possibly allowing steady-state operation. Since observations on ATF indicate that the density limit during

ECH may not be linked directly to the ECH cutoff density, one must be careful in assuming that a higher density limit is possible by simply increasing the frequency of the ECH-launched wave. Fortunately, preliminary experiments on Wendelstein VII-AS using 140-GHz ECH have attained heating in electron densities approximately twice the value of the density when using 70-GHz ECH.² Future experiments are necessary to see if this density limit can be extended to four times the 70-GHz density limit.

These experiments coupled with the ion orbit studies presented in Chapter 4 have addressed most of the issues outlined in Section 1.4, though some of these issues still remained unresolved. Below is a brief review of these issues and the results of the ion studies conducted on ATF:

- Theoretically, ion orbit effects should play an important role in ATF.

The results of the ion orbit studies presented in Chapter 4 suggest that the loss region in ATF is quite large. This result is not surprising since the ATF magnetic configuration was not optimized in terms of orbit confinement. Experimentally, however, there is no confirmation that orbit effects limit plasma performance in ATF. In fact, the plasma parameters attained in ATF magnetic configurations that are optimized in terms of orbit confinement are essentially the same as those attained in configurations with poor confinement properties (e.g., see Fig. 5.7).

- Theoretically, the presence of a radial electric field has been shown to significantly affect the orbit confinement properties in ATF. The studies presented in Section 4.3 suggest that a strong positive electric field (i.e., directed outward) is required for a substantial improvement. On the other hand, a negative electric field is potentially damaging because of the existence of the so-called helical resonance (see Section 4.3), which

causes a large loss of thermal particles. This resonance occurs in ATF at approximately the energy $E = -4\Phi_0$.

- Some orbit effects have been measured in ATF, indicating that the results of the numerical and analytical studies of the orbit topology are correct. For example, the lack of the typical "two-temperature" feature in the NPA-measured energy spectra (see Fig. 5.3) is attributable to loss region directly in front of the NPA (see Fig. 4.14). Also, the "hole" observed in the perpendicular energy spectra measured during NBI (see Fig. 6.7) is most likely a result of the helical resonance described in Section 4.3.
- Ion transport in ATF has been shown to be consistent with neoclassical theory (see Fig. 5.7), though large uncertainties exist in both the ion temperature measurement and the neoclassical prediction.
- Theoretically, ion orbit confinement properties in ATF change drastically as the magnetic configuration is changed (see Section 4.2). Orbit confinement properties tend to improve as the magnetic axis is shifted inward and as the plasma is squeezed vertically (see Figs. 4.6 and 4.7). Experimentally, however, the degree of orbit confinement seems to have little impact on plasma performance (see Fig. 4.9).
- The excellent agreement of the FPACX-simulated energy spectra with the NPA-measured spectra during NBI indicates that the energetic ions behave classically in ATF (e.g., see Fig. 6.20).
- In general, the energetic ions are confined quite well (i.e., very little orbit losses) in the operating regimes obtained to date on ATF, though measurements indicate that over 50% of the injected beam power is not coupled to the plasma because of large charge-exchange and shine-through losses (see Fig. 6.22).

- Simulations using the PROCTR transport analysis code indicate that these losses strongly affect plasma performance and are most likely the cause of thermal collapse seen in low-density discharges in ATF.
- Simulations using the DESORBS Monte Carlo simulation code indicate that orbit losses would be significant in higher-temperature ($T_e \sim 2$ keV), higher-density plasmas (see Table 4.1). Because there is no operating regime in ATF where $\tau_s \ll \tau_{cx}$ and $E_{crit} \sim E_{inj}$ simultaneously, this result cannot be confirmed experimentally. However, these results suggest that the design of a future stellarator device should consider the effect of the loss region on the heating efficiency of NBI and ICH.

7.2 Proposed Future Work

The unique scanning capability of the NPA on ATF and the inherently rich orbit topology in ATF should provide an excellent basis for further studies of ion behavior in ATF. The results presented in this work represent only a small fraction of the foreseen opportunities in this area. This section outlines some of the work necessary for fully understanding ion behavior in ATF.

First, studies of the orbit topology in ATF are crucial to an understanding of ion behavior in ATF. Although substantial progress was made in studying some aspects of the orbit topology (see Chapter 4), several key issues are still left unaddressed. Most important of these is the influence of the definition of the loss boundary on ion confinement. As pointed out in Chapter 4, calculations have shown that particles that pass outside the last closed flux surface (LCFS) of ATF do not necessarily strike the vacuum vessel wall before reentering the plasma. Therefore, the definition of the LCFS as the loss boundary is subject to some debate. Since

the orbit-following and J^* calculations presented in Chapter 4 assumed that the loss boundary is defined by the LCFS, some work is required to see what influence this assumption has on the orbit topology. To extend the J^* calculations outside the LCFS, some form of magnetic coordinates must be defined in a consistent manner in this region. Work is now under way to define a magnetic coordinate system outside the LCFS (e.g., see Ref. 3).

In the area of thermal ion confinement, several key issues remain owing to the limited operating space in which the studies presented in Chapter 5 were conducted. In this context, future thermal ion confinement studies on ATF should be conducted in slightly higher density plasmas with significantly higher ion temperatures. Higher densities ($n_e = 3.0 \times 10^{13} \text{ cm}^{-3}$) are required to reduce the neutral density, thereby reducing the charge-exchange and convective losses to small enough values that an accurate measurement of the ion heat diffusion coefficient χ_i can be made. Higher ion temperatures ($\sim 500 \text{ eV}$) are necessary so that the principal ion profile diagnostics (NPA and spectroscopy) are operating in a temperature range in which they are quite accurate. Because NBI has been shown to be ineffective at the required densities, ECH and ICH seem to be the only methods for obtaining these conditions. ECH can only be used if the frequency is raised from 53.2 GHz since at this frequency the launched wave is cut off at $n_e = 1.2 \times 10^{13} \text{ cm}^{-3}$. More power than the currently available 400 kW is probably also necessary to obtain the higher ion temperatures. High-power ICH seems to be a logical choice, though there is no experimental confirmation to date that ICH will work at these densities.

Although the work presented in Chapter 6 has addressed several key points about fast-ion confinement in ATF, much work is still needed to completely characterize ion behavior in ATF. The primary focus of subsequent work should be the characterization of fast-ion confinement in medium-density discharges. These discharges are characterized by peculiar transient behavior, which may be due to

changes in fast-ion confinement. The understanding of confinement in this regime would bridge the gap between the low-density and high-density regime studies presented in Chapter 6 and provide a basis for attempting to obtain steady-state discharges at medium density levels.

Since the heating mechanisms associated with ICH create energetic ions with substantial perpendicular velocity, fast-ion confinement studies during ICH provide a unique opportunity to study the effect of the orbit topology on the confinement of highly energetic particles near the loss region. Although the density at which these experiments can be conducted is limited because of the reduction of charge-exchange flux at higher densities, experiments in relevant density regimes ($n_e = 5.0 \times 10^{13} \text{ cm}^{-3}$) should be possible. These experiments should be carried out in a deuterium plasma using hydrogen minority heating. Scenarios using He^{3+} as the minority species are generally more successful in ion heating; however, NPA measurements of He^3 are quite limited because of the reduced probability of double charge-exchange taking place in the plasma.

REFERENCES

- ¹ M. Kwon, *Fast Wave Ion Cyclotron Resonance Heating Experiments on the Advanced Toroidal Facility*, PhD thesis, Georgia Institute of Technology, 1990.
- ² Private communications with J. F. Lyon, ORNL (1991).
- ³ A. H. Boozer, *Phys. Fluids B* **3**, 875 (1991).

Appendix A

Charge-Exchange Neutral Analysis on ATF

The main ion diagnostic on ATF is a horizontally and vertically scanning neutral particle analyzer. Neutral particle analysis is a well established diagnostic for studying ion behavior in fusion plasmas.¹ Brief descriptions of the diagnostic technique and of its advantages and disadvantages are presented in Section A.1. The design and calibration of the NPA installed on ATF is discussed in Section A.2. Finally, the equations necessary for analysis of the measured data are derived and discussed in Section A.3.

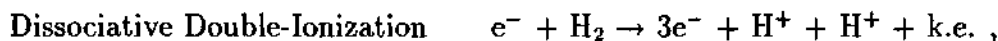
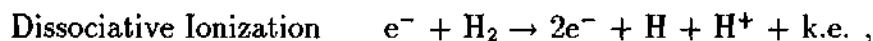
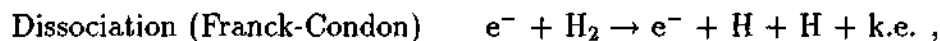
A.1 Using Charge-Exchange Neutrals as an Ion Diagnostic

Even so-called "fully ionized," high-temperature fusion plasmas are permeated by a small background of neutral hydrogen atoms. Naively, one would think that the magnitude of this neutral density would be quite small (even negligible) because the mean free path for ionization of a room-temperature neutral atom entering the plasma from the edge is typically ~ 1 cm. However, several measurements have shown that there is a significant neutral density in the central regions of the plasma.

The main source of neutral hydrogen entering the plasma column is from the plasma edge. This flux of neutrals is made up of three distinct sets of particles: (1) cold (room-temperature) hydrogen molecules desorbed from the wall because of imperfect confinement of plasma ions and electrons, (2) cold hydrogen molecules

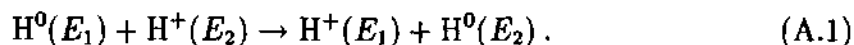
injected for plasma fueling purposes, and (3) energetic (on the order of the edge ion temperature) hydrogen atoms reflected from the limiter or walls.

As the cold hydrogen molecules (wall-desorbed and injected) enter the plasma, their population is depleted by electron dissociation and electron-impact ionization processes. Although the electron-impact ionization process has a higher cross section in the energy range of interest (electron energies ≤ 40 eV), the most important effect in the development of a substantial neutral density is the electron dissociation processes. The dissociation of a hydrogen molecule can take three forms:²



where k.e. is the small amount of kinetic energy acquired by the dissociated products in each of these processes. Studies have shown that the products of the first process (known as Franck-Condon dissociation) each acquire about 2-4 eV of energy.³ This allows the product hydrogen atoms (known as Franck-Condon neutrals) to penetrate much farther into the plasma than the room-temperature hydrogen molecules. Obviously, the energetic hydrogen atoms that are reflected from the limiter surface also penetrate quite deeply into the plasma before being ionized.

The second effect with a significant bearing on the magnitude of the neutral density in the central regions of the plasma is the resonant charge-exchange reaction (discussed in more detail in the next section):



Because this reaction is resonant, the cross section for charge-exchange is as least as large as that for electron-impact ionization for all energies and is much larger at higher energies (see Fig. A.1).⁴ Hence, the ionization of the Franck-Condon neu-

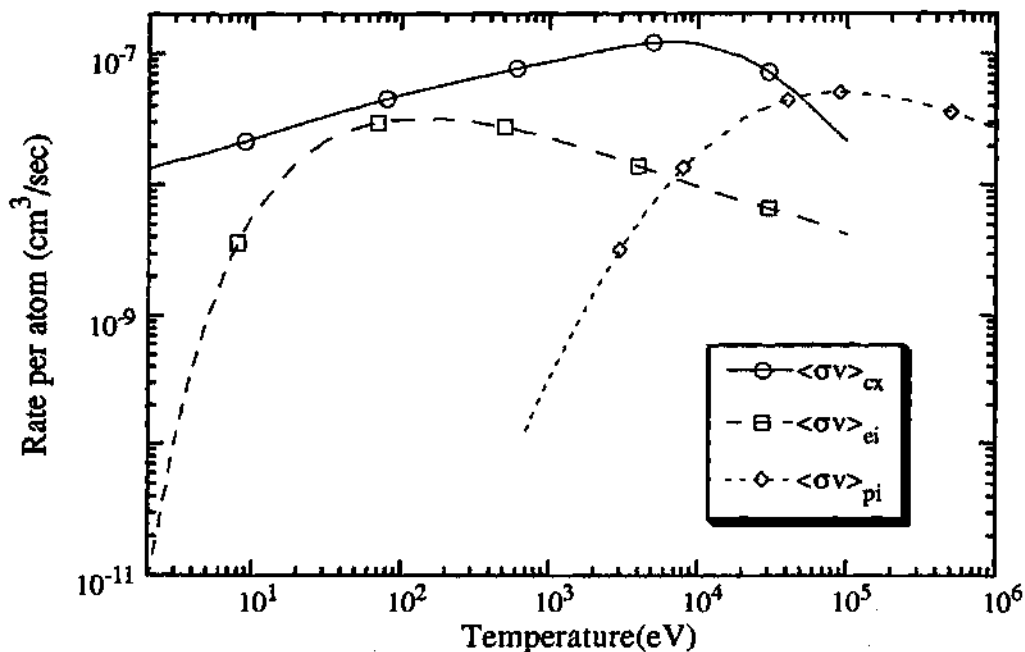


Figure A.1: Reaction rate for ionization of a neutral atom by charge-exchange ($\langle \sigma v \rangle_{cx}$), electron-impact ionization ($\langle \sigma v \rangle_{ei}$), and proton-impact ionization ($\langle \sigma v \rangle_{pi}$) [Ref. 4].

trals is mostly due to charge-exchange.² These Franck-Condon neutrals then charge-exchange with more energetic ions within the plasma, giving rise to subsequent generations of hotter neutrals, which are able to penetrate more and more deeply into the discharge. In this way, a neutral background is formed whose magnitude is large enough that its effect must be considered. If the cross section for electron-impact ionization were much greater than the cross section for resonant charge-exchange, only one generation of neutrals could exist and the neutral background could not permeate the plasma column.

Although the majority of neutral hydrogen atoms originate from these effects, other processes must also be taken into account in determining the magnitude of the neutral density. Neutral beam injection (NBI, described in Chapter 1) creates secondary neutrals (known as halo neutrals) with energies typical of the plasma ion temperature as a result of a charge-exchange event between an injected neutral and a plasma ion. Another process that increases the central neutral density is electron-

ion recombination. Because the reaction rate for this process is small, its effect is significant only in high-density plasmas. Studies have shown that in high-density plasmas, electron-ion recombination can raise the central neutral density by several orders of magnitude.⁵ Although measuring the neutral density profile has proven to be extremely difficult, several experiments have been conducted in an attempt to do so.⁶⁻⁸ Each measurement indicates that the neutral density is typically high at the periphery and much lower at the center (depending on the magnitude of the electron density).

Within the plasma, energetic ions may exchange an electron with one of the cold neutral hydrogen atoms via the resonant charge-exchange reaction [see Eq. (A.1)]. This reaction is simply an electron capture process where the particles interact only on an atomic level. There is very little kinetic energy interchange, and consequently any scattering that occurs is nearly negligible.³ Hence, the energetic neutral particle that results carries with it all the properties (energy, direction, etc.) of the original plasma ion. Furthermore, the resultant neutral particle is able to escape the plasma system readily since it does not interact with electric or magnetic fields. This reaction represents a net energy loss on the average because generally $E_2 > E_1$ and because a higher-energy neutral is more likely to escape from the plasma than a less energetic neutral.⁹ Assuming that the resultant neutral is unconfined, a net amount, $E_2 - E_1$, of plasma energy is lost in the exchange. Although this reaction is obviously undesirable from a plasma performance point of view, the escape of these fast neutrals allows a direct measurement of the ion velocity distribution by a detector located outside the plasma device. These detectors are usually called neutral particle analyzers (NPAs) or charge-exchange neutral analyzers, and the analysis of the measured data is called charge-exchange neutral analysis (CXNA).

A.1.1 Advantages of CXNA

The principal advantage of CXNA is that it affords an almost direct measurement of the plasma ion distribution, from which ion behavior (e.g., the plasma ion temperature) can be determined. Since little energy or momentum is exchanged in the charge transfer process and since the resonant hydrogen charge-exchange cross sections are well known over a wide range of energies,¹⁰ the detected neutral flux can legitimately be interpreted in terms of plasma ion behavior. Other ion diagnostics are much less direct. They depend on the neutrons resulting from deuterium-deuterium fusion reactions,^{11,12} on Doppler broadening measurements of radiation emitted by impurity ions,¹³ on far-infrared photons scattered by the Debye shielding clouds surrounding the ions,¹⁴ or on the small-angle scattering of injected neutral atoms by the plasma ions.^{15,16} Note that CXNA is currently the only developed diagnostic capable of providing a direct measurement of the ion distribution function. In most cases, the flux of escaping neutrals is sufficient to make measurements on a time scale (2–10 ms) that is shorter than the time scale of most fusion experiments (e.g., $\tau_E \simeq 10\text{--}30$ ms, $t_{\text{exp}} \simeq 200\text{--}1000$ ms), such that an effectively continuous measurement may be made.¹⁷

Since the ion distribution function is directly measured, any nonthermal effects, such as those associated with NBI or ion cyclotron heating (ICH), are directly observed, and that information can be used to assess the validity of any inference of the plasma ion temperature. Finally, CXNA is nonperturbing and uses a relatively simple apparatus to detect the escaping neutrals. Since the technique takes advantage of an inherent loss mechanism, it also provides a means to infer the magnitude of the loss itself.

A.1.2 Disadvantages of CXNA

For the reasons given in the Section A.1.1, CXNA is the principal ion diagnostic for several medium-size tokamaks and stellarators. However, as new devices become larger and extend their parameters into regimes of higher density and temperature, some difficulties in using CXNA are encountered. The neutrals measured by a CXNA diagnostic are those which originate along a chord through the plasma and whose velocities are directed toward the analyzer entrance aperture, within some small solid angle. Hence, the measured flux is in fact a chord-integrated quantity. The local birth rate at each point along this chord is proportional to the product of the local ion and neutral densities. Typical profiles are such that while the ion density and temperature tend to peak near the center, the neutral density is maximum at the edge and several orders of magnitude smaller at the center because the primary neutral sources are outside the plasma. A small fraction of these neutrals is able to cascade into the plasma core, but this fraction decreases, roughly exponentially, with plasma density. The result is that the measured spectra can be strongly dominated by contributions from the outer layers of the plasma. This difficulty worsens with increasing density and machine size and limits the usefulness of CXNA as a diagnostic technique.¹⁸

To overcome this difficulty, a common analysis method is simply to emphasize the high-energy component of the measured neutral spectra in determining the ion temperature.^{9,19} The basic premise behind this method (known as the asymptotic slope method) is that the more energetic ions must originate predominantly from the hottest regions of the plasma, despite the relative scarcity of target neutrals there. However, there are disadvantages in using this method to infer the central ion temperature. The main disadvantage is that the signal strength will be relatively weak in the energy range of interest, making it difficult to obtain useful data. Also, there is uncertainty as to how well the more energetic ions represent the

bulk plasma. Distortions of the thermal ion population are fairly common in auxiliary heated plasmas and would cause the temperature inferred from the high-energy spectrum to differ from that representative of the bulk plasma.⁹

A second method of overcoming this difficulty is to enhance the source of charge-exchange neutrals at a particular point along the viewing chord by employing a diagnostic neutral beam.²⁰ The relative enhancement due to the beam, R_b , is approximately

$$R_b = (n_b \sigma_{cx}(E_b) E_b^{1/2}) / (n_o \sigma_{cx}(E) E^{1/2}) ,$$

where n_b and E_b are the beam density and energy, n_o is the unperturbed neutral density, and σ_{cx} is the charge-exchange cross section.¹⁸ The typical method of isolating the beam contribution to the observed neutral flux is to modulate the beam during a discharge. The flux that originates from the small volume where the beam and the analyzer viewing chord intersect can then be determined. Hence, the measurement is a local measurement of the ion distribution, requiring a minimum of assumptions to interpret the data. The main disadvantage of this technique is the neutral beam injector, which is expensive and difficult to operate and maintain. Moreover, this technique, in common with passive CXNA, still must overcome the problem of transmitting the "target" neutrals to the center of the dense plasmas. The intensity of the beam is attenuated according to the equation

$$I = I_o \exp(-x/\lambda_i) ,$$

where λ_i is the mean free path against ionization of the injected neutrals. Since $\lambda_i \propto 1/n$, where n is the plasma density, the transmission of a sufficient number of "target" neutrals to the center of dense plasmas is difficult. Therefore, to obtain a significant flux enhancement in high-density plasmas, very intense or highly energetic neutral beams are required.

Since there is no diagnostic neutral beam installed on ATF, all of the NPA measurements are necessarily "passive" measurements. The analysis method used to obtain the ion temperature and other ion characteristics is discussed in Section A.3.

A.2 Neutral Particle Analyzer on ATF

The main component of the neutral particle analysis system on ATF is an $E\parallel B$ mass- and energy-analyzing spectrometer developed at Princeton Plasma Physics Laboratory and similar to analyzers used on TFTR.²¹ The main components of this spectrometer are shown schematically in Fig. A.2. The analyzer consists of two chambers, with the main chamber containing the field region and the detector and the smaller chamber housing the stripping cell. These two chambers are differentially pumped by a turbomolecular pump such that the main chamber pressure is maintained near 10^{-6} torr while the stripping cell pressure is maintained near 10^{-3} torr. Neutral atoms entering the analyzer are first incident on the stripping cell filled with helium gas. The stripping cell is 26 cm long with 1.5-mm-diam apertures on each end. The stripping cell pressure is maintained at a steady level by feedback control between a high-pressure ionization gauge located just outside the stripping cell and a gas-control system that feeds helium gas directly into the stripping cell area.

The ions exiting the stripping cell are then mass- and energy-analyzed in the $E\parallel B$ field region in the manner shown in Fig. A.3. Upon exiting the stripping cell, the ions enter perpendicularly into a semicircular sector of parallel magnetic and electric fields. While traversing a semicircular arc due to the magnetic field (magnitude B), the ions are displaced parallel to the electric field, E . The time of flight between entering the field region and arriving at the collector is simply a function of the gyrofrequency of the j th species, which is independent of the velocity

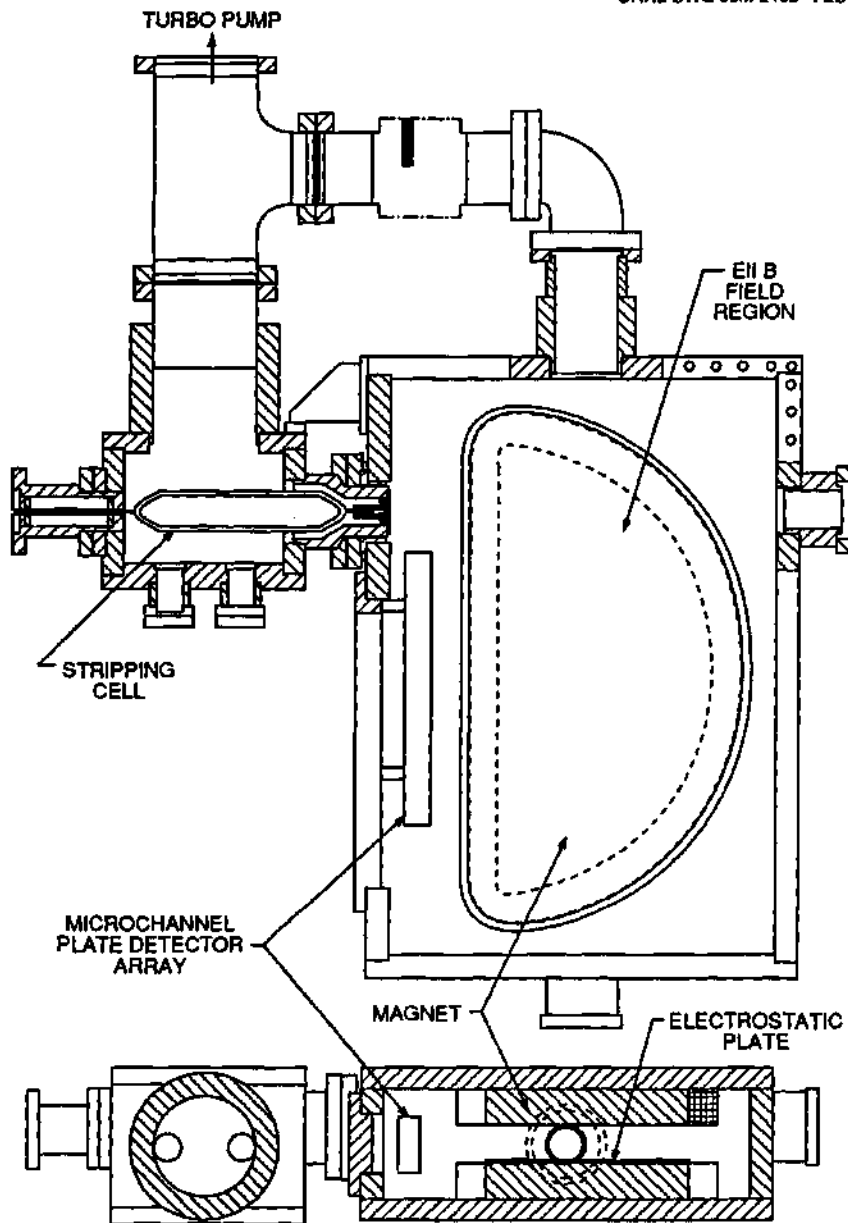


Figure A.2: Schematic of the $E||B$ analyzer used on ATF

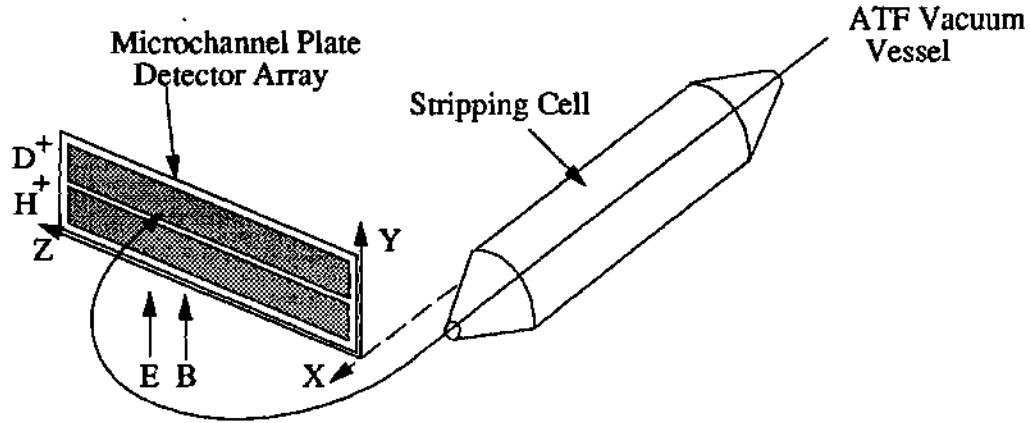


Figure A.3: Schematic of how the $E||B$ design selects mass and energy of incoming ion.

of the particle:

$$t_j = \frac{\pi}{\Omega_j} = \frac{\pi}{B} \left(\frac{m}{q} \right)_j,$$

where Ω_j is the gyrofrequency for the j th species. The displacement of species j parallel to the electric field is given by

$$Y_j = \frac{1}{2} \left(\frac{q}{m} \right)_j E t_j^2 = \frac{\pi^2}{2} \left(\frac{E}{B^2} \right) \left(\frac{m}{q} \right)_j,$$

which is also independent of velocity, so that all particles of a given m/q ratio are displaced along the electric field direction by the same amount. The ion species $(m/q)_j$ entering with velocity v_k is displaced a distance

$$Z_{jk} = 2 \times r_L = \frac{2}{B} \left(\frac{m}{q} \right)_j v_k$$

by the magnetic field from the entrance point in a direction perpendicular to $\vec{v}_k \times \vec{B}$. The collection plane thus exhibits parallel columns of analyzed ions, each column containing energy dispersed ions of a given m/q ratio.

The magnetic field for the NPA described here is provided by a 60-cm-diam D-shaped electromagnet. The electric field is produced between one magnet pole face at ground potential and a negatively biased, D-shaped electrode mounted

against, but electrically insulated from, the opposite pole face. The analyzer has 3.2-cm-thick soft iron walls, which provide the return yoke for the electromagnet and sufficient shielding of the detector against possible noise sources such as X-rays and neutrons.

A large, multianode, chevron multichannel plate (MCP) is used for particle detection.²² The detector is composed of three 4.5- by 13-cm independently biased subsections assembled together for a 39-cm total length. The anodes are arrayed in two mass columns with each column having 75 discrete energy channels. Each energy channel anode is 0.4 cm wide with a 0.1 cm separation between adjacent anodes. The anodes on the first mass column are 2.0 cm high while those on the second mass column are only 1.5 cm high. The mass columns are configured such that there is 2.25-cm center-to-center separation. To suppress cross talk between adjacent channels, every other anode on each subsection is grounded, leaving 39 available channels per mass column.

To provide horizontal and vertical scanning capability, the analyzer has been mounted on the carriage shown in Fig. A.4.²³ The carriage is moved horizontally on a rail supported about 2 m above floor level. For vertical movement, two 2-m drive screws mounted on each side of the analyzer drive the analyzer along the vertical track shown in Fig. A.4. When the analyzer is scanned horizontally, its viewing angle can be changed from perpendicular to tangential (in both directions) to the axial magnetic field. When the analyzer is scanned vertically, it can view from below to above the plasma column of ATF.

The location of the pivot point was chosen so as to provide maximum viewing capabilities for the analyzer. Finding the optimum location for this pivot point proved to be fairly difficult. Because of the complex orbit topology of ions in ATF and the corresponding loss regions (see Fig. 4.14), the analyzer must be able to scan from tangential to the magnetic field (in both directions) to perpendicular to the

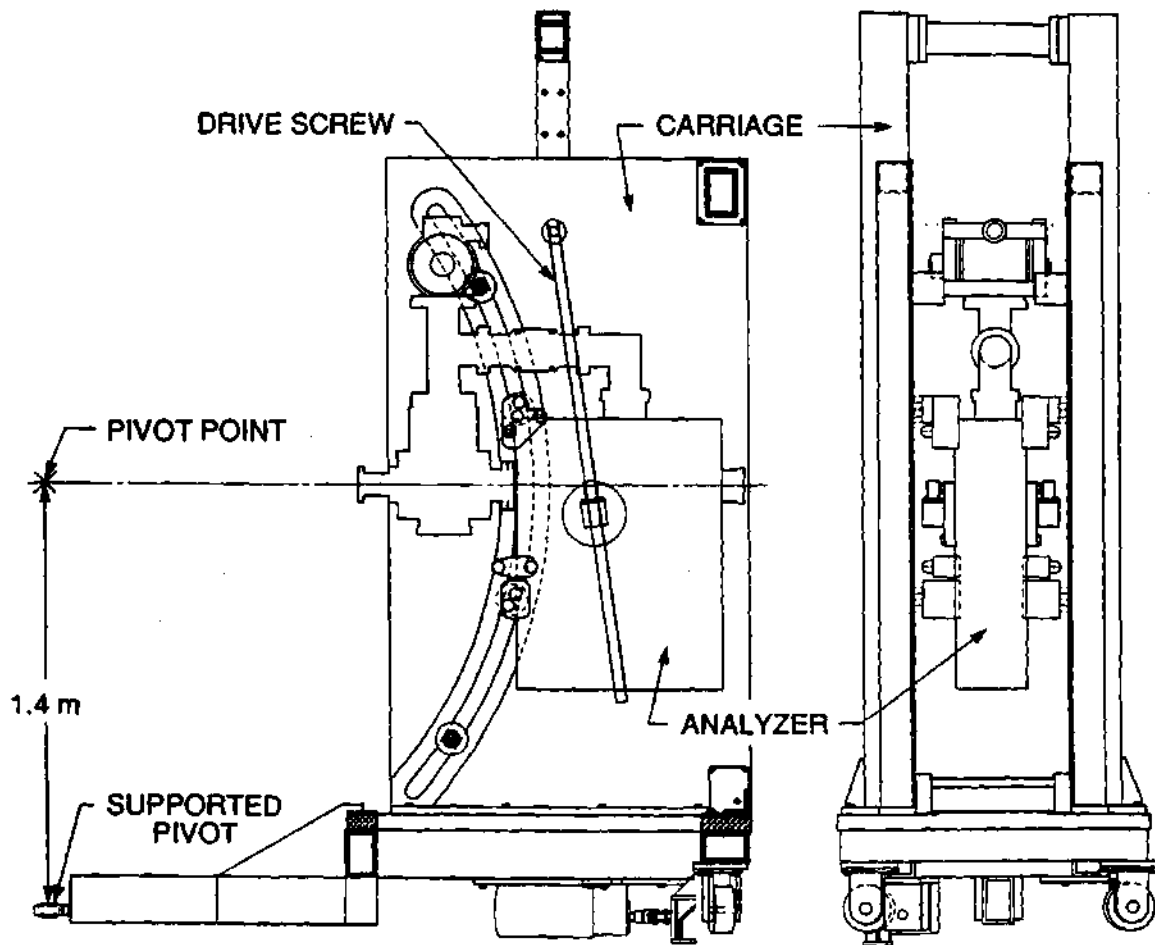


Figure A.4: Side and rear views of the analyzer in the moving carriage. The analyzer is designed with an unsupported pivot point in the sight line and rotates horizontally about a fixed point located directly below the real pivot point. The analyzer moves horizontally on the wheels shown at the bottom. The vertical motion is produced by a pair of 2-m drive screws that move the analyzer on the curved vertical track [Ref. 23].

magnetic field. This allows the analyzer to view all classes of orbits in ATF and to detect the tangentially injected beam ions before they enter a loss region. To avoid having the sightline blocked by the outer wall of the ATF vacuum vessel, the pivot point was chosen to be reentrant to the vacuum vessel.

Because of limited access to this pivot point, the carriage was designed so that the pivot point remained fixed while being unsupported (i.e., the pivot point is not held mechanically rigid). The final design, as shown in Fig. A.4, fixes the horizontal pivot point by providing a rigid pivot point 1.4 m directly below the nominal pivot point of the analyzer. In the vertical direction, the arc of the curved track on the carriage (see Fig. A.4) was chosen so that the sightline of the analyzer passes through the pivot point at all vertical angles. Alignment tests confirm that the analyzer does in fact rotate about this pivot point, with the sightline passing within $\simeq 2$ mm of the pivot point at all horizontal and vertical angles. The sightline of the analyzer is connected to the ATF vacuum vessel by a small flexible bellows designed to handle all possible analyzer positions.

A.2.1 Data Acquisition and Control System

The signal handling and data acquisition system for the NPA is depicted in Fig. A.5. The signal processing electronics for each anode consist of a charge-sensitive buffer circuit located inside the vacuum at the back of the detector and a preamplifier/discriminator (PAD) located outside the vacuum but close to the analyzer. The buffer circuit converts charge pulses (originating from the MCPs) to voltage pulses. These pulses are then sent into combined pulse amplifiers and discriminators that provide TTL level pulses. These TTL pulses are then sent to a CAMAC system using BiRa scalers with local memory.²⁴ The scalers are gated at a variety of data acquisition rates by a Jorway time sequencing module²⁵ driven by a LeCroy clock.²⁶ All of the available 78 channels are fully instrumented, and enough

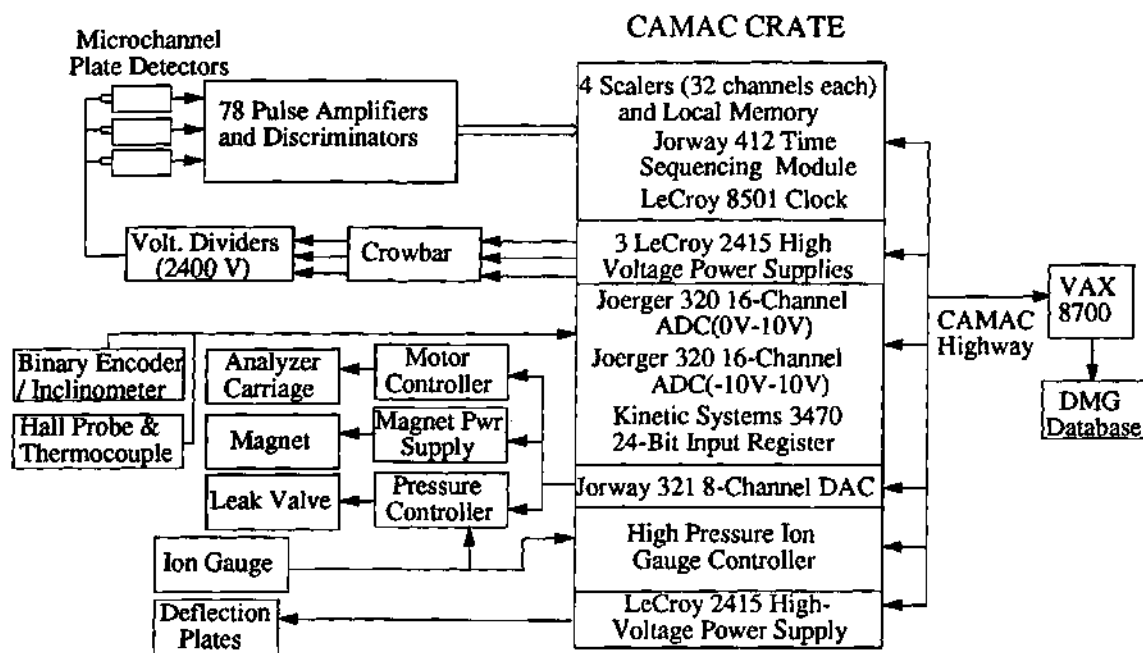


Figure A.5: Schematic of the signal and data acquisition system for the NPA.

memory is available for all channels to be used simultaneously.

The biasing for the microchannel plate detectors is controlled by three LeCroy high-voltage power supplies²⁷ (one for each plate). The output of these modules is routed through a high-voltage crowbar (to prevent high voltage on the plates when the analyzer pressure is too high) and a voltage divider. The deflection voltage for the electric field is also controlled by the same type of power supply. The computer-programmed output of a Jorway 8-channel digital-to-analog converter²⁸ (DAC) controls the position of the analyzer through the motor controller, the current supplied to the magnet from the magnet power supply, and the setpoint for feedback control of the stripping cell pressure.

Two Joerger 16-channel analog-to-digital converters²⁹ (ADCs) (one configured for inputs 0 V to +10 V and another for -10 V to +10 V) monitor the magnetic field measured by a Hall probe, the cell pressure measured by an ionization gauge, the vertical angle of the analyzer measured by an inclinometer, and the readouts of various components of the analyzer vacuum system (such as baratron pressures and turbopump speed). The output of the binary encoder is monitored by a Kinetic Systems input register.³⁰ The voltages applied across both the microchannel plates and the electric field deflection plates are monitored by the LeCroy high-voltage power supplies.

To incorporate the available information into a user interface, a control program has been developed for remotely changing and monitoring the settings of the various analyzer components. This program continuously monitors all of the available signals from the NPA and displays them on a computer terminal. The user can modify most analyzer settings (magnetic and electric fields, cell pressure, etc.) to values required by the experiment.

At the end of each discharge, the signals of the 78 energy channels along with all information pertaining to the status of the analyzer are read through a serial

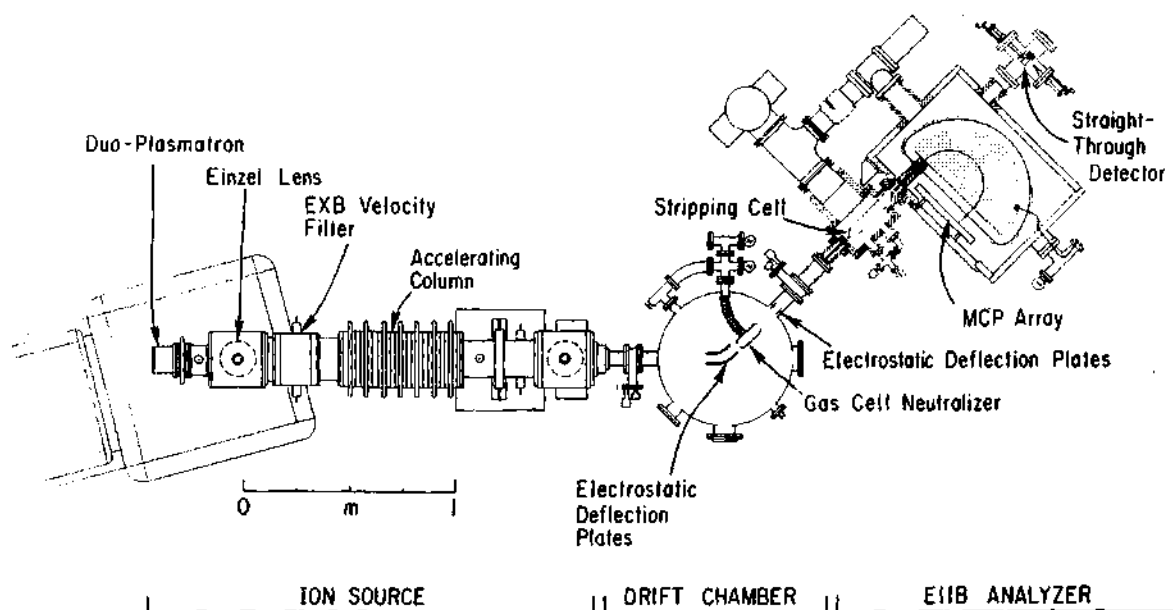


Figure A.6: Schematic of the calibration facility, which consists of an ion source, drift chamber, and the $E||B$ analyzer [Ref. 34].

highway driver to a VAX 8700.³¹ The data is stored in the ATF Data Management System³² for later recall. A data analysis package then reads the raw data and displays plots of the analyzed data between ATF shots. This analysis package is menu-driven (full-screen menus) and provides the user with a large degree of flexibility in both data analysis and data display.

A.2.2 Calibration of NPA components

To provide accurate measurements, various characteristics of the detection system of the NPA must be calibrated. These characteristics include the ionization (stripping) efficiency of the stripping cell versus cell pressure and incident neutral energy, the energy resolution of each detector element, and the relative detection efficiency of each detector element. A diagram of the facility³³ used to calibrate the NPA is shown in Fig. A.6. An ion beam is extracted from the ion source and accelerated into the drift chamber. This beam is then neutralized by a neutralizer cell located in the drift chamber, and all residual ions are then removed from the

beam by electrostatic deflection plates. The resulting neutral beam is then directed into the NPA, which is equipped with an additional microchannel plate detector located on the straight-through port.

This facility was used to determine the variation of the stripping efficiency η_{sj} with energy and pressure in the following manner.³⁴ First, the count rate at the straight-through detector was measured with helium gas in the stripping cell and no applied magnetic field. In this case, the measured count rate corresponds to the rate of particles (neutrals and ions) exiting the stripping cell. Second, the same measurement was carried out with a 2-kG applied magnetic field, in which case the measured count rate corresponds to the rate of neutrals exiting the stripping cell. Finally, the same measurement was carried out with no gas in the stripping cell, in which case the measured count rate represents the incident count rate. The stripping efficiency was then computed from the difference between the count rates with the deflection magnet turned on and off divided by the incident count rate. The dependence of the stripping efficiency on energy and pressure was determined by repeating this procedure with different settings of the ion source acceleration voltage and the analyzer stripping cell pressure. For a given stripping cell pressure, a polynomial fit was then used to produce smooth curves for data analysis purposes. The results of these fits are shown in Fig. A.7, where the stripping efficiency versus particle energy is shown for five different stripping cell pressures.

The energy resolution of each detector channel was also calibrated using this facility in the following manner. A monoenergetic beam from the ion source was energy-analyzed by a magnetic field chosen such that the beam was focused on a particular anode of the detector array. Because of the finite size of the stripping cell apertures and stray fields in the magnetic field region, the beam was not entirely focused on a single anode. Hence, signal was expected to be present on adjacent anodes (or energy channels). The measured energy resolution, defined as the FWHM

of the measured energy distribution of this monoenergetic beam, is shown in Fig. A.8 along with the theoretically expected value. This theoretically expected value,

$$\frac{\Delta E}{E} = \frac{\Delta Z_j}{Z_j},$$

is simply a function of displacement along each mass column. Here, ΔZ_j is the width of each anode, and Z_j is the distance of the j th anode from the stripping cell aperture.

Finally, a relative detection efficiency was measured for each channel in the following manner. A monoenergetic beam from the ion source was energy-analyzed by a slowly varying magnetic field in the analyzer such that the beam was swept from the first anode to last anode fairly slowly. A relative detection efficiency for each anode was then determined by normalizing the measured count rate for each anode against a chosen reference anode. The measured detection efficiencies for both mass columns are given in Table A.1.

As evidenced by Fig. A.7, an accurate measurement of the stripping cell pressure is important in determining the overall detection efficiency of the analyzer. This pressure is measured by a high-pressure ionization gauge located just outside the stripping cell. Since the stripping cell is filled with helium gas and the ionization gauge readings are calibrated for hydrogen gas, a correction factor must be determined so that the gauge readings can be converted to true pressures of helium gas. This gauge factor was determined by calibrating the readings of the ionization gauge against an MKS baratron gauge and a spinning rotor gauge. The gauge factor was found to be approximately 4.0, which is consistent with the difference in the ionization energies of helium and hydrogen.

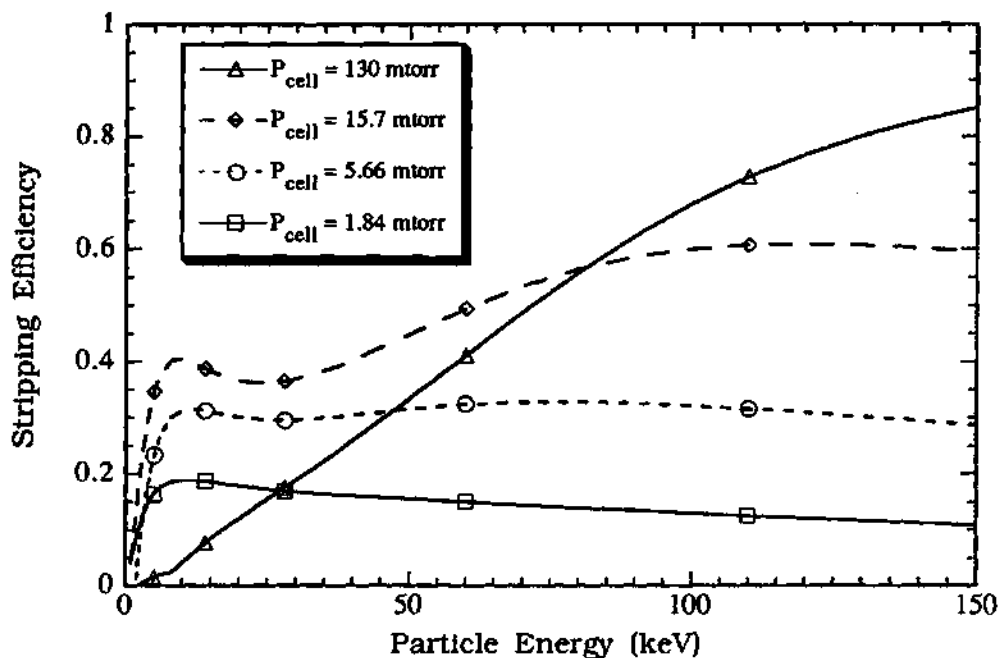


Figure A.7: Stripping efficiency versus energy for various stripping cell pressures (using helium gas). These curves are the best polynomial fits to the measured data.

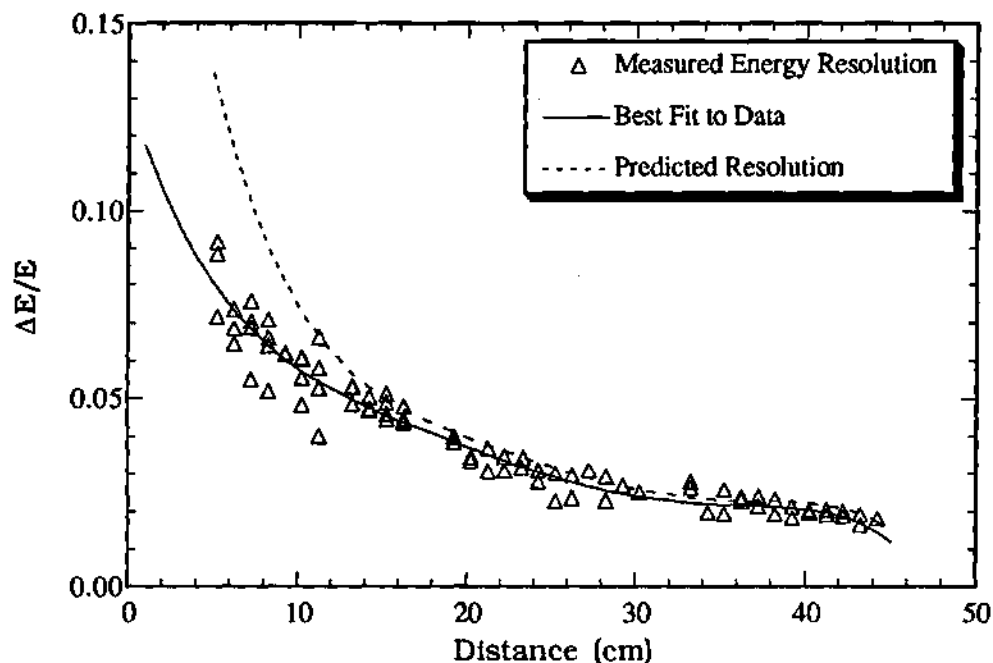


Figure A.8: Variation of the measured energy resolution ($\Delta E/E$) as a function of the distance along the detector array. There is a one-to-one correspondence between this distance and particular anodes. Also shown are the best polynomial fit to the measured data, which is used for data analysis purposes, and the best fit to the theoretically expected value of the energy resolution.

Table A.1: Relative detection efficiency of NPA energy channels.

Anode Number	Relative Detection Efficiency	
	Mass Column 1	Mass Column 2
1	0.38	X ^a
2	0.45	0.32
3	0.58	0.66
4	0.71	0.62
5	0.74	0.68
6	0.56	0.78
7	0.59	0.74
8	0.81	0.78
9	1.05	0.87
10	1.04	0.85
11	0.90	0.81
12	0.86	0.76
13	0.88	0.86
14	0.97	0.93
15	1.06	1.08
16	1.00 (Ref) ^b	1.00 (Ref)
17	0.98	0.99
18	1.02	0.96
19	1.01	0.99
20	1.06	1.01
21	0.91	0.97
22	1.02	1.03
23	1.01	0.99
24	0.92	1.05
25	1.03	0.97
26	X	1.00
27	1.09	0.90
28	1.27	0.96
29	0.89	0.92
30	0.92	0.87
31	0.92	0.92
32	0.86	0.81
33	0.91	0.83
34	0.92	0.68
35	0.95	0.81
36	0.97	0.77
37	0.93	0.78
38	0.93	0.83
39	0.47	X
^a X - Anode not operational.		
^b Ref - Reference channel.		

A.3 Data Analysis

Although the measurement of the escaping neutral flux is quite simple, the analysis of the obtained data is generally quite complicated. This is because the measured flux is dependent on many plasma parameters. The dependence of the theoretically expected neutral flux on these parameters is derived in Section A.3.1. The raw data collected by the NPA are in the form of measured count rates; to compare the measured data to the theoretically expected flux, a conversion must be made from the raw data to an experimental flux. This conversion is explained in Section A.3.2. The method by which ion temperatures are obtained from these data is then presented in Section A.3.3.

A.3.1 Theoretical Flux

Energetic neutrals of velocity \vec{v} are produced in a plasma primarily by charge exchange between neutral atoms and ions of that velocity. To a lesser extent, neutrals are also produced by ion-impurity and ion-electron recombination. The importance of the former increases with ion energy and that of the latter with density. Once born, neutrals either escape from the plasma or are reionized by electron-impact ionization, proton-impact ionization, or a subsequent charge-exchange event before they reach the edge.

The total neutral birth rate at a position s within the plasma along the analyzer sightline is given by

$$\begin{aligned} R_o(s) &= R_{cx}(s) + R_{rec}(s) \\ &= n_o(s)n_i(s) \int d\vec{v}_o f_o(s, \vec{v}_o) \int d\vec{v} f_i(s, \vec{v}) \sigma_{cx}(|\vec{v} - \vec{v}_o|) |\vec{v} - \vec{v}_o| \\ &\quad + n_e(s)n_i(s) \int d\vec{v}_e f_e(s, \vec{v}_e) \int d\vec{v} f_i(s, \vec{v}) \sigma_{rec}(|\vec{v} - \vec{v}_e|) |\vec{v} - \vec{v}_e|, \end{aligned} \quad (A.2)$$

where $n_o(s)$, $n_i(s)$, and $n_e(s)$ represent the neutral, ion, and electron densities at

position s , respectively; $f_o(s, \vec{v}_o)$, $f_i(s, \vec{v})$, and $f_e(s, \vec{v}_e)$ represent the neutral, ion, and electron velocity distributions at position s , respectively; and σ_{cx} and σ_{rec} are the cross sections for charge-exchange and electron-ion recombination, respectively. Although the contribution of recombination is negligible in a moderate-density device, it is retained here for completeness and would become important for sufficiently dense plasmas.⁵

Equation A.3 can be simplified in several ways. First, the small electron-ion mass ratio essentially guarantees that the electron velocity will always be much greater than the ion velocity. Therefore, $|\vec{v} - \vec{v}_e| \simeq v_e$ and the recombination term can be rewritten as

$$R_{rec}(s) = n_e(s)n_i(s) \int d\vec{v} f_i(s, \vec{v}) \int d\vec{v}_e f_e(s, \vec{v}_e) \sigma_{rec} v_e. \quad (A.3)$$

If the electron velocity distribution is assumed to be Maxwellian, the second integral in Eq. (A.3) can be evaluated. This quantity is commonly called the electron-ion recombination rate coefficient, $\langle \sigma v_e \rangle_{rec}$. Experimentally determined values for this quantity can be found in Ref. 35.

The other double integral in Eq. (A.3) is more difficult to reduce analytically. The double integral can be evaluated computationally assuming a Maxwellian distribution for the neutral distribution and a delta function velocity distribution for the ion distribution (or vice versa).³⁵ The result of such a calculation is shown in Fig. A.9. From this figure, it is apparent that the reaction rate is essentially constant for neutral temperatures below the ion energy. In general, the energy range measured by the NPA is much greater than the local neutral temperature (or ion temperature). Hence, the neutral temperature can be taken to be zero without loss of accuracy in this calculation. This effectively reduces the neutral velocity distribution to a Dirac delta function, $\delta(\vec{v}_o)$, and the double integral can be reduced to $\int d\vec{v} f_i(s, \vec{v}) \sigma_{cx}(v) v$.

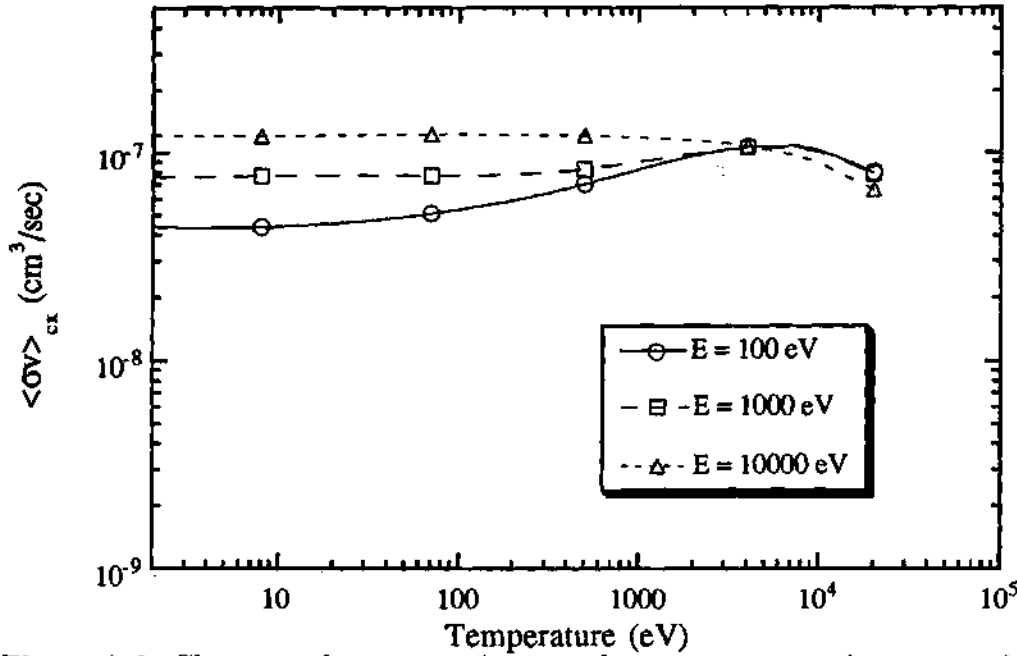


Figure A.9: Charge-exchange reaction rate for a monoenergetic proton with energy E passing through a Maxwellian neutral distribution with temperature T .³⁵

The total neutral birth rate due to charge-exchange and ion-electron recombination at position s is then given by

$$R_o(s) = n_i(s) \int d\Omega \int dv v^2 f_i(s, v, \Omega) [n_o(s) \sigma_{cx} v + n_e(s) \langle \sigma v_e \rangle_{rec}] . \quad (A.4)$$

Here, the integration over $d\vec{v}$ has been replaced by an integration over speed dv and direction $d\vec{\Omega}$.

The NPA has a fixed viewing angle and thus can only detect those neutrals originating at position s that have trajectories along the entrance axis of the analyzer. Therefore, the birth rate of neutrals detectable by the NPA emitted from position s is

$$\mathcal{R}_o(s) = n_i(s) \int dv v^2 f_i[s, v, \Omega_{view}(s)] [n_o(s) \sigma_{cx} v + n_e(s) \langle \sigma v_e \rangle_{rec}] . \quad (A.5)$$

For the purposes of CXNA, a spherical coordinate system is usually chosen for velocity space with the axis of symmetry ($\theta = 0$) oriented in the direction of the local magnetic field, $\hat{b}(s)$. The system is assumed to be azimuthally symmetric.

The distribution function is usually chosen to be of the form $f_i[s, v, \xi(s)]$, where $\xi(s) = \cos \theta = \vec{\Omega} \cdot \hat{b}(s)$.

Writing the "viewed" ion distribution function as $f_i[s, E, \xi_{\text{view}}(s)]$ and changing the integration in Eq. (A.5) from an integral over v to an integral over E (where $E = mv^2/2$), one finds that the detectable neutral birth rate can be written as

$$\begin{aligned} \mathcal{R}_o(s) = & n_i(s) \int dE \left(\frac{E\nu^2}{2A^2} \right) f_i[s, E, \xi_{\text{view}}(s)] \\ & \times \left\{ n_o(s) \sigma_{\text{cx}}(E) + \left(\frac{A}{E\nu} \right)^{1/2} n_e(s) \langle \sigma v_e \rangle_{\text{rec}} [T_e(s)] \right\}. \end{aligned} \quad (\text{A.6})$$

Here, A is in amu and ν is defined such that $\nu = 2A/m = 1.93 \times 10^{12} \text{ cm}^2/\text{sec}^2/\text{eV}$. The birth rate of neutrals with energy E at position s is simply the integrand of Eq. (A.6),

$$\begin{aligned} S(s, E) = & 1.8625 \times 10^{24} n_i(s) \left(\frac{E}{A^2} \right) f_i[s, E, \xi_{\text{view}}(s)] \\ & \times \left\{ n_o(s) \sigma_{\text{cx}}(E) + \left(\frac{A}{E\nu} \right)^{1/2} n_e(s) \langle \sigma v_e \rangle_{\text{rec}} [T_e(s)] \right\}. \end{aligned} \quad (\text{A.7})$$

Once a neutral particle has been produced, it is free to move across the magnetic field lines and escape from the plasma. However, the neutral may be reionized by electron-impact ionization, proton-impact ionization, or even a subsequent charge-exchange event before exiting the plasma. This attenuation of the neutral flux must be taken into account, especially in high-density plasmas. The amount of attenuation is governed by the equation

$$\frac{d\phi_o(s)}{ds} = -\frac{1}{\lambda(s)} \phi_o(s)$$

where $\phi_o(s)$ is the neutral flux at position s and $\lambda(s)$ is the local mean free path against ionization,

$$\frac{1}{\lambda(s)} = \frac{1}{v} [n_i(s) \langle \sigma v \rangle_{\text{cx}} + n_e(s) \langle \sigma v \rangle_{\text{ei}} + n_i(s) \langle \sigma v \rangle_{\text{pi}}].$$

Here, $\langle\sigma v\rangle_{cx}$, $\langle\sigma v\rangle_{ei}$, and $\langle\sigma v\rangle_{pi}$ represent the reaction rate coefficients for charge-exchange, electron-impact ionization and proton-impact ionization, respectively.

The escape probability is defined as the ratio of the number of neutrals that reach the edge of the plasma to the number produced at position s with energy E ,

$$\begin{aligned} P(s, E) &= \frac{\phi_{o,edge}}{\phi_o(s)} \\ &= \exp \left\{ - \left[\int_s^{edge} \frac{1}{\lambda(s', E)} ds' \right] \right\}. \end{aligned} \quad (A.8)$$

Finally, the flux that the analyzer should measure can be computed. The flux that the NPA should measure consists of those particles born at some point along the analyzer's sightline with velocity vector parallel to this sightline that are not subsequently reionized before exiting the plasma. Analytically, the flux should have the form (neglecting the electron-ion recombination contribution)

$$\begin{aligned} \phi_o(E) &= \int_{chord} ds \mathcal{S}(s, E) P(s, E) \\ &= 1.8625 \times 10^{24} \frac{\sigma(E)E}{A^2} \int_{chord} ds n_o(s) n_i(s) f_i[s, E, \xi_{view}(s)] P(s, E). \end{aligned} \quad (A.9)$$

Hence, if the values of $T_e(s)$, $n_e(s)$, $n_i(s)$, and $n_o(s)$ were available, the ion energy distribution $f_i[s, E, \xi_{view}(s)]$ could apparently be extracted.

Most of this information is available from experimental measurements. The electron density $n_e(r)$ and electron temperature $T_e(r)$ profiles are obtained by laser Thomson scattering measurements.³⁶ The hydrogen density profile is generally taken to be a constant fraction of the electron density. The ion deficiency n_H/n_e can be calculated using the definition³⁷

$$n_e Z_{eff} = \sum_i n_i Z_i^2, \quad (A.10)$$

where n_i and Z_i are the density and charge of the i th ion species. The quantity Z_{eff} can be identified as the average ionic charge available for momentum transfer and

is generally determined from the plasma resistance or from visible bremsstrahlung measurements.³⁸ The ion deficiency is then given by

$$\frac{n_H}{n_e} = Z_{\text{eff}} - \sum_I \frac{n_I Z_I^2}{n_e}, \quad (\text{A.11})$$

where n_H represents the hydrogen density and the sum now only includes impurity ions. The application of Eq. (A.11) requires accurate density profiles for each of the impurity species. Since impurity density profiles are difficult to obtain, the sum in Eq. (A.11) usually includes only the contributions of the major impurity ions in the plasma. In the absence of any impurity density profiles, it is sufficiently accurate to estimate the ion deficiency by including only the dominant impurity species in the sum. Invoking quasi-neutrality, $n_e = \sum n_i Z_i$, the ion deficiency can be calculated using the formula⁹

$$\frac{n_i}{n_e} = \frac{Z_0 - Z_{\text{eff}}}{Z_0 - 1}, \quad (\text{A.12})$$

where the charge state of the dominant impurity species Z_0 can be determined spectroscopically.

Unfortunately, the neutral density profile has proven more difficult to measure experimentally. Hence, numerical codes are generally used to provide self-consistent neutral density profiles with measured electron density and temperature profiles used as experimental inputs. To properly formulate the problem of neutral hydrogen transport, the Boltzmann equation [Eq. (2.50)] must be used. Conceptually, this problem could be handled by the fluid equations, but because the scale length of the background plasma may be shorter than the mean free paths for ionization or charge-exchange of the neutrals, the validity of this treatment is questionable.³⁹ The steady-state kinetic equation for the neutral distribution is⁹

$$\begin{aligned} \nabla \cdot n_o(\vec{r}) \vec{v} f_o(\vec{r}, \vec{v}) = & -n_o(\vec{r}) f_o(\vec{r}, \vec{v}) \{n_e(\vec{r}) \alpha_{ei} [T_e(\vec{r})] + n_i(\vec{r}) \langle (\sigma_{cx} + \sigma_{pi}) |\vec{v} - \vec{v}_i| \rangle \} \\ & + n_o(\vec{r}) n_i(\vec{r}) f_i(\vec{r}, \vec{v}) \langle \sigma_{cx} |\vec{v} - \vec{v}_o| \rangle + S_o(\vec{r}, \vec{v}), \end{aligned} \quad (\text{A.13})$$

where $n_o(\vec{r})$, $n_i(\vec{r})$, and $n_e(\vec{r})$ are the neutral, ion, and electron densities, respectively; $\alpha_{ei}[T_e(\vec{r})]$ is the ionization rate due to electron-impact ionization; σ_{cx} and σ_{pi} are the cross sections for charge-exchange and proton-impact ionization, respectively; and $f_o(\vec{r}, \vec{v})$ and $f_i(\vec{r}, \vec{v})$ are the neutral and ion velocity distributions at position \vec{r} . The first term on the right-hand side of Eq. (A.13) contains the losses due to electron-impact ionization, charge-exchange, and proton-impact ionization. The second term represents "creation" of neutrals by charge-exchange. Typical source terms that can be included in S_o are

- (1) Franck-Condon neutrals resulting from dissociation of molecular hydrogen that has been desorbed from the wall or introduced by gas fueling,
- (2) energetic neutrals resulting from energetic ions being reflected from the limiter,
- (3) thermal neutrals resulting from charge-exchange trapping of injected neutrals by plasma ions,
- (4) thermal neutrals resulting from recombination of plasma ions and electrons, and
- (5) cold neutrals resulting from pellet ablation.

In general, Eq. (A.13) is typically solved on a one-dimensional grid using either a slab model⁴⁰ or a cylindrical model.³⁹ The reliability of calculating the neutral density profile from this equation is fairly good since Eq. (A.13) is linear, the neutral trajectories are independent of electromagnetic forces, and the atomic physics is reasonably simple. In fact, a number of codes that solve Eq. (A.13) have been written by several authors and are in substantial agreement with one another.^{39,41}

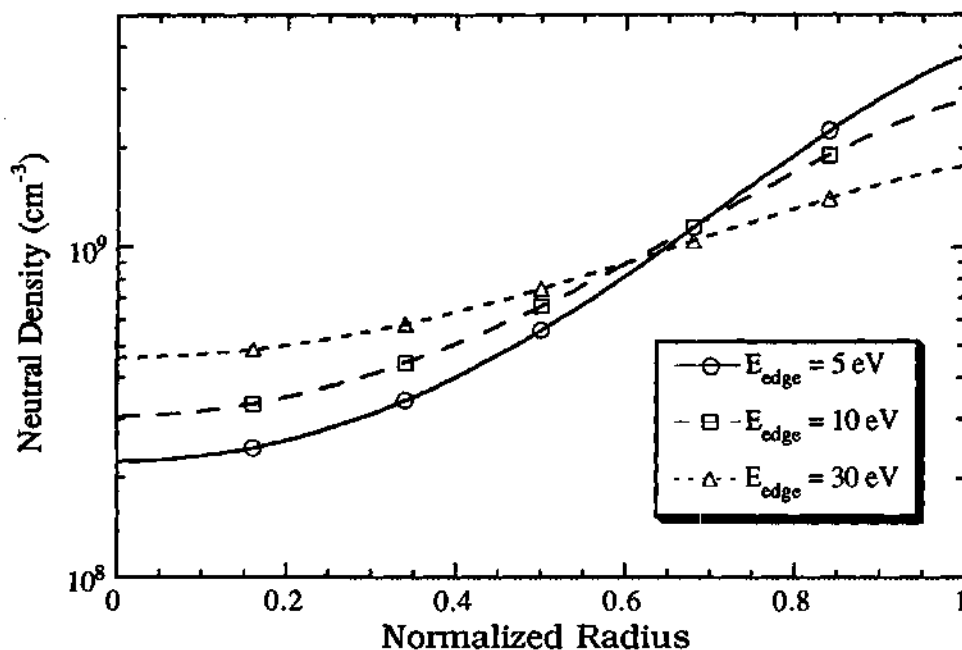


Figure A.10: Variation of calculated neutral density with assumed average edge neutral energy. All parameters are held fixed except for the assumed average edge neutral energy.

The main problem with computing the neutral density profile is the proper choice for the average edge neutral energy. As discussed in Section A.1, there are several sources of neutrals streaming into the plasma, with each process having a different characteristic energy. For example, the Franck-Condon neutrals usually have approximately 5 eV of energy, while the neutrals reflected from the limiter surface may have energies up to 2-3 times the plasma edge temperature (~ 50 eV). Since these higher-energy neutrals penetrate into the plasma column farther than the Franck-Condon neutrals, the neutral density at the center is necessarily higher. For a fixed neutral source rate at the edge, the corresponding edge neutral density must decrease. This effect is shown in Fig. A.10. Hence, solving for the neutral density profile using Eq. (A.13) and assuming two justifiable average edge neutral energies could lead to radically different neutral density profiles. Experimentally, the average edge neutral energy has proven very difficult to measure. Hence, the calculations are left with an uncertain boundary condition that affects not only the

magnitude of the neutral density profile but also its shape.

The standard method of computing the neutral density profile in this work is to solve Eq. (A.13) with a cylindrical neutrals transport code.³⁹ The neutral source is defined by two user-defined inputs: (1) the global confinement time, which provides an estimate of the source rate from the wall, and (2) the average edge neutral energy, which determines the degree of penetration of the neutral influx. The global confinement time τ_p in steady-state ATF discharges can generally be estimated from H_α signals and from the estimated neutral density measured by the NPA. However, the average edge neutral energy E_{edge} generally cannot be quantified. For most of the cases analyzed in Chapters 5 and 6, E_{edge} is assumed to be 5 eV.

A.3.2 Experimental Flux

For a given energy channel, j , of the NPA, data are collected in the form of counts, N_j , detected during a selected time interval, Δt . The count rate, $C_j = N_j/\Delta t$, can be related to the neutral source rate $\mathcal{S}(s, E)$ [given by Eq. (A.7)] by the equation¹⁹

$$C_j = \eta_{Dj} \eta_{sj} \int \Delta E_j \frac{\Delta \Omega}{4\pi} \mathcal{S}(s, E) P(s, E) A \, ds ,$$

where η_{Dj} is the detection efficiency of the j th detector, η_{sj} is the stripping efficiency at energy E_j , ΔE_j is the energy bandwidth of the j th detector, $\Delta \Omega$ is the solid angle of the analyzer system, A is the area viewed by the analyzer, and $P(s, E)$ is the escape probability given by Eq. (A.8). The solid angle of the analyzer is $\Delta \Omega = A_{\text{ent}}/l_{\text{cell}}^2$ where A_{ent} is the area of the entrance aperture of the stripping cell and l_{cell} is the length of the stripping cell. The area viewed by the plasma is given by the the area of the exit aperture of the stripping cell, A_{exit} .

An energy-independent geometric efficiency F_j can be defined for the j th

detector as

$$F_j = \eta_{Dj} \left(\frac{A_{\text{ent}}}{4\pi l_{\text{cell}}^2} A_{\text{exit}} \right) \left(\frac{\Delta E_j}{E_j} \right).$$

Noting that F_j is independent of the integration variable ($A\Delta\Omega$ does not vary along s), the following equation can be written for the theoretically expected count rate of the j th detector:

$$C_j = F_j \eta_{sj} E_j \phi_o(E),$$

where $\phi_o(E)$ is given by Eq. (A.9).

The measured flux can thus be expressed in terms of the measured count rate C_j by the equation

$$\begin{aligned} \phi_{\text{meas}}(E_j) &= \frac{C_j}{F_j \eta_{sj} E_j} \\ &= \frac{N_j}{A_{\text{ent}} \frac{A_{\text{exit}}}{4\pi l_{\text{cell}}^2} \left(\frac{\Delta E}{E} \right)_j E_j \eta_{sj} \eta_{Dj} \Delta t}. \end{aligned} \quad (\text{A.14})$$

The most practical units for this flux is particles/cm²/sr/eV/sec. The calibrated energy resolution of each channel $\left(\frac{\Delta E}{E} \right)_j$ and stripping cell efficiency η_{sj} can be obtained from Figs. A.8 and A.7, respectively. Although the absolute value of the detection efficiency is not known, the relative detection efficiencies for each channel η_{Dj} can be obtained from standard calibration and are given in Table A.1. Since the other factors in Eq. (A.14) are known, the energy dependence of the neutral flux incident on the analyzer can be extracted from the collected data. Data are collected for all 78 energy channels simultaneously to determine the energy dependence of the neutral flux. Data acquisition rates usually vary between 1 kHz and 50 Hz, depending on the application, although the data acquisition system allows rates up to 1 MHz.

The experimental error associated with the measurement of ϕ_{meas} is given by⁴²

$$\sigma_{\phi}^2 = \sigma_{N_j}^2 \left(\frac{\partial \phi_{\text{meas}}}{\partial N_j} \right)^2,$$

$$= \frac{\phi_{\text{meas}}^2}{N_j} \quad (\text{A.15})$$

where $\sigma_{N_j} = \sqrt{N_j}$ is the statistical error associated with the measurement of N_j . Systematic errors associated with inaccuracies in calibration results are estimated to be $\sim 10\%$.

A.3.3 Inference of Ion Temperature from Measured Data

As discussed in Section 2.2.2, the background plasma is assumed to be in thermal equilibrium where the ion distribution is given by a Maxwellian distribution [see Eq. (2.56)]. Starting from Eq. (A.5) and using Eq. (2.56) for the ion distribution function, the following equation for the expected flux measured by the NPA results (neglecting recombination):

$$\phi_o(E) = 1.24 \times 10^5 \frac{\sigma_{\text{cx}}(E)E^{1/2}}{A^{1/2}} \int \frac{n_o(s)n_i(s)}{T_i(s)^{3/2}} e^{-E/T_i(s)} P(s, E) ds. \quad (\text{A.16})$$

The common method of analysis used to extract the ion temperature from the measured data is known as the asymptotic slope method. This method simply assumes that the more energetic measured neutrals must have originated predominantly from the hottest regions of the plasma. The justification for the use of this method can be seen by computing the energy spectrum that the NPA should measure using representative neutral density, ion density, and ion temperature profiles in Eq. (A.16). The results of one such computer simulation using typical ATF parameters are shown in Fig. A.11. In this figure, the five dashed lines are the contributions of different layers (each 20% deeper in the plasma) to the measured charge-exchange flux, while the bold, solid line represents the total contribution of the entire plasma. Although the total distribution is generally not a linear function of energy, the basis for the assumption used in the asymptotic method is seen; the high-energy component of the total distribution does in fact closely resemble the neutral flux emanating from the central regions of the plasma.

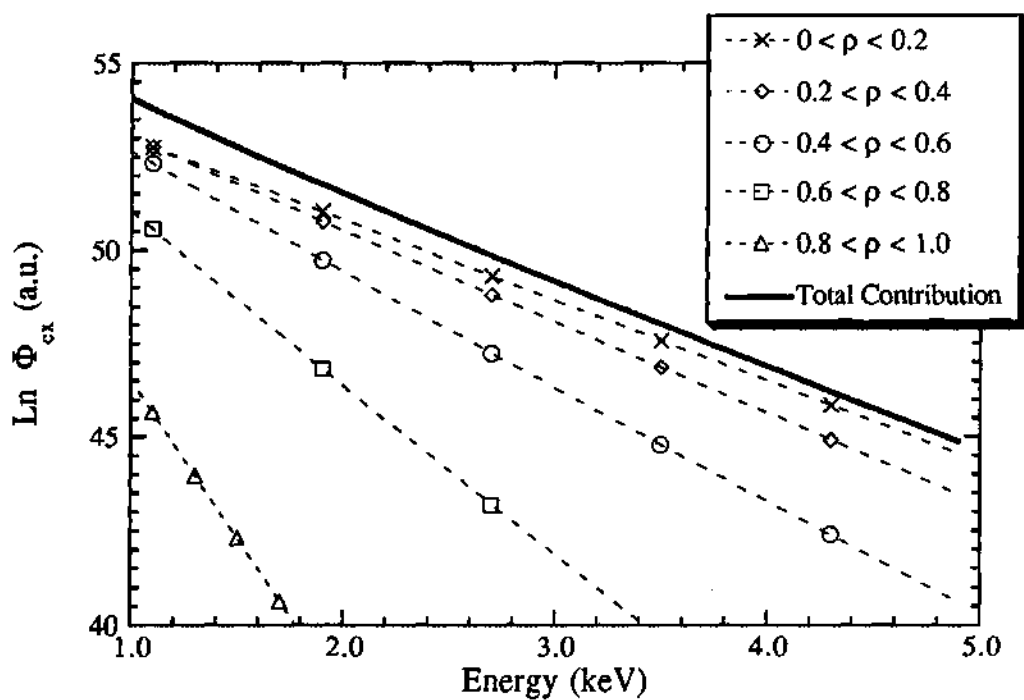


Figure A.11: Expected contributions to the charge-exchange flux from various layers of a typical ATF plasma. Each of the dashed lines represents the contribution of a different layer of the plasma to the measured charge-exchange flux. The bold, solid line represents the total contribution from the entire plasma. The ion temperature profile in this case is parabolic.

Assuming that the measured flux at high energies originates from some small region δs along the viewing chord, Eq. (A.16) then reduces to¹⁹

$$\phi(E) \propto \frac{\sigma_{cx}(E)E^{1/2}}{A^{1/2}} \frac{n_{oo}n_{io}}{T_{io}^{3/2}} \exp(-E/T_{io})P(s, E)\delta s, \quad (\text{A.17})$$

where n_{oo} , n_{io} , and T_{io} are the central neutral density, ion density, and ion temperature, respectively. The central ion temperature can be deduced from the shape of the measured neutral energy spectrum by

$$\frac{1}{T_{io}} = -\frac{d}{dE} \ln \hat{\phi}, \quad (\text{A.18})$$

where

$$\hat{\phi}(E) = \frac{\phi(E)}{\sigma_{cx}(E)E^{1/2}P(0, E)} \quad (\text{A.19})$$

is the corrected flux.

Although the escape probability $P(0, E)$ can be evaluated numerically using the known viewing geometry and density profile information from Thomson scattering, it is usually chosen to be unity. The ion temperature is determined from the best linear fit to the measured neutral spectrum using a weighting function W_i that is inversely proportional to the statistical uncertainty in the measured value of $\ln \phi(E_i)$ at each point. The weighting function is given by⁹

$$W_i = \left(\frac{1}{N_i} + R^2 \right)^{-1},$$

where N_i is the number of counts in a particular energy channel, and the extra factor R^2 arises from a combination of the estimated shot-to-shot reproducibility and systematic errors such as inaccuracies in the various calibration parameters. These systematic errors are estimated to be $\sim 10\%$.

Since the energy limits of the fit are critical in determining the correct ion temperature from this method, the analysis code iterates the fit several times with the ion temperature from each successive fit used to yield better energy fit limits.

These fit limits are constrained such that the fit for the $(j+1)$ th iteration is generally taken between $4T_j$ and $10T_j$, where T_j is the ion temperature computed for the j th iteration. The convergence of this method is generally very quick.

In general, one finds that the small underestimate in T_{io} that results from contributions to the measured flux from regions away from the plasma center is partially compensated by the overestimate in T_{io} associated with the inability of low-energy neutrals to escape from the plasma center. The result is that at moderate $n_{el}/T_i \sim 10^{15} \text{ cm}^{-2} \cdot \text{keV}^{-1}$ the slope of the high-energy region tends to give a surprisingly accurate measure of T_{io} .¹ However, in very high density plasmas, the measured data far out on the tail of the distribution may be poor in quality or nonexistent. In this case, modeling of the processes by which the spectrum is produced becomes necessary in order to deduce the central ion temperature by "passive" techniques.

A by-product of this analysis is an estimate of the central neutral density since the absolute magnitude of the charge-exchange outflux is dependent on the neutral density. The intercept of the best fitting line as determined above is given by

$$\ln \hat{y}_0 = \ln \left(\frac{n_{oo} n_{io} \delta s}{T_{io}^{3/2}} \right). \quad (\text{A.20})$$

The application of this technique is difficult because the inferred neutral density is extremely sensitive to the chord-integrated nature of the NPA measurement. In addition, it requires absolute calibration (as opposed to relative channel efficiency) of the NPA system.

In principle, a direct measurement of the ion temperature profile can be made by scanning the sightline of the analyzer across the cross section of the plasma, taking sequential temperature measurements at each angle. All of the analysis is the same as described above except that the extracted ion temperature is that of the hottest point along the viewing chord. This method assumes that the ion

temperature profile is monotonically decreasing as the plasma minor radius increases (i.e., $dT_i/dr < 0$). The ramifications if this condition is not met are elaborated upon in Chapter 5.

REFERENCES

- ¹ R. J. Goldston, in *Diagnostics for Fusion Reactor Conditions*, Varenna, p. 263 (CEC, Brussels, 1982).
- ² C. B. Wharton, in *Course on Plasma Diagnostics and Data Acquisition Systems*, p. 70 (1975).
- ³ E. W. McDaniel, *Collision Phenomena in Ionized Gases* (John Wiley & Sons, Inc., New York, 1964).
- ⁴ R. L. Freeman and E. M. Jones, Technical Report CLM-R 137, Culham Laboratory (1974).
- ⁵ V. V. Afrosimov and A. I. Kislyakov, in *Diagnostics for Fusion Reactor Conditions*, Varenna, p. 289 (CEC, Brussels, 1982).
- ⁶ H. Zushi et al., J. Phys. Soc. Jpn. **51**, 2673 (1982).
- ⁷ D. Okano et al., J. Nucl. Mater. **145**, 504 (1987).
- ⁸ R. D. Bengtson, P. M. Valnaju, A. Ouroua, and W. L. Rowan, Rev. Sci. Instrum. **61**, 3110 (1990).
- ⁹ G. H. Neilson, Technical Report ORNL/TM-7333, Oak Ridge National Laboratory (1980).
- ¹⁰ C. F. Barnett et al., Technical Report ORNL/TM-5206, Oak Ridge National Laboratory (1977).
- ¹¹ H. Brysk, Plasma Phys. **15**, 611 (1973).
- ¹² J. D. Strachan, T. Nishitani, and C. W. Barnes, Rev. Sci. Instrum. **59**, 1732 (1988).
- ¹³ R. C. Isler, Nucl. Fusion **24**, 1599 (1984).
- ¹⁴ D. P. Hutchinson and K. L. VanderSluis, Technical Report ORNL/TM-5071, Oak Ridge National Laboratory (1975).
- ¹⁵ V. G. Abramov et al., Sov. Phys.-Tech. Phys. **16**, 1520 (1972).
- ¹⁶ A. A. E. van Blokland et al., Rev. Sci. Instrum. **61**, 3117 (1990).
- ¹⁷ G. H. Neilson, Technical Report ORNL/TM-6823, Oak Ridge National Laboratory (1979).

- ¹⁸ M. P. Petrov, *Sov. J. Plasma Phys.* **2**, 201 (1976).
- ¹⁹ S. L. Davis, D. Mueller, and C. J. Keane, *Rev. Sci. Instrum.* **54**, 315 (1983).
- ²⁰ H. P. Eubank, in *Course on Plasma Diagnostics and Data Acquisition Systems*, p. 152 (1975).
- ²¹ A. L. Roquemore et al., *Rev. Sci. Instrum.* **56**, 1120 (1985).
- ²² J. L. Wiza, *Nucl. Instrum. Methods* **162**, 587 (1979).
- ²³ M. R. Wade et al., *Rev. Sci. Instrum.* **61**, 3202 (1990).
- ²⁴ BiRa Systems, Inc., Model 911 and 903, Albuquerque, NM 87107.
- ²⁵ Jorway Corp. Model 412, Westbury, NY 11590.
- ²⁶ LeCroy Research Systems Corp. Model 8501, Palo Alto, CA 94303.
- ²⁷ LeCroy Research Systems Corp. Model 2415, Palo Alto, CA 94303.
- ²⁸ Jorway Corp. Model 321, Westbury, NY 11590.
- ²⁹ Joerger Enterprises, Inc., Model 320, East Northport, NY 11731.
- ³⁰ Kinetic Systems Corp. Model 3470, Lockport, IL 60441.
- ³¹ Digital Equipment Corp., Westminister, MA 01473.
- ³² K. L. Kannan and L. R. Baylor, *Rev. Sci. Instrum.* **59**, 1783 (1988).
- ³³ A. L. Roquemore et al., *Bull. Am. Phys. Soc.* **25**, 950 (1980).
- ³⁴ R. J. Colchin et al., *Rev. Sci. Instrum.* **59**, 1667 (1988).
- ³⁵ R. K. Janev, W. D. Langer, K. Evans, Jr., and D. E. Post, Jr., *Elementary Processes in Hydrogen-Helium Plasmas — Cross Sections and Reaction Rate Coefficients* (Springer-Verlag, Berlin, 1987).
- ³⁶ J. Sheffield, *Plasma Scattering of Electromagnetic Radiation* (Academic Press, Orlando, 1975).
- ³⁷ W. M. Stacey, *Fusion Plasma Analysis* (John Wiley & Sons, Inc., New York, 1981).
- ³⁸ I. H. Hutchinson, *Principles of Plasma Diagnostics* (Cambridge University Press, Cambridge, 1987).

- ³⁹ K. H. Burrell, *J. Comput. Phys.* **27**, 88 (1978).
- ⁴⁰ K. Audenaerde, G. Emmert, and M. Gordinier, *J. Comput. Phys.* **34**, 268 (1980).
- ⁴¹ J. T. Hogan and J. F. Clarke, *J. Nucl. Mater.* **53**, 1 (1982).
- ⁴² P. R. Bevington, *Data Reduction and Error Analysis for the Physical Sciences* (McGraw-Hill, New York, 1969).

Appendix B

FPACX Simulation Code

Because the physical processes governing the thermalization of the injected ions are extraordinarily complicated, modeling the evolution of the energetic-ion distribution function is usually necessary to infer information from NPA measurements. To model the data measured by the NPA during neutral beam injection (NBI) in ATF, the FPACX simulation code has been developed by the author. This simulation is based on a finite-difference solution to the Fokker-Planck equation [Eq. (2.64)]. The basic steps involved in this simulation are described in some detail in Section B.1. This equation does not take into account the effect of the magnetic configuration on the distribution function, so care must be taken in using this simulation, because loss regions and other orbit effects that are not taken into account may deplete the distribution in certain regions of velocity space. The restrictions in the case of ATF are briefly discussed in Section B.2.

B.1 Physics Models in FPACX

The energy spectra measured by the NPA are dependent on two basic quantities: the local ion distribution function and the neutral density at each point along the analyzer viewing sightline [see Eq. (A.9)]. Because each of these quantities is difficult to quantify analytically, and because of the chord-integrated nature of the measurement, it is generally necessary to simulate the measured spectra numerically.

There are four basic steps (each of which is described in more detail in the

following sections) in this process. Since this simulation is based on the Fokker-Planck equation, the first step in the simulation is the computation of the fast-ion source term, $S(\rho, v, \xi, t)$ in Eq. (2.64). Next, a self-consistent neutral profile is calculated solving the neutrals transport equation in cylindrical geometry with electron density and temperature profiles inferred from experimental data.¹ Third, the fast-ion distribution is calculated on each of 50 radial mesh locations. This is accomplished in FPACX by using the FIFPC code developed by R. H. Fowler.² Finally, the expected measured flux is calculated by performing the integral given in Eq. (A.9) using the calculated distribution function and folding in the calculated neutral density profile and the geometry of the NPA on ATF.

Since the energetic-ion Fokker-Planck equation [Eq. (2.64)] describes the evolution of the velocity distribution at a particular point in physical space, a configuration space coordinate system must be chosen. For the purposes of this calculation, a cylindrical coordinate system has been chosen. The system is assumed to be axially and azimuthally symmetric so that the distribution function is simply dependent on the radial coordinate. In toroidal devices, most plasma parameters are constant on a flux surface, labeled by the flux coordinate ψ . Hence, it is natural to choose ψ (or, equivalently, the normalized radius ρ) as the radial coordinate (these coordinates are discussed further in Section 2.1). Velocity space is assumed to be defined by an azimuthally symmetric spherical coordinate system where the distribution function is defined in terms of the velocity v and the pitch angle variable $\xi = \cos \theta$.

B.1.1 Computation of the Source Term

The form of the source term $S(\rho, v, \xi, t)$ is important in determining the overall magnitude and energy dependence of the energetic-ion distribution. In the case of NBI, this source term is determined by the position in real and velocity

space where the incoming fast neutrals are ionized by the plasma. Since the cross sections of the processes involved in this process are fairly well known, the form of the source term can be computed quite accurately. Because of the finite size of the beam and plasma, simple expressions such as $S(\rho, v, \xi, t) = S_0(\rho)\delta(v - v_{inj})\delta(\xi - \xi_{inj})$ are inappropriate when accuracy is required. In this case, the source term must be numerically evaluated.

Since the physics of the beam injection process is simple, the calculation of the beam deposition profile would seem to be straightforward. However, the complicated geometry associated with a finite-size beam passing through a non-circular plasma makes the calculation of this profile complex. The variation of S with speed and time is usually fairly well known, since these are just intrinsic properties of the injector itself. However, the dependence of S on plasma radius ρ and pitch angle ξ must be computed to obtain an accurate representation of the source term. Two methods are provided in FPACX to compute this term. The first method calculates the normalized deposition profile $H(\rho)$ based on an analytic formula. The second method determines $H(\rho)$ using Monte Carlo techniques that simulate the injection and ionization of the injected neutrals. Each of these methods is described in more detail in the following sections.

Analytic Beam Deposition Profile The ionization of the injected neutrals in a pencil beam as they pass through the plasma is governed by the equation

$$\frac{dN_b}{ds} = -\frac{N_b}{\lambda(s)}, \quad (\text{B.1})$$

where $\lambda(s)$ is the mean free path against ionization of a particle at point s within the plasma. The general solution of this equation is

$$N_b(s) = N_b(0) \exp \left[-\int_0^s \frac{ds'}{\lambda(s')} \right]. \quad (\text{B.2})$$

Since the rate of fast-ion production is just the negative of the rate of beam loss due to ionization, the rate at which fast ions are produced for a pencil beam can be computed easily from Eq. (B.2). Integrating over the face of the beam provides the total fast-ion birth distribution. The details of this calculation have been described by Rome et al.³ and the results are summarized here.

The fast-ion source rate on a given flux surface for a cylindrical beam injected with a tangency radius R_{tan} into a plasma device having major radius R_o and minor radius a , elongation κ , and flux surfaces (denoted by ρ) shifted by $\Delta(\rho)$ is given by

$$\dot{n}_f(\rho) = \frac{I_b}{eV_p} H(\rho), \quad (B.3)$$

where I_b is the beam current, V_p is the plasma volume, and $H(\rho)$ is the normalized deposition profile given by⁴

$$H(\rho) = H^+(\rho) + H^-(\rho), \quad (B.4)$$

where the contribution from the outer (H^+) and inner (H^-) intersection of the beam with the flux surface is

$$H^\pm(\rho) = 2 \int_0^{z_u} dz_b \int_{R_L}^{R_u^\pm} dR_b J_b(\alpha) h^\pm(\rho, R_b, z_b). \quad (B.5)$$

The integration variables R_b and z_b are the major radius and distance from the vertical plane of each differential beamlet. The integration in R_b and z_b extends over the beam cross section. The integration limits

$$\begin{aligned} z'_u &= \min[\kappa r_\rho, r_b], \\ R_L &= R_{tan} - (r_b^2 - z_b^2)^{1/2}, \\ R_u^\pm &= \min \left\{ R_o \pm [r_p^2 - (z_b/\kappa)^2]^{1/2}, R_{tan} + (r_b^2 - z_b^2)^{1/2} \right\} \end{aligned}$$

ensure that only beamlets intersecting the given flux surface ρ contribute to $H(\rho)$. The current density distribution within the beam cross section is assumed to be

Gaussian in shape and is given by

$$J_b(\alpha) = \begin{cases} \frac{1}{\pi\sigma^2} [1 - \exp(-r_b^2/\sigma^2)]^{-1} \exp(-\alpha^2/\sigma^2), & 0 < \alpha \leq r_b \\ 0, & \alpha > r_b \end{cases}$$

$$\alpha = [(R_b - R_{tan})^2 + z_b^2]^{1/2},$$

where α is the perpendicular distance from the beam centerline and σ is the Gaussian half-width of the current density profile.

The normalized deposition profile for each differential beamlet is given by

$$h^\pm(\rho, R_b, z_b) = \frac{a^2}{2} \left(1 + \frac{\Delta(\rho)}{R_o}\right)^{-1} \frac{R}{(R^2 - R_b^2)^{1/2}} \frac{1}{[r_\rho^2 - (z_b/\kappa)^2]^{1/2}} \\ \times \{\exp(-D_0) + \gamma_d \exp[-(D_0 + 2D_1)]\} \frac{1}{\lambda(\rho)},$$

where

$$R = R_o \pm [\rho^2 - (z_b/\kappa)^2]^{1/2},$$

$$D_0 = D \left\{ R, R_o + [a^2 - (z_b/\kappa)^2]^{1/2} \right\},$$

$$D_1 = D(R_b, R).$$

The factor γ_d determines whether the second intersection of the beamlet with the flux surface is included. Thus, $\gamma_d = 1$ when the beam intersects the outside wall (tangential injection) and $\gamma_d = 0$ when the beam intersects the inside wall (perpendicular injection).

The beam decrement D along the beamlet path between major radii R_1 and R_2 is

$$D(R_1, R_2) = \int_{R_1}^{R_2} \frac{R' dR'}{(R'^2 - R_b^2)^{1/2}} \frac{1}{\lambda(\rho')},$$

where λ is the local mean free path for ionization of the injected neutral evaluated at

$$r_\rho(\rho') = [(R' - R_o)^2 + (z_b/\kappa)^2]^{1/2}.$$

Neutral ionization due to electron impact, hydrogenic-ion charge-exchange and impact, impurity charge-exchange and impact, and charge-exchange with fast ions are all included in the formulation of λ .

Although complex in form, $H(\rho)$ is fairly easy to calculate numerically since the cross sections of the various ionization processes are well known and the rest is just simple integration. The only necessary input parameters are the various plasma parameters (such as density and temperature of the plasma constituents) and the energy of the injected beam particles.

The fast ion source rate on each flux surface $\dot{n}_f(\rho)$ provides the spatial dependence of the source term in Eq. (2.64). The pitch-angle dependence of the source term is handled in the following manner in FPACX. First, a "central" pitch angle is derived for each flux surface by calculating the angle at which a pencil beam passing down the centerline of the neutral beam injector intersects concentric toroidal surfaces with characteristic major radius R_0 and minor radius r_ρ . This pitch angle can be calculated from simple geometry and is given by

$$\xi_{inj}(\rho) = \frac{R_{tan}}{R_0 + r_\rho(\rho)}.$$

The velocity-space dependence of the source term is then assumed to be of the form

$$S(v, \xi) = \exp \left\{ -\frac{[v - v_{inj}(\rho)]^2}{\Delta v^2} - \frac{[\xi - \xi_{inj}(\rho)]^2}{\Delta \xi^2} \right\}, \quad (\text{B.6})$$

where Δv and $\Delta \xi$ are defined by the user. For most of the simulations presented here, $\Delta \xi$ has been chosen to be of the same width as the Gaussian half-width of the beam. In principle, the value of Δv should be chosen to be as small as possible in order to simulate the delta function nature of the source. However, because of numerical instability near these delta functions, it was found that Δv could not be reduced below a certain value without losing accuracy near the energies associated with the three components of the beam. Therefore, for most of the simulations presented in this dissertation, $\Delta v \simeq 0.03$.

Monte Carlo Beam Deposition A second approach used in FPACX to calculate the beam deposition profile is to simulate the injection process itself via Monte Carlo techniques using the NFREYA beam deposition code developed by R. H. Fowler.⁵ This approach (originally used by Lister et al.⁶) involves modeling the injection process by simulating the "optical" properties of the neutral injector and following individual particles until they are ionized within the plasma or strike the wall of the vacuum vessel or beam duct. The NFREYA code was adapted for use on ATF by R. N. Morris and is described in more detail in Ref. 7.

The finite-width neutral beam is modeled by an array of parallel rays traveling horizontally into the plasma from the ion source. Initial spatial coordinates are chosen randomly in a fashion that makes the beam either circular or rectangular. The initial velocity coordinates are generated randomly from a Gaussian distribution centered about the vertical and horizontal focal lengths of the injector and with widths determined by the vertical and horizontal divergence of the injector. The energies of the injected particles are randomly selected with probability proportional to the measured beam intensity at E_{inj} , $E_{inj}/2$, and $E_{inj}/3$. If the initial location and trajectory of the particle are such that the particle is stopped by the injector aperture, the particle is discarded.

The deposition of injected particles can be determined by the usual Monte Carlo technique⁸ for simulating exponential attenuation [see Eq. (B.2)]. A random number η is selected such that $0 < \eta < 1$. The integral

$$I = \int \frac{ds}{\lambda(s)}$$

is then performed, where s is the distance along the path of the beam and λ is the mean free path against ionization at position s . At the point along the trajectory where $I = \ln(1/\eta)$, the beam neutral is taken to be ionized, and its physical coordinates (ψ or ρ) and velocity coordinates (v, ξ) are stored. By simulating the

injection of a large number of particles in this manner, the beam deposition profile for a particular energy component, E_k , can be computed. The profile is given by⁵

$$H_k(\psi) = \frac{n_k(\psi)}{\Delta^3\psi} \frac{V_p}{N_k}, \quad (\text{B.7})$$

where $n_k(\psi)$ is the number of ions with birth locations in the volume element $\Delta^3\psi$, V_p is the plasma volume, and N_k is the number of neutral atoms injected with energy E_k .

As evidenced by Eqs. (2.29) and (2.30), the injected ions have finite excursions from their original flux surface during the period of a single orbit. Because the slowing-down time of these particles is much longer than the bounce time (defined as the amount of time for a single orbit), the choice of the flux surface to which a particle should be assigned is not unique. To alleviate this problem, the fast ion created by the ionization process above is followed along its initial orbit for one-half of a bounce orbit. The beam deposition profile is then given by

$$H_k(\psi) = \frac{\langle n_k(\psi) \rangle}{\Delta^3\psi} \frac{V_p}{N_k}, \quad (\text{B.8})$$

where

$$\langle n_k(\psi) \rangle = \sum_i \frac{\Delta t_{\psi,i}}{\tau_{B,i}}.$$

Here, $\Delta t_{\psi,i} = (t_{\psi+\Delta\psi})_i - t_{\psi,i}$ is the amount of time spent by particle i in the volume element $\Delta^3\psi$ and $\tau_{B,i}$ is the bounce time of particle i . This effectively "smears" the contribution of a particle to the beam deposition profile over its initial orbit.

The source function $S(\rho, v, \xi, t)$ can then be accurately formulated since the dependences on ρ and ξ have been computed. As with most other Monte Carlo techniques, the main disadvantage of using this type of beam deposition simulation is the amount of computational time required for good statistics, which could be restrictive, especially in time-dependent cases. However, since the beam deposition profile is a slowly varying function of the plasma parameters, it is generally not necessary to perform this calculation at each time step.

Most of the calculations described in this work have been made using the analytic $H(\rho)$ calculation. The main advantage of using this method is computational speed. Benchmark comparisons of these two methods have been made for the low-density case described in Section 6.3. The results obtained through each method were extremely similar, indicating that the analytic $H(\rho)$ calculation is sufficiently accurate for this type of simulation.

B.1.2 Calculation of the Neutral Density Profile

The magnitude and shape of the neutral density profile play an important role in both the calculation of the ion distribution function (through charge-exchange losses) and the integration of the charge-exchange flux that is measured by the NPA. In general, the neutral density is a three-dimensional (3-D) quantity because of the local nature of various gas sources such as gas injectors or limiters. Unfortunately, computing the 3-D dependence of the neutral density requires the use of time-consuming Monte Carlo techniques.⁹ Typically, the neutral density is strongly dependent on the plasma parameters, so that this calculation would be required at each time step of the simulation, making the use of this method prohibitive. Hence, the neutral density is generally assumed to be dependent only on the radial coordinate ρ , and the neutral density profile $n_o(\rho)$ is computed using a cylindrical neutrals transport model.¹

Studies have shown that the neutral density profile shape is generally independent of toroidal location, although the magnitude near a localized gas source may be enhanced by up to two orders of magnitude.^{10,11} Therefore, the toroidally averaged profile computed by FPACX is probably incorrect in regions near a localized source. This inaccuracy should not affect the calculation of the fast-ion distribution since the fast ions, in general, experience a toroidally averaged neutral density. However, care must be taken in using this neutral density profile to calcu-

late the expected charge-exchange flux to be measured by the NPA. The placement of the gas valve directly in front of the NPA virtually ensures that there is some enhancement of the neutral density in regions near the NPA. However, since most of the simulations of the measured fast-ion energy spectra are for viewing angles near tangential, this enhancement is not a large effect because the sightline of the NPA in this case does not pass through the center of the plasma until almost an entire field period away from the gas valve. Therefore, the enhancement of the neutral density due to the location of the gas valve should not cause significant problems in the analysis.

This code requires several inputs. Most important among these are the electron density and temperature profiles and the rate and energy at which neutrals are added to the plasma at the edge. The electron density and temperature profiles are generally taken from Thomson scattering measurements. Although theoretically the neutral source rate could be inferred from H_α measurements, this method is, in practice, very difficult. In FPACX, the neutral source rate is estimated from the particle balance equation:

$$\frac{dN}{dt} = -\frac{N}{\tau_p} + R\frac{N}{\tau_p} + S_{ext}, \quad (B.9)$$

where N is the total number of electrons in the plasma, τ_p is the global particle confinement time, R is the wall recycling coefficient, and S_{ext} is the neutral source rate from external sources. Since the wall recycling coefficient is generally not known, the two source terms on the right-hand side of this equation can be combined to give a total source rate S_{tot} . The total neutral source rate is then given by

$$S_{tot}(t) = \frac{dN}{dt} + \frac{N}{\tau_p}. \quad (B.10)$$

The total source rate is then determined by the choice of the global particle confinement time τ_p , since all other quantities on the right-hand side of this equation are known. Typically, the global particle confinement time τ_p is chosen to be on

the order of 10-30 msec for the simulations. For all of the studies conducted in this work, the average edge neutral energy has been assumed to be 5 eV. This choice is discussed further in Section 5.3.

B.1.3 Calculating the Fast-Ion Distribution

The true quantity of interest in this entire simulation is the fast-ion distribution function. Various aspects of fast-ion confinement and thermalization may be obtained from certain characteristics of this distribution. To compute the fast-ion distribution function, FPACX uses the fast-ion Fokker-Planck code FIFPC developed by R. H. Fowler at ORNL, the details of which are described in Ref. 2. In FPACX the fast-ion distribution function is computed independently on 50 different radial mesh locations. The distribution function is computed on each of these mesh locations in terms of a 40-by-40 grid in velocity space (v and θ). This fairly large number of mesh locations was necessary because of complications associated with the NPA viewing geometry. The effects of loss regions and the radial diffusion of the fast ions are neglected in this simulation, since neither of these can be quantified from experimental observation.

A large number of parameters describing the plasma conditions and the fast-ion source from the beam are required as inputs. The plasma parameters necessary for this calculation include the electron and ion density and temperature profiles, the Z_{eff} profile, and the neutral density profile. As in the calculation of the neutral density profile, the electron and temperature profiles are inferred from Thomson scattering measurements. Typically, these profiles are available for only a few times of interest during the discharge. For intermediate times, the shapes of these profiles are assumed to be constant, with the magnitude adjusted such that the simulated central electron temperature and density were consistent with other measured quantities, namely, the central electron temperature measured by a 16-channel

ECE system and the electron line density measured by a 2-mm interferometer.

The ion density is taken to be a fraction of the electron density, usually between 0.9 and 0.95. The ion temperature profile is assumed to be parabolic, with the central temperature inferred from NPA or spectroscopic measurements. The Z_{eff} profile is assumed to be flat with the magnitude chosen in one of two ways. In simulations where visible bremsstrahlung data are available, Z_{eff} is obtained from the empirical formula given in Ref. 12. Otherwise, Z_{eff} is inferred from spectroscopic measurements.

B.1.4 Computing the Theoretically Expected Charge-Exchange Flux

The charge-exchange flux that should be measured by the NPA can then be computed using Eq. (A.9). Some considerations must be addressed in performing this integration because of the complicated geometry associated with the analyzer's "view" of the plasma. Typically, both the normalized plasma radius ρ and the pitch angle "viewed" by the analyzer ξ vary as a function of the distance along the analyzer sightline s . This variation is shown quite clearly in Figs. B.1 and B.2, where the variation of ρ and ξ with the distance along various NPA chords in the standard ATF magnetic configuration are plotted. These quantities are obtained by using a full 3-D representation of the magnetic field and an accurate representation of the analyzer viewing geometry. Typically, these quantities are computed at 4-cm spacings along the analyzer sightline. The values of quantities such as the electron temperature, neutral density, etc., along the chord are then computed using standard interpolation techniques. For example, the local neutral density at any location along the sightline n_s is computed by first determining the normalized plasma radius of this location $\rho(s)$. Then, the local neutral density is obtained by interpolation on the previously calculated neutral density profile.

The ion distribution function as computed by FIFPC is defined in terms

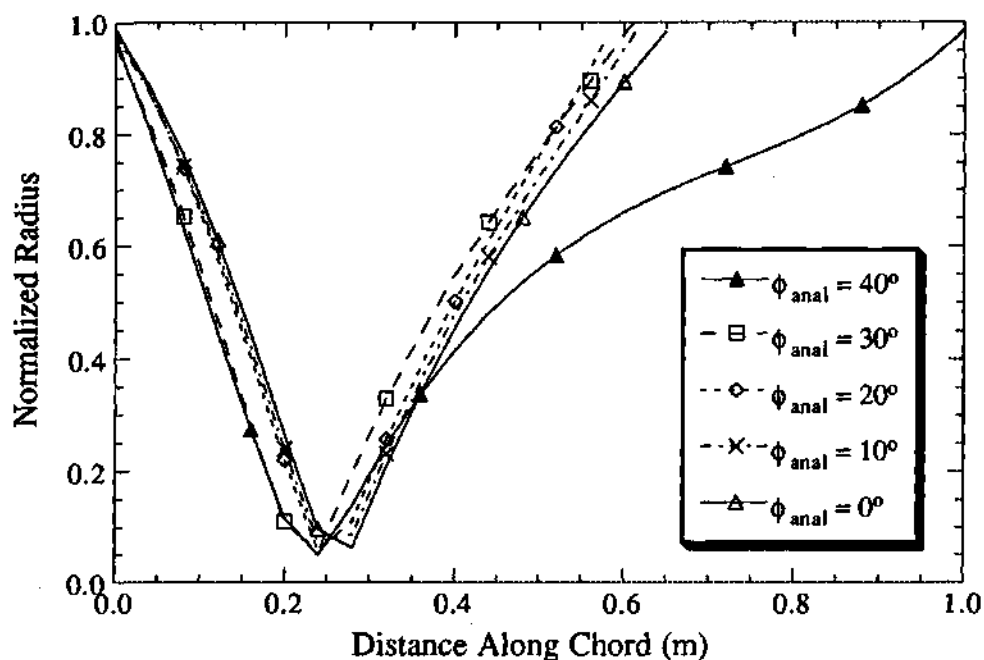


Figure B.1: Variation of the plasma normalized minor radius along the length of various viewing chords of the NPA on ATF.

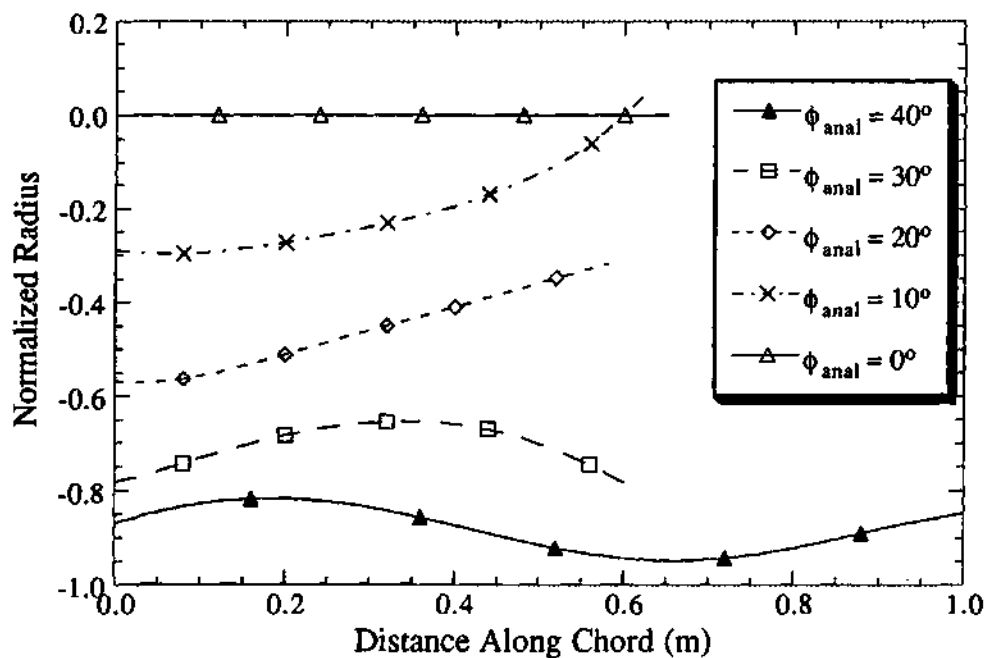


Figure B.2: Variation of the viewed pitch angle along the length of various viewing chords of the NPA on ATF.

of the velocity-space variables v and θ . The transformations $E = mv^2/2$ and $\xi = \cos \theta$ are used to transform the computed ion distribution function into the form specified in Eq. (A.9). Care must be taken in including only the contributions of the appropriate pitch angle of the distribution function in the integration of Eq. (A.9).

B.2 Restrictions on using FPACX for ATF

As discussed in Section B.1.3, the effects of loss regions and the radial diffusion of the fast ions are neglected in this model. Because each of these processes can have a distinct effect on the actual distribution function, care must be taken in the application and interpretation of the results of this simulation. In this section, these restrictions and their effect on the simulation of the energy spectra measured by the NPA are briefly discussed.

As discussed in Chapter 4, the loss regions in ATF are quite large, especially in regions of velocity space near $v_{\parallel} = 0$. In general, there are two ways to handle the loss regions. The first way is to set $f_b = 0$ inside the loss regions and then solve Eq. (2.64) with this restriction.³ This effectively models the physics of a loss region in which particles that scatter into the loss region are instantly lost from the system. The main problem with using this method in ATF is the specification of the loss region. Because the loss region is a complicated function of pitch angle, energy, and position, the loss region is difficult to specify from analytic considerations, as has been done in the tokamak case.³ Without an accurate representation of the loss region, the calculated distribution function in the vicinity of the loss region is inaccurate.

The second method is simply to neglect the effect of the loss region and only consider parts of the distribution function in which the loss region has a small effect. Although the effect of the loss region is not simply confined to the loss region itself

because of the tendency of the distribution function to diffuse into these depleted regions, the largest effects are fairly localized to regions of velocity space near the loss region. This is the method used in FPACX since the tangentially injected ions can be detected by the NPA (when oriented properly) before they have pitch-angle scattered into regions where the effect of orbit losses is important. The motivation for this choice is twofold. The first reason is that the loss region is difficult to represent analytically, making it necessary to compute the loss region with time-consuming numerical codes. Because the loss region is dependent on many different variables, a full survey of the possible permutations of these variables would require an enormous amount of computational time. The second reason for neglecting the effects of the loss region is the distinct change of the orbit topology in ATF as the particles approach the trapping boundary. As discussed in Chapter 4, there are two distinct sets of ion orbits in ATF — circulating particles and helically trapped particles. In general, the circulating particles have fairly small excursions from a flux surface. Hence, one of the basic assumptions made in the calculation of the fast-ion distribution function — that particles remain on the same flux surface as they slow down — is justified. However, in the case of helically trapped particles, this assumption is not justified since, in general, these particles make large excursions from their original flux surface. The corresponding convective motion of these particles is not taken into account in Eq. (2.64). Since the transition from circulating to helically trapped usually takes place in the vicinity of the loss region, computing the ion distribution function near the loss region would be extraordinarily difficult even if the exact location of the loss region was known.

In neglecting the effect of the loss region, the range of validity of this particular approach is limited to regions of velocity space far away from the loss region. Fortunately, the ions injected tangentially into ATF via the neutral beam injectors are in a region of velocity space well away from the loss region. Furthermore, the

NPA on ATF can be oriented such that it views particles that are well away from the loss region. Therefore, this method is fairly accurate in simulating the energy spectra measured by the NPA for viewing orientations in which $|\phi_{\text{anal}}| \geq \pm 20^\circ$.

REFERENCES

- ¹ K. H. Burrell, J. Comput. Phys. **27**, 88 (1978).
- ² R. H. Fowler, J. Smith, and J. A. Rome, Comput. Phys. Commun. **13**, 323 (1978).
- ³ J. A. Rome, J. D. Callen, and J. F. Clarke, Nucl. Fusion **14**, 141 (1974).
- ⁴ H. C. Howe, Technical Report ORNL/TM-11521, Oak Ridge National Laboratory (1990).
- ⁵ R. H. Fowler, J. A. Holmes, and J. A. Rome, Technical Report ORNL/TM-6845, Oak Ridge National Laboratory (1979).
- ⁶ G. G. Lister, D. E. Post, and R. J. Goldston, in *Third Symposium on Plasma Heating in Toroidal Devices, (Varennna, 1976)* (Editrice Compositori, Bologna, 1976).
- ⁷ R. N. Morris et al., Nucl. Technol./Fusion **12**, 281 (1987).
- ⁸ E. D. Cashwell and L. L. Carter, Technical Report TID-26607, U.S. ERDA Critical Review Series, National Technical Information Service (1978).
- ⁹ J. T. Hogan, J. Nucl. Mater. **111 & 112**, 413 (1982).
- ¹⁰ G. H. Neilson, Technical Report ORNL/TM-7333, Oak Ridge National Laboratory (1980).
- ¹¹ W. A. Davis and R. J. Colchin, Phys. Fluids **29**, 2249 (1986).
- ¹² S. Morita et al., Technical Report ORNL/TM-11737, Oak Ridge National Laboratory (1991).

VITA

Mickey Ray Wade, son of Bobby R. Wade and Ella W. Wade, was born December 30, 1962, in Kinston, North Carolina. He graduated from Kinston High School in 1981 and entered college at Virginia Polytechnic Institute and State University (Virginia Tech) in Blacksburg, Virginia, that same year, where he studied Nuclear Science and Engineering. He was a member of the Virginia Tech varsity golf team during the 1982-83 and 1983-84 seasons and in December 1984 received the degree of Bachelor of Science in Nuclear Science and Engineering.

After graduation, Mr. Wade worked as an application programmer at the University of North Carolina in Chapel Hill, North Carolina. In the fall of 1986, he began his graduate studies in Nuclear Engineering and Fusion Technology at the Georgia Institute of Technology in Atlanta, Georgia. In December 1987, he received the degree of Master of Science in Nuclear Engineering. In the summer of 1988, he worked as a summer research assistant at Oak Ridge National Laboratory, where his primary responsibility was the design and development of a data acquisition and control system for the neutral particle analyzer installed on the Advanced Toroidal Facility (ATF). Upon completion of the necessary course work for his doctorate, he moved to Knoxville, Tennessee, in December 1988 to continue his research studying ion behavior in ATF.

In May 1991, he was awarded a U.S. Department of Energy Fusion Energy Postdoctoral Research Program appointment to work on the DIII-D tokamak at General Atomics in San Diego, California, beginning in the fall of 1991.

Mr. Wade is married to Stephanie Harper, also formerly of Kinston, North Carolina, and is the proud father of Abigail Renee Wade, born October 29, 1990.